MODELING VAN DER WAALS INTERACTIONS WITH DENSITY FUNCTIONAL THEORY

BY

TREVOR CHARLES JENKINS

A Dissertation Submitted to the Graduate Faculty of

WAKE FOREST UNIVERSITY GRADUATE SCHOOL OF ARTS AND SCIENCES

in Partial Fulfillment of the Requirements

for the Degree of

DOCTOR OF PHILOSOPHY

Physics

May 2025

Winston-Salem, North Carolina

Approved By:

Timo Thonhauser, Ph.D., Advisor

Wendu Ding, Ph.D., Chair

Martin Guthold, Ph.D.

Oana Jurchescu, Ph.D.

Stephen Winter, Ph.D.

Acknowledgements

To begin this dissertation, I would like to extend my deepest gratitude to my advisor, Prof. Timo Thonhauser, for his terrific mentorship over these past six years. His teaching has given me all of the necessary tools to succeed as a physicist, and imparted to me a curiosity and drive that I will take with me for the rest of my career. I am also grateful for the group culture that Timo has cultivated, emphasizing close collaboration and mutual-learning. Since joining his group, I have had the privilege to work with many amazing people who have fully enriched my graduate experience. I would especially like to thank my great friends and colleagues—Dr. Saif Ullah, Dr. Haardik Pandey, Wells Graham, Chris Fivecoat, and Eric Chapman—who have embodied this culture during my time here.

My time in the Thonhauser group has also given me the privilege to work with some amazing people from other institutions. I thank Prof. Jing Li and Prof. Kui Tan for our many collaborations during my time here. I would also particularly like to thank Prof. Kristian Berland, who has been a great mentor and colleague over the years. Our research partnership in that time has led to some really cool discussions and even cooler papers, and I owe a lot of my current knowledge of density functional theory to him.

I extend my appreciation to the members of my research advisory committee, Prof. Steve Winter and Prof. Oana Jurchescu, for their gracious advice and encouragement in the pursuit of my Ph.D. Likewise, I thank Prof. Martin Guthold and Prof. Wendu Ding for the privilege of having them on my defense committee.

The last and biggest thanks go to my family—my Mom, Dad, Stepmom, and siblings—who have supported me every step of the way on my journey to becoming a physicist. I would not be who I am today without them.

Contents

List of Figures

List of Tables

List of Abbreviations

22DMB	2,2-dimethylbutane
23DMB	2,3-dimethylbutane
3MP	3-methylpentane
4-PyC	4-pyradinecarboxylate
ACF	adiabatic connection formula
ACFDT	adiabatic connection fluctuation dissipation theorem
AFM	antiferromagnetic
AIMD	*ab initio* molecular dynamics
B86R	revised B86b exchange
BO	Born-Oppenheimer
BZ	Brillouin zone
c-NEB	climbing image nudged elastic band
CaMOF	Ca(H_2tcpb) (tcpb = 1,2,3,4-tetrakis(4-carboxphenyl)-benzene)
CBM	conduction band minimum
cx13	LV-PW86r exchange
DFT	density functional theory
DMC	diffusion Monte Carlo
ELF	electron localization function
FM	ferromagnetic
FPA	full potential approximation
GBRV	Garrity-Bennett-Rabe-Vanderbilt ultrasoft pseudopotentials
GGA	generalized gradient approximation

HER	hydrogen evolution reaction
HOF	hydrogen-bonded organic framework
ICSD	inorganic crystal structure database
ITC	isothermal titration calorimetry
LDA	local density approximation
LDOS	local density of states
MAD	mean absolute deviation
MARD	mean absolute relative deviation
MD	mean deviation
MOF	metal–organic framework
NEB	nudged elastic band
nHex	linear n-hexane
ONCV	optimized norm-conserving Vanderbilt pseudopotentials
optB88	re-optimized B88 exchange
PAW	plane-augmented wave pseudopotentials
PBE	Perdew-Burke-Ernzerhof exchange-correlation functional
PDOS	phonon density of states
PP	pseudopotential
PW	plane-wave basis set
PW86r	revised PW86 exchange
QE	Quantum ESPRESSO
revPBE	revised PBE exchange
RON	research octane number
SCAN	strongly constrained and appropriately normed semilocal density functional
SCF	self-consistent field
SI	supporting information
STM	scanning tunneling microscopy
THD-C	tetra-, hexa-, dodeca-membered carbon allotrope
TMD	transition metal dichacogenides

TPD	temperature-programmed desorption
TPSS	Tao-Perdew-Staroverov-Scuseria meta-generalized gradient approximation functional
VASP	Vienna *Ab initio* Simulation Package
VBM	valence band maximum
vdW-DF	van der Waals density functional
vdW-DFT	van der Waals density functional theory
WMARD	weighted mean absolute relative deviation

Abstract

Materials physics has been a driving force in human industry and technology for thousands of years. This is truer now than ever before, with the theory of quantum mechanics providing the first-ever accurate model of materials at the atomic scale. With accurate quantum mechanical modeling, a path is opened to address pressing needs in industry by developing novel "functional materials", such as the porous metal–organic frameworks (MOFs). These materials show remarkable adsorption properties, with possible uses in gas storage, fuel refinement, catalysis, and many other fields. Many MOF species have been developed and synthesized, but their usefulness is limited without adequate theoretical description of their behavior. To this end, my work uses density functional theory (DFT) to characterize and predict the behavior of these functional materials. In particular, I use van der Waals density functional theory (vdW-DFT) to model the subtle, long-range forces that drive adsorption in MOFs. For example, we examine differences in adsorption energy between guest molecules, which can be used to separate gas mixtures. With careful modeling, we can identify whether this separability is a function of the MOF's unique structure—as we see with the "gate opening" behavior of RPM3–Zn—or whether it arises from a thermodynamic property of the adsorbate mixture. We observe the latter in the case of Ca(H_2tcpb), solving a long-standing mystery of its temperature-dependent uptake of C6 isomers. Observing and correctly defining these mechanisms requires a high level of accuracy, which can not always be assumed for approximation methods such as DFT. For this reason, several of my projects have aimed to improve the accuracy of vdW-DFT methods. Two projects examine the effect of exchange—which derives from the Pauli exclusion principle—on binding energy in dispersion-dominated systems. Drawing on the lessons learned from these studies, we also

design vdW-DF3-mc, a third-generation nonlocal functional optimized for molecular solids, which can be used to accurately describe thousands of industrially significant materials. These projects demonstrate how vdW-DFT can be used to accelerate progress in industry, and the many available avenues to improving the method's predictive power.

Chapter 1

Materials Physics

1.1 Introduction

The world that we live in is a material one. We, ourselves, and everything with which we interact on a daily basis, are made up of ordinary matter. This matter can be subdivided into states (solid, liquid, gas), or elements (carbon, oxygen, iron, etc.). Even in antiquity, human progress was measured by the most important materials of the time; the stone, bronze, and iron ages. But crucially, all matter obeys the same laws of physics. Understanding the nuances of how different forms of matter interact—how we influence our environment, and vice versa—is thus an ongoing endeavor, one which forms the basis of *materials physics*. Throughout the course of human history, materials physics has been a major driver of technological advancement. One example, as previously alluded to, is metallurgy, wherein many alloys have been created for use in construction and tool-making. Another is chemistry, where understanding the interactive properties of different elements and compounds is vital in the pharmaceutical and fuel industries. And perhaps the most important advancement of the last century is that of silicon-based electronics, which was only made possible by an accurate description of electronic structure in semi-conducting materials. Now more than ever, materials physics is being used to solve long-standing problems in these industries. The problem of energy consumption, for example, is of ever-present focus to the scientific community. Currently, a significant portion of global energy consumption is dedicated to fuel refinement, which often requires raising the octane number of gasoline as

one might see on a gas pump. This octane number is related to the proportion of branched vs. unbranched hydrocarbons in the mixture. Separating such chemically similar species often requires significant heating or cooling, making currently used cryogenics and distillation processes very costly. But there exists a promising alternative in the development of "functional materials", tailor-made solids that can separate these hydrocarbon isomers. Porous functional materials such as metal organic frameworks can be designed to uptake certain species and exclude others, inducing separation with little to no energy cost. The synthesis and testing of novel MOFs on industrially relevant mixtures is thus an active field, growing exponentially over the past decade with the creation of hundreds of new structures.

But while the use of MOFs and other functional materials is an exciting prospect, progress is still hindered unless the theory behind these materials agrees with real-world observations. When modeling a given material, we thus strive toward the standard of *chemical accuracy*, a threshold where the general behavior of materials described by the model matches with those seen in experimental settings. Achieving this level of accuracy for general systems is no small task, and improving materials modeling has thus been the subject of concerted scientific effort for over a century. One important milestone in this development was the discovery of the atom, the fundamental building block of nearly all materials. It subsequently discovered that atoms can be sorted by the number of their constituent particles, into the so-called periodic table of elements. From observation, it was known that different elements can exhibit vastly different properties, and we now know that these properties largely owe to their *electronic structure*. Unlike macroscopic objects, which behave deterministically under the laws of classical mechanics, these electrons are described by quantum mechanics as being probabilistic in nature.

Quantum mechanics thus plays a central role in the advancement of materials physics. With better understanding of what contributions make up the energy states of an electron, we can more accurately predict how matter behaves down to the smallest scales. Some of these contributions are well-known and accounted for in even the simplest models of electronic structure. For example, we know that electrons are charged particles, attracted to opposite charges (protons) and repellant to like charges (other electrons). It is also known that electrons are fermions subject to the Pauli exclusion principle, which means that two

identical electrons cannot occupy the same state at the same time. However, there are many more properties of electron interaction that can impact their structure in subtle but important ways. One common example is that of hydrogen bonding, which is responsible for nucleotide binding in DNA and many intriguing structural properties of water. Hydrogen bonds arise from permanent electric dipoles; when a hydrogen atom binds with another element, it "shares" its one electron and the charge becomes unevenly distributed across the two. Then, when two such complexes are near each other, their dipoles align, creating an attractive force between them. Research in how best to model these bonds is very much an active field in materials physics, and even simple simulations of water have much room for improvement before chemical accuracy is reached.

A similar, even more subtle effect is that of the *van der Waals forces*, which manifest even in the absence of permanent dipoles. In the classical framework, they are said to arise from "instantaneous dipoles", time-dependent fluctuations in the electronic structure that lead to attraction between one or more atoms. Quantum mechanically, the mechanism behind van der Waals forces is known to be somewhat more complex due to the probabilistic nature of the electron. Partly for this reason, and due to its denotation as a "weak force", van der Waals interactions are often overlooked in *ab initio* materials modeling, which derives the properties of a system from its wave function or—in the case of DFT—electron density. However, these interactions are ubiquitous in nature, and there are a great many systems that cannot be modelled effectively without an adequate description of them. Many MOFs, for example, rely on physisorption for gas separation, which is only made possible by van der Waals forces.

This dissertation is about my research into several such systems, and how I model the van der Waals effects that are vital to their description. The remainder of this chapter provides some examples of problems that motivate my research. Chapter 2 is an in-depth explanation of the mathematical modeling used in said research. Chapter 3 onwards details specific projects that I have worked on, several of which are reprinted from their respective published articles.

1.2 Molecules

In systems with isolated atoms, van der Waals forces are usually not the dominant interaction. An important result of quantum mechanics is that electrons occupy a quantized set of states around an atom's positively-charged nucleus. These states are called "orbitals", based on the classical idea that electrons orbit the nucleus in the same way that the earth orbits the sun. Nature tends to prefer low energy states, and so these orbitals are often filled in order of lowest to highest energy—beginning with the so-called ground state of the atom. For the majority of elements in their electrically neutral ground state, the highest-energy occupied orbitals are only partially filled. Instead, these orbitals are filled by pairing with other atoms to form a *molecule*. Usually, such intramolecular bonding is either ionic or covalent in nature, and both types are far stronger than any van der Waals effect. Notable exceptions to this rule are the noble gases, elements which do possess completely filled orbitals. These gases, which include helium, neon, and radon, are very non-reactive and interact with other systems almost exclusively through the van der Waals forces. They are, however, not common in industry and thus mainly used as test cases in computational materials physics.

A much more common problem arises when one has multiple molecules within the same system. Each molecule is presumably electrically neutral and has, in some way or another, filled the electron orbitals of its constituent atoms. While van der Waals effects would make a negligible contribution to the *intra*-molecular force, it is in fact necessary for the qualitative and quantitative description of the *inter*-molecular force. One industrially relevant example of this phenomenon is that of benzene. Benzene is a cyclic hydrocarbon with the chemical formula C_6H_6, and is present in a wide variety of materials such as petroleum, plastics, and dyes. Benzene is also carcinogenic and flammable, which makes it highly beneficial to model the substances computationally rather than in a laboratory setting. Ordinary benzene is electrically neutral and non-polar, but two such molecules may still bind to one another via van der Waals forces, forming a dimer. The binding profile of the benzene dimer is shown in Fig. 1.1. Smaller separations are limited by the Pauli exclusion principle, while larger separations yield an attractive potential on the approximate order of $-1/R^6$, with R being

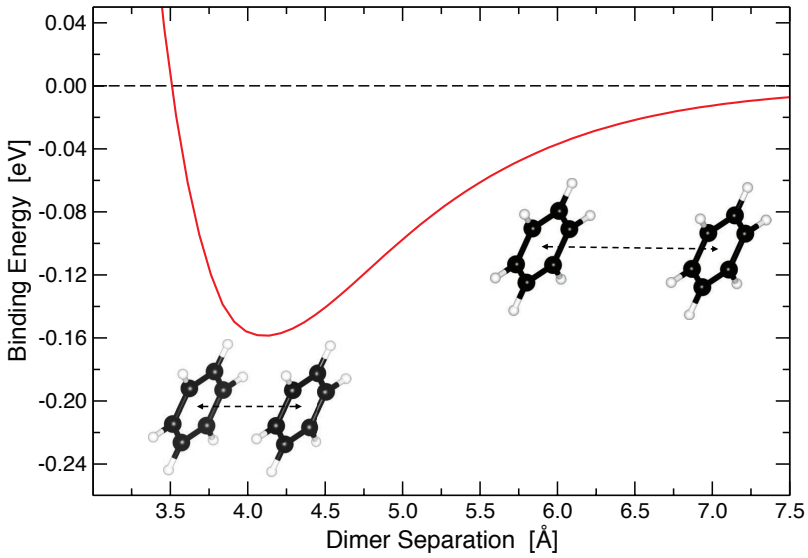

Figure 1.1: Interaction energy as a function of molecular separation in the benzene dimer. The horizontal dashed line at 0 eV indicates the reference energy, that of two completely non-interacting benzene molecules. A more negative interaction energy is indicative of a more favorable configuration.

the inter-molecular distance. This interaction, though weaker than the electrostatic force, is still strong enough for benzene to maintain a liquid state at room temperature and even solidify near 0 °C.

Similar qualitative effects due to van der Waals forces can be seen in many other industrial compounds, highlighting the need for their accurate theoretical treatment. But in particular, benzene is an important test case because its electronic structure can be generalized to many systems of greater complexity, known as *aromatic* compounds. Toluene, for example, is a common ingredient in paint thinner and other solvents, and appears as a benzene molecule with one hydrogen replaced by a methyl group. Aspirin, a popular anti-inflammatory drug, consists of a benzene ring terminated by a carboxyl group and an acetate on adjacent sites. Naphthalene, the main ingredient in mothballs, is a polycyclic structure consisting of two conjoined carbon rings, as opposed to benzene's one. Even graphene, one of the most and widely-studied materials of the last twenty years, consists of many carbon rings conjoined into a single layer. Graphene itself is also broadly important as a test case for the family of $2D$ materials, whose unique electronic structures and binding characteristics are the subject of extensive ongoing research in materials physics, and make

them highly sought after in industry.

In this dissertation, Chapter 3 contains an in-depth analysis of the interactions between molecules. In Sections 3.5.1 and 3.5.2, I also give particular focus to the benzene dimer as a representative case.

1.3 Graphite and Layered Structures

In the previous section, many of the molecules discussed owed their intramolecular structures to the chemical properties of carbon. This is no coincidence, as carbon is highly versatile among the elements for its ability to form up to four covalent bonds simultaneously. For that reason, carbon-based compounds make up the extensive field of study known as organic chemistry, and are nigh omnipresent in our everyday life. Another consequence of carbon's reactivity is its ability to form into numerous different stable allotropes. Diamond is a well-known example, a three-dimensional solid consisting exclusively of covalently-bound sp^3 carbon. Another, more stable allotrope is graphite. Unlike diamond, the carbon atoms in graphite are all sp^2 coordinated, meaning they form only three bonds. As a result, $3D$ graphite is actually composed of many layers—individually known as graphene—which bind together through van der Waals interactions. This weak interlayer binding makes graphite much more brittle than diamond, and is the reason for its common use in pencil lead.

Though the structural properties of bulk graphite may seem unremarkable, its individual graphene layers are much sought after and studied for their many applications in industry. Electrically, graphene is semimetallic in character, making it electrically conductive at room temperature and giving it potential use in electronics manufacturing. Graphene can also be readily functionalized, or transformed into different shapes to exploit its unique properties. It can, for example, be cut into *nanoribbons*, which possess unique electronic properties depending on their width and orientation. These nanoribbons can also be folded to create carbon *nanotubes*. Nanotubes may be either fully metallic or semiconducting depending on their configuration, and as a $3D$ material they possess extraordinary tensile strength.

Perhaps the most sought after property of graphene, however, is its ability to act as a substrate for adsorption. As mentioned previously, bulk graphite is composed of many

van der Waals bonded graphene layers. But these bond types are not just limited to interlayer interaction. If one has a single layer of graphene, they will find that many different types of molecules can bind, or *adsorb*, to its surface. This is particularly useful in battery manufacturing. In the battery's anode, alkali metal ions such as lithium act as a primary charge carrier. With a substrate such as graphene in the anode, these ions can bind to individual carbon rings, and diffuse by "hopping" from site to site. Surface adsorption is yet another example of van der Waals interaction, and not necessarily an intrinsic property of graphene. Nevertheless, graphene and other $2D$ carbon allotropes are particularly desirable due to their structural stability and relative ease of synthesis. As such, the discovery and characterization of novel carbon allotropes is an active subfield of funtional materials physics. In the case of alkali metals adsorption, this could be done by increasing the size of carbon rings, which positively correlate with binding strength. It could also mean maximizing the number of adsorption sites per unite cell, which would mean raising the maximum storage capacity of the anode. Some examples of $2D$ carbon allotropes are shown in Fig. 1.2.

The use of functional materials for surface adsorption is a powerful tool, with a wide range of applications beyond just battery manufacturing. And part of the reason that $2D$ materials are so useful as substrates is their extreme surface-area-to-volume ratio. However, a single-layered material is still not the best choice for maximizing adsorption uptake. If, for example, our goal were to draw gas molecules out of the air and have them adsorb to a single sheet of graphene, that sheet would quickly become saturated without putting any significant dent in the number of free-floating molecules. To amend this, we might imagine having many monoloyers, spaced far enough apart that they do not interact with one another. And to keep the structure cohesive, we might want to add occasional scaffolding to connect these distant layers. The resulting structure would then be three-dimensionally coordinated, like graphite or diamond, but retain the high surface-area-to-volume ratio of monolayer graphene. There are in fact multiple classes of functional materials with these properties, designed and synthesized for specific applications using gas adsorption. Perhaps the most well-studied example of the last decade is that of *metal–organic frameworks*, which are $3D$ coordinated structures that can be tailor-made from a combination of organic

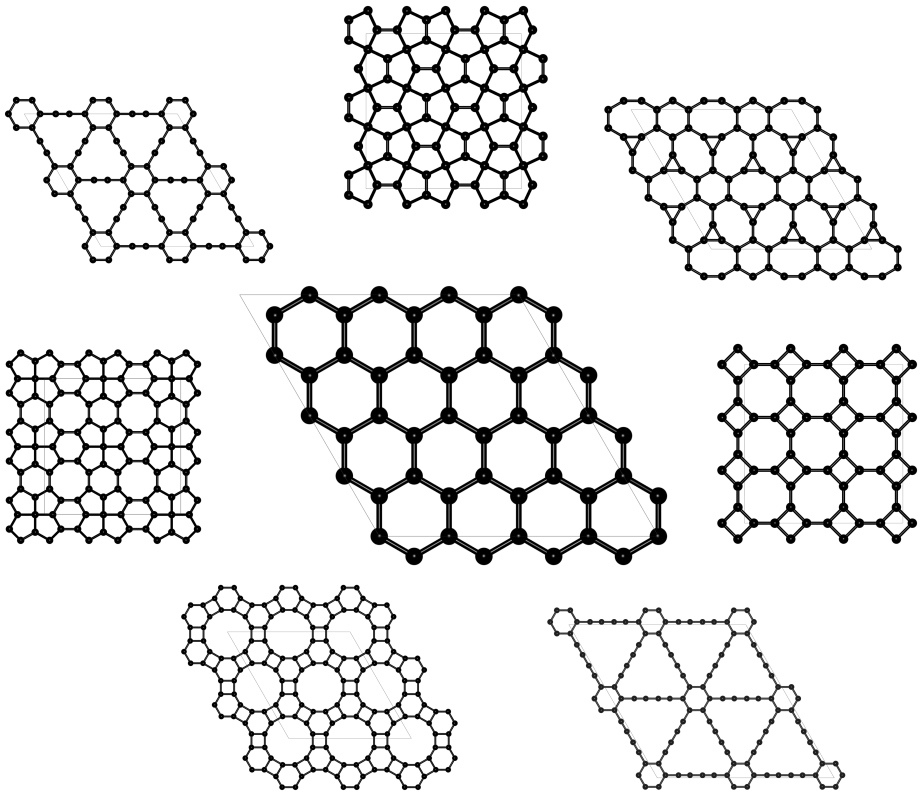

Figure 1.2: Several $2D$ allotropes of carbon, including graphene **(center)** as well as **(clockwise from top)** pentagraphene, irida-graphene, t-graphene, graphdiyne, graphenylene, me-graphene, and graphyne.

molecules—which act as linkers—and metal clusters as vertices. Because the most desirable properties of these materials depend on van der Waals interactions, a large part of my research has been characterizing MOF adsorption properties with theory and computation. In the next section, I outline just a few of the diverse applications of these materials.

Several of my papers study the physics of $2D$ materials. In Section 3.5.4, we examine the effect of charge density gradients in interlayer binding for several layered structures. Chapter 4 centers around similar analyses, but for molecular adsorption on single-layer graphene. And in Chapter 8, we propose and characterize an entirely new $2D$ material that is an allotrope of carbon, which we name THD-C after its characteristic tetra-, hexa-, and dodeca-membered rings.

1.4 Metal–Organic Frameworks

As the name implies, metal–organic frameworks are $3D$ crystalline materials composed of organic linkers and metal clusters to act as vertices. MOFs are not the first porous materials to see common use in industry; before their rise in popularity around 2010, zeolites were the most commonly used porous material for catalysis and adsorption applications. But MOFs carried several advantages over other porous materials, including ease of synthesis, tunable design parameters, and perhaps most importantly, increased porosity. Mere grams of certain MOFs could contain the equivalent of a football field's surface area within their structure, making them ideal for large-scale gas adsorption.

The ability to adsorb large amounts of a gas with little to no energy cost is an enticing prospect for many different industries. One commonly-studied example is the adsorption of hydrogen gas, which has been proposed as a possible green alternative to fossil fuels. Using intense cooling to store liquid hydrogen is extremely energy intensive, but many MOFs are able to adsorb large quantities of H_2 even at room temperature. Hydrogen storage was, in fact, one of the earliest studied applications of MOFs [1]. Similar studies of pure gas sorption, such as N_2, Ar, and C_6H_{12}, were also a motivating factor in the synthesis of the prototypical MOF, MOF-74 (shown in Fig. 1.3) [2]. Even in cases where hydrogen storage is not an intended application, adsorption of H_2 remains useful for the purposes MOF characterization, as it presents an effective means of experimentally measuring pore volume and/or surface area.

Another common point of interest in MOFs is *competitive* adsorption. In flue gases, for example, carbon dioxide and water are common waste products of industrial processes. Water is mostly harmless and already makes up a significant portion of Earth's natural atmosphere. CO_2, on the other hand, is one of the main contributors to climate change, and the reduction of CO_2 emmissions is a critical task for limiting environmental damage. In the past, the common method to separate these gases is cryogenics: using refrigeration cooling to exploit the differences in their condensation temperature. But this is, as mentioned previously, extraordinarily costly, making up a large portion of the world's yearly energy consumption. For this case as well, MOFs represent a promising alternative. For a given

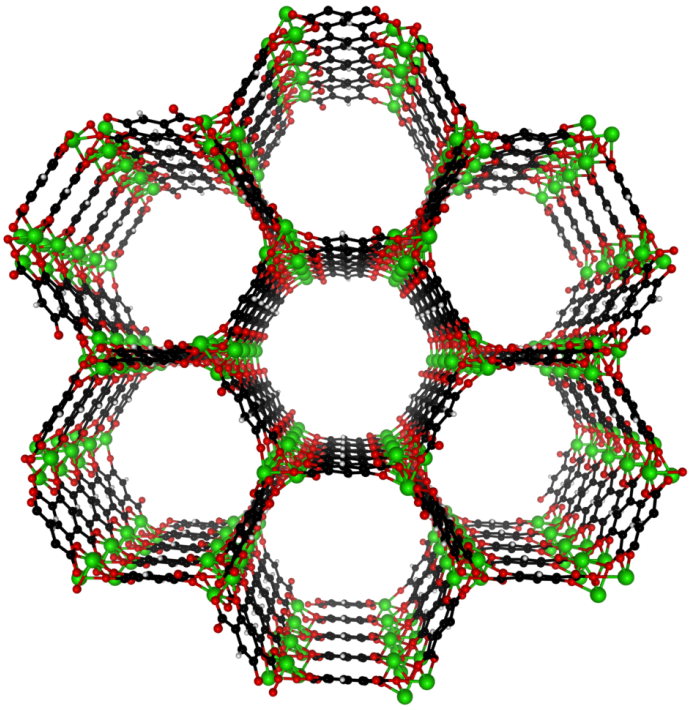

Figure 1.3: The atomic structure of a prototypical metal–organic framework, Zn MOF-74. Green, red, black, and white atoms are representative of zinc, oxygen, carbon, and hydrogen, respectively.

mixture of CO_2 and H_2O, a well-designed MOF could effectively filter the two by way of competitive adsorption. That is if one molecule readily adsorbs within the MOF, while the other is effectively excluded.

This highly sought after filtration behavior can arise in one of two ways. In one case, the adsorption energies of two different guest molecules may differ enough that the more strongly bound guest saturates the MOF, leaving no room for the other. In the other case, the MOF pore may possess corrugation or some other feature that impedes the diffusion of a specific guest molecule. These are known as thermodynamic and kinetic effects, respectively. The MOFs that most effectively separate their targeted guest molecules may make use of both effects simultaneously. This may be done, for example, by designing a MOF which has pore sizes on the same order as one or more intended guest molecules. Another useful application of such size effects is the separation of hydrocarbon isomers. Some hydrocarbons which make up different types of fuel, such as C_6H_{12}, can exist in several different geometric forms with identical chemical formulae. The so-called "linear" n-alkanes commonly possess

branched variants, which despite their similar structure, exhibit unique chemical behaviors. Importantly, it is the proportion of branched isomers in a mixture that dictate its octane rating—the kind that one might see on a fuel pump at a gas station. Branched isomers tend to be more sought after because they raise the octane number of a fuel mixture. However, raising or lowering the octane number of a mixture requires filtration. And hydrocarbon isomers are extremely difficult to separate using cryogenics techniques because of their identical masses and very similar shapes. Certain MOFs, however, may do so very effectively by possessing pore geometries that are tailor-made for certain isomers.

1.5 Dissertation Outline

The previous section outlines just a few of the many possible applications of MOFs, which, in-turn, is only one subset of the broader study of functional materials. The study of adsorption in $2D$ materials and MOFs has made up a sizeable portion of my own research, which could collectively be categorized as applications-based materials physics. The remainder of my research is in theory development, the goal of which is to develop or improve upon the mathematical models that describe materials. Now that I have provided some context for the importance of applications-based materials physics, it is appropriate to also give some background for the computational methods that I use for this research. Thus, Chapter 2 goes over these methods in detail, beginning with their derivation from the quantum many-body problem.

The remainder of my dissertation summarizes my research using density functional theory. Chapter 3 is an in-depth study of many different van der Waals complexes, for which we calculate contributions to the interaction energy as a function of s, the reduced-gradient of the electron density. This so-called reduced-gradient analysis is also prominent in Chapter 4, which is a computational study that compares the performance of several different density functionals with respect to molecular adsorption on graphene. Through this analysis, we show not only which functionals are the most accurate, but provide much-needed context as to how and why. Reduced-gradient analysis can also be used to inform the design of new functionals, as I show in Chapter 5. There, I outline the ongoing development of a van

der Waals density functional for the accurate description of molecular crystals. Similarly, in Chapter 6, I examine avenues toward the development of an improved van der Waals density functional, with focus on the nonlocal correlation and possible improvements to the plasmon-pole model that is used in the first van der Waals density functional of Dion *et al.* [3].

Chapter 7 onward focuses more on applications-based research, beginning with a thermodynamic study of adsorption in porous materials. In Chapter 8, we design our own functional material, a $2D$ allotrope of carbon called THD-C, and examine in detail its many interesting properties. Chapter 9 also briefly summarizes several other projects that I have been a part of. All of these relate to gaseous adsorption and separation within metal–organic frameworks, for which my DFT calculations provided necessary context to the behaviors observed in experiment.

Chapter 2

Materials Modeling

In materials physics, if one wanted to characterize a particular material, there are two general ways of doing so. One would be to obtain a sample of the material and perform tests on it in a controlled laboratory environment. A common example of this is spectroscopy, which uses light to probe the nano-scale properties of the material. Such practices fall under the broad umbrella of "experiment". An alternative option would be to construct a mathematical model of the system and *derive* its properties via theory and computation. Though such calculations could be done by hand for simple systems and test cases, in practice it usually entails the use of digital processors for bulk computation. There are advantages and disadvantages to either of these methods. Experiment tends to be more accurate for characterizing materials, but can be very costly due to the need to obtain samples and perform upkeep on measurement tools. Additionally, some compounds can be toxic, corrosive, or flammable, further complicating lab procedure. Theory and computation lack these issues, and in some cases can be performed quickly and at low-cost. However, it may also be less accurate for complicated systems.

Because of their complementary strengths and weaknesses, the past century of scientific progress has seen an increasing emphasis on cooperation between experiment and theory. Experiment is necessary for an accurate description of materials properties, but theory has the potential to prescribe these properties accurately and efficiently. However, for much of the history of materials physics, theory has lagged in this role. It was not until the 1920's that an accurate model of atomic structure and interactions was devised in

the form of quantum mechanics. With important contributions from Erwin Schrödinger, Werner Heisenberg, Niels Bohr, and others, quantum mechanics established a probabilistic model of small particles. Each individual particle or system of particles is described by a wavefunction, the properties of which are dictated by the Schrödinger equation. In the quantum mechanical framework, the form of a given system's wave function corresponds to its hamiltonian, and should account for all particles that are present. Once obtained, the wave function can be used to find any relevant measurable quantity of the system, most notably the energy. But as we will soon find, solving for the wave function analytically becomes infeasible for even a small number of interacting identical particles. For systems such as bulk solids, which at macroscopic scales may exceed 10^{23} particles, it thus becomes effectively impossible to compute the exact wavefunction. Instead, an approximate solution must be reached by making successive assumptions about the system. As I will detail below, one such approximation begins with the exact many-body hamiltonian and simplifies down to the Kohn-Sham equation, which forms the basis of DFT. Because it is derived from exact characteristics of the many-body problem, DFT is an example of an *ab initio* model, also known as "First Principles".

2.1 The Many-Body Problem

In the many-body problem, we first imagine a system of atoms, which are collectively made up of electrons and nuclei at positions $\mathbf{r}_i$ and $\mathbf{R}_I$, respectively. The exact hamiltonian includes terms for the kinetic energy of each particle and all particle-particle interactions, and can be written in SI units as the following:

$$\begin{aligned} H \;=\; & -\frac{\hbar^2}{2m}\sum_i \nabla_i^2 \;-\; \sum_I \frac{\hbar^2}{2M_I}\nabla_I^2 \\ & +\; \sum_{i\neq j}\frac{k_e e^2}{|\mathbf{r}_i-\mathbf{r}_j|} \;+\; \sum_{I\neq J}\frac{k_e Z_I Z_J e^2}{|\mathbf{R}_I-\mathbf{R}_J|} \;-\; \sum_{i,I}\frac{k_e Z_I e^2}{|\mathbf{r}_i-\mathbf{R}_I|}\,, \end{aligned} \tag{2.1}$$

where M_I and Z_I represent the mass and charge of nucleus I, respecively. The first approximation one can make to simplify this problem is the Born-Oppenheimer approximation: because the mass of any given nucleus is much greater than that of the electron, we may

disregard the nuclear kinetic term which goes as $1/M_I$. In physical terms, this effectively treats the nuclei as a fixed part of the environment. Following that logic, we may also rewrite the inter-nuclear interaction term as a constant additive term E_{IJ}, and the electron-nuclear interaction as a fixed external potential U_{ext}. While E_{IJ} has no dependence on the electronic states, U_{ext} forms a contribution that depends on where each electron lies within the potential. Thus, it is written in full as

$$U_{\text{ext}} = \sum_i U_{\text{ext}}(\mathbf{r}_i) \ . \tag{2.2}$$

Applying these changes simplifies Eq. 2.1 considerably, allowing us to write it as

$$H = -\frac{\hbar^2}{2m}\sum_i \nabla_i^2 + \sum_{i\neq j}\frac{k_e e^2}{|\mathbf{r}_i - \mathbf{r}_j|} + \sum_i U_{\text{ext}}(\mathbf{r}_i) + E_{IJ} \ . \tag{2.3}$$

When calculating the properties of a material, we often have information about the number of particles present and the initial positions of the nuclei. Using this information, our goal is to find the ground state wavefunction Ψ and energy E that solves the time-independent Schrödinger equation,

$$H\Psi = E\Psi \ . \tag{2.4}$$

In a system of N electrons, the wavefunction contains information about each of their positions, meaning that we can write it as $\Psi = \Psi(\mathbf{r}_1, \mathbf{r}_2, \ldots, \mathbf{r}_N)$. If we take eqs. 2.3 and 2.4 together, we can hypothetically solve for the ground state by finding the smallest eigenvalue of the equation

$$\left[-\frac{\hbar^2}{2m}\sum_{i=1}^{N} \nabla_i^2 + \sum_{i\neq j}\frac{k_e e^2}{|\mathbf{r}_i - \mathbf{r}_j|} + \sum_{i=1}^{N} U_{\text{ext}}(\mathbf{r}_i) + E_{IJ}\right]\Psi = E\Psi \ . \tag{2.5}$$

However, this task is still nontrivial, and even further approximation is needed if we are to solve it analytically.

The simplest possible approximation that can be applied to our current hamiltonian is to neglect all interactions between individual electrons and their environment. This eliminates the terms of $k_e e^2/|\mathbf{r}_i - \mathbf{r}_j|$ and $U_{\text{ext}}(\mathbf{r}_i)$. And because E_{IJ} has no impact on the electron

wavefunction Ψ, we may also subtract it from both sides of Eq. 2.5. This approximation is known as the "free-electron gas", as it is similar to macroscopic ideal gases in which molecules never collide with one another. The valence electrons within certain metals may reasonably be treated as free-electron gases, as conducting electrons are allowed to travel relatively unimpeded throughout the material. With this new approximation, we now only need to solve

$$-\frac{\hbar^2}{2m}\sum_{i=1}^{N}\nabla_i^2\Psi = E\Psi \ . \tag{2.6}$$

Neglecting exchange, we then rewrite the all-electron wavefunction as the product of many one-electron wavefunctions, letting $\Psi(\mathbf{r}_1, \mathbf{r}_2, ..., \mathbf{r}_N) = \psi(\mathbf{r}_1)\psi(\mathbf{r}_2)...\psi(\mathbf{r}_N)$. This, in-turn, allows us to treat each electron seperately within the Schrödinger equation, such that

$$-\frac{\hbar^2}{2m}\nabla_i^2\psi(\mathbf{r}_i) = \varepsilon_i\psi(\mathbf{r}_i) \ . \tag{2.7}$$

This is satisfied when the one-electron wavefunction takes the form of a plane wave, subject to some boundary conditions. The simplest application of this is to place electrons in an open cube of arbitrary side length L and volume $V = L^3$, with periodic boundary conditions on each side. Under these conditions, the wave function must satisfy

$$\psi(\mathbf{r}_i) = \psi(\mathbf{r}_i + L\hat{\mathbf{x}}) = \psi(\mathbf{r}_i + L\hat{\mathbf{y}}) = \psi(\mathbf{r}_i + L\hat{\mathbf{z}}) \ . \tag{2.8}$$

Doing this, we get a set of solutions to the Schrödinger equation for each electron, with

$$\psi_{\mathbf{k}}(\mathbf{r}_i) = \frac{1}{\sqrt{V}}e^{i\mathbf{k}\cdot\mathbf{r}_i} \ . \tag{2.9}$$

Here, $\mathbf{k} = \frac{2\pi}{L}(l_x, l_y, l_z)$, where l_x, l_y, and l_z may be any integer from $-\infty$ to ∞. The coefficient of $1/\sqrt{V}$ normalizes the wavefunction within our boundaries. With the knowledge of the one-electron wavefuntion, we can now easily solve for the one-electron energy as well. We find that it is

$$\varepsilon(k) = \frac{\hbar^2 k^2}{2m} \ , \tag{2.10}$$

where k is the norm of the wavevector $\mathbf{k}$. The one-electron energy and wavefunction can

then be converted back into the many-body case, yielding

$$\Psi = \prod_{i=1}^{N} \frac{1}{\sqrt{V}} e^{i\mathbf{k}_i \cdot \mathbf{r}_i} \ , \tag{2.11}$$

$$E = \sum_{i=1}^{N} \varepsilon(k_i) \ . \tag{2.12}$$

Though the free-electron gas is a very simple approximation, the results that it yields prove quite useful. This is not just because of its applicability to metals, but because those results can now be extrapolated to more realistic problems.

Next, we reintroduce the external potential U_{ext} to the system. Since our eventual goal is to model bulk systems, a reasonable assumption could be made that U_{ext} is periodic in three dimensions. This would allow us to write it as

$$U_{\text{ext}}(\mathbf{r}) = U_{\text{ext}}(\mathbf{r} + \mathbf{R}) \ , \tag{2.13}$$

where $\mathbf{R}$ is some linear combination of three unit cell dimensions. The current problem is now that of Eq. 2.5 with electron-electron interactions neglected, giving:

$$\Big[-\frac{\hbar^2}{2m} \sum_{i=1}^{N} \nabla_i^2 + \sum_{i=1}^{N} U_{\text{ext}}(\mathbf{r}_i) \Big] \Psi = E\Psi \ . \tag{2.14}$$

The one-electron solution to this equation is similar to that of the free-electron gas,

$$\psi_{\mathbf{k}}(\mathbf{r}_i) = \frac{1}{\sqrt{\nu}} e^{i\mathbf{k}\cdot\mathbf{r}_i} u(\mathbf{r}_i) \ , \tag{2.15}$$

where $u(\mathbf{r}_i)$ is a cell-periodic function dependent on the external potential and ν is the number of unit-cells per volume V. Equation 2.15 is known as Bloch's Theorem, stating that the wavefunction of a periodic potential takes the form of a plane wave modulated by $u(\mathbf{r})$. This proves to be vital for the characterization of bulk materials, as it means that we only need information about a single unit-cell of the material to calculate properties of the entire system. However, while this model forms a good starting point in the description of materials, more detail about electron interactions is still necessary for the characterization

of insulators and semi-conductors.

2.2 The Hartree-Fock Method

If we take the non-interacting Schrödinger equation as it is written out in Eq. 2.14, there are two possible ways to reintroduce the interactions. The most rigorous approach would be to fully include interaction terms in the hamiltonian and find the updated solution to the wavefunctions and energies. But in most practical cases, this proves to be analytically infeasible. The second approach offers a simpler alternative, which is to take the electron-electron interactions as an effective potential. Such approximations are often referred to as "Hartree-like" after David Hartee, who made use of an effective potential to account for coulombic effects.

Ideally, an effective potential for interacting electrons should take into account not just coulombic effects, but exchange effects as well. These exchange effects arise from the Pauli exclusion principle, which states that no two electrons may occupy the same state at a given time. We can implement this property into the all-electron wavefuntion for a given system by writing it as a Slater determinant of the one-electron wavefunctions:

$$\Psi(\mathbf{r}_1, \mathbf{r}_2, ..., \mathbf{r}_N) = \frac{1}{\sqrt{N!}} \begin{vmatrix} \psi_1(\mathbf{r}_1) & \psi_1(\mathbf{r}_2) & \dots & \psi_1(\mathbf{r}_N) \\ \psi_2(\mathbf{r}_1) & \psi_2(\mathbf{r}_2) & \dots & \psi_2(\mathbf{r}_N) \\ \vdots & \vdots & \ddots & \vdots \\ \psi_N(\mathbf{r}_1) & \psi_N(\mathbf{r}_2) & \dots & \psi_N(\mathbf{r}_N) \end{vmatrix} . \tag{2.16}$$

Note that this assumes that all electrons in the system have the same spin. In a spin *unpolarized* system, the wavefunction could instead be written in terms of two-electron orbitals. With the current wavefunction, one may calculate the energy of the system $E\{\Psi\}$

using the hamiltonian of Eq. 2.3. This results in the expression

$$\begin{aligned}\langle\Psi|\, H\,|\Psi\rangle =& E_{IJ} + \sum_i \int d\mathbf{r}\ \psi_i^*(\mathbf{r})\Big[-\frac{\hbar^2}{2m}\nabla_i^2 + U_{\text{ext}}(\mathbf{r})\Big]\psi_i(\mathbf{r}) \\ &+ \frac{1}{2}\sum_{i,j}\int d\mathbf{r}d\mathbf{r}'\psi_i^*(\mathbf{r})\psi_j^*(\mathbf{r}')\frac{k_e e^2}{|\mathbf{r}-\mathbf{r}'|}\psi_i(\mathbf{r})\psi_j(\mathbf{r}') \\ &- \frac{1}{2}\sum_{i,j}\int d\mathbf{r}d\mathbf{r}'\psi_i^*(\mathbf{r})\psi_j^*(\mathbf{r}')\frac{k_e e^2}{|\mathbf{r}-\mathbf{r}'|}\psi_i(\mathbf{r}')\psi_j(\mathbf{r})\ .\end{aligned} \tag{2.17}$$

This introduces two terms of the electron interaction, the so-called "direct" and "exchange" terms. The direct term can be used to derive an effective potential for the Coulomb interaction, known as the Hartree potential. We write it as

$$U_{\text{H}}(\mathbf{r}) = \int d\mathbf{r}'\frac{k_e n(\mathbf{r})e^2}{|\mathbf{r}-\mathbf{r}'|}\ , \tag{2.18}$$

where $n(\mathbf{r})$ is the electron density. It should be noted that, because $n(\mathbf{r})$ encompasses *all* electrons in the system, the Hartree potential introduces a spurious self-interaction for each electron. However, this self-interaction is cancelled out by the $i = j$ part of the exchange term in Eq. 2.17. As for the exchange potential, we can derive it from the one-electron exchange contribution, which is

$$\langle\psi_i|\, U_{\text{x}}^i(\mathbf{r})\,|\psi_i\rangle = -\sum_j \int d\mathbf{r}d\mathbf{r}'\psi_i^*(\mathbf{r})\psi_j^*(\mathbf{r}')\frac{k_e e^2}{|\mathbf{r}-\mathbf{r}'|}\psi_i(\mathbf{r}')\psi_j(\mathbf{r})\ . \tag{2.19}$$

On the right-hand side, we may multiply and divide by $\psi_i(\mathbf{r})$ to find that

$$U_{\text{x}}^i(\mathbf{r}) = -\sum_j \int d\mathbf{r}'\psi_j^*(\mathbf{r}')\frac{k_e e^2}{|\mathbf{r}-\mathbf{r}'|}\psi_i(\mathbf{r}')\frac{\psi_j(\mathbf{r})}{\psi_i(\mathbf{r})}\ . \tag{2.20}$$

By deriving effective potentials for the direct and exchange terms, we can now easily separate the energy of a given system into contributions from each of the constituent electrons. These one-electron energies, now written as

$$\langle\psi_i|\, H\,|\psi_i\rangle = \int d\mathbf{r}\ \psi_i^*(\mathbf{r})\Big[-\frac{\hbar^2}{2m}\nabla_i^2 + U_{\text{ext}}(\mathbf{r}) + U_{\text{H}}(\mathbf{r}) + U_{\text{x}}^i(\mathbf{r})\Big]\psi_i(\mathbf{r})\ , \tag{2.21}$$

form what are known as the "Hartree-Fock equations". The Hartree-Fock equations, in-turn, form the basis of the "Hartree-Fock method", which involves solving for the ground-state energy of a system via the variational method. Given a hamiltonian and a reasonable initial estimate of the wavefunction Ψ, one can solve for the ground state by minimizing $E\{\Psi\}$. This can be done using a Lagrange multiplier,

$$\delta[\langle\Psi| H |\Psi\rangle - E(\langle\Psi|\Psi\rangle - 1)] = 0 \,, \tag{2.22}$$

wherein each electron wavefunction ψ_i is a degree of freedom within Ψ.

The Hartree-Fock method represents a substantial improvement over the free-electron gas model, being able to accurately describe a much broader set of systems. However, its use still comes with two major drawbacks. The first is computational cost. The use of a Slater determinant to represent the wavefunction means that the complexity of Ψ increases as the factorial of the number of electrons in the system. This becomes especially costly for large-celled structures like MOFs, which may contain hundreds of atoms and thus thousands of electrons. The other shortcoming of Hartree-Fock lies in the form of its wavefunction. Taking Ψ to be a single slater determinant gives equal weight to all antisymmetrized pairs of single-electron wavefunctions. In reality, $E\{\Psi\}$ could be lowered further by letting Ψ be a weighted sum of many determinants. This hypothetical lowering in $E\{\Psi\}$ is known as the "correlation energy", which happens to form a substantial contribution in many materials.

2.3 Density Functional Theory

2.3.1 The Kohn-Sham Method

As my research has mostly dealt with large, correlated systems such as metal-organic frameworks, I have required a technique with improved accuracy over Hartree-Fock. One such technique, known as DFT, represents one of the most important advances in computational physics of the last century. Unlike the Hartree-Fock method and other techniques deriving from the Schrödinger equation, DFT calculates the properties of a system based on the

electron density rather than the wavefunction. The electron density is defined as

$$n(\mathbf{r}) = \sum_{i=1}^{N} \psi_i^*(\mathbf{r})\psi_i(\mathbf{r}) \ , \tag{2.23}$$

where each $\psi_i(\mathbf{r})$ is the wavefunction of a single electron within the system. By using $n(\mathbf{r})$ as a basis for computing the energy, we now need only work in three dimensions, rather than the $3N$ dimensions of Ψ, substantially reducing computational cost.

The foundations of DFT were laid out by Pierre Hohenberg and Walter Kohn in 1964 in two theorems [4, 5], which can be summarized as follows:

1. For any given system of electrons in an external potential, the ground-state energy corresponds to a unique electron density $n_0(\mathbf{r})$.

2. There exists a universal functional such that the ground-state electron density $n_0(\mathbf{r})$ and energy $E[n_0(\mathbf{r})]$ of any given system correspond exactly to those obtained by solving the Schrödinger equation.

These ideas were subsequently expanded upon by Kohn and Lu Jeu Sham, work that would eventually win the 1998 Nobel Prize in Chemistry. The Kohn-Sham method involves replacing the electron density with an auxiliary system of non-interacting particles. The energy of that system is then expressed as

$$E_{\mathrm{KS}}[n] = T[n] + U_{IJ} + \int d\mathbf{r}[U_{\mathrm{ext}}(\mathbf{r}) + U_{\mathrm{H}}(\mathbf{r})]n(\mathbf{r}) + E_{\mathrm{xc}}[n] \ . \tag{2.24}$$

In this equation, the coulombic potentials U_{IJ}, U_{ext}, and U_{H} form exactly-known contributions to the total energy. In principle, one could also calculate the kinetic energy $T[n]$ using only the electron density, but in practice it is typically computed exactly from a non-interacting many-electron wave function. The remaining term E_{xc} is known as the "exchange-correlation energy", and includes all other quantum effects present in the system. By taking $n(\mathbf{r})$ in a non-interacting auxiliary framework, the exchange-correlation

may be treated as a Hartree-like potential. That is, we let

$$U_{\mathrm{xc}} = \frac{\delta E_{\mathrm{xc}}}{\delta n(\mathbf{r})} \ . \tag{2.25}$$

This is a significant outcome, as it means that any given functional is as accurate as its exchange-correlation term. Thus, if our ultimate goal is to find the "universal functional" mentioned in the 2nd Hohenberg-Kohn theorem, we need only make improvements to the accuracy of U_{xc}.

Since the advent of DFT, substantial effort has been made to improve the general description of the exchange and correlation. Two major advancements, which prove vital for accurately modeling covalent- and dispersion-bonded systems, are discussed in detail in the next two sections. But before that, it is important that we first consider the simplest possible cases and use their results as a framework to build upon. And for DFT, as with any technique that seeks to solve the many-body problem, we look first to the homogeneous electron gas.

2.3.2 The Local Density Approximation

In deriving an expression for U_{xc}, it is easiest to take the exchange and correlation separately. For characterization of the exchange, we use the free-electron gas model of Section 2.1 as a starting point. Although that particular model neglects electron-electron interactions, it remains true that the electron eigenstates in an electron gas are given by Eq. 2.9. Thus, it's simple enough to reintroduce exchange effects by filling the $\mathbf{k}$ states one-by-one, beginning with the lowest energies. We begin with two electrons at $\mathbf{k} = (0, 0, 0)$, one with spin up and another with spin down. Then we continue adding electron pairs at progressively higher energy levels, corresponding to higher absolute values of $\mathbf{k}$. In fourier space, the end result is that the filled states form a sphere of radius k_F, known as the Fermi wavevector. From here, the exchange energy can be calculated analytically via the Hartree Fock method, yielding

$$\epsilon_{\mathrm{x}}^{\mathrm{unif}} = -\frac{3e^2}{4\pi} k_F \ , \tag{2.26}$$

where $k_F = (3\pi^2 n(\mathbf{r}))^{1/3}$. And while this solution is only exact in the case of the homogeneous electron gas, it can easily be generalized for non-uniform systems by taking Eq. 2.26 to be our exchange potential U_{x}. That is, we let

$$E_{\mathrm{x}}[n] = \int d\mathbf{r} \epsilon_{\mathrm{x}}^{\mathrm{unif}}(\mathbf{r}) n(\mathbf{r}) \ . \tag{2.27}$$

This is known as the "Local Density Approximation" (LDA), as we are treating the density at any given coordinate as approximately uniform within its locale.

The LDA may also be applied to the correlation energy. But unlike exchange, the correlation contribution in a homogeneous electron gas can not be found analytically. Instead, formulations of the LDA correlation have historically been based on the results of Quantum Monte Carlo or Random-Phase Approximation simulations, methods that are extremely accurate but also very computationally expensive and time-consuming. In the widely-used formulation of John Perdew and Yue Wang, the LDA correlation energy is taken as a rather complicated function of the Wigner-Seitz radius, which is related to the Fermi wavevector by $r_s = (9\pi/4)^{1/3}/k_F$. Similar to the LDA exchange, the LDA correlation for general systems can be expressed as

$$E_{\mathrm{c}}[n] = \int d\mathbf{r} \epsilon_{\mathrm{c}}^{\mathrm{unif}}(\mathbf{r}) n(\mathbf{r}) \ . \tag{2.28}$$

Taking eqs. 2.27 and 2.28 together as our exchange-correlation functional results in a computational model that is fairly accurate for a broad range of systems, and offers much improved efficiency over the Hartree-Fock method. However, as its name might imply, the LDA is best-suited for uniform systems such as metals. It still struggles to describe covalently-bonded complexes, which are not as closely bound and thus may feature steep gradients in the electron density.

2.3.3 Exchange in the Generalized Gradient Approximation

To achieve greater accuracy for inhomogeneous systems, one can devise an extension of the LDA that includes terms of the *gradient* of the electron density, known as the "Generalized

Gradient Approximation" (GGA). In its most general form, such a functional can be written as

$$E_{\mathrm{xc}}^{\mathrm{GGA}}[n] = \int d\mathbf{r} f(n(\mathbf{r}), \nabla n(\mathbf{r})) \; . \tag{2.29}$$

In early iterations of the GGA, the optimum form of $f(n(\mathbf{r}), \nabla n(\mathbf{r}))$ was a matter of frequent debate, and in many cases led to GGA functionals that disagreed with the LDA in the uniform density limit. But in 1996, John Perdew, Kieron Burke, and Matthias Ernzerhof introduced a new formalism with their paper "Generalized Gradient Approximation Made Simple" [6]. The Perdew-Burke-Ernzerhof functional (PBE) introduced new forms of the exchange and correlation,

$$E_{\mathrm{x}}^{\mathrm{PBE}}[n] = \int d\mathbf{r}\, n(\mathbf{r}) \epsilon_{\mathrm{x}}^{\mathrm{unif}}(n(\mathbf{r})) F_{\mathrm{x}}(s) \; , \tag{2.30}$$

$$E_{\mathrm{c}}^{\mathrm{PBE}}[n] = \int d\mathbf{r}\, n(\mathbf{r}) [\epsilon_{\mathrm{c}}^{\mathrm{unif}}(n(\mathbf{r})) + H(n(\mathbf{r}), t)] \; , \tag{2.31}$$

where s and t are two dimensionless density gradients proportional to $|\nabla n(\mathbf{r})|/n(\mathbf{r})^{4/3}$. Since the development of the PBE functional, this form has become the standard for the description of both exchange and correlation in the GGA. However, my research has focused on materials where long-range dispersion interactions make significant contributions to the energy. These interactions arise from correlation effects, but are poorly accounted for even in the GGA. As is discussed in detail in the next section, dispersion interactions are better described by a fully nonlocal correlation functional, which computes the energy from a pairwise integration over the density.

The GGA exchange, however, remains an important component even in dispersion-dominated systems. This behavior, which is sometimes described as "semilocal", owes to the form of the exchange enhancement factor $F_{\mathrm{x}}(s)$. When considering the GGA exchange of spin-unpolarized systems, the authors of PBE used three main conditions:

1. In systems of uniform density where $s = 0$, let Eq. 2.30 agree with the LDA. That is, let $F_{\mathrm{x}}(0) = 1$.

2. In the slowly-varying density limit, the LDA has been observed to still be an excellent

approximation. Therefore, forgo a first order term in s and let $F_{\mathrm{x}}(s) \approx 1 + \mu s^2$ for small s, where μ is some appropriately-chosen constant.

3. Even in very inhomogeneous systems, the exchange energy should still satisfy the Lieb-Oxford bound:

$$E_{\mathrm{x}}[n] \geq -Ce^2 \int d\mathbf{r}\, n(\mathbf{r})^{4/3} \,. \tag{2.32}$$

This bound, in essence, defines the maximum possible difference between the "true" electron-electron interaction and the direct term of Eq. 2.17. In PBE, obeying this bound means that $F_{\mathrm{x}}(s)$ must grow monotonically in s to some finite maximum value.

The authors of PBE devise a simple form of the enhancement factor that satisfies all of the above constraints:

$$F_{\mathrm{x}}^{\mathrm{PBE}}(s) = 1 + \frac{\mu s^2}{1 + \mu s^2/\kappa} \,. \tag{2.33}$$

However, this is only one of many possible enhancement factors that do so. And since the development of PBE, many other GGA functionals have arisen that either re-optimize $F_{\mathrm{x}}^{\mathrm{PBE}}(s)$ with respect to μ and κ or possess altogether novel forms that satisfy these conditions.

2.3.4 The Nonlocal Correlation Functional

The creation of the generalized gradient approximation represents a significant advancement in the accuracy of DFT. But, as mentioned previously, it still struggles to adequately model dispersion interactions, which are ubiquitous in nature and include hydrogen bonds and van der Waals forces. Including these interactions has therefore been one of the most important advances in density functional theory over the last two decades. Different methods have been developed to account for this error. One option is to use force-field corrections at long-range, as is done by the DFT-D functionals. Another is to further extend the GGA to include terms of the electron kinetic energy density $\tau = |\nabla n(\mathbf{r})|^2/8n(\mathbf{r})$. These so-called "meta-GGA" functionals originated with the work of Tao-Perdew-Staroverov-Scuseria (TPSS) [7], and have found further success following the development of the "strongly constrained & appropriately normed semilocal density functional" (SCAN) [8].

The method that I have used most extensively in my research is that of the fully nonlocal van der Waals density functional (vdW-DF). Here, "nonlocal" refers to the correlation energy specifically. When electrons become correlated at large distances, a dipole moment may spontaneously arise between them, which creates the weak attractive interaction known as the van der Waals force. In its simplest form, the nonlocal correlation energy can be written as

$$E_{\mathrm{c}}^{\mathrm{nl}}[n] = \frac{1}{2}\int d\mathbf{r}d\mathbf{r}' n(\mathbf{r})\Phi(\mathbf{r},\mathbf{r}')n(\mathbf{r}') \; . \tag{2.34}$$

In this formulation, we effectively take every pair of coordinates in a given density and sum up their interactions according to a general function $\Phi(\mathbf{r},\mathbf{r}')$, known as the interaction kernel. The simplicity of Eq. 2.34 is deceptive, as it still requires constructing a kernel *ab initio* that is accurate and computationally efficient for general geometries. This task was first successfully carried out by Bengt Lundqvist and coworkers in 2003, when they developed the first van der Waals density functional (vdW-DF1) [3].

They begin their derivation of the interaction kernel with the adiabatic connection formula, which defines the exchange correlation energy as an integration over a coupling constant. When spectator contributions to inter-electronic interaction are omitted, this formula becomes simplified in what is known as the "Full Potential Approximation". In this form, it is written as

$$E_{\mathrm{c}}^{\mathrm{nl}} = \int_0^\infty \frac{du}{2\pi}\mathrm{tr}[\ln(1 - V\tilde{\chi}) - \ln\epsilon] \; , \tag{2.35}$$

where u is an imaginary frequency, V is the interelectronic Coulomb potential, ϵ is the dielectric function, and $\tilde{\chi}$ is the density response to the potential V.

If we rewrite Eq. 2.35 in terms of a plasmon propagator function $S \equiv 1 - \epsilon^{-1}$, then $E_{\mathrm{c}}^{\mathrm{nl}}$ may be expanded to first order as

$$E_{\mathrm{c}}^{\mathrm{nl}} \approx \int_0^\infty \frac{du}{4\pi}\mathrm{tr}\left[S^2 - \left(\frac{\nabla S\cdot\nabla V}{4\pi e^2}\right)^2\right] \; . \tag{2.36}$$

The trace may be done in either real or fourier space, though the latter is significantly easier to work with. In this case, the plasmon propagator is rewritten as $S_{\mathbf{q},\mathbf{q}'}$, the interaction between two fragments of different momenta. In this form, the nonlocal correlation energy

can now be evaluated as

$$E_{\mathrm{c}}^{\mathrm{nl}} = \int_0^\infty \frac{du}{4\pi} \int\int \frac{d\mathbf{q} d\mathbf{q}'}{(2\pi)^6} [1 - (\hat{\mathbf{q}} \cdot \hat{\mathbf{q}}')^2] S_{\mathbf{q},\mathbf{q}'} S_{\mathbf{q}',\mathbf{q}} \, . \tag{2.37}$$

At this point, the authors of vdW-DF1 were required to choose a suitable form for $S_{\mathbf{q},\mathbf{q}'}$, which would ideally be derived from a known formula of the dielectric function *and* result in an easy-to-evaluate kernel. They begin with a simple model of the dielectric function, which derives from the equation of motion for an electron subject to a time-dependent external field $\mathbf{E}(\mathbf{r}, t)$. If the field varies harmonically with frequency ω, then an expression for $\epsilon(\omega, \mathbf{r})$ may be derived by solving for the position $\mathbf{r}(t)$ of the electron. This is expressed as

$$\epsilon(\omega, \mathbf{r}) = 1 + \frac{\omega_p(\mathbf{r})^2}{\omega_q(\mathbf{r})^2 - \omega_p(\mathbf{r})^2 - \omega^2} \, , \tag{2.38}$$

where ω_p is the plasmon frequency in the slowly varying limit of the electron density, and ω_q is the so-called "plasmon dispersion law", which contains additional terms for the description of more inhomogeneous cases. To ensure that their $S_{\mathbf{q},\mathbf{q}'}$ generally agrees with Eq. 2.38, the authors of vdW-DF1 apply four exact physical constraints in its construction:

1. The f-sum rule: $S_{\mathbf{q},\mathbf{q}'} \to -(4\pi e^2/m\omega^2) n_{\mathbf{q}-\mathbf{q}'}$ for large ω, where n_k is the Fourier transform of the density.

2. Exactly known self-correlation: $\int_{-\infty}^{\infty} du \, S_{\mathbf{q},\mathbf{q}'}(iu) \to 8\pi^2 N e^2/q^2$ for large q, where N is the number of electrons.

3. Time reversal invariance: $S_{\mathbf{q},\mathbf{q}'} = S_{-\mathbf{q}',-\mathbf{q}}$.

4. Charge conservation: As q or $q' \to 0$, $S_{\mathbf{q},\mathbf{q}'}(\omega)$ must be finite for all nonzero values of ω .

They arrive at the following form, which satisfies all of the above conditions:

$$S_{\mathbf{q},\mathbf{q}'} = \int d\mathbf{r} \, e^{-i(\mathbf{q}-\mathbf{q}')\cdot\mathbf{r}} \left[\frac{\omega_p(\mathbf{r})^2}{(\omega_q(\mathbf{r}) + \omega)(\omega_{q'}(\mathbf{r}) - \omega)} + \frac{\omega_p(\mathbf{r})^2}{(\omega_{-q'}(\mathbf{r}) + \omega)(\omega_{-q}(\mathbf{r}) - \omega)} \right] . \tag{2.39}$$

The definitions the plasmon frequency ω_p and plasmon dispersion law ω_q play an important

role in the evaluation of $S_{\mathbf{q},\mathbf{q}'}$. Both have exactly-known forms, those being

$$\omega_p(\mathbf{r}) = \sqrt{\frac{4\pi n(\mathbf{r})e^2}{m}}\ , \tag{2.40}$$

$$\omega_q(\mathbf{r}) = \sqrt{\omega_p(\mathbf{r})^2 + (3\pi^2 n(\mathbf{r}))^{2/3}\hbar^2 q^2/3m^2 + (\hbar q^2/2m)^2}\ . \tag{2.41}$$

However, taking this ω_q explicitly within Eq. 2.39 quickly makes the evaluation of E_c^{nl} intractable. As a way around this problem, the authors devise a simplified form of the plasmon dispersion law, letting $\omega_q(\mathbf{r}) = \hbar q^2/2mh(q/q_0(\mathbf{r}))$. This form is merely the high q-limit of Eq. 2.41 modulated by a switching function $h(q/q_0(\mathbf{r}))$, the purpose of which is to gradually "turn on" long-range dispersion effects at high q. While this method sacrifices some of the accuracy of Eq. 2.41, it greatly simplifies the integrations in E_c^{nl} by having $\omega_q(\mathbf{r})$ depend on a single length-scale $1/q_0(\mathbf{r})$.

Since its development in 2004, vdW-DF1 has seen extensive use in the materials community. Likewise the family of van der Waals density functionals has grown immensely, improving upon the accuracy of vdW-DF1 for a wide array of system types. Often, the development of such new functionals focuses on replacing or reparameterizing the GGA exchange, rather than the nonlocal correlation itself. But some functionals, such as VV10 [9], vdW-DF2 [10], and vdW-DF3 [11], have made great leaps in accuracy with only minor alterations to the E_c^{nl} devised by Dion *et al.* And as you will see, my research encompasses both of these approaches, researching and optimizing the accuracy of the GGA exchange and nonlocal correlation simultaneously.

Chapter 3

Reduced-Gradient Analysis of van der Waals Complexes

 Supporting Information for this chapter can be found at DOI: 10.1088/2516-1075/ac25d7. I am the first author on this paper, with contributions in the form of theory, calculations, writing, and editing.

3.1 Abstract

Different methods to describe dispersion interactions within density functional theory have been developed, which is essential to describe binding in van der Waals complexes. However, several key aspects of such complexes—including binding energies, lattice constants, and binding distances—also depend on the exchange description that is paired with the description of dispersion interactions. This is particularly true for the vdW-DF family of van der Waals density functionals, which has a clear division between truly nonlocal correlations and semilocal generalized-gradient exchange. Here, we present a systematic analysis of the reduced-gradient values that determine the semilocal exchange for different classes of van der Waals complexes. In particular, we analyze molecular dimers, layered structures, surface adsorption, and molecular crystals. We find that reduced-gradient values of less than $\sim$1 to $\sim$1.5—depending on the system—contribute attractively to the exchange bind-

ing, while reduced gradients above those values are repulsive. We find that the attractive contributions can be attributed to low-density regions between the constituents with disk-like iso-surfaces. We further identify a mechanism wherein the surface area of these disks decreases through merging with other iso-surfaces and switches the gradient-correction to exchange from attractive to repulsive. This analysis allows us to explain some of the differences in performance of vdW-DF variants and initiates a discussion of desirable features of the exchange enhancement factor. While our analysis is focused on vdW-DF, it also casts light on van der Waals binding in a broader context and can be used to understand why methods perform differently for different classes of van der Waals systems.

3.2 Introduction

van der Waals interactions provide crucial contributions to the binding and structure of an ever-growing list of technologically relevant materials, reaching from photovoltaics and organic electronics [13–16], to ferroelectrics [17, 18], pharmaceuticals [19], and applications in gas storage/sequestration [20–22], sensing [23], and catalysis [24]. Density functional theory has long struggled to correctly describe those materials, but over the last two decades numerous approaches have been developed to overcome this problem [3, 9, 25–40]. Among these, the vdW-DF family [3, 11, 38–41] of nonlocal density functionals is of particular interest because it can describe van der Waals interactions based on knowledge of the electron density $n(\mathbf{r})$ alone. The latest release of this family, i.e. vdW-DF3 [11], exhibits the highest accuracy for different classes of dispersion-bonded systems in the vdW-DF family. However, during the construction of vdW-DF3 it became apparent that further efforts to improve its accuracy are inhibited by a lack of in-depth understanding of the mechanisms causing different vdW-DF variants to perform differently for different classes of systems.

The van der Waals interactions within vdW-DF are captured through a nonlocal correlation contribution to the exchange-correlation energy [3, 40]. This nonlocal correlation functional provides the majority of the energetics that contributes to the binding of van der Waals complexes. However, the remainder of the exchange-correlation functional—in particular the semilocal exchange—plays a crucial role in determining structural aspects such as binding separations or lattice constants. Within the generalized-gradient approximation [6], the semilocal exchange is typically expressed in terms of an exchange enhancement factor $F_{\mathrm{x}}(s)$, which describes gradient corrections to the local density approximation in terms of the reduced gradient $s(\mathbf{r}) \propto |\nabla n(\mathbf{r})|/n(\mathbf{r})^{4/3}$. Various exchange enhancement factors used in the vdW-DF family are plotted in Fig. 3.1 and lead to quite different results for different classes of van der Waals complexes [11]. Different features of $F_{\mathrm{x}}(s)$ and its derivative play an important role in determining the various aspects of van der Waals systems, possibly leading to competing requirements for $F_{\mathrm{x}}(s)$ to achieve high accuracy, as discussed for molecular dimers vs. molecular crystals in Ref. [11]. In this paper, we provide a systematic analysis of which values of s are most important for different systems. This allows us to explain some

of the performance differences of the various exchanges that have been used throughout the history of the vdW-DF development, and it also forms the basis for identifying desirable features of the exchange enhancement factor. Such an s-analysis has a long history for general systems [42–44] and was first applied to a limited set of van der Waals complexes in Ref. [45]. While our paper emphasizes a quantitative analysis of energetic and force contributions to vdW-DF, our analysis can also provide a starting point to understand and improve other schemes to include dispersion interactions in density functional theory. In addition, our reduced-gradient analysis can also be used to assess the nature and existence of non-covalent bonding from a method-independent perspective following Refs. [46, 47].

3.3 Theory

Within the vdW-DF framework, the exchange-correlation energy $E_{\rm xc}$ is given by

$$E_{\rm xc}[n] = E_{\rm x}^{\rm GGA}[n] + E_{\rm c}^{\rm LDA}[n] + E_{\rm c}^{\rm nl}[n] \; . \tag{3.1}$$

Here, the semilocal exchange $E_{\rm x}^{\rm GGA}[n]$ is given at the GGA level, the purely local correlation $E_{\rm c}^{\rm LDA}[n]$ is evaluated at the LDA level, and the nonlocal contribution is given by

$$E_{\rm c}^{\rm nl}[n] = \frac{1}{2} \int d\mathbf{r} \int d\mathbf{r}' \; n(\mathbf{r}) \, \Phi(\mathbf{r}, \mathbf{r}') \, n(\mathbf{r}') \; , \tag{3.2}$$

where the kernel $\Phi(\mathbf{r}, \mathbf{r}')$ is a function of the charge density and its gradient at the points $\mathbf{r}$ and $\mathbf{r}'$ [3]. Note the lack of gradient corrections to the local correlation in Eq. 3.1 [40], which ensures that there is no double-counting of semilocal correlation contributions. The nonlocal contribution is derived from a many-body starting point and observes four physical constraints [40, 48–51]. The semilocal exchange is typically expressed as

$$E_{\rm x}^{\rm GGA}[n] = \int d\mathbf{r} \; n(\mathbf{r}) \, \epsilon_{\rm x}^{\rm hom}\big(n(\mathbf{r})\big) \, F_{\rm x}(s) \; , \tag{3.3}$$

and describes the enhancement (through the exchange enhancement factor $F_{\rm x}(s)$) over the exchange of the homogeneous electron gas $\epsilon_{\rm x}^{\rm hom}$. It is Eq. 3.2 that allows vdW-DF to capture

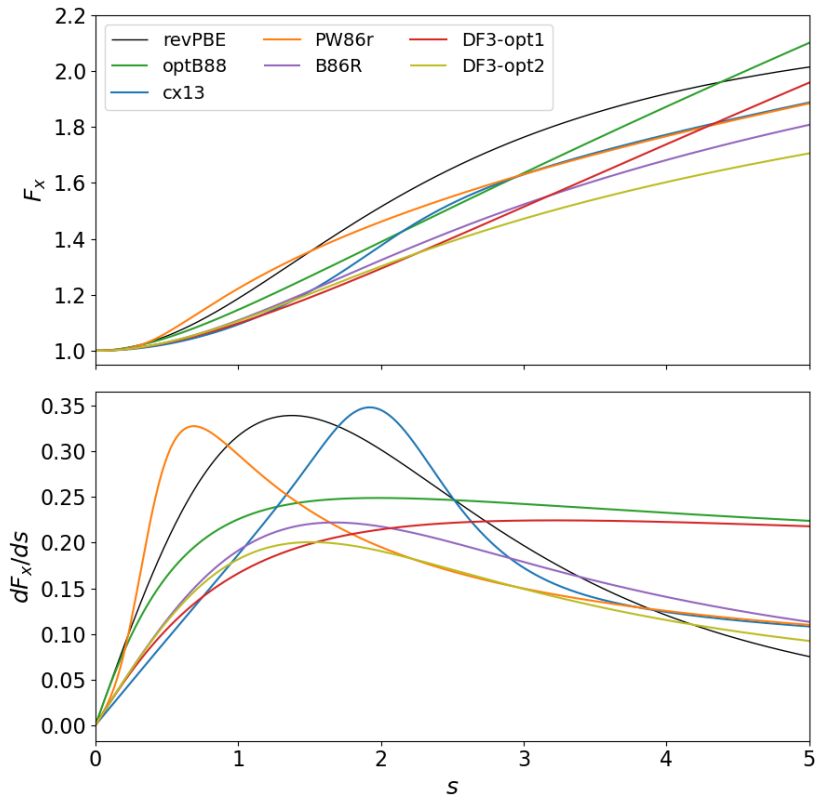

Figure 3.1: **(top)** Exchange enhancement factors $F_{\mathrm{x}}(s)$ used in various vdW-DF variants and **(bottom)** their derivatives.

van der Waals interactions [40] and distinguishes the vdW-DF family from other, popular semilocal functionals such as PBE [6] and hybrid functionals such as PBE0 [52] and B3LYP [53] (which do not have an explicit mechanism to describe long-range London dispersion forces and are thus often paired with C_6-based correction schemes such as DFT-D3 [54]). Note that hybrid functionals include a fraction of the exact exchange in conjunction with a density functional like Eq. 3.3.

Much research has gone into improving the exchange enhancement factor within vdW-DF. The original choice of revPBE [55,56] for the GGA-type exchange in vdW-DF1, with its rapidly increasing $F_{\mathrm{x}}(s)$ in the $s = 0.5-2$ range (see Fig. 3.1), avoids nonphysical exchange-based binding in van der Waals systems at binding separations [3, 45]. However, that same choice of revPBE is also responsible for the too large binding separations observed with vdW-DF1 [57–60]. Further research indicated that $F_{\mathrm{x}}(s) \propto s^{2/5}$ in the limit of large s also avoids such non-physical binding using a formal argument and can provide good agreement with Hartree-Fock calculations [45]. This argument was used to support the use of PW86r

in vdW-DF2 [10]. It has also been shown that the separation overestimation in vdW-DF1 can be avoided by using an $F_{\rm x}(s)$ that increases more slowly with s for small values of $s < 1$ [61].

Clearly, the features of $F_{\rm x}(s)$, in particular for values $0 < s < 3$, have a profound impact on van der Waals complexes. But, in order to make improvements, we have to identify which s values in that range are the most important for a particular class of complexes and deduce desirable shapes of $F_{\rm x}(s)$ in more limited ranges of s to improve a particular class of systems. To identify s values important for the binding of van der Waals complexes, we compute the s-resolved exchange interaction energy as the difference between the GGA and LDA values [45]

$$\Delta e_{\rm gx}(s) = e_{\rm gx}^{\rm tot}(s) - \sum_i e_{\rm gx}^i(s) \ , \tag{3.4}$$

where the "tot" superscript refer to the total system and "i" refers to the individual fragments. The individual gradient portions of the exchange energy are calculated as

$$e_{\rm gx}(s) = -\frac{3}{4}\left(\frac{3}{\pi}\right)^{1/3}\int d\mathbf{r}\ n^{4/3}\ \big[F_{\rm x}\big(s(\mathbf{r})\big) - 1\big]\delta\big(s - s(\mathbf{r})\big) \ , \tag{3.5}$$

where the $\big[F_{\rm x}\big(s(\mathbf{r})\big) - 1\big]$ singles-out the purely semilocal gradient corrections to exchange by removing contributions from the local LDA exchange, which all vdW-DF functional have in common.[1] Similarly, in Eq. 3.1 all vdW-DF functionals have the same local correlation $E_{\rm c}^{\rm LDA}$, allowing us to relate performance differences mostly to differences in semilocal gradient exchange, Eq. 3.5, for all functionals that share the same $E_{\rm c}^{\rm nl}$. The main focus of our analysis will be the comparison of $\Delta e_{\rm gx}(s)$ from Eq. 3.4 for various different classes of van der Waals complexes as well as different functionals of the vdW-DF family. Another property of interest is the s-integrated quantity

$$\Delta E_{\rm gx}(s) = \int_0^s ds'\ \Delta e_{\rm gx}(s') \ . \tag{3.6}$$

Then, $\Delta E_{\rm gx}(\infty)$ gives the total gradient-corrected exchange portion of the interaction energy.

[1] This expressions will give energies in "a.u.", i.e. Hartree.

For an analysis of binding separations, the corresponding forces are essential. In parallel to the s-resolved exchange energy $\Delta e_{\rm gx}(s)$ we define a s-resolved exchange force $\Delta k_{\rm gx}(s)$ as the energy derivative

$$\Delta k_{\rm gx}(s) = -\frac{d\Delta e_{\rm gx}(s)}{d|a|} \ , \tag{3.7}$$

where **a** is a suitably defined separation between fragments of the van der Waals complex. Such forces are related to the exchange *potential*, which in turn includes terms of the form $dF_{\rm x}(s)/ds$ [62, 63]. Performance with respect to binding separations will thus make connections to the bottom panel of Fig. 3.1. Similarly to Eq. 3.6, we define the s-integrated quantity $\Delta K_{\rm gx}(s)$; where $\Delta k_{\rm gx}(s)$ is analogous to $\Delta e_{\rm gx}(s)$, $\Delta K_{\rm gx}(s)$ is the integrated analogue to $\Delta E_{\rm gx}(s)$.

3.4 Computational Details

The computational details are mostly identical those in Ref. [11]. Our calculations were based on the QUANTUM ESPRESSO (QE) package [64] with PBE ultrasoft pseudopotentials designed by Garrity, Bennett, Rabe, and Vanderbilt (GBRV) [65]. Where applicable, all systems were structurally optimized with a wave-function cutoff of 50 Ryd and a density cutoff of 600 Ryd. The energy convergence criterion was 1×10^{-8} Ryd and the force convergence criterion was 1×10^{-6} Ryd/Bohr. Calculations on molecular dimers/monomers were performed in boxes with at least 15 Å of vacuum for padding. Layered structures were obtained from the Inorganic Crystal Structure Database (ICSD) and we used the procedure in Refs. [66–68] to optimize those systems, i.e. we relaxed the inter-layer c-axis with $12 \times 12 \times 6$ k-points and kept the a-lattice constant at the experimental value. Single layers were calculated with fixed a-lattice constant and with at least 12 Å vacuum along the c-axis, utilizing a $12 \times 12 \times 1$ k-mesh. The structure of the molecular crystals for the X23 dataset were obtained from Ref. [69] and all structural degrees of freedom were optimized, sampling only the Γ-point of the Brillouin zone. Finally, for the adsorption of benzene on the (111) surface of the coinage metals Cu, Ag, and, Au we used 6 atomic metal layers [70] of which we kept the three bottom layers fixed; we used 9 Å vacuum and a $4 \times 4 \times 1$ k-mesh.

While the physical aspects of all systems are well converged with the kinetic energy

cutoffs provided above, plots of $\Delta e_{\rm gx}(s)$ from Eq. 3.4 are very noisy due to the finite spatial integration grid in plane-wave calculations used for $n(\mathbf{r})$ and $s(\mathbf{r})$ in Eq. 3.5. While increasing the energy cutoff results in a denser grid, it only provides diminishing returns for noise reduction; we explored density cutoffs up to 1920 Ryd. To limit the grid sensitivity, we introduced broadening by first integrating $\Delta e_{\rm gx}$

$$\Delta E_{\rm gx}(s) \approx \int_0^\infty ds' \, \Delta e_{\rm gx}(s') \, G(s,s') \, , \tag{3.8}$$

where

$$G(s,s') = \frac{1}{e^{(s'-s)/\beta}+1} \tag{3.9}$$

is a Fermi-type function, and then calculated the numerical derivative to arrive at a broadened $\Delta e_{\rm gx}(s)$. This procedure drastically reduces the gird-sensitivity. We found that small values of $\beta = 0.03$ are sufficient. However, even with this approach some systems required density cutoffs as high as 1920 Ryd to ensure low noise in $\Delta e_{\rm gx}(s)$.

In addition to $\Delta e_{\rm gx}(s)$ and $\Delta E_{\rm gx}(s)$, we calculate the s-resolved exchange force $\Delta k_{\rm gx}(s)$ from Eq. 3.7 through a finite difference method wherein we calculate $\Delta e_{\rm gx}(s)$ for two different distances. For example, for the benzene dimer, we move the "frozen" monomers along the natural direction defined by the S22×5 [71] dataset by 0.05 Å.

We also compare the performance of various well-used members of the vdW-DF family. In particular, we will be using vdW-DF (vdW-DF1) [3], vdW-DF1-optB88 [72], vdW-DF1-cx [60, 73], vdW-DF2 [10], vdW-DF2-B86R [74], vdW-DF3-opt1 [11], and vdW-DF3-opt2 [11] and we will use the following corresponding abbreviations: DF1, DF1-optB88, DF1-cx, DF2, DF2-B86R, DF3-opt1, and DF3-opt2. Furthermore, the functionals include the following exchanges: revPBE [55, 56], optB88 [72], cx13 [73], PW86r [75], B86R [74], DF3-opt1 [11], and DF3-opt2 [11].

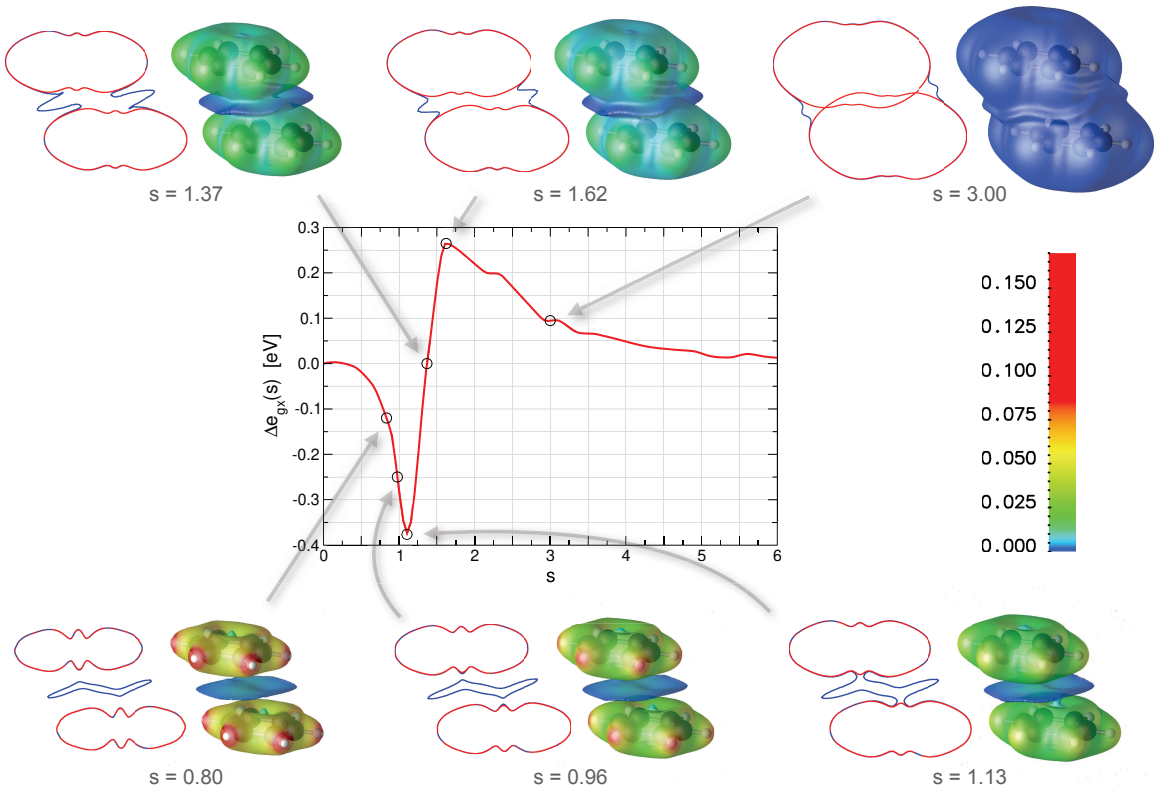

Figure 3.2: **(center)** s-resolved exchange interaction energy $\Delta e_{\mathrm{gx}}(s)$ for the benzene dimer in C_{2h} configuration for the optimal CCSD(T) separation, calculated with DF3-opt1. **(top and bottom insets)** Iso-surfaces for different values of s. The electronic charge density is mapped onto the iso-surface in color and can be read off the color bar in units of e/Bohr^3. Each iso-surface is further mapped onto a plane that goes through the center of the dimer, resulting in iso-lines; lines of the dimer are blue and lines of the individual monomers are red.

3.5 Results

3.5.1 The Benzene Dimer

Figure 3.2 provides a detailed s-analysis of one representative van der Waals-bound dimer, i.e. the benzene dimer in C_{2h} configuration, which is part of the commonly studied S22×5 set of molecular dimers [71,76]. The center of Fig. 3.2 shows the s-resolved exchange interaction energy $\Delta e_{\rm gx}(s)$ of the benzene dimer for the optimal "1.0" CCSD(T) separation. Unless otherwise noted, all such curves are generated with the GGA exchange of DF3-opt1. The curve has a negative regime at low s, contributing in an attractive way to binding, and a positive regime at higher values of s, contributing in a repulsive way. The various motifs in Fig. 3.2 show iso-surfaces of the benzene dimer at different values of s. These can be linked to the shape of $\Delta e_{\rm gx}(s)$ and the different spatial regions contributing to it. For clarity, the adjacent blue iso-lines show intersections of the dimer iso-surfaces with a plane crossing the center of the dimers, overlaid by red iso-lines corresponding to individual monomers. Consider first the attractive low-s regime. For $s = 0.80$ and $s = 0.96$, three distinct surfaces are apparent: two surrounding the individual monomers and one disk-shaped surface in-between them. For these s values, the iso-surfaces of the monomers are nearly identical to the corresponding portions of the dimer iso-surface. Thus, for these low-s values, there is a near-perfect cancellation of the contributions of these surfaces to $\Delta e_{\rm gx}(s)$ in Eq. 3.4 and the attractive energy therefore comes almost exclusively from the disk region.

As the iso-surfaces grow with increasing s, they eventually start overlapping and merging. At $s = 1.13$, the onset of this merger has begun, as evident in the iso-lines. The merger causes both the disk and molecular iso-surfaces to effectively loose surface area. This reduces the attractive contributions from the disk and gives rise to repulsive contributions to the s-resolved exchange energy due to less and less cancellation of the monomer iso-surfaces. This merging thus causes the crossover from negative to positive $\Delta e_{\rm gx}(s)$. Once the merger has completed, the overall shape of the combined dimer iso-surface remains similiar while growing outwards around the benzene dimer. As the s iso-surface grows, the charge density decrease, which is the cause for the decrease in $\Delta e_{\rm gx}(s)$ beyond the positive peak at $s = 1.62$. In Fig. S1 in the Supporting Information (SI) of Ref. [12], we provide a s–n

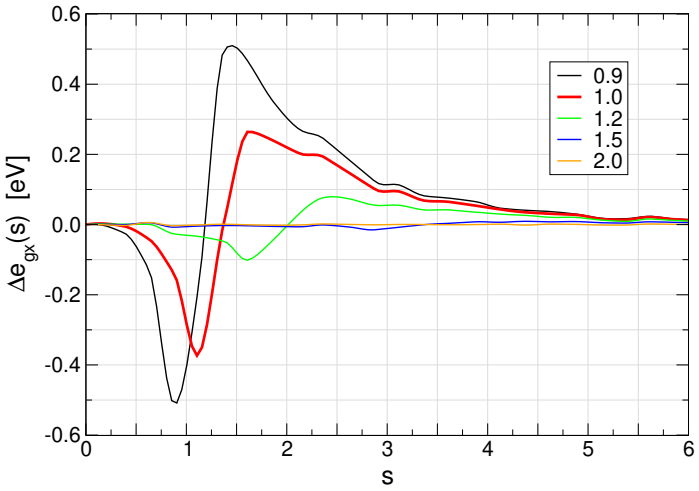

Figure 3.3: s-resolved exchange interaction energy $\Delta e_{\rm gx}(s)$ for the benzene dimer in C_{2h} configuration for separations ranging from 0.9 to 1.0, 1.2, 1.5, and 2.0 times the optimal CCSD(T) binding separation, as defined in the S22×5 dataset [71].

scatter-plot [46,47], which complements this analysis.

In Fig. 3.3, we show $\Delta e_{\rm gx}(s)$ for the five separations defined in the S22×5 dataset, from 0.9 to 1.0, 1.2, 1.5, and 2.0 times the optimal CCSD(T) binding separation. The crossover and ranges spanned by the attractive and repulsive regimes vary significantly with respect to separation, but the overall shapes of the curves remain quite similar. The analysis of the benzene dimer at optimal separation allows us to also interpret the change in $\Delta e_{\rm gx}(s)$ with separation. On the one hand, the onset of the merger in s increases with separation, as the central disk has more room to grow before merging, causing the shift in $\Delta e_{\rm gx}(s)$ to larger s values with increasing separation. On the other hand, the decrease in magnitude of $\Delta e_{\rm gx}(s)$ with increasing separation can be explained by the lower electronic densities in the inter-molecular region.

3.5.2 Comparison of Exchange Functionals at Optimal Separation

Table 3.1 shows the total interaction energy ΔE of the benzene dimer at the "1.0" separation, the corresponding gradient exchange portion $\Delta E_{\rm gx}(\infty)$, the nonlocal correlation contribution $\Delta E_c^{\rm nl}$, the gradient exchange portion of the force $\Delta K_{\rm gx}(\infty)$, and the dimer distance resulting from a full optimization for various vdW-DF functionals. Comparison

Table 3.1: Total interaction energy ΔE of the benzene dimer in C_{2h} configuration at the optimal CCSD(T) distance [eV], corresponding gradient exchange portion $\Delta E_{\rm gx}(\infty)$ [eV], nonlocal correlation contribution $\Delta E_c^{\rm nl}$ [eV], gradient exchange portion of the force $\Delta K_{\rm gx}(\infty)$ [eV/Å], and dimer distance [Å] resulting from a full optimization. CCSD(T) results are given for reference [71, 76].

Functional	reference	DF1	DF2	DF1-optB88	DF1-cx	DF2-B86R	DF3-opt1	DF3-opt2
Exchange	—	revPBE	PW86r	optB88	cx13	B86R	DF3-opt1	DF3-opt2
ΔE [eV]	−0.1219	−0.0881	−0.0968	−0.1416	−0.1120	−0.0937	−0.1191	−0.1234
$\Delta E_{\rm gx}(\infty)$ [eV]	—	0.4281	0.3056	0.3626	0.3891	0.3094	0.2990	0.2783
$\Delta E_{\rm c}^{\rm nl}$ [eV]	—	−0.3879	−0.2865	−0.3980	−0.3969	−0.2923	−0.3090	−0.2891
$\Delta K_{\rm gx}(\infty)$ [eV/Å]	—	0.6998	0.5389	0.5203	0.5449	0.4561	0.3930	0.4175
Distance [Å]	3.765	4.214	4.064	3.939	4.089	3.989	3.864	3.914

with CCSD(T) reference values shows that the performance of the different functionals can vary significantly. Trends in the interaction energy ΔE can be related to $\Delta E_{\rm gx}(\infty)$—taking the differences in $\Delta E_c^{\rm nl}$ into account—which in turn can be related to $\Delta e_{\rm gx}(s)$ (top panel of Fig. 3.4) and $F_{\rm x}(s)$ (top panel of Fig. 3.1). The optimized binding distances are related to forces $\Delta k_{\rm gx}(s)$ (bottom panel of Fig. 3.4), which can be related to $dF_{\rm x}(s)/ds$ (bottom panel of Fig. 3.1).

When integrating $\Delta e_{\rm gx}(s)$ to get $\Delta E_{\rm gx}(s)$ in Fig. 3.4, at some point the negative and positive contributions of $\Delta e_{\rm gx}(s)$ cancel, causing $\Delta E_{\rm gx}(s)$ to cross the zero line. Since $F_{\rm x}(s)$ varies quite slowly with s, this crossing occurs at quite similar values of s for most functionals (in the case of the benzene dimer at $s \approx 2$). All net contributions to $\Delta E_{\rm gx}(\infty)$ are therefore given by the shape of $F_{\rm x}(s)$ beyond this crossing point. However, even small differences in the crossing point—or correspondingly the value of $\Delta E_{\rm gx}(s = 2)$—do matter, since the $\Delta e_{\rm gx}(s)$ curve is so steep in this region, making the values of $F_{\rm x}(s)$ below this crossing point also important. Here, we discuss differences in $\Delta E_{\rm gx}(\infty)$ caused by different $F_{\rm x}(s)$ in terms of contributions of negative and positive regions in $\Delta e_{\rm gx}(s)$, but one could alternatively analyze it in terms of shifts in crossing points of $\Delta E_{\rm gx}(s)$ and the values of $F_{\rm x}(s)$ beyond that. Such an analysis is provided in Fig. S2 in the SI of Ref. [12].

We now discuss how specific shapes of $F_{\rm x}(s)$ and $\Delta e_{\rm gx}(s)$ give rise to different values of $\Delta E_{\rm gx}(\infty)$. We first compare PW86r, DF3-opt2, and B86R. These have quite similar $\Delta E_{\rm gx}(\infty)$, but the $F_{\rm x}(s)$ values of PW86r are consistently larger than those of DF3-opt2 and B86R. However, since those larger values partially cancel through negative and positive contributions of $\Delta e_{\rm gx}(s)$, the end result is quite similar values of $\Delta E_{\rm gx}(\infty)$. The slightly

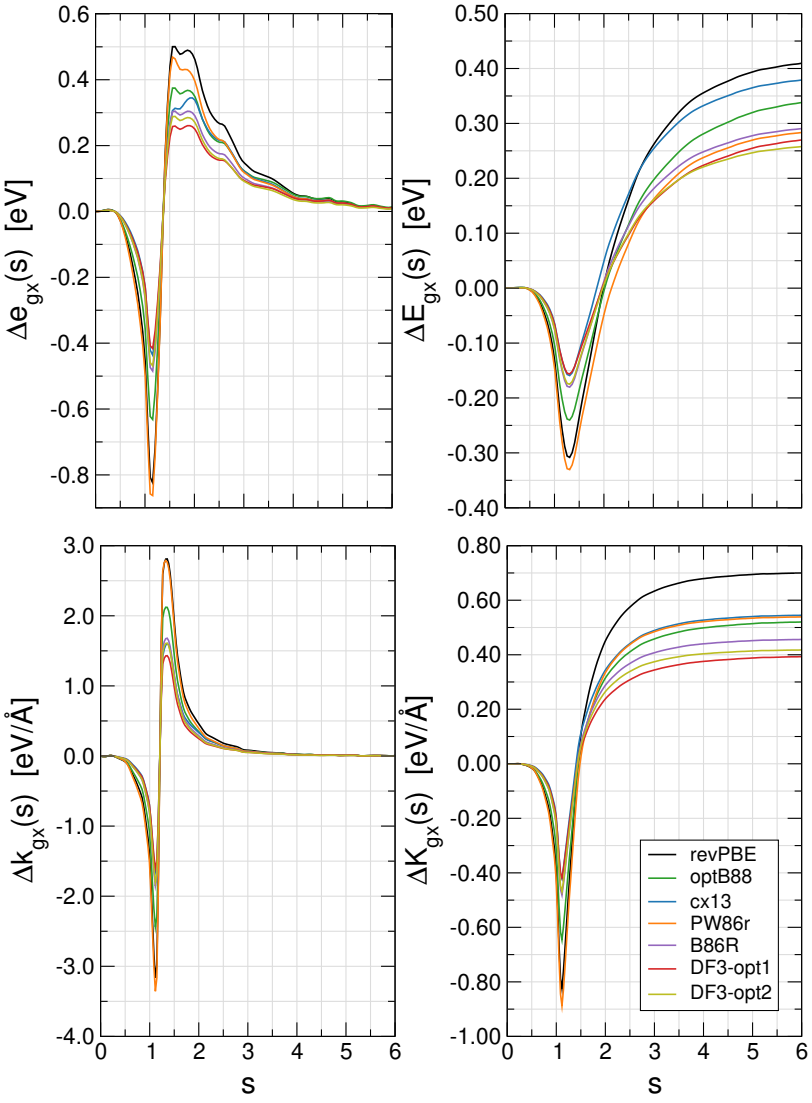

Figure 3.4: s-resolved exchange interaction energy $\Delta e_{\mathrm{gx}}(s)$, exchange energy $\Delta E_{\mathrm{gx}}(s)$, s-resolved exchange force $\Delta k_{\mathrm{gx}}(s)$, and exchange force $\Delta K_{\mathrm{gx}}(s)$ for the benzene dimer in C_{2h} configuration for several different exchange functionals. Further analysis can be found in Fig. S2 in the SI of Ref. [12].

lower values of DF3-opt2 compared to B86R can be related to the smaller values of $F_{\mathrm{x}}(s)$ for large s. Comparing cx13 and PW86r gives a different weighing. On the one hand, $F_{\mathrm{x}}(s)$ of cx13 is lower than that of PW86r (as is B86R) in the attractive regime, but on the other hand, at larger s, $F_{\mathrm{x}}(s)$ becomes more similar until they become identical at large s [73]. cx13 therefore has a significantly reduced attractive portion of the exchange compared to PW86r, but retains quite similar repulsive contributions, resulting in significantly larger $\Delta E_{\mathrm{gx}}(\infty)$. This analysis shows how PW86r and B86R, both with quite different $F_{\mathrm{x}}(s)$, can give quite similar energies when combined with DF2 nonlocal correlation. cx13, with its much larger value of the exchange energy, is comparable with DF1, which has a much larger negative nonlocal correlation energy contribution to the binding. Similar to PW86r, revPBE has quite large values of $F_{\mathrm{x}}(s)$ in the attractive regimes, but more than compensates for this by having even larger values of $F_{\mathrm{x}}(s)$ than the other functionals in most of the repulsive regime, with the end result of a too low interaction energy even when combined with DF1 nonlocal correlation. For most values of s, optB88 falls somewhere in-between cx13 and revPBE, making it a suited companion to DF1 nonlocal correlation, which is what it was fitted to [72]. However, since optB88 in the repulsive regime is closer to cx13 than revPBE, it has a lower exchange energy than cx13 and DF1-optB88 overestimates the full interaction energy for this system.

Looking at the forces, we find that the slope of the enhancement factor at typical s values plays a significant role. In the lower panels of Fig. 3.4 we see how the s-resolved force $\Delta k_{\mathrm{gx}}(s)$ crosses zero at $s_0^{\Delta k} = 1.21$ and $\Delta K_{\mathrm{gx}}(s)$ crosses zero at almost precisely $s_0^{\Delta K} = 1.45$, which is also approximately the location of the upward peak in $\Delta e_{\mathrm{gx}}(s)$. The force curves are much more narrow and localized than the corresponding s-resolved exchange energy curves. Because they are so narrow and the negative and positive regions partially cancel, the slope of dF_{x}/ds around $s_0^{\Delta k}$ becomes very important for analysis, since it effectively determines the weighing of the relative negative and positive portions. Moreover, typical $\mathrm{d}F_{\mathrm{x}}/ds$ differ more from each other than typical $F_{\mathrm{x}}(s)$ in this regime. In fact, comparing Fig. 3.1 and Table 3.1 and the lower left panel of Fig. 3.4, we observe a strong correlation between $dF_{\mathrm{x}}/ds\,(s_0^{\Delta k})$ and the total exchange force for each functional. The ordering from largest-to-smallest $\mathrm{d}F_{\mathrm{x}}/ds\,(s_0^{\Delta k})$—i.e. revPBE, cx13 $\approx$ PW86r, optB88, B86R, DF3-opt2,

and DF3-opt1—matches the ordering of $\Delta K_{\rm gx}(\infty)$.

This ordering can also be connected to the differences in binding separations in Table 3.1, which in a first-order approximation is proportional to the differences in the exchange force for the same nonlocal correlation. Even for the cases where the nonlocal correlation differs the comparison has merit as the nonlocal correlation has a slower distance dependence than the exchange [77]. Thus, the trend in $dF_{\rm x}/ds\,(s_0^{\Delta k})$ explains why standard DF1 with revPBE has the largest binding distance and DF3-opt1 has the shortest. The only exception is the somewhat larger separation of DF2-B86R compared to DF1-optB88, which can be attributed to the smaller attractive force of DF2 nonlocal correlation compared to DF1.

The fact that differences in forces can be attributed to a rather narrow region of $dF_{\rm x}/ds$ and somewhat lower values of s compared to differences in energies, explains why updating the exchange of DF1 to that of e.g. optB88 and cx13 had the capability to improve both binding energies and distances, and likewise for the switch from PW86r to B86R for DF2. However, as shown in Fig. 3.3, the typical s values shift with separation and good performance at binding separations is no guarantee that the interaction energies beyond the binding separation is accurate for a given nonlocal correlation functional. In fact, inaccurate interaction energies beyond the binding separation were one of the key motivations for developing vdW-DF3 [11].

3.5.3 S22×5 Dataset at Optimal Separation

We next analyze the s-resolved exchange interaction energy $\Delta e_{\rm gx}(s)$ (upper panel of Fig. 3.5) and force $\Delta k_{\rm gx}(s)$ (lower panel for Fig. 3.5) for the 22 dimers in the S22×5 set at the "1.0" separation [71]. In general, the iso-surfaces for these dimers exhibit the same main features as for the benzene dimer, i.e. the formation of a disk in-between the molecules at low-s values, a merger process, and subsequent iso-surface growth. The similar shapes of the $\Delta e_{\rm gx}(s)$ curves compared to the benzene dimer (system 11) is reflected in the statistical representation in the upper panel. The blue band indicates the domain that covers 80% of the negative part of the curve, centered around the median (blue curve). The wider red band is the corresponding data for the positive curve; the much larger domain above the median (red curve) reflects the longer tails of the $\Delta e_{\rm gx}(s)$ curves. The black curve indicates

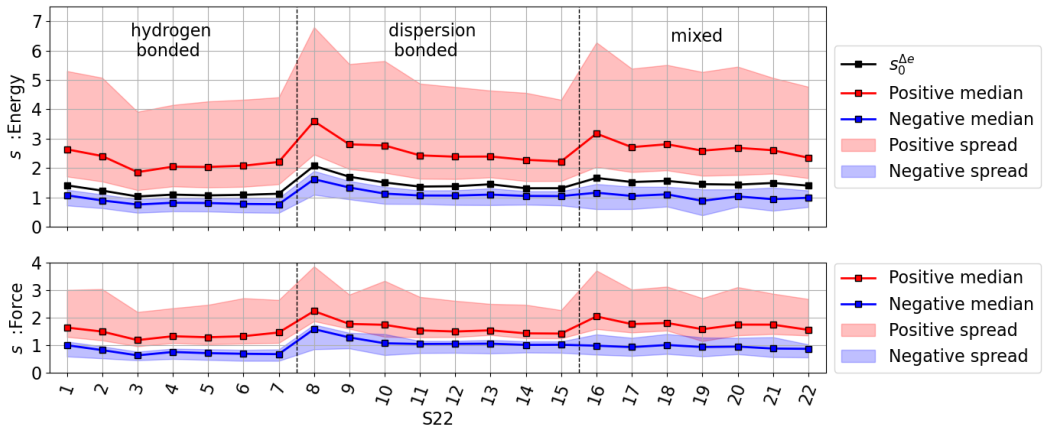

Figure 3.5: Statistical data for the S22 dataset of molecular dimers. For full $\Delta e_{\mathrm{gx}}(s)$ curves and for dimer numbering see Fig. S3. The median and spread for each dimer are calculated separately for the positive and negative regions of $\Delta e_{\mathrm{gx}}(s)$ and $\Delta k_{\mathrm{gx}}(s)$, see Fig. S4 for details.

$s_0^{\Delta e}$, i.e. the point where $\Delta e_{\mathrm{gx}}(s)$ crosses zero.

A number of trends can be seen from Fig. 3.5. Comparing the hydrogen-bonded and dispersion-dominated systems, the average $s_0^{\Delta e}$ value increases from 1.15 to 1.51, with similar shifts in magnitude for the medians. For systems involving the smallest molecules and in which hydrogen atoms are involved in the binding, the typical $s_0^{\Delta e}$ value is shifted to larger values, which is particularly evident for the methane dimer (system 8, $s_0^{\Delta e} = 2.1$) and the ethene-ethyne dimer in the T-configuration (system 16, $s_0^{\Delta e} = 1.7$). For some of the mixed systems and dispersion-bonded systems, the iso-surfaces have several merging points at different values of s, resulting in more wiggled $\Delta e_{\mathrm{gx}}(s)$ curves. This is reflected in the broader blue bands for the mixed systems than for the hydrogen- and dispersion-bonded systems.

As for the benzene dimer (see Fig. 3.4), the force bands are noticeably narrower than the energy bands and shifted to lower s-values; for instance the negative median is shifted from an average of 1.25 to 0.96. An added complication for the force curves is that for systems with more complicated iso-surface mergers, this can cause rapid oscillations in $\Delta k_{\mathrm{gx}}(s)$. The exact $s_0^{\Delta k}$ roots of these curves can be hard to disentangle and depend on broadening choices in Eq. 3.9 and therefore are not shown. These oscillations are also the reason why some of the blue and red bands partially overlap in the lower panel of Fig. 3.5.

As for the benzene dimer, trends in the curves for the entire S22×5 set at the "1.0"

separation (provided in Fig. S3) can be compared with Fig. 3.4. In line with the analysis for the benzene dimer, such a comparison suggests that more local changes in $F_{\mathrm{x}}(s)$ in Fig. 3.1 may allow for targeted improvements, in particular for the binding separations. Such modifications could potentially overcome the competing requirements uncovered in Ref. [11]. Our results can for instance explain why DF1-cx significantly overestimates the methane dimer binding separation (system 8, by 0.25 Å) compared to an almost perfect agreement with the reference data for DF3-opt1 (see Table S1 in the SI of Ref. [12]). As seen in the lower panel of Fig. 3.5, the crossing region between the blue and red bands around $s \approx 1.6-1.8$ coincides with the region in which dF_{x}/ds values of cx13 become larger than those of revPBE (DF1 overestimates this dimer distance by 0.175 Å). DF3-opt2 is the only functional underestimating the separation of this dimer (-0.02 Å) and also has the lowest dF_{x}/ds in this region, whereas DF3-opt1 with slightly larger dF_{x}/ds in this region, has a perfect agreement with the reference data.

The precise reason why a functional like DF1-cx can give fairly accurate binding energies for the benzene dimer (see Tables S2 and S3) while having an initially slow increase in $F_{\mathrm{x}}(s)$—which is why the functional provides excellent lattice constants of covalent solids—is the increase to larger $F_{\mathrm{x}}(s)$ starting at $s \approx 1.5$. Without this increase, the repulsive components are not sufficiently weighted to counteract the large energetic contribution from the nonlocal correlation of DF1. In the case of DF-cx, $dF_{\mathrm{x}}(s)/ds$ is particularly large around $s \approx 2$, which is significantly beyond the crossing points of most of the dimers, but not the smallest ones. Thus, our analysis indicates that it is not possible to design very accurate and broadly applicable functionals by tuning the GGA exchange as long as one relies on DF1 nonlocal correlation.

3.5.4 Layered Structures

Next, we analyze the reduced-gradient for a set of nine layered structures, a subset of systems that has been used in several other studies [11, 67, 68, 78]. First, we focus on graphite as a representative case within this subset. Figure 3.6 shows the iso-surface of $s = 1.0$ for a graphite supercell with charge-density mapping. As for the benzene dimer, there are two types of iso-surface to consider: the "monomer" iso-surfaces that grow around

the individual layers and the "disk", which is here more like a "sheet", that represents the interaction between adjacent layers.

In parallel to the benzene dimer, at very low-s values the iso-surfaces formed around the individual layers are almost identical to those of graphene sheets, so that these low-s iso-surfaces cancel out and only the inter-layer sheet contributes to the interaction energy. As we move to higher s, the iso-surfaces grow outward from their planes of origin. By $s = 1.0$, as shown in Fig. 3.6, the iso-surfaces have expanded to the point that they begin to merge with one another through spatially periodic "tunnels". In the benzene-dimer case this merger corresponds to immediate losses in attractive energy. For graphite, however, the parts of the inter-layer sheet that have not been "annihilated" continue to grow in the direction of the carbon atoms, increasing the charge density on that iso-surface. It is this increase in charge density that temporarily offsets the decrease in surface area. The loss in surface area does not begin to dominate until $s = 1.17$, which is the downward peak of graphite's $\Delta e_{\mathrm{gx}}(s)$, as shown in the red curve in Fig. 3.7. After this point, the inter-layer iso-surface is gradually "annihilated" along with the monolayer iso-surfaces in the dimer, resulting in a shift from negative energy (attraction) to positive energy (repulsion). By $s = 1.31$, the location of graphite's upward peak in $\Delta e_{\mathrm{gx}}(s)$, the iso-surfaces in graphite completely vanish. This means that any contribution to the interaction energy above that s value is repulsive and entirely dependent on the energy of a single graphene layer.

Though we use graphite as our main example, the same iso-surface behavior is true of all of our layered systems. This is demonstrated by the fact that they all have the same overall shape of $\Delta e_{\mathrm{gx}}(s)$, see Fig. 3.7: an attractive contribution to interaction energy at low s, followed by a sharp transition to repulsive energy at higher s, and then a regression to zero exchange interaction energy after the full layered system no longer contributes to the interaction. This regression is due to the decrease in charge density as iso-surfaces of s grow more distant from the monolayer. We find that all layered structures abide by this sequence with only slight variations between individual types of systems, but there are some clear differences in the relevant value of s. $PdTe_2$, in particular, has a $\Delta e_{\mathrm{gx}}(s)$ curve that is shifted to the left compared to the other systems, also evident in the statistical data provided in Fig. 3.8. This shift is caused by the partly covalent character of this inter-layer binding,

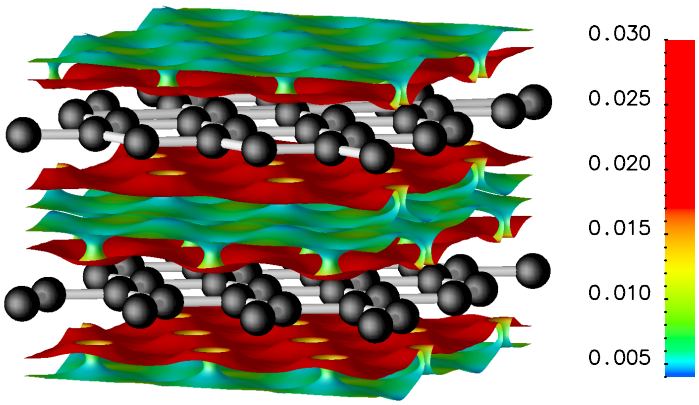

Figure 3.6: Iso-surface of $s = 1.0$ for a graphite supercell; electronic charge density in units of e/Bohr^3 is mapped onto the iso-surface. Along the edge one can see cut-open "tunnels" connecting individual surfaces, showing the beginning of a merger that gradually depletes attractive interaction energy in the system.

evidenced by the sizable GGA-level binding energy found in e.g. Ref. [79]. This results in the shortest distance between any inter-planar atoms in all of our layered structures. Thus, the "disk" iso-surface that arises between the tellurium atoms has less space to grow, resulting in less contribution from higher-s values. We also see that certain systems such as MoS_2, $MoSe_2$, and WS_2 have a tendency for their $\Delta e_{\rm gx}(s)$ to plateau slightly before hitting peak attraction. We believe that this is due to asymmetry in the iso-surfaces, where parts of the interplanar disk merge with the monolayer iso-surfaces long before the remainder does. This results in a brief and small repulsive contribution even as the attractive energy continues to build.

It is instructive to compare the shifts in $\Delta e_{\rm gx}(s)$ with the predicted inter-layer separations in Table S4 and the form of $dF_{\rm x}/ds$ for different functionals. In particular, DF2 has notoriously inaccurate interlayer separations for some systems [40, 73, 79]; in the case of $PdTe_2$ by as much as 0.9 Å, while for $HfTe_2$ and $MoSe_2$ by approximately 0.6 Å. WS_2, $HfSe_2$, and MoS_2 have similar curves and DF2 overestimates their separation by 0.4 Å. Graphite, BN, and HfS_2 also have similar curves and DF2 overestimates their separation by approximately 0.15 Å. For these three, DF1 has somewhat larger overestimation of inter-layer separations, i.e. by 0.2 Å. The trends in binding separation can be linked to the much larger $dF_{\rm x}/ds$ of PW86r for $s \approx 0.2$ to $s \approx 0.8$ used in DF2, compared to all others, while

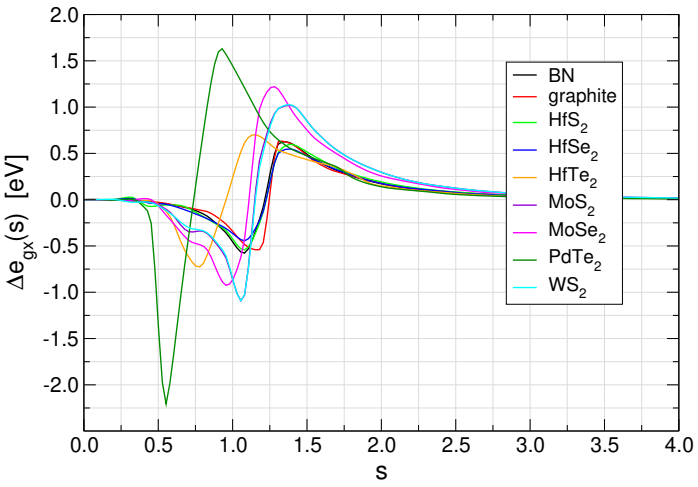

Figure 3.7: s-resolved exchange interaction energy $\Delta e_{\mathrm{gx}}(s)$ for a set of nine layered systems.

the regions for which DF1 gives larger separations can be linked to the crossing of dF_x/ds for PW86r and revPBE at $s \approx 1$. Trends in inter-layered binding energies are harder to distinguish, since the separations are influenced by the functional. However, we can infer that the overall more accurate energies of DF1-cx compared to DF1-optB88 can be linked to the larger $F_{\mathrm{x}}(s)$ for smaller s and similar magnitude for larger s, causing the exchange attraction to be weighted more for optB88 and thus resulting in larger binding energy overestimation.

Finally, we give attention to the fact that all vdW-DFs with accurate inter-layer separation overestimate the binding energy of layered systems as seen in Table S4, with DF3-opt1 being the best performing with a MARD of 13.55%. While improving this may require updating the nonlocal correlation further, it is interesting to analyze the role of the exchange energy compared to the molecular dimers. While being a quite accurate functional for the energies at the "1.0" separation for the S22×5 set in Table S3, optB88 is the worst performing for the energies of layered systems (MARD of 32.36%). If we disregard revPBE and PW86r (as DF1 and DF2 have inaccurate inter-layer separations), optB88 has the largest $F_{\mathrm{x}}(s)$ among the functionals beyond $s = 2.9$. In this tail region, optB88 picks up significant repulsive contributions for the molecular dimers, while for layered systems this tail region has almost vanished, clearly evident by comparing Fig. 3.5 and Fig. 3.8.

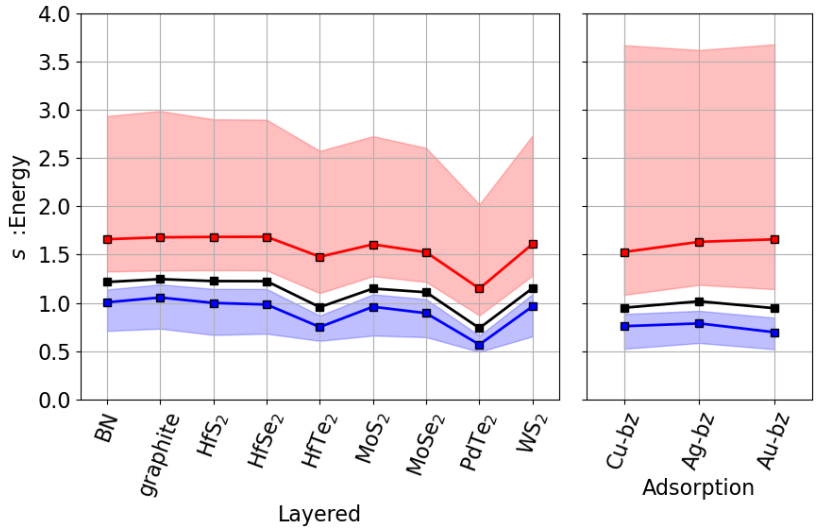

Figure 3.8: Statistical analysis of $\Delta e_{\rm gx}(s)$ for **(left)** nine layered systems and **(right)** benzene adsorbed on three surfaces. See legend in Fig. 3.5 for more details.

3.5.5 Benzene Adsorption on Cu/Ag/Au(111)

Molecular adsorption on coinage metals has traditionally been a challenging problem to model with DFT methods [60] due to very distinct properties of the surface and the molecule as well as different response properties of the surface and bulk regions of the metal. Here, we study the adsorption of benzene on the (111) surface of Cu, Ag, and Au and analyze the s dependence. Figure 3.9 shows the profile of $\Delta e_{\rm gx}(s)$ for these three cases; corresponding statistical properties of the domains are indicated in the right panel of Fig. 3.8. Moreover, Fig. 3.10 shows the iso-surfaces of s for benzene on Ag(111) as a representative system. As for the other systems, we find that the iso-surfaces growth and merger dictates the dependence of the exchange interaction energy on s. The first iso-surface is at $s = 0.50$, which is below the 80% negative domain (see Fig. 3.8). We observe three distinct types of surfaces: ones surrounding and intrinsic to the benzene molecule, ones permeating and surrounding the Ag lattice, and a single, very-low charge-density surface directly between the benzene and metal surface. As the iso-value of s grows, so too does the interaction iso-surface until it runs out of space and begins to "annihilate" on contact with the benzene and Ag iso-surfaces. The lower panel of Fig. 3.10 shows the iso-surface for $s = 0.84$, i.e. the location of the negative peak in $\Delta e_{\rm gx}(s)$ for this system. Here, the interaction iso-surface

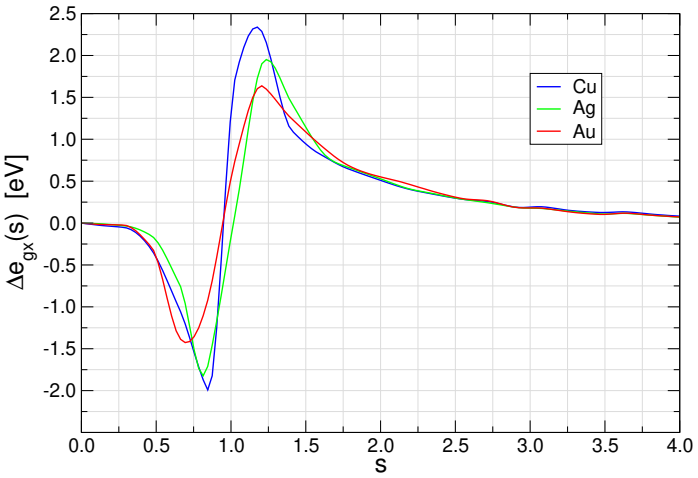

Figure 3.9: $\Delta e_{\mathrm{gx}}(s)$ for benzene adsorbed on the coinage metals Cu, Ag, and Au.

has been partially "annihilated" on the side facing the Ag atoms and is just beginning to merge with the benzene molecule as well. As this merger progresses, the interaction iso-surface loses surface area and charge density, leaving the energies of the isolated benzene and Ag surfaces to dominate the interaction. This results in the permanent transition to repulsive exchange interaction energy that we see around $s \approx 1.0$.

The dissimilarity between the benzene molecule and metal surface makes this system interesting to compare with the molecular dimers and layered systems. The negative parts of the curves in Fig. 3.9 have an onset at lower values of s, almost as low as for $PdTe_2$, in particular for Au. The localization and negative/positive peak magnitude can also be ranked as Cu > Ag > Au. For the negative region, the surface adsorption peaks are more localized than the ones for layered systems, while for the positive region they are much broader, see Fig. 3.8. The shift to lower-s values and localization on the negative side can be understood from the asymmetry of the "annihilation" of the molecule and metal-surface iso-surfaces; the broadening on the positive side arises from the distinctness of the individual surfaces and that of benzene. We further note that benzene on Ag(111) exhibits a shifting to larger-s values on the positive side and a slight broadening compared to the Cu case, while for Au(111) we only see broadening. This slight shift in trend is a testament to the distinct electronic properties of these surfaces and might be related to the lower binding energy on Ag(111), a trend only DF1-cx gets right among the functionals, see Table S5.

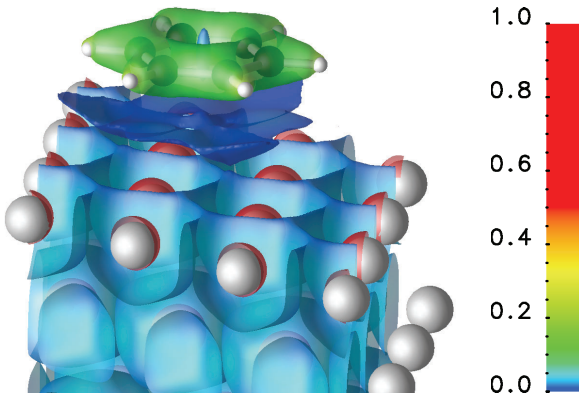

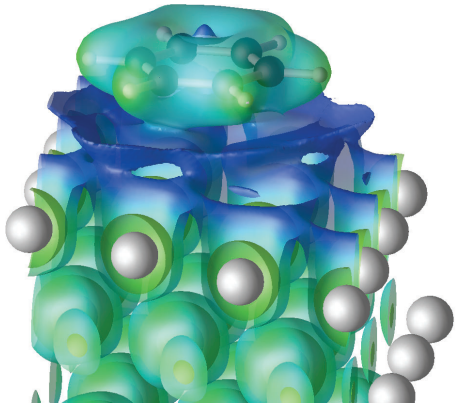

Figure 3.10: Iso-surface of $s = 0.50$ and $s = 0.84$ for benzene adsorbed on the Ag(111) surface. The electronic charge density in units of e/Bohr^3 is mapped onto the iso-surface.

Finally, all the $\Delta e_{\rm gx}(s)$ curves have very similar large-s behavior, which is primarily due to the benzene monomer contributions.

3.5.6 Molecular Crystals

Finally, our reduced-gradient analysis was also done for the X23 dataset of molecular crystals [80]. Figure 3.11 shows the statistical analysis of $\Delta e_{\rm gx}(s)$ for the full dataset and the individual curves are provided in Fig. S5 in the SI of Ref. [12]. Among these systems we find a high degree of similarity and no particular structure to serve as a representative. Nonetheless, the mechanism behind their interactions can still be described similar to the benzene dimer. However, whereas the benzene dimer features a single interacting iso-surface between the two molecules, we see several iso-surfaces between adjacent molecules in the molecular crystals. And, due to differences in orientation of the molecules relative to one another, we find that the iso-surfaces residing between them take a variety of different shapes and sizes. Still, the same mechanisms of how these iso-surfaces contribute to the s-resolved exchange interaction energy come into effect: At low s, iso-surfaces form around and in-between atoms, with the ones in-between causing exchange attraction. In the case of the X23 dataset, the crossing point from positive to negative values occurs on average at $s_0^{\Delta e} = 1.44$, with the negative and positive medians on average at 1.01 and 2.27.

Comparing the statistical data for molecular dimers in Fig. 3.5 with those of molecular crystals in Fig. 3.11, we speculate that the crystals are more similar to each other than the dimers. This might be due to the stronger attractive dispersion forces arising due to the three-dimensional geometry in crystals, which compresses some of the most weakly bonded systems—but, the effect is smaller for crystals made out of larger molecules since the effect of the three-dimensional geometry is smaller. In effect, the effective packing distances in terms of the s iso-surfaces become more similar. In turn, this analysis suggests that it could be possible to design functionals that provide accurate performance for all molecular crystals in the X23 data set at the same time.

Comparing molecular crystals with molecular dimers and layered systems (Figs. 3.5, 3.8, and 3.11), it becomes evident that the exchange interaction of molecular crystals is more similar to molecular dimers than layered systems including graphite. A consequence of this

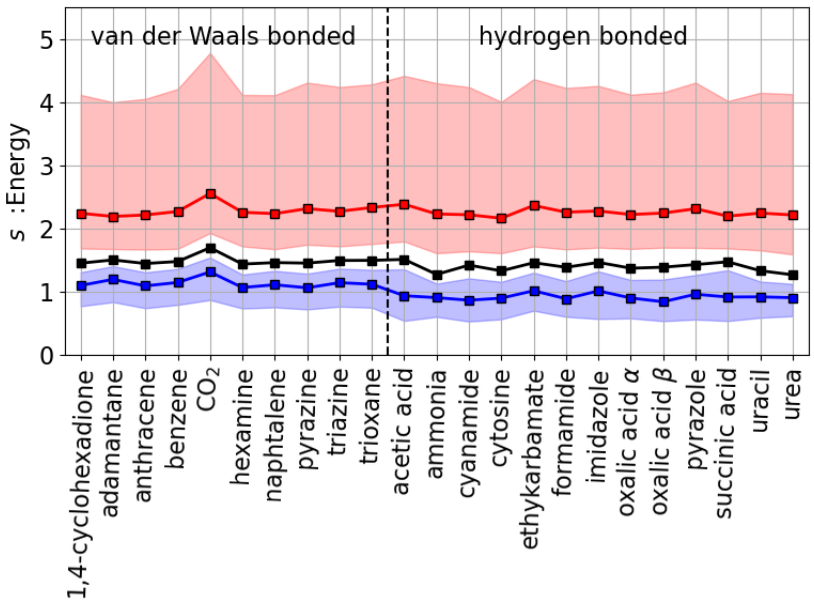

Figure 3.11: s-resolved exchange interaction energy $\Delta e_{\mathrm{gx}}(s)$ for the X23 dataset of molecular crystals [80]. See legend in Fig. 3.5 for more details.

is that DF2 on one hand can provide accurate volumes of molecular crystals, but on the other severely overestimates separations of layered systems, whereas DF1-cx is accurate for both (see Tables S4 and S6). This can be related to their crossing of dF_{x}/ds at $s = 1.34$, i.e. slightly below $s_0^{\Delta e} = 1.44$, which is a good match considering the shift in s-resolved exchange interaction energy and forces in Fig. 3.4.

3.6 Conclusions

Our study provides a thorough analysis of reduced-gradient values, their spatial distribution, and how they contribute to the exchange component of the binding of a variety of different van der Waals complexes. We find that attractive contributions to the exchange interaction energy can be attributed to low-density regions between the constituents with disk-like iso-surfaces. We further identify a mechanism wherein the surface area of these disks decreases through merging with other iso-surfaces and switches the gradient-correction to exchange from attractive to repulsive. Our analysis shows that there are clear differences in the reduced-gradient resolved exchange interaction energy for different classes of van der Waals complexes. Analyzing these differences provides a way to explain why different exchange

functionals used in vdW-DF perform differently for different classes of systems. In turn, this can provide valuable guidance for constructing even more accurate functionals, whether for broadly applicable ones or ones that target good performance for particular classes of systems. At this point, it is not clear that all our identified desirable features for the enhancement factor are mutually compatible and will lead to clear improvements across all classes of van der Waals complexes. Currently ongoing work will clarify this question and seeks to develop an updated variant of the vdW-DF family that implements a maximum of these features. The optimization of such a new vdW-DF variant is not an easy task—large amounts of benchmark calculations, covering large datasets and different classes of van der Waals complexes, are needed to ensure a meaningful local minimum in the high-dimensional parameter space of not only the exchange but also the nonlocal correlation energy. More evidence supporting the impact of our reduced-gradient analysis on improving vdW-DF will thus be addressed and provided in our future work showcasing the utility of this insight for the development of nonlocal functionals. While this paper emphasizes how the effects play out for the vdW-DF family of functionals, the same analysis approach may prove fruitful when analyzing the performance of other approaches to describe van der Waals binding within DFT.

Chapter 4

Reduced-Gradient Analysis of Molecular Adsorption on Graphene with Nonlocal Density Functionals

This chapter is a reprint of a published article with permission from Phys. Rev. B **109**, 035427 (2024) [81]. Supporting Information for this chapter can be found at DOI: 10.1103/PhysRevB.109.035427. I am the first author on this paper, with contributions in the form of calculations, writing, and editing.

4.1 Abstract

Graphene has garnered tremendous interest in the last decade due to its great potential for applications in almost every scientific and engineering discipline. The adsorption of molecules onto graphene is itself also of significant interest, including in catalysis and trace molecule detection. However, density functional theory has traditionally struggled to accurately model surface adsorption involving long-range dispersion interactions between a molecule and a substrate, accentuating the need for comprehensive benchmarking and analysis. Here, we test the accuracy of several functionals in describing the adsorption energy of graphene-molecule adsorption complexes, including several van der Waals density functionals as well as the nonlocal correlation functional rVV10 and the dispersion-corrected

PBE-D3. We find that the highest accuracy is provided by vdW-DF2 and the two realizations of vdW-DF3, the most recent generations of the van der Waals density functional family. In addition, we use a reduced-gradient analysis technique to examine the material's exchange energy. This analysis resolves contributions to the exchange interaction energy as a function of the reduced-gradient s, revealing regimes of s that are important components of the interaction energy of these systems. In doing so, we identify the best functionals currently available and initiate discussion on desirable traits of each functional for modeling surface adsorption.

4.2 Introduction

Molecular surface adsorption has seen wide use and great impact on technology and industry, the properties of which vary greatly depending on the molecule or substrate used. Graphene in particular is a material that has experienced a rapid growth of interest—as an adsorption substrate it has been studied in many different contexts including catalysis [82–84], lubrication [85–87], corrosion [88], modeling astrophysical conditions [89], and many more [90–93]. Advancements have also been made towards water filtration [94–96], DNA sequencing [97–99], and trace molecule detection with methods such as surface-enhanced Raman spectroscopy, for which graphene was found to act as an excellent nanoplatform due to its stability and uniform structure [100].

The inclusion of dispersion forces, vital for accurately modeling surface adsorption, has been one of the most important advances in the development of density functional theory in the last two decades [27, 37, 40, 101–103]. Such dispersion forces are missing in widely used generalized gradient approximation [3, 25, 104–107], and one approach to include them is through the use of a correction to an already existing functional, as is done with the DFT-D methods [25, 54, 108, 109]. Another method to treat these cases is with a meta-generalized gradient approximation (meta-GGA) functional. First created by Tao and Perdew in the form of TPSS, derivatives such as M06L and SCAN better account for dispersion-bonded systems [7, 8, 110, 111]. One can also use an explicit nonlocal correlation term that accounts for long-range dispersion interactions as a functional of the electron density alone. Langreth, Lundqvist, and coworkers developed the first of these so-called van der Waals density functionals (vdW-DF), a family that has grown significantly since its inception [3, 9–11, 61, 72–74, 112–115]. The vdW-DF functional introduced nonlocal correlation as a separate term containing a density-density interaction kernel that was inspired by the plasmon-pole model and adheres to four exact physical constraints. It also retains a gradient-corrected exchange at the GGA-level of theory, which is based on the local electronic density $n(\mathbf{r})$ and the reduced-gradient, $s(\mathbf{r}) \propto |\nabla n(\mathbf{r})|/n(\mathbf{r})^{4/3}$, and is vital to the short- and mid-range regions of binding curves; in fact, using an exchange description at the LDA level, using only $n(\mathbf{r})$, causes significant spurious binding [45, 77].

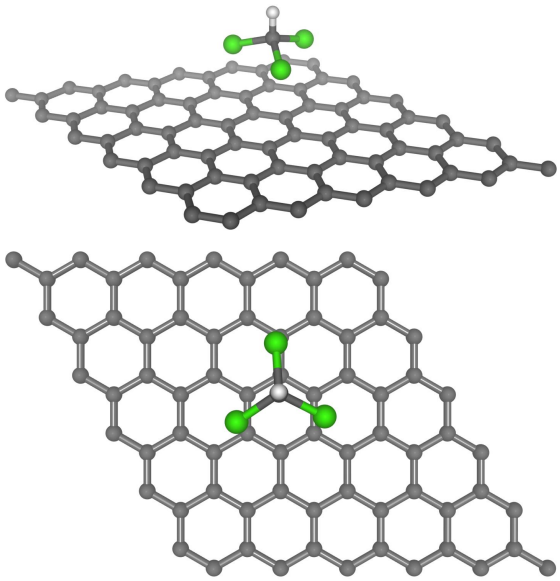

Figure 4.1: Side and top view of chloroform ($CHCl_3$) adsorbed onto a graphene. H is in white, Cl in green, and C in black.

The potential applications of these functionals towards graphene adsorption were recognized soon after the development of vdW-DF, and were the subject of extensive research by Schröder and coworkers: early examples included studies of vdW-DF on the adsorption of aromatic organic molecules and later branched out into more varied and complex systems [116–123]. The variety of adsorbates studied over the last two decades, combined with the growing presence of new and improved nonlocal density functionals, makes clear the need for a comprehensive benchmark review of graphene adsorption. In this study, we apply nine such functionals to a data set of 21 different molecules adsorbed onto graphene. These 21 systems are subdivided into six classes consisting of noble gases [124], chloroform (as shown in Fig. 4.1) [125], diatomic molecules [124], n-alkanes of the form C_nH_{2n+2} [126], aromatic hydrocarbons [127], and nucleobases [128]. All reference energies, save for the nucleobases and chloroform, stem from temperature-programmed desorption (TPD) [129]. Nucleobase adsorption energies were instead obtained via isothermal titration calorimetry (ITC) [130], while the chloroform adsorption energy comes from single-atom gas chromatography [131].

While dispersion interactions have an important role in physisorption, they vary far more slowly with separation than the exchange effects, which are related to orbital overlaps [12,45,77]. Crafting appropriate GGA-exchange-enhancement factors, $F_{\mathrm{x}}(s)$, has thus been

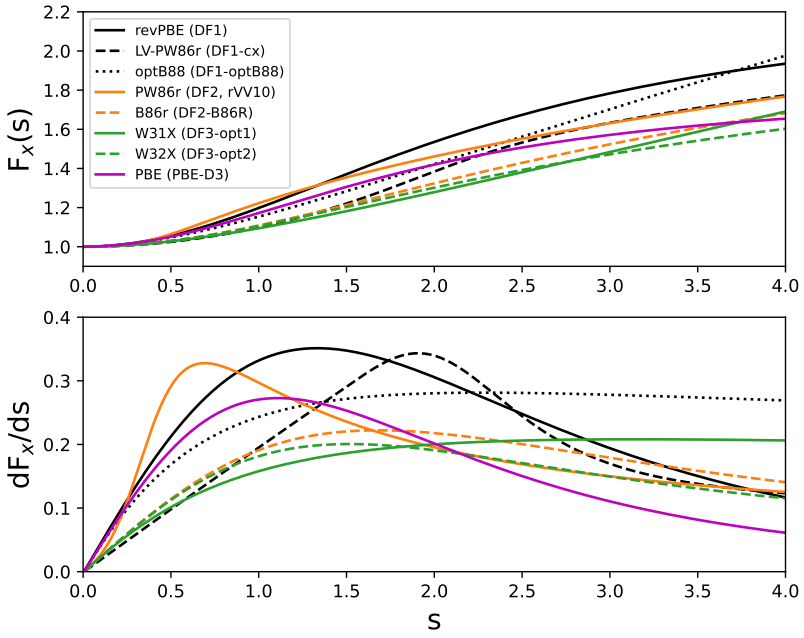

Figure 4.2: Exchange enhancement factors and their derivatives for the eight functionals included in our study. The rVV10's enhancement factor is the same as DF2's, i.e. revised PW86 exchange [45].

an important part of vdW-DF development, and is related to the GGA exchange energy by

$$E_{\mathrm{x}}^{\mathrm{GGA}}[n] = \int d\mathbf{r}\; n(\mathbf{r})\, \epsilon_{\mathrm{x}}^{\mathrm{LDA}}\big(n(\mathbf{r})\big)\, F_{\mathrm{x}}(s)\;, \tag{4.1}$$

where $\epsilon_{\mathrm{x}}^{\mathrm{LDA}}\big(n(\mathbf{r})\big)$ is the exchange energy per particle at the LDA level of theory. is the exchange enhancement factor. Various exchange-enhancement factors are shown in Fig. 4.2. To analyze trends arising from the exchange choice, we resolve the exchange energy in s, as follows,

$$e_{\mathrm{gx}}(s) = -\frac{3}{4}\left(\frac{3}{\pi}\right)^{1/3}\int d\mathbf{r}\; n^{4/3}\,\left[F_{\mathrm{x}}\big(s(\mathbf{r})\big) - 1\right]\delta\big(s - s(\mathbf{r})\big)\;, \tag{4.2}$$

similar to the reduced-gradient analysis in Refs. [12, 45, 132]. Moreover, we recently applied this analysis to a range of material classes, explaining why good functional performance for one class of systems in no way guarantees strong performance for other classes of systems [12]. Thus, using reduced-gradient analysis can highlight a means to improve graphene adsorption modeling in future functional development.

4.3 Computational Details

All calculations were done using the QUANTUM ESPRESSO (QE) package [64] and PBE ultrasoft pseudopotentials of Garrity, Bennett, Rabe, and Vanderbilt (GBRV) [65], with a wave function cutoff of 50 Rydberg and a density cutoff of 600 Rydberg.

Optimized lattice parameters of graphene were first calculated for each functional. These calculations were performed with a spacing of 20 Å between individual layers of graphene, and a $12 \times 12 \times 1$ k-point mesh in the sampling of the Brillouin zone. Optimizations of the adsorption system and its separate constituents used Γ-point sampling of the Brillouin zone and convergence criteria of 1×10^{-8} Rydberg for energies and 1×10^{-4} Rydberg/Bohr for forces. For each adsorbate, $n \times n \times 1$ supercells of graphene were chosen to provide a minimum 8.0 Å cushion between molecules in adjacent cells.

For nucleobases, Ref. [128] provides experimental adsorption results in an alkaline environment and reports separately the solvation energies for each nucleobase. Following the definition of the solvation energy outlined in Refs. [128] and [133], we take the reported experimental adsorption energy minus the solvation energy as the reference value in these calculations. Out of the four nucleobases, we found unusually large errors in the adsorption energy for thymine relative to experiment. We believe that this could be due to a possible error in the experimental measurements, as other DFT studies show similar disagreement for thymine [134, 135]. For this reason, we have chosen to omit thymine from the results shown here. Results including the thymine-graphene system are given in the Supporting Information of Ref. [81].

In the reduced-gradient analysis, we compute the change arising due to adsorption by

$$\Delta e_{\mathrm{gx}}(s) = e_{\mathrm{gx}}^{\mathrm{system}}(s) - e_{\mathrm{gx}}^{\mathrm{molecule}}(s) - e_{\mathrm{gx}}^{\mathrm{graphene}}(s) \; . \tag{4.3}$$

We may also resolve the gradient contribution to the interaction force, defined as

$$\Delta k_{\mathrm{gx}}(s) = -\frac{d\Delta e_{\mathrm{gx}}(s)}{d|a|},$$

where a is the separation between the adsorbate and graphene sheet.

In our illustration of the gradient contribution to the exchange interaction energy, $\Delta e_{\mathrm{gx}}(s)$, the DF3-opt1 enhancement factor is used. The overall appearance of the exchange interaction curves has a similar shape for different functionals with a scale factor given by $F(s)/F_{\mathrm{DF3-opt1}}(s)$, in addition to smaller self-consistent effects of updating the electronic density $n(\mathbf{r})$ and the Kohn-Sham orbitals. However, this scaling significantly impacts the binding separations and total energy. To calculate the gradient contribution to the exchange force $\Delta k_{\mathrm{gx}}(s)$ of adsorbed chloroform, we took the difference between two $\Delta e_{\mathrm{gx}}(s)$: one at equilibrium distance from the graphene sheet, and one displaced by 0.1 Å from equilibrium.

In our study, we include several van der Waals density functionals: vdW-DF [3], vdW-DF-optB88 [72], vdW-DF-cx [73], vdW-DF2 [10], vdW-DF2-B86R [74], vdW-DF3-opt1 [11], and vdW-DF3-opt2 [11]. For brevity, they are referred to as DF1, DF1-optB88, DF1-cx, DF2, DF2-B86R, DF3-opt1, and DF3-opt2, respectively. These functionals differ only in their nonlocal correlation and GGA exchange terms. Their enhancement factors, $F_{\mathrm{x}}(s)$, are shown in Fig. 4.2. We also include the nonlocal correlation functionals rVV10 [115]—a revision of the earlier VV10 [9] that is better suited for plane waves—and the popular force-field dispersion-corrected GGA [6] variant PBE-D3 [54], with zero/damping. While these cannot be compared with the van der Waals density functionals through a reduced-gradient analysis focused solely on the exchange, we nonetheless include them in the benchmark study.

4.4 Results and Analysis

4.4.1 Lattice Constants

The full results of our benchmark for the graphene lattice constants are given in the supporting information. All the functionals predict experimental lattice constants with an absolute relative deviation less than 1%. Among them, vdW-DF1-cx and vdW-DF3-opt1 have the best agreement with experiment, both falling within the range of the reported measurement error [136].

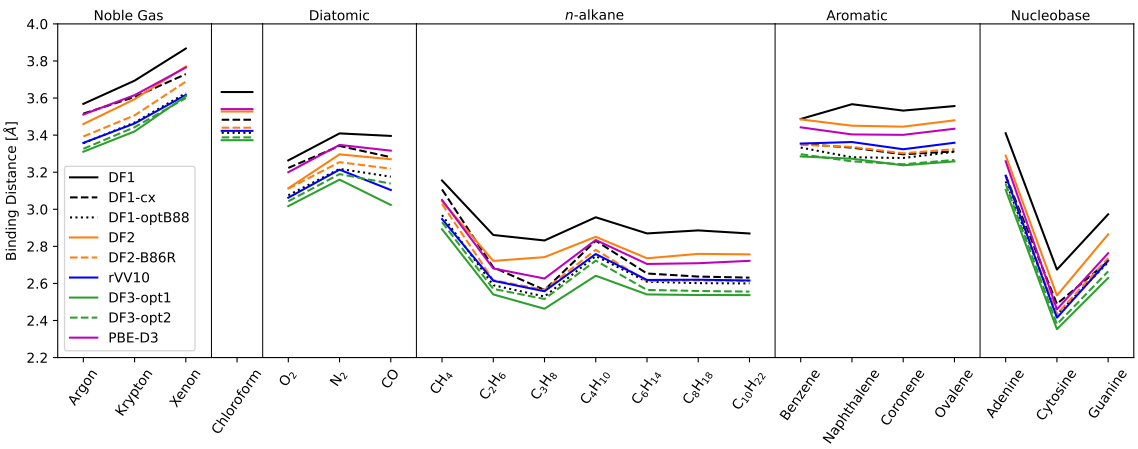

Figure 4.3: Binding distances for all systems in the benchmark set. Vertical lines divide each subgroup of the set. All distances are provided in the SI of Ref. [81]

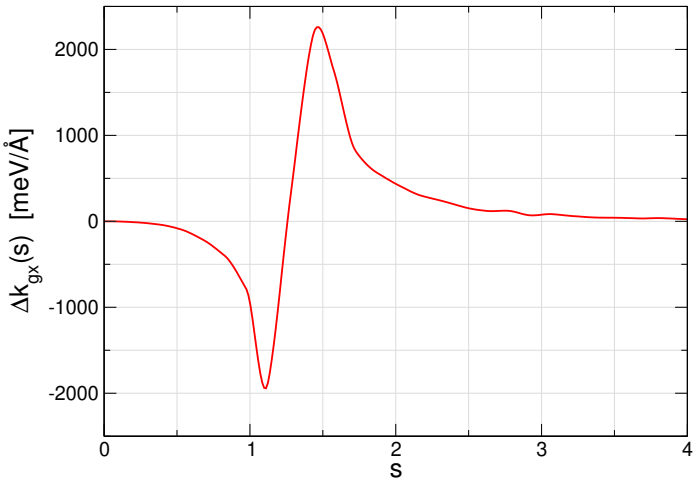

Figure 4.4: s-resolved gradient contribution to the exchange interaction force $\Delta k_{\mathrm{gx}}(s)$ between chloroform and graphene.

4.4.2 Adsorption Distances

Figure 4.3 shows the distance between each of our adsorbates and the graphene substrate for all of the tested functionals. DF1 demonstrates the greatest adsorption distance for every adsorbate studied. This can be traced back to its exchange form, as neither DF1-cx nor DF1-optB88 follow the same trends. The difference in separations for DF2 and DF2-B86R is smaller, with notable exceptions for the aromatic hydrocarbons and certain n-alkanes. In these cases, separations predicted by DF2 exceed those of DF2-B86R by as much as 0.1 Å. DF3-opt1 and DF3-opt2 also deviate little from one another.

Figure 4.4 shows $\Delta k_{\mathrm{gx}}(s)$ for adsorbed chloroform. This force is relevant to the binding distance and is generally dependent on lower values of s than the energy. Comparing this curve with each functional's enhancement factor in Fig. 4.2 can explain much of the trend; in particular, the position of the zero-crossing, here around $s = 1.2$, is crucial. For DF1, we see that the positive region of $\Delta k_{\mathrm{gx}}(s)$ beyond that point is enhanced much more than the negative region, resulting in a greater repulsive contribution from the gradient exchange. DF2 predicts similarly large binding distances, and had previously been observed to overestimate solid lattice constants due to the fact that its PW86r enhancement factor grows very quickly in the region of $s < 0.5$. DF2-B86R implements an enhancement factor that increases slower in the low s limit, as can be seen by its derivative in Fig. 4.2. This reduced enhancement is also present in higher ranges of s, which are more relevant to dispersion-based geometries. For this reason, DF2-B86R displays shorter binding distances than DF2 within our study.

4.4.3 Adsorption Energies

Figure 4.5 shows the adsorption energies and respective relative deviations for all systems in our data set. The accuracy varies significantly between the different functionals, with variants using DF1 correlation tending to overestimate binding energies while PBE-D3 and the later DF2 variants slightly underestimate on average. DF2 takes a coefficient of the internal exchange, $Z_{ab} = -1.887$, that is larger than DF1's -0.8491, effectively "scaling" the dispersion interactions to larger separations and causing reduced dispersion interactions [40,77]. This corrects for the overbinding in the molecular dimers [10,137], and has also resulted in smaller binding for other classes of systems [11].

rVV10 and the two DF3 variants generally give relative deviations between those of DF1 and DF2 variants. While the optimizations of DF3 take different Z_{ab}'s, DF3-opt1 being that of DF1 and DF3-opt2 being that of DF2, they also use a form of the nonlocal correlation that is based on a different dispersion model than the previous generations. These new vdW-DF3 functionals also improved performance for a broad variety of systems, including benzene-to-metal surface adsorption, which is structurally similar to the systems in our benchmark.

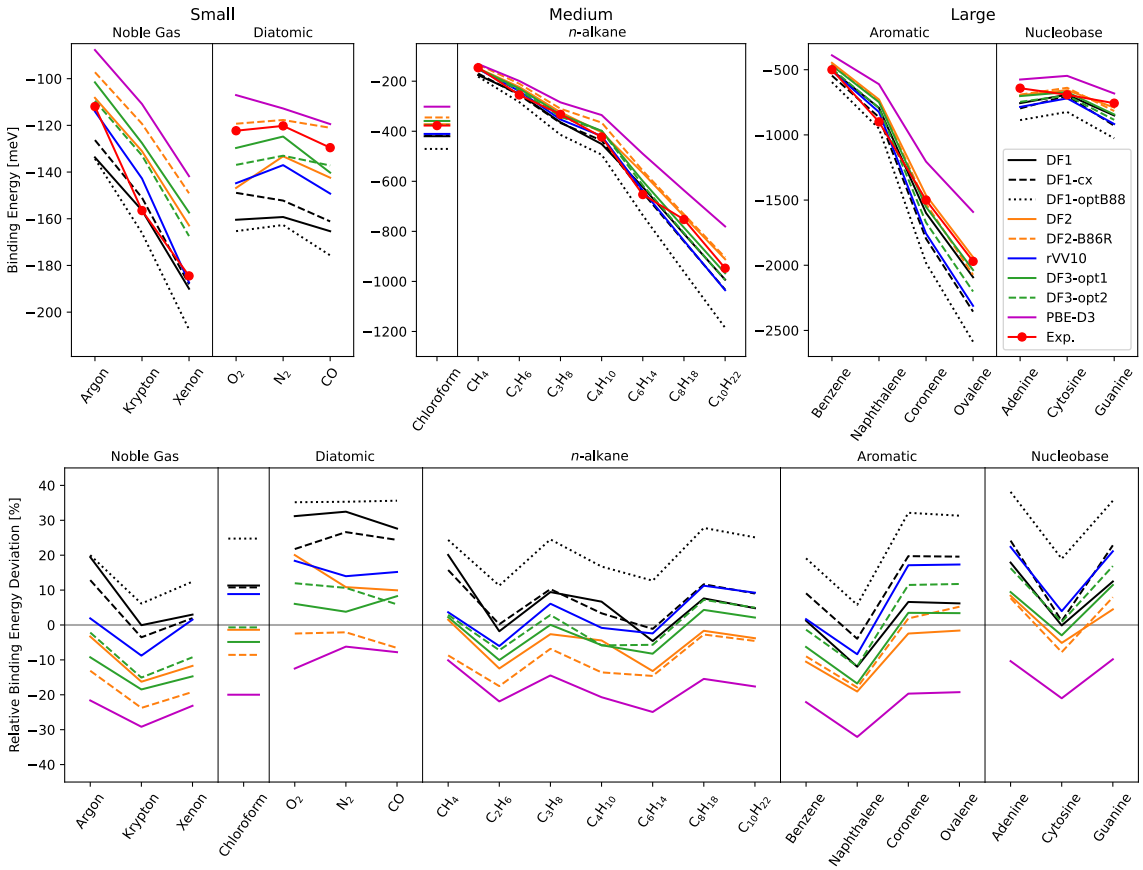

Figure 4.5: Interaction energies (top) and relative deviations in the interaction energy (bottom) for all systems in the benchmark set. All energies and deviations are provided in the SI of Ref. [81].

It is notable that the noble gases, diatomic molecules, and nucleobases all deviate from the observed trends of DF1-, DF2-, and DF3-type functionals. More functionals tend to underestimate the binding of noble gases and overestimate that of the diatomic molecules. The binding of adenine and guanine are also more often overestimated, though this trend does not extend to cytosine.

Figure 4.6 shows the mean deviations (MD), mean absolute deviations (MAD), and mean absolute relative deviations (MARD) of all system classes in our data set. Due to the weak-binding nature of the diatomics and nucleobases, the MARD's of DF1 generation functionals are all high for those systems, exceeding 10% in all cases. For other system classes, the n-alkanes and aromatic hydrocarbons, accuracy is dependent on size. As Fig. 4.5 shows, relative deviations in binding energy tend to increase slightly with respect to n-alkane

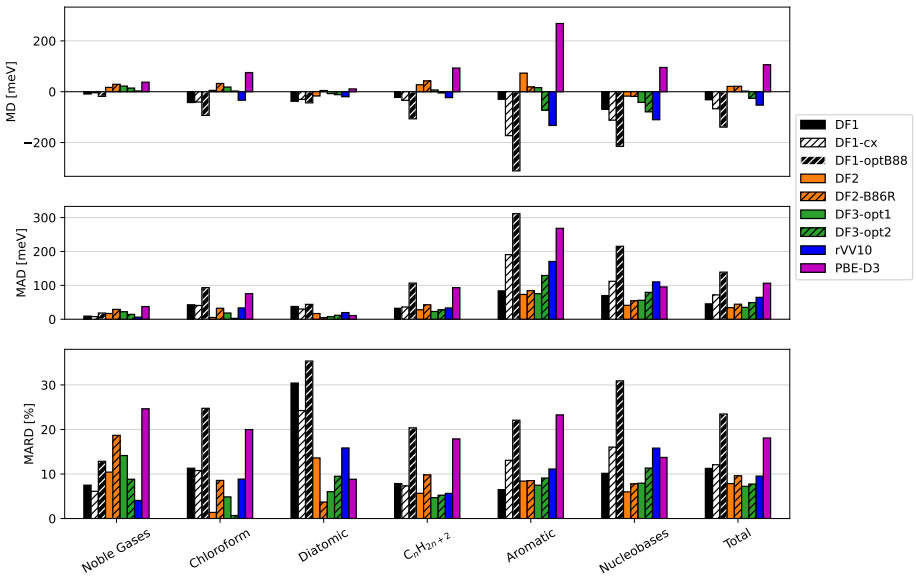

Figure 4.6: Comparison of mean deviation (MD), mean absolute deviation (MAD), and mean absolute relative deviation (MARD) for six classes of graphene adsorption systems. Individual system energies, as well as the MD, MAD, and MARD of each class, are provided in the SI of Ref. [81].

size. For aromatics, the experimental binding energies shift from strong to weak binding as adsorbates increase in size, particularly between naphthalene and coronene.

In Fig. 4.7 we show two components of the adsorption energy for each of the n-alkanes in our study, the nonlocal correlation and gradient contribution to exchange, adjusted for the number of carbon atoms in each molecule. With the nonlocal correlation providing an attractive contribution and the gradient exchange providing a repulsive contribution, the overbinding of DF1-type functionals can be traced to the large nonlocal correlation that is not sufficiently compensated by the gradient exchange form. We also note that the nonlocal contributions of DF2 and DF3 are very similar for this class of systems. This benefits the accuracy of DF3-opt1 in particular, which has a slightly smaller gradient exchange contribution that prevents it from underbinding to the same extent as DF2 and DF2-B86R.

4.4.4 Reduced-Gradient Analysis of Binding Energies

To further understand the factors that drive functional performance in our study, we make use of reduced-gradient analysis. As outlined in the Introduction, we begin with the gen-

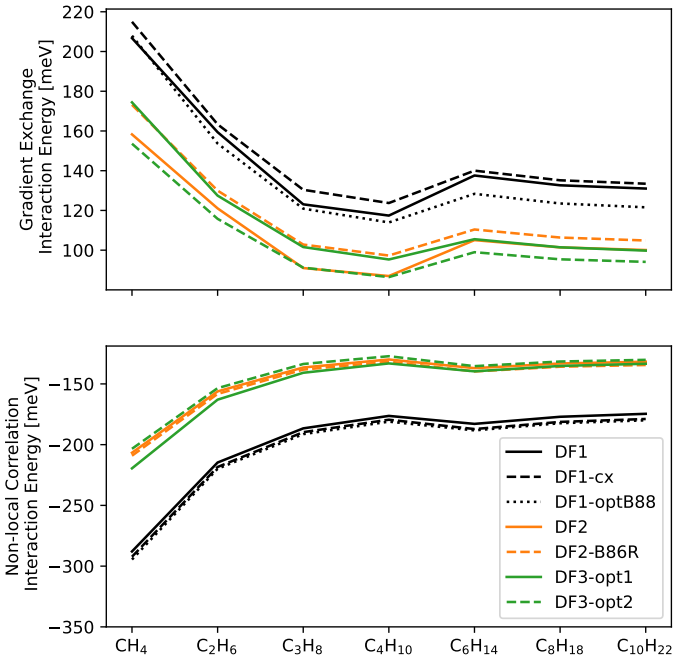

Figure 4.7: Components of the adsorption energy of the n-alkanes (per carbon atom) on graphene, as calculated by each of the van der Waals density functionals in our study.

eralized gradient approximation of exchange and isolate contributions from the gradient of the charge density. For a given system, we resolve the gradient contribution to the interaction energy as a function of the reduced density gradient s, a dimensionless parameter that forms the argument of the exchange enhancement factor $F_{\mathrm{x}}(s)$. This s-resolved gradient contribution to the exchange interaction is denoted by $\Delta e_{\mathrm{gx}}(s)$. By calculating $\Delta e_{\mathrm{gx}}(s)$ for select systems in our data set, we reveal which values of the reduced gradient contribute the most to interaction energy. This, in-turn, allows us to draw a line of cause-and-effect between the shape of a van der Waals density functional's exchange enhancement factor and its performance.

Figure 4.8 shows $\Delta e_{\mathrm{gx}}(s)$ curves for a few representative systems in our benchmark. Each curve possesses a negative region, causing attraction, and a positive region, causing repulsion. The mechanism by which the gradient exchange transitions from attraction to repulsion can be elegantly described in terms of the topological evolution of s iso-surfaces, which is discussed in the appendix. For our analysis, we use the ratio $F_{\mathrm{x}}(s_{\mathrm{max}})/F_{\mathrm{x}}(s_{\mathrm{min}})$ as

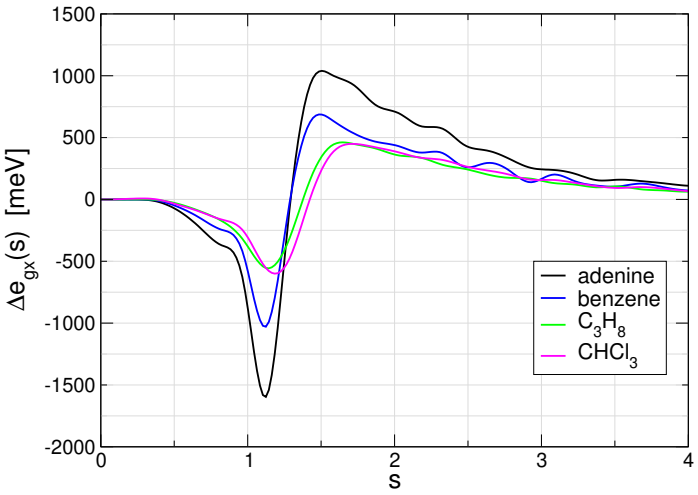

Figure 4.8: s-resolved gradient exchange interaction energy $\Delta e_{\mathrm{gx}}(s)$ for some representative systems within our study: adenine from the nucleobases, benzene from the aromatic hydrocarbons, propane from the n-alkanes, and chloroform.

a shorthand for how a given enhancement factor balances these two regions, with s_{min} and s_{max} denoting the location of peaks in the negative and positive region, respectively. The larger this ratio is for a given functional, the more repulsive is its gradient contribution to the exchange interaction energy.

We can demonstrate this with the example of adsorbed chloroform, which has a s_{min} and s_{max} of 1.19 and 1.71, respectively. DF1-optB88 severely overbinds this system to a degree that ordinary DF1 and DF1-cx do not. We trace this behavior directly to their respective enhancement factors, as the ratio $F_{\mathrm{x}}(s_{\mathrm{max}})/F_{\mathrm{x}}(s_{\mathrm{min}})$ is 1.142, 1.129, and 1.117 for DF1, DF1-cx, and DF1-optB88, respectively. As a result, DF1-optB88 recieves a smaller repulsive contribution from exchange, insufficient to offset the strong binding of DF1's nonlocal correlation.

We also apply our analysis to the entire benchmark set in aggregate. For the $\Delta e_{\mathrm{gx}}(s)$ curves in Fig. 4.8 we find an average s_{min} of 1.18 and an average s_{max} of 1.79. The corresponding $F_{\mathrm{x}}(s_{\mathrm{max}})/F_{\mathrm{x}}(s_{\mathrm{min}})$ ratios are 1.167 for DF1, 1.154 for DF1-cx, and 1.138 for DF1-optB88, so we expect the average exchange energies to scale as DF1 $>$ cx13 $>$ optB88. This is exactly what we see in Fig. 4.6, with MD's of -32, -67, and -140 meV for DF1, DF1-cx, and DF1-optB88, respectively. All three overestimate binding however, which sug-

gests that a functional with DF1 nonlocal correlation should have an enhancement factor that increases more sharply in the regime of $1.18 < s < 1.79$ in order to describe these systems accurately.

We draw a similar comparison between DF2 and DF2-B86R, as they are both identical to one another except for their forms of the enhancement factor. The ratio $F_{\mathrm{x}}(1.79)/F_{\mathrm{x}}(1.18)$ is 1.127 for ordinary DF2 and 1.124 for DF2-B86R, though the B86R enhancement factor increases more quickly beyond $s = 1.8$, suggesting that the interaction energy of these two functionals should be nearly the same across our entire set, but that DF2-B86R's should be slightly larger. Again this is exactly what we observe, with DF2 having an overall MD of 20.9 meV, just a bit lower than DF2-B86R's 21.4 meV. The underestimation of binding energies by these two functionals suggests the need for a slowly increasing enhancement factor in the regime of $1.2 < s < 1.8$. This is in fact fulfilled by DF3-opt2 in its revised B86b form. While DF3-opt2's nonlocal correlation differs from that DF2, the second optimization was designed to be an improved analog to DF2 in both its exchange and correlation. Indicative of this, DF3-opt2 has $F_{\mathrm{x}}(1.79)/F_{\mathrm{x}}(1.18) = 1.106$, significantly smaller than either of the DF2 forms.

A motivation for analyzing the set in aggregate is to compare the s signature with other types of systems. In Ref. [12], we calculated the s signatures of molecular dimers in the S22 test set, molecular crystals in the X23 test set, several layered systems, and three coinage metals with adsorbed benzene. These signatures are characterized in part by the s value at which gradient exchange contributions switch from negative to positive, called $s_0^{\Delta e}$. For the graphene adsorption systems analyzed here, we find an average $s_0^{\Delta e}$ of 1.41. Of the systems studied in Ref. [12], by far the closest to this are the X23 molecular crystals with an average $s_0^{\Delta e}$ of 1.44, followed by dispersion-bonded dimers at 1.51. The other system types—hydrogen-bonded dimers, layered systems, and benzene-metal adsorption systems—all averaged less than 1.2 in $s_0^{\Delta e}$. For future functional development, this would suggest a low degree of tunability between graphene adsorption and molecular crystals. The good performance of DF3 for graphene adsorption, and its subpar performance in the X23 [11], illustrates the challenges of further improving the accuracy within the vdW-DF framework. However, the s signatures of our graphene data set are much more diverse than those of the

X23 or S22, which makes it a valuable benchmark set for functionals.

4.5 Conclusion

We have presented a benchmark study of the adsorption of molecules onto graphene, and in the process we have compared the accuracy of various van der Waals density functionals from each of the first three generations. We have found that all functionals perform well in the calculation of the graphene lattice constant, but that significant differences lie in the adsorption energies. vdW-DF2 and the two forms of vdW-DF3, opt1 and opt2, show the best accuracy out of the functionals tested. We find that the first generation of vdW-DF broadly overestimates binding energies, and that this effect is mitigated or exacerbated by the choice in the GGA exchange, as shown by the difference between DF1 and DF1-optB88. The nonlocal correlation functional rVV10 also shows good accuracy within our set. However, its performance is also unbalanced; it excels in modeling noble gas and n-alkane adsorption but falls behind in the case of nucleobases and diatomic molecules. Despite good accuracy in our benchmark, it is worth keeping in mind that DF2 struggles more broadly with coinage metal surface adsorption, interlayer separations (including that of graphite), and solid lattice constants [11, 60, 74, 78, 138]. We also find that PBE-D3 almost always underestimates binding by a significant amount.

We have also shown how reduced-gradient analysis can be used to account for the differences between different variants of vdW-DF within each vdW-DF generation. This analysis shows that s values of 1.18 and 1.79 are the most significant contributors to the adsorption energy of these systems, and that the accuracy of a functional for a given nonlocal correlation is largely dependent on the shape of its exchange enhancement factor between these two points. Our analysis also provides insight as to what characteristics help or hurt a functional's evaluation of a given system, revealing matches of the GGA exchange to each nonlocal correlation that optimize the accuracy of the interaction energy.

In summary, we find that the most recent vdW-DF generation, vdW-DF3, offers not just improved accuracy but improved consistency over past functionals that have sought to model long-range dispersion interactions. Moreover, the insights provided by reduced-

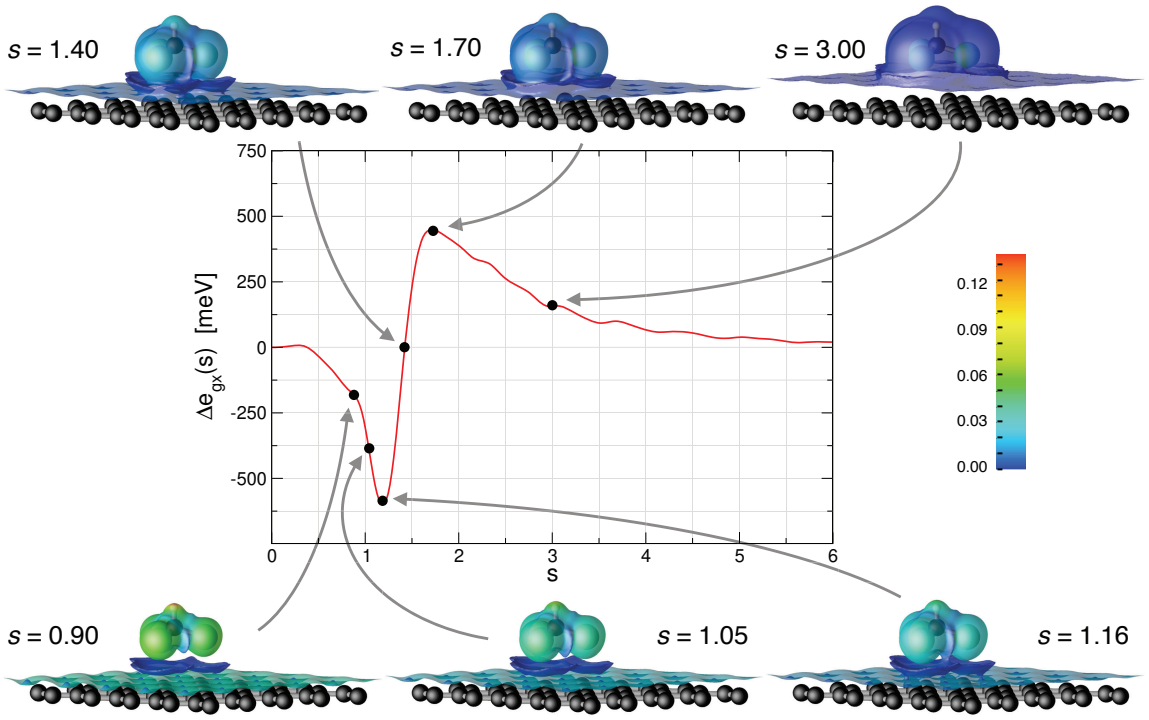

Figure 4.9: Iso-surfaces of s in $CHCl_3$ adsorbed onto graphene with their corresponding values of $\Delta e_{\mathrm{gx}}(s)$, as generated using vdW-DF3-opt1. Charge density [e/Bohr^3] is color mapped onto each iso-surface. Although plots of charge transfer during bond formation [139–143] show some similarities to iso-surfaces of s, they convey an important but fundamentally different concept of van der Waals bonding that is less relevant in the context of a reduced-gradient analysis.

gradient analysis point to avenues of improvement for several of the functionals in our study. These insights can guide further functional development for dispersion-bonded systems.

4.6 Appendix: Reduced-Gradient Analysis

Reference [12] describes the mechanism by which gradient exchange contributions switch from attractive to repulsive with increasing s. For a broad array of systems including molecular dimers, molecular crystals, and layered structures, this process is shown to be the result of a topological change between the s iso-surfaces of a given system. Figure 4.9 shows several iso-surfaces of s for graphene-adsorbed chloroform. Each iso-surface of s corresponds to a point in chloroform's $\Delta e_{\mathrm{gx}}(s)$ that contributes to the exchange energy. Onto each iso-surface we map the charge density as a color. When calculating the exchange energy of a certain s value, we are effectively integrating over the two-dimensional space

of the iso-surface according to Eq. 4.2, so areas of high charge density contribute more to the energy. For $s = 0.90$ there are three distinct surfaces of s: one around the chloroform molecule, one above the graphene substrate, and one in between them. When calculating the interaction energy of this system using Eq. 4.3, we subtract out the chloroform and substrate surfaces, leaving only the "disk" in the center. The charge density on this disk forms the sole negative contribution to $\Delta e_{\mathrm{gx}}(s = 0.90)$. When we increase the iso-value to $s = 1.05$, each of the three surfaces grow outward from their respective center points. Now not only is the disk larger, giving more area to integrate over for the exchange, but the charge density on the surface is higher due to its closer proximity to the molecule and substrate. As a result there is an increase in the negative exchange interaction, which is reflected by a downward slope in $\Delta e_{\mathrm{gx}}(s = 1.05)$. At $s = 1.16$ the central disk begins to merge with the molecule and substrate surfaces, meaning that positive contributions from $e_{\mathrm{gx}}^{\mathrm{system}}$ in Eq. 4.3 are no longer being cancelled out. As a direct consequence, $\Delta e_{\mathrm{gx}}(s)$ shifts to a positive energy. Then, at larger iso-values such as $s = 1.40$, 1.70, and 3.00, the merger completes itself and $\Delta e_{\mathrm{gx}}(s)$ regresses asymptotically to zero due to a lowering of charge density as the s iso-surface grows farther away from the molecules.

This pattern of expansion, merging, and regression that dictates the rise and fall of the gradient exchange interaction can also be seen in all other systems. We show this using the butane-graphene complex as an example, shown in Fig. 4.10. Even though butane is highly dissimilar from chloroform in its geometry, we still see the same three iso-surfaces: one surrounding the butane molecule, one above the graphene sheet, and an interactive "disk" in the middle. Note that at an iso-surface of $s = 1.10$ as shown in the figure, the disk has barely begun to merge with the other surfaces at its edges. Accordingly, butane's $\Delta e_{\mathrm{gx}}(s)$ curve in Fig. 4.8 reaches a global minimum at around this point and then begins to increase with higher s.

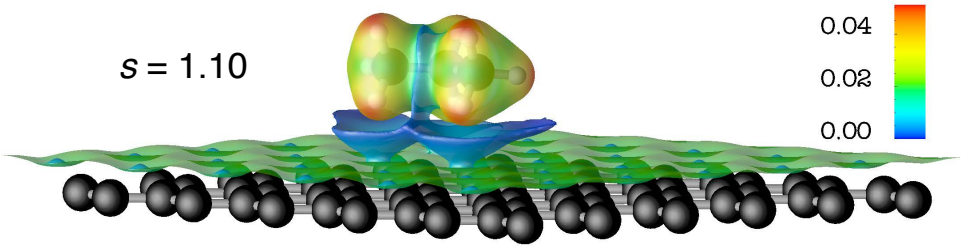

Figure 4.10: An iso-surface of $s = 1.10$ in a butane-graphene complex with charge density [e/Bohr^3] in color mapped onto the surface. Charge densities were obtained using the DF3-opt1 functional.

Chapter 5

Van der Waals Density Functional Optimized for Molecular Solids

This chapter is a pre-print of a forthcoming article, and as such some of the text may be repetitive of previous chapters.

5.1 Introduction

The ubiquity of van der Waals interactions in nature is well documented, and a correct quantum mechanical description of these interactions is therefore vital for the accurate modeling of a wide variety of systems. But traditional DFT has historically struggled to incorporate these interactions, though much research has been dedicated to amending that fact [3, 9, 25–40]. The family van der Waals density functionals, beginning with the work of Dion *et al.* in 2004 [3], represents one of the most important developments in this field. Through the use of a fully nonlocal correlation functional which obeys four exact physical constraints, vdW-DF1, for the first time, provided an accurate description of dispersion interactions in general geometries. Since then, the family of vdW-DF functionals has grown significantly, including the development of a third generation in 2020, vdW-DF3 [11]. The two optimizations of vdW-DF3 made use of a new parametrization of vdW-DF's nonlocal correlation functional, achieving a high degree of accuracy for many different dispersion-dominated systems. But during the development of vdW-DF3, it was found that there

are competing interests between different system types which limited its all-around performance. This posed several hurdles in the optimization process, and particularly limited vdW-DF3's accuracy with respect to $3D$ molecular solids. More recently, investigations by the authors of this paper revealed a major cause behind this competition: that different system types possess unique profiles of the electron density gradient [12, 81]. Due to the way that exchange is computed in the Perdew-Burke-Ernzerhof formalism of the generalized gradient approximation [6], these differences in profile have a profound effect on calculated energies and geometries.

To fill this important niche, we put forth a new optimization within the vdW-DF3 framework that is tailored to molecular crystals, which we name vdW-DF3-mc. In order to take full advantage of the information provided by our reduced-gradient analysis, we have designed a new form of the enhancement factor for the GGA exchange. This enhancement factor is highly flexible, allowing us to target qualitative properties of individual or groups of systems. We also re-parameterize the nonlocal correlation of vdW-DF3 to achieve greater accuracy in tandem with this new exchange. With these alterations, we optimize our functional on a test set of 23 molecular crystals, 2 layered systems, and 24 molecular dimers. Layered systems are included to represent molecular solids with interplanar dispersion interactions such as π–π stacking, while the molecular dimers are included to represent porous $3D$ materials with long-range interactions, such as the highly ubiquitous covalent organic frameworks and hydrogen-bonded organic frameworks. We find that vdW-DF3-mc yields greatly improved accuracy over its predecessors for a wide variety of $3D$ solids, both within and beyond our optimization set. For energetics and geometries of conventional molecular crystals, its accuracy is comparable to that of the force-field corrected DFT-D3 [54]. Moreover, vdW-DF3-mc's improved accuracy over hydrogen bonds gives it excellent suitability for systems with water and the ever-growing family of hydrogen-bonded organic frameworks (HOF).

5.2 Theory

5.2.1 Constructing Exchange in the GGA

In van der Waals density functionals, the exchange correlation is typically expressed as a sum of the GGA exchange, the local density approximation of correlation, and the nonlocal correlation. That is,

$$E_{\rm xc}[n] = E_{\rm x}^{\rm GGA}[n] + E_{\rm c}^{\rm LDA}[n] + E_{\rm c}^{\rm nl}[n]. \tag{5.1}$$

Here, the GGA exchange and nonlocal correlation are particularly important in the accurate description of binding in van der Waals complexes. To improve upon the overall accuracy of vdW-DF3, we thus devote our attention to these two terms.

In the framework of Perdew, Burke, and Ernzerhof [6], the total GGA exchange can be written as

$$E_{\rm x}^{\rm GGA}[n] = \int d\mathbf{r}\ n(\mathbf{r})\varepsilon_{\rm x}^{\rm hom}(n(\mathbf{r}))F_{\rm x}(s) \tag{5.2}$$

where $\varepsilon_{\rm x}^{\rm hom}$ is the exchange energy of a homogeneous electron gas, and $F_{\rm x}(s)$ is the enhancement factor, a function of the reduced-density gradient $s \propto |\nabla n(\mathbf{r})|/n(\mathbf{r})^{4/3}$ that contributes to the total energy of inhomogeneous systems. The precise form of $F_{\rm x}(s)$ varies from functional to functional, and in Chapter 3 we have shown that key features of the enhancement factor—such as its asymptotic behavior at high s or the maximum value of $dF_{\rm x}(s)/ds$—have a direct and traceable impact on the energy and forces of a system [12]. We have also investigated in Chapters 3 and 4 the "signature" of the reduced-gradient for several types of van der Waals complexes, effectively resolving the interaction energy as a function of s [12, 81]. Through our reduced-gradient analysis, we found that different system types have different s-signatures, meaning that individual systems can be targeted by an appropriately chosen enhancement factor to yield greater accuracy.

For this reason, it is important that our enhancement factor be flexible enough to match the reduced-gradient signatures of as many system types as possible. The original vdW-DF3 functionals, opt1 and opt2, used GGA exchange forms inspired by optB88 and B86R, respectively. Both enhancement factors contain two adjustable parameters: μ, which controls the second derivative of $F_{\rm x}(s)$ at low s, and κ, which primarily affects the "tail" of

$F_{\mathrm{x}}(s)$ at high s. To retain these degrees of freedom while including additional flexibility for mid-range s, we define vdW-DF3-mc's enhancement factor as

$$F_{\mathrm{x}}(s) = \begin{cases} \mu s^2 + As^4 + Bs^6, & \text{if } s < s_0 \\ C + \kappa s^{-3/5} + Ds^{-8/5} + Es^{-13/5}, & \text{if } s \geq s_0. \end{cases} \tag{5.3}$$

Here, μ and κ retain their functions as stated above. This enhancement factor also implicitly includes parameters which we call s_0 and A_0. We define s_0 as the value of s at which the $d^2F_{\mathrm{x}}(s)/ds^2 = 0$, while A_0 is $dF_{\mathrm{x}}(s)/ds$ evaluated at s_0. In addition to setting s_0 and A_0, the coefficients A, B, C, D, and E are constrained to ensure that $F_{\mathrm{x}}(s)$ remains smooth (to 2nd order) and continuous at the boundary $s = s_0$.

5.2.2 Re-optimizing Nonlocal Correlation

In the van der Waals density functional of Dion *et al.*, the nonlocal correlation energy is expressed as a functional of electron density $n(\mathbf{r})$:

$$E_{\mathrm{c}}^{\mathrm{nl}}[n] = \frac{1}{2}\int d\mathbf{r}\; d\mathbf{r}' n(\mathbf{r})\Phi(\mathbf{r},\mathbf{r}')n(\mathbf{r}'), \tag{5.4}$$

where $\Phi(\mathbf{r},\mathbf{r}')$ is a kernel to describe the self-interaction of the electron density. By rigorously expanding to second-order the adiabatic connection formula (ACF), it becomes possible to derive such an expression for the kernel, where the nonlocal correlation energy can be rewritten as

$$E_{\mathrm{c}}^{\mathrm{nl}}[n] = \int_0^\infty \frac{du}{4\pi}\int \frac{d\mathbf{q}}{(2\pi)^3}\frac{d\mathbf{q}'}{(2\pi)^3}[1-\mathbf{q}\cdot\mathbf{q}']^2 \times S_{\mathbf{q},\mathbf{q}'}(iu)S_{\mathbf{q}',\mathbf{q}}(iu), \tag{5.5}$$

where $\mathbf{q}$ is a plasmon momentum, and the function $S_{\mathbf{q},\mathbf{q}'}$ represents the plasmon propagator with spectator contributions omitted. Partially derived from the dielectric function of an electron gas, and made to obey four exact physical constraints, Dion *et al.* construct the

following form of the plasmon propagator:

$$S_{\mathbf{q},\mathbf{q}'}(\omega) = \frac{1}{2}\int d\mathbf{r}\, e^{-i(\mathbf{q}-\mathbf{q}')\cdot\mathbf{r}} \times \left[\frac{\omega_p^2(\mathbf{r})}{(\omega+\omega_q(\mathbf{r}))(-\omega+\omega_{q'}(\mathbf{r}))} + \frac{\omega_p^2(\mathbf{r})}{(\omega+\omega_{-q'}(\mathbf{r}))(-\omega+\omega_{-q}(\mathbf{r}))}\right]. \quad (5.6)$$

Here, $\omega = iu$, $\omega_p(\mathbf{r})$ is the classical plasmon frequency $\sqrt{4\pi n(\mathbf{r})}$, and $\omega_q(\mathbf{r})$ is an appropriately chosen plasmon dispersion law. For the sake of making Eq. 5.5 analytically integrable over u, they take

$$\omega_q(\mathbf{r}) = \frac{q^2}{2}\frac{1}{h(q/q_0(\mathbf{r}))}, \quad (5.7)$$

where $h(y)$ is a switching function of a single length scale $1/q_0(\mathbf{r})$, which ensures that ω_q behaves as $q^2/2$ at large q in order to reproduce the exactly known self-correlation. The value of $q_0(\mathbf{r})$ is chosen so that a first order expansion of the ACF in S yields a GGA-type form of the local exchange-correlation functional. This so-called "internal functional" $\varepsilon_{\mathrm{xc}}^{\mathrm{int}}$, can be written as

$$\begin{aligned}\varepsilon_{\mathrm{xc}}^{\mathrm{int}} &= \pi\int\frac{d\mathbf{q}}{(2\pi)^3}\left[\frac{1}{\omega_q(\mathbf{r})} - \frac{2}{q^2}\right] \\ &= -\frac{1}{\pi}q_0(\mathbf{r})\int_0^\infty dy[1-h(y)].\end{aligned} \quad (5.8)$$

In vdW-DF1, the switching function is chosen as $h_{\mathrm{DF1}}(y) = 1 - e^{4\pi y^2/9}$ so that the above integral over y evaluates to 3/4. With this, $q_0(\mathbf{r})$ can be conveniently written as a ratio of the internal and LDA exchange functionals:

$$q_0(\mathbf{r}) = (\varepsilon_{\mathrm{xc}}^{\mathrm{int}}/\varepsilon_{\mathrm{x}}^{\mathrm{LDA}})k_{\mathrm{F}}(\mathbf{r}), \quad (5.9)$$

where $k_{\mathrm{F}}(\mathbf{r})$ is the Fermi wavevector, equal to $(3\pi^2 n(\mathbf{r}))^{1/3}$. More recently, in the development of vdW-DF3, this definition of $q_0(\mathbf{r})$ is retained, but the switching function is reconstructed as

$$h_{\mathrm{DF3}}(y) = 1 - \frac{1}{1+\gamma y^2 + (\gamma^2-\beta)y^4 + \alpha y^8}, \quad (5.10)$$

where γ, β, and α are variational parameters. With this definition of $h_{\mathrm{DF3}}(y)$, the plasmon frequency can be conveniently expanded as

$$\omega_q \sim \frac{y^2}{2h_{\mathrm{DF3}}(y)} = \frac{1}{\gamma} + \frac{\beta}{\gamma^2}y^2 + \left(\frac{\beta^2}{\gamma^3} - \frac{2\beta}{\gamma} + \gamma\right)y^4 + ... \tag{5.11}$$

The low-q behavior of ω_q in vdW-DF3 should have been well accounted-for by γ and β, with α serving to normalize Eq. 5.8. But in practice, this aggressive constraint on α worked counter to the contributions of β for mid-range q. As a result, $h_{\mathrm{DF3}}(y)$ offered less flexibility than anticipated, with an optimum β of 0.0 for both vdW-DF3-opt1 and vdW-DF3-opt2.

To amend this problem and restore flexibility to $h_{\mathrm{DF3}}(y)$ in vdW-DF3-mc, we instead constrain α for smoothness, rather than the satisfaction of Eq. 5.9. For given values of γ and β, α is chosen to minimize second-order changes in the switching function, given by $d^2h(y)/dy^2$. While this decision does result in a $q_0(\mathbf{r})$ that is some scalar factor different from that of vdW-DF1, it has no significant impact on the evaluation of the kernel $\Phi(\mathbf{r}, \mathbf{r}')$, nor does it break any of the four exact physical constraints that are essential to vdW-DF1's original design. In fact, past functionals have also broken vdW-DF1's constraint on Eq. 5.8, achieving equal or improved accuracy in the process [144].

5.2.3 Optimization Procedure

We optimize vdW-DF3-mc on a test set selected to represent a broad variety of molecular crystals. Included in this set were the X23 molecular crystals, the two layered structures graphite and hexagonal boron nitride, and several dimers from the extended S22×5 and S66×8 data sets. With the inclusion of layered systems, we improve performance for more two-dimensional molecular crystals. Similarly, dimers were included to better model long-range interactions, which are especially prevalent in porous materials such as covalent organic frameworks and hydrogen-bonded organic frameworks.

We began by optimizing solely the exchange, calculating the stress tensors of our test systems in their reference geometries. We take $\mu = \mu_{\mathrm{PBEsol}} \approx 0.1234$, which has shown good agreement with experiment for ionic systems, and optimize with respect to s_0, A_0, and B of Eq. 5.3. This involved minimizing the MD of stress tensor elements for all $3D$

structures in our test set. That is, for the n systems in our set, we optimize with respect to

$$\mathrm{MD} = \frac{1}{n}\sum_{\mathrm{sys}=1}^{n} \sigma_{xx}^{i} + \sigma_{yy}^{i} + \sigma_{zz}^{i} + 2(\sigma_{xy}^{i} + \sigma_{xz}^{i} + \sigma_{yz}^{i}), \tag{5.12}$$

where σ_{jk}^{i} is a stress tensor element of the system indexed by i.

Next, taking the optimized exchange, we calculated binding energies for our test set with varying combinations of γ and β from Eq. 5.10. For molecular crystals and layered structures, we calculate cohesive energy per fragment as

$$E_{\mathrm{coh}} = \frac{1}{N}E_{\mathrm{tot}} - \frac{1}{N}\sum_{i} E_i, \tag{5.13}$$

for a system comprised of N separate molecules/layers. For the dimers in our test set, we calculate the total binding energy as

$$E_{\mathrm{bind}} = E_{\mathrm{tot}} - E_A - E_B, \tag{5.14}$$

with E_A and E_B being the energies of molecule A and B in the gas phase, respectively. To optimize our nonlocal correlation functional with respect to the energy, we simultaneously minimize the MARD of the cohesive energy for the solids, and the weighted mean absolute relative deviation (WMARD) for the dimers, which accounts for the smaller interaction energies of non-equilibrium geometries. These are defined as

$$\mathrm{MARD} = \frac{1}{n}\sum_{\mathrm{sys}=i}^{n} \frac{|E_{\mathrm{sys}}^{\mathrm{DFT}} - E_{\mathrm{sys}}^{\mathrm{ref}}|}{E_{\mathrm{sys}}^{\mathrm{ref}}} \times 100 \tag{5.15}$$

$$\mathrm{WMARD} = \frac{1}{n}\frac{1}{m}\sum_{\mathrm{sys}=1}^{n}\sum_{\mathrm{sep}=1}^{m} \frac{|E_{\mathrm{sys,sep}}^{\mathrm{DFT}} - E_{\mathrm{sys,sep}}^{\mathrm{ref}}|}{E_{\mathrm{sys,opt}}^{\mathrm{ref}}} \times 100. \tag{5.16}$$

For the range-separated dimers, $E_{\mathrm{sys,opt}}^{\mathrm{ref}}$ denotes the reference energy of the dimer at equilibrium distance. We found that, as with vdW-DF3-opt1 and vdW-DF3-opt2, the binding energies were only slightly dependent on β, with an optimum at zero.

Once we were sufficiently close to the optima for exchange and correlation, we performed a final search of the four parameters A_0, s_0, B, and γ. We optimized with respect to both

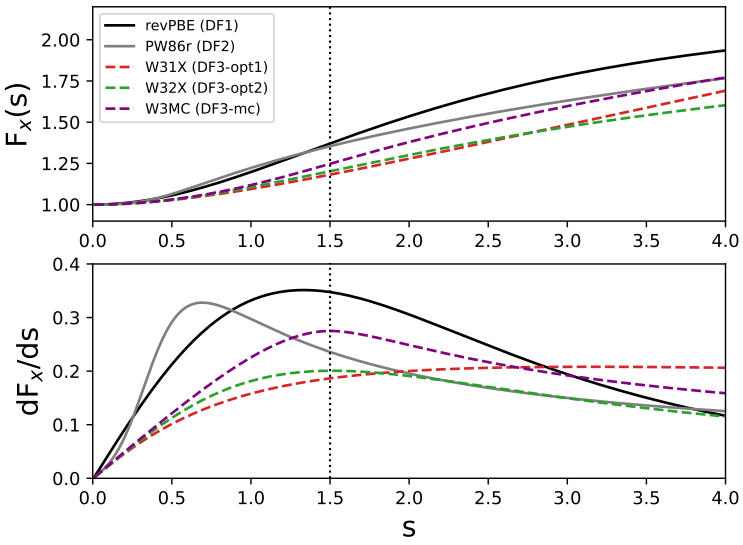

Figure 5.1: **(top)** The exchange enhancement factor $F_{\mathrm{x}}(s)$ of vdW-DF3-mc, denoted as "W3MC", and **(bottom)** the derivative of F_{x} with respect to s, compared with those of several other vdW-DF. The vertical dotted line indicates the location of s_0, the boundary between the two parts of Eq. 5.3.

binding energies and unit cell geometries, the latter of which were calculated via variable-cell relaxations of the molecular crystals and layered structures. Doing so yielded the parameters for the GGA exchange: $A_0 = 0.275$, $s_0 = 1.50$, and $B = 0.88$, and for the nonlocal correlation: $\alpha = 0.0532$, $\beta = 0.0$, $\gamma = 1.420$. The exchange enhancement factor of vdW-DF3-mc and its derivative is compared with those of several other vdW-DF's in Fig. 5.1. Here, we observe that our peak in $dF_{\mathrm{x}}(s)/ds$ occurs at higher s than that of either vdW-DF1 or vdW-DF2, ensuring more slowly-varying corrections due to the density gradient. On the other hand, vdW-DF3-mc generates a larger contribution than either of its predecessors opt1 or opt2, particularly in the region $1.5 < s < 3.5$. This region was found to be the largest contributor of repulsion in the X23 molecular crystals, a positive indicator that this optimization avoids the overbinding of vdW-DF3-opt1 and -opt2 [11,12].

Lastly, we show in Fig. 5.2 the switching function of vdW-DF3-mc's nonlocal correlation, alongside other known switching functions for comparison. Despite the differing constraints on $q_0(\mathbf{r})$ between these functionals, we note no significant visual distinctions in their plasmon dispersions.

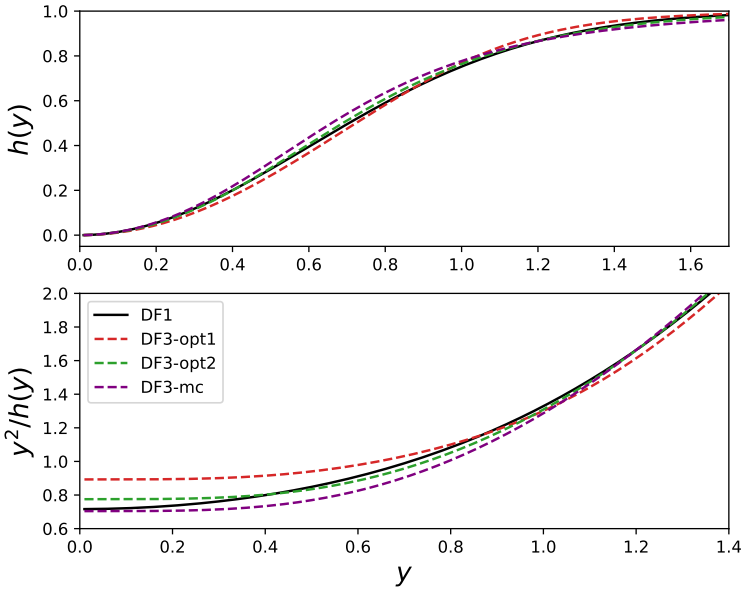

Figure 5.2: **(top)** The switching function $h(y)$ of vdW-DF3-mc's nonlocal correlation term, and **(bottom)** its corresponding $y^2/h(y)$ function, which is analogous to the plasmon dispersion law ω_q. Both functions are compared with those of vdW-DF1, and the previous two optimizations of vdW-DF3.

5.3 Computational Details

All calculations were done using the QUANTUM ESPRESSO (QE) package. We used the SG15 optimized norm-conserving Vanderbilt (ONCV) pseudopotentials [145]. For optimizations of the GGA exchange and nonlocal correlation, we find convergence for a wavefunction cutoff of 80 Ryd and a charge density cutoff of 320 Ryd. Energies and forces in the system were made to converge within 1×10^{-6} Ryd and 1×10^{-4} Ryd/bohr respectively. For initial searches in the exchange parameter space, we performed non-variable-cell relaxations on the $3D$ materials in our test set, allowing only atomic positions to optimize. For the final optimization of both the exchange and correlation, we do full variable-cell relaxations. Where applicable in our optimization, we use convergence thresholds of 10^{-6} Ry for self-consistent field (SCF) energies, 10^{-4} Ry/bohr for atomic forces, and 0.5 kbar for unit cell pressure. For our optimization, we minimize the deviation from reference values in Refs. [71, 80, 146] with respect to unit cell stress/dimensions and binding energies. We perform additional calculations, testing the optimized vdW-DF3-mc on several validation sets of molecular

solids and layered structures, including several well-studied polymorphic materials. These calculations use the same convergence criteria as in the functional optimization.

5.4 Results

5.4.1 Studied Benchmarks

Several benchmark data sets were used, both for the optimization of vdW-DF3-mc, and for accuracy testing of the completed functional. We make use of the X23 set of molecular crystals [80], which uses zero-point corrected experimental lattice constants, as well as vibrational corrections to the experimental sublimation enthalpy. Another is the G60, a larger and somewhat more diverse molecular crystal set that also includes some halogenated materials. Originally compiled by Maschio *et al.* in Ref. [147], we use the reference energies of Ref. [148], which applies a constant $-2RT$ correction to experimental sublimation enthalpies.

We also examine polymorphs of ice, some of which are compiled in the ICE10 and DMC-ICE13 data sets. ICE10 compiles ten ice polymorphs with lattice parameters drawn from low-temperature neutron diffraction experiments and subsequently corrected for zero-point effects [149]. The DMC-ICE13 set provides lattice energies for each of the ICE10 polymorphs, plus ice IV, XI, and XVII, which are taken from Diffusion Monte Carlo (DMC) calculations [150].

The POLY59 set compiles a total of 59 polymorphs of five different molecular solids [151]. Each of the five compounds possesses one or more experimentally-known optimum configurations, making it useful for the blind testing of different computational methods.

Beyond the scope of $3D$ molecular solids, we also examine several hand-picked $2D$ layered systems. For ease of comparison, we take the same layered systems used in the development of vdW-DF3-opt1 and opt2 [11]. Additionally, we study several molecular dimers from the range-separated S22×5 and S66×8 data sets [71, 146]. By including non-equilibrium geometries, we aim to achieve greater accuracy for porous and flexible materials, such as covalent– and metal–organic frameworks. We also give particular attention to the hydrogen-bonded dimers, given their applicability to the modeling of water, acids, and the

increasingly popular hydrogen-bonded organic frameworks.

5.4.2 The Optimization Set

Our optimization set for vdW-DF3-mc was comprised of three parts: the full X23 set of molecular crystals, the two layered materials graphite and hexagonal boron nitride (h-BN), and 24 hand-selected molecular dimers. Fourteen of the dimers are from the S22×5: four h-bonded dimers, prioritizing those with multiple bonds, and five each from the dispersion and mixed-character groups, selected for representation of hydrocarbon interactions and π–π stacking. The remaining ten dimers come from the S66×8, with similar criteria. Four of these systems are h-bonded, including the water dimer, while the other six are π–π and TS configurations of benzene and nucleotide dimers. In cases where a particular dimer was present in both sets, we used the S66×8 configurations as our reference due to its larger sampling of non-equilibrium geometries. With our new, flexible form of the exchange, we were able to achieve comparable accuracy for the molecular crystals and dimers within our set—a noticeable improvement over vdW-DF3's initial two optimizations. However, achieving comparable accuracy for graphite and h-BN posed a challenge, as those systems preferred different regions within our parameter space than the X23 complexes and dimers. Nevertheless, we retain them in our optimization so that we do not neglect planar interactions.

5.4.3 X23 and G60

In Fig. 5.3, we show a detailed summary of vdW-DF3-mc's accuracy on the X23 set and comparison to some other functionals. It is perhaps unsurprising that vdW-DF3-mc performs well for these systems, given that they account for nearly half of our optimization set. It is, however, still encouraging that we find surpassing accuracy over every major van der Waals density functional, including the first two optimizations of vdW-DF3. Out of this group, vdW-DF3-mc shows the best accuracy in cohesive energies, with a MD of only −6 meV, as well as unit cell volumes at a MARD of 0.44%. Remarkably, vdW-DF3-mc also compares favorably with the dispersion-corrected DFT-D3, which is a popular choice for simulating molecular solids. DFT-D3 possesses a cohesive energy MD of −16 meV and a

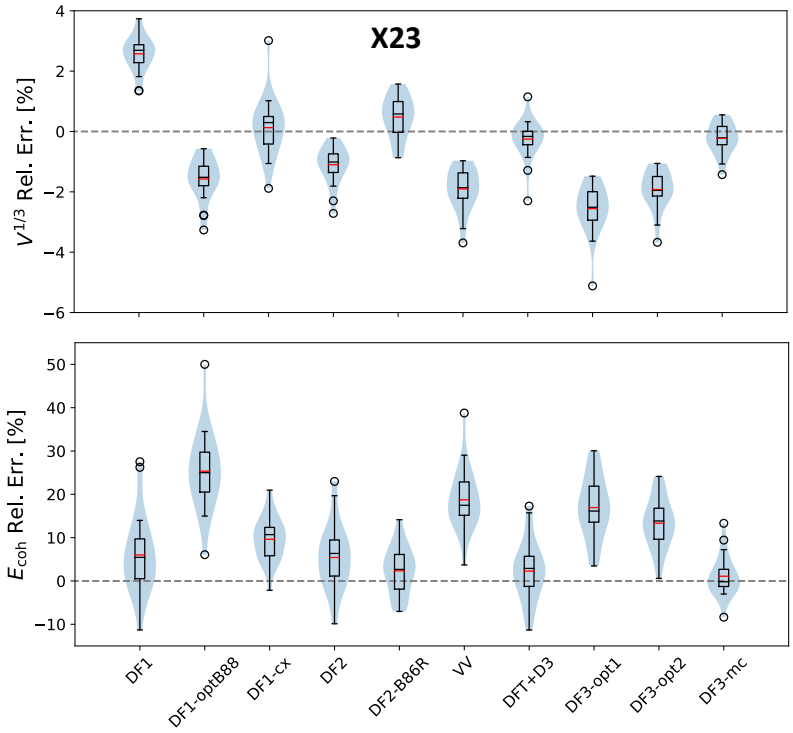

Figure 5.3: Accuracy of vdW-DF3-mc on the X23 set of molecular solids, comparing relative deviations in the cube roots of unit cell volume **(top)** and cohesive energies **(bottom)** with several other nonlocal and dispersion-corrected density functionals. Box plots indicate the first and third quartile values, as well as the median (black) and mean (red). Whiskers extending from the box lie at 1.5 times the inter-quartile range. Individual systems beyond this range are shown as circles.

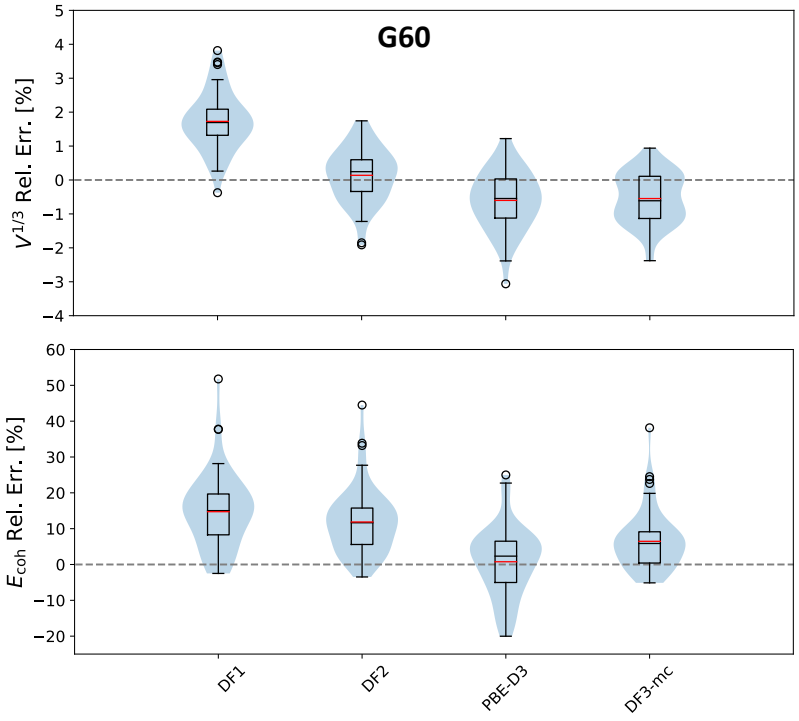

Figure 5.4: Accuracy of vdW-DF3-mc on the G60 set of molecular solids, comparing relative deviations in the cube roots of unit cell volume **(top)** and cohesive energies **(bottom)** with several other nonlocal and dispersion-corrected density functionals.

cell volume MARD of 0.87 % for the X23.

To assess the accuracy of vdW-DF3-mc for systems outside of its optimization set, we perform calculations on the G60 set of molecular crystals. Due to its more diverse sampling in comparison with the X23 set, and little overlap between the two, the G60 presents an effective way of gauging our functional's extendibility. Figure 5.4 showcases the accuracy of vdW-DF3-mc, the previous two generations of vdW-DF1 and vdW-DF2, and PBE-D3. We choose these functionals primarily to compare different treatments of the dispersion interactions, for which all four of these functionals differ. We find that, in general, vdW-DF3-mc retains its exceptional accuracy for both cohesive energies and geometries. For the former, its MD of -45 meV is only narrowly surpassed by that of PBE-D3. And for unit cell volumes, vdW-DF3-mc demonstrates greater accuracy than PBE-D3, with a MARD of only 2.17 %. We also make note of vdW-DF3-mc's unusually high precision among the studied functionals, a positive sign for its applicability outside of our studied data sets.

5.4.4 POLY59, ICE10, and DMC-ICE13

An important subfield in the study of molecular solids is that of polymorphs. The existence of multiple stable configurations of chemically identical materials poses an immense challenge in computational physics, and in some cases requires sub-chemical accuracy—on the order of 1 kcal/mol—to adequately predict. With the POLY59 test set of polymorphs, we can gain some idea for how vdW-DF3-mc fairs for these scenarios. Figure 5.5 shows the computed cohesion energies for each of the five compounds in this set, with experimental ground state configurations indicated by the horizontal axis. We find that vdW-DF3-mc correctly predicts the ground state in three out of the possible five cases. This result may seem surprising, given its aforementioned success in predicting cohesion energies. However we note that the two failed predictions, System 25 and System 26, deviate from the ground state by no more than 20 meV.

To continue our study of polymorphism and gauge accuracy for H-bond-dominated systems, we examine several polymorphs of ice. A statistical summary of our ICE10 and ICE13 calculations is presented in Table 5.1. We find that for these sets, vdW-DF3-mc demonstrates excellent accuracy with respect to both the cohesive energy and cell dimensions of ice.

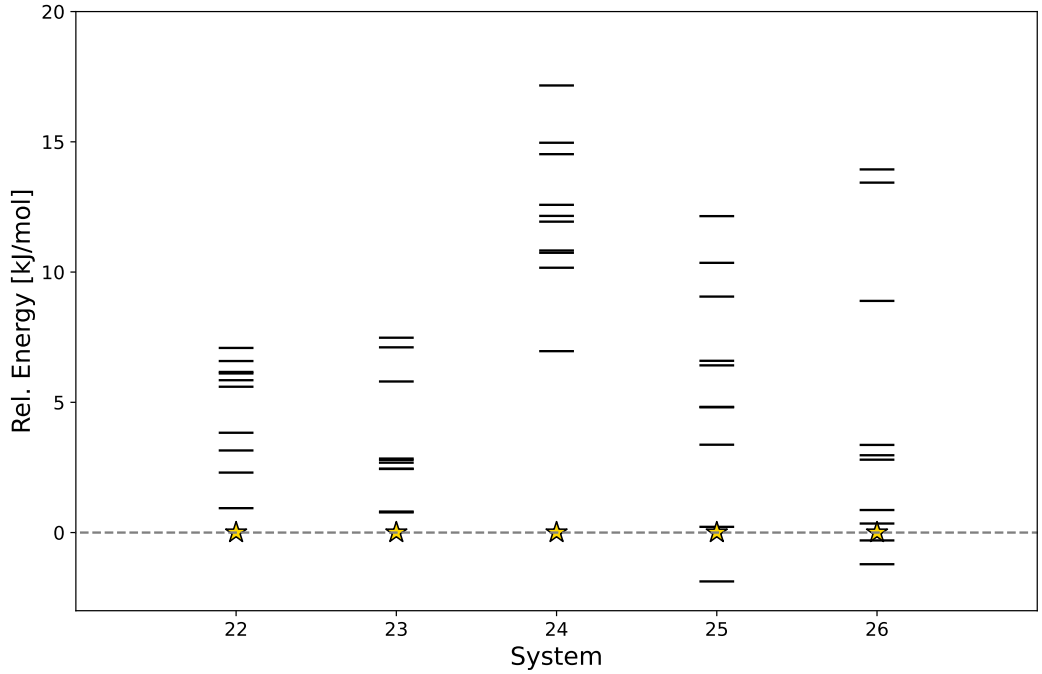

Figure 5.5: Energies for five different polymorphic compounds, as calculated with vdW-DF3-mc. Gold stars represent the calculated energies of experimentally-realised polymorphs, and all other configurational energies are taken relative to these values.

These systems present a challenge for force-field dispersion corrections, as ordinary PBE-D3 and the three-body corrected PBE-D3^{atm} both result in significantly stronger binding than uncorrected PBE, and by extension a larger deviation from diffusion Monte Carlo reference values. In contrast, vdW-DF1 yields comparable cohesive energies to PBE, and vdW-DF2 presents a significant improvement over both with a MARD of only 2.37%. Despite this, vdW-DF2 suffers from a systemic underbinding for all 13 ice polymorphs. For this reason, we find the performance of vdW-DF3-mc to be particularly promising, with a volume MARD that is less than half of PBE or PBE-D3, and an energetic MARD nearly one full percentage point smaller than vdW-DF2. We attribute this success in modeling to our optimization set, which was carefully curated to include a diverse sample of hydrogen-bonded complexes, particularly those with multiple points of interaction.

Table 5.1: Calculated volumes per water molecule (Å^3) and cohesive energies (kJ/mol) for the ICE10 and DMC-ICE13 sets, respectively.

	Ref.	PBE	PBE-D3	PBE-D3^{atm}	vdW-DF1	vdW-DF2	vdW-DF3-mc
				Volumes			
Ih	30.9	30.2	29.1	29.2	-	-	30.8
II	24.0	24.5	23.2	23.3	-	-	24.4
III	25.3	26.2	24.4	24.6	-	-	25.2
VI	22.0	22.3	20.9	21.0	-	-	21.9
VII	19.3	20.4	18.9	19.0	-	-	19.7
VIII	19.1	20.4	19.1	19.2	-	-	19.7
IX	25.0	26.2	24.1	24.3	-	-	25.2
XIII	23.0	23.6	22.2	22.4	-	-	23.3
XIV	22.1	22.9	21.5	21.6	-	-	22.5
XV	21.7	22.4	21.1	21.2	-	-	22.0
MD [Å^3]		0.7	−0.8	−0.7	-	-	0.2
MAD [Å^3]		0.8	0.8	0.7	-	-	0.3
MARD [%]		3.6	3.2	2.8	-	-	1.3
				Cohesive Energies			
Ih	−59.45	−62.23	−70.80	−70.39	−53.59	−59.43	−60.59
II	−59.14	−55.54	−68.37	−67.75	−53.78	−60.16	−58.53
III	−58.20	−57.85	−68.47	−67.94	−52.86	−58.40	−59.09
VI	−57.67	−51.58	−66.17	−65.41	−52.74	−59.18	−57.62
VII	−54.46	−43.79	−60.66	−59.76	−49.13	−56.49	−54.23
VIII	−55.22	−45.05	−61.79	−60.90	−50.47	−57.80	−54.19
IX	−58.85	−57.65	−68.97	−68.38	−54.19	−59.87	−59.66
XIII	−57.33	−54.54	−67.76	−67.07	−53.81	−59.92	−58.57
XIV	−57.75	−53.24	−67.11	−66.37	−53.60	−59.84	−58.17
XV	−57.71	−51.56	−66.00	−65.25	−52.96	−59.30	−57.31
IV	−55.62	−52.85	−65.82	−65.15	−52.03	−57.93	−57.57
XI	−59.29	−62.60	−71.29	−70.87	−53.59	−59.43	−59.71
XVII	−57.70	−61.52	−69.75	−69.42	−51.84	−58.06	−59.01
MD [kJ/mol]		2.95	−9.58	−8.94	4.91	−1.34	−0.45
MAD [kJ/mol]		4.48	9.58	8.94	4.91	1.34	0.81
MARD [%]		7.88	16.60	15.48	8.52	2.37	1.41

5.5 Conclusions

We have presented a new optimization of the third generation van der Waals density functional, which we call vdW-DF3-mc. Using lessons learned from prior studies of gradient contributions to exchange, we created a novel form of the exchange enhancement factor, prioritizing the flexibility needed to target desirable features of molecular solids' binding profile. We also re-optimize the vdW-DF3 nonlocal correlation with a new constraint on $q_0(\mathbf{r})$, which yields back vdW-DF3's intended flexible design. With these combined innovations, and an extensive optimization set that includes molecular solids, dimers, and layered structures, vdW-DF3-mc achieves extraordinarily accurate energies and cell geometries for a variety of systems. This includes not just solids within our test set, like the X23, but a large number of outsider systems like the G60, POLY59, and ICE10 benchmark sets. With this, we not only put forth a functional for broad use in the simulation of $3D$ dispersion-based materials, but also a developmental framework through which additional, highly-accurate nonlocal functionals may be created.

Chapter 6

Van der Waals Density Functional with a Novel Form of the Nonlocal Correlation Kernel

6.1 Past Developments in vdW-DFT

Reduced-gradient analysis represents a powerful tool for functional development, and vdW-DF3-mc is a natural conclusion of its applicability. But exchange is only one half of the story for van der Waals density functionals, and vdW-DF3-mc's high performance was only made possible by the flexible nonlocal correlation functional of vdW-DF3. Section 2.3.4 provides some insight into the development of vdW-DF1, including its approximation of the plasmon dispersion law by way of a switching function $h(q/q_0)$. In the original vdW-DF, the switching function is kept to a simple form $h_{\mathrm{DF1}}(y) = 1 - e^{4\pi y^2/9}$, with constants chosen to obey exact physical constraints. As is described in Section 5.2, vdW-DF3 improves upon the flexibility of this model by taking a switching function in the form of Eq. 5.10. With three variational parameters α, β, and γ, one can be used to obey the same constraints as DF1, while the other two can be freely adjusted to yield greater general accuracy. The success of vdW-DF3, both in its original form and the vdW-DF3-mc optimization, highlights the importance of the nonlocal correlation functional. The fact that this minor change to the

original model of Dion *et al.* can have such a profound impact on performance also makes it enticing to explore alternative descriptions of the nonlocal correlation kernel. In this chapter, I outline a project that is still early in development, the objective of which is to create a novel, accurate form of the nonlocal correlation. Though it has not yet reached the calculation phase, our research thus far is included here for documentation purposes.

In our search for a suitable form of nonlocal correlation, we may begin by reiterating the design principles of vdW-DF1 [3]. Dion and coworkers provide a description of van der Waals interactions that is based on the plasmon- pole model and derived from the adiabatic connection fluctuation dissipation theorem (ACFDT) in the full potential approximation (FPA). In general, their goal is to write the nonlocal correlation energy in the form

$$E_{\mathrm{c}}^{\mathrm{nl}}[n] = \frac{1}{2}\int d\mathbf{r}\, d\mathbf{r}'\, n(\mathbf{r})\Phi(\mathbf{r},\mathbf{r}')n(\mathbf{r}'), \tag{6.1}$$

where $\Phi(\mathbf{r},\mathbf{r}')$ is the density-density interaction kernel. In the original framework laid out by Dion *et al.*, this form of the nonlocal correlation can be reached by expanding $E_{\mathrm{c}}^{\mathrm{nl}}$ to first order in terms of the plasmon propagator S:

$$E_{\mathrm{c}}^{\mathrm{nl}}[n] \approx \int \frac{du}{4\pi}\mathrm{tr}\left[S^2 - \left(\frac{\nabla S \nabla V}{4\pi e^2}\right)\right], \tag{6.2}$$

Here, the response function S is related to the dielectric function ϵ. Rather than use an exact S, an approximation was needed in order to reduce this form into an easy-to-use kernel. Dion *et al.* require S to fulfill the four exact constraints:

1. The f-sum rule: $S_{\mathbf{q},\mathbf{q}'} \to -(4\pi e^2/m\omega^2)n_{\mathbf{q}-\mathbf{q}'}$, where $n_{\mathbf{q}-\mathbf{q}'}$ is the Fourier transform of the density.

2. Exactly known self-correlation: $\int_{-\infty}^{\infty} du\, S_{\mathbf{q},\mathbf{q}'}(iu) \to 8\pi^2 N e^2/q^2$ for large q, where N is the number of electrons.

3. Time reversal invariance: $S_{\mathbf{q},\mathbf{q}'} = S_{-\mathbf{q}',-\mathbf{q}}$.

4. Charge conservation: As q or $q' \to 0$, $S_{\mathbf{q},\mathbf{q}'}(\omega)$ is finite for all nonzero values of ω.

These constraints led them to define S as

$$\begin{aligned} S^{\mathrm{DF1}}_{\mathbf{q},\mathbf{q}'} &= \frac{1}{2}\left[\tilde{S}_{\mathbf{q},\mathbf{q}'} + \tilde{S}_{-\mathbf{q}',-\mathbf{q}}\right], \\ \tilde{S}_{\mathbf{q},\mathbf{q}'} &= \int d\mathbf{r}\, e^{-i(\mathbf{q}-\mathbf{q}')\cdot\mathbf{r}}\, \frac{4\pi n e^2/m}{[\omega+\omega_q(\mathbf{r})][-\omega+\omega_{q'}(\mathbf{r})]}, \end{aligned} \tag{6.3}$$

with ω_q defined by a switching function, which smoothly interpolates between analytical low-q and high-q asymptotes of the plasmon dispersion. This approximation for S in Eq. 6.3, and the use of a switching function for ω_q, has remained the standard for vdW-DF1's successors, such as vdW-DF2 and vdW-DF3.

However, one could devise alternative forms of S and ω_q which make the resulting non-local correlation more efficient to compute or more accurate for general systems. Examples of this can be seen in vdW-DF-09, VV09, and VV10 functionals developed by Oleg Vydrov and Troy van Voorhis [9, 32, 144]. In the first of these papers, titled "Improving the accuracy of the nonlocal van der Waals density functional with minimal empiricism", Vydrov and van Voorhis draw comparison between Bengt Lundqvist's plasmon dispersion law (see Eq. 2.41) and the approximation used within vdW-DF1. They show that a Taylor series expansion of vdW-DF1's ω_q^2 yields the small-q approximation

$$\omega_q(\mathbf{r})^2 \approx \frac{q_0(\mathbf{r})^4}{4\beta^2} + \frac{q_0(\mathbf{r})^2}{4\beta}q^2 + \frac{5}{48}q^4 + ... \tag{6.4}$$

where $\beta = 4\pi/9$. In this expansion, all three coefficients differ from those of the analytical plasmon dispersion law. To correct this, Vydrov and van Voorhis choose a simpler form of ω_q for vdW-DF-09, letting it be

$$\omega_q(\mathbf{r}) = \frac{q^2}{2} + \frac{q_0(\mathbf{r})^2}{3}, \tag{6.5}$$

such that the q^2 and q^4 terms of Lundqvist's dispersion law are recaptured. And though it was not intended to define a new switching function, one can be inferred from the above equation, taking the form of an inverted Lorentzian, $h_{\mathrm{DF09}}(y) = 1 - 1/(1+\beta y^2)$, as opposed to the Gaussian form used in vdW-DF1.

In addition to their change to ω_q, Vydrov and van Voorhis also use a simplified form of

$S_{\mathbf{q},\mathbf{q}}$, taking

$$S^{\mathrm{DF09}}_{\mathbf{q},\mathbf{q}'} = \int d\mathbf{r}\, e^{-i(\mathbf{q}-\mathbf{q}')\cdot\mathbf{r}}\, \frac{4\pi n e^2/m}{\frac{1}{4}[\omega_{q'}(\mathbf{r}) + \omega_q(\mathbf{r})]^2 - \omega^2}. \tag{6.6}$$

Though only accounting for a single pole at the average of two plasmon frequencies, this propagator function can be shown to satisfy each of the four exact constraints laid out by Dion and coworkers. There is a numerical advantage to using this form as well. When evaluating Eq. 6.1, the traditional method is to construct a lookup table as the kernel, with numerical integrations for many possible combinations of $n(\mathbf{r})$ and $n(\mathbf{r}')$. But with Vydrov and van Voorhis' simplified $S_{\mathbf{q},\mathbf{q}'}$, one half of this integral can be performed analytically, greatly simplifying the evaluation of the energy. They also demonstrate, using some selected dimers for example, that vdW-DF09 shows accuracy that is comparable to or better than vdW-DF1.

Soon after publishing their vdW-DF09 paper, Vydrov and van Voorhis developed a second nonlocal density functional in a paper titled "Nonlocal van der Waals Density Functional Made Simple" [32]. The primary design principle for this functional, named VV09, targets a particular weakness of vdW-DF1's design, which is its poor recapturing of C6 coefficients. To obtain proper coefficients, Vydrov and van Voorhis begin by defining $S_{\mathbf{q},\mathbf{q}}$ in the long-range limit of $q = q' = 0$ and then extrapolating to higher values. They begin with a model for $\epsilon(\omega)$ in this limit, citing the work of Levine and Louie [152], which is

$$\epsilon(\omega) = 1 + \frac{\omega_p^2}{\omega_g^2 - \omega^2}, \tag{6.7}$$

where $\omega_p = \sqrt{4\pi n e^2/m}$ and $\hbar\omega_g$ is a band gap. The original vdW-DF1 paper defines the plasmon propagator function as $S \equiv 1 - 1/\epsilon(\omega)$. This leads Vydrov and van Voorhis to define the long-range limit of the plasmon propagator function as

$$S_0(iu) = \int d\mathbf{r}\, \frac{\omega_p^2(\mathbf{r})}{\omega_p^2(\mathbf{r})/3 + \omega_g^2(\mathbf{r}) + u^2}, \tag{6.8}$$

where the band gap frequency ω_g is given by $C\frac{\hbar^2}{m^2}|\nabla n(\mathbf{r})/n(\mathbf{r})|^4$ [153]. The coefficient C is a variational parameter, used to obtain the most accurate C6 coefficients for a range of systems. To generalize S_0 for all q and q', the authors arrive at the following form through

trial and error:

$$S^{\mathrm{VV09}}_{\mathbf{q},\mathbf{q}'}(iu) = \int d\mathbf{r}\, \frac{\omega_p^2(\mathbf{r})}{\omega_p^2(\mathbf{r})/3 + \omega_g^2(\mathbf{r}) + u^2} \exp\left[-\frac{q^2 + q'^2}{k_s^2 \phi^2} \right], \tag{6.9}$$

where k_s is the Thomas-Fermi screening vector $\sqrt{4k_F/\pi a_0}$ and ϕ is a spin scaling factor, given as

$$\phi = \frac{1}{2}\left[\left(1 + \frac{n_\uparrow - n_\downarrow}{n}\right)^{2/3} + \left(1 - \frac{n_\uparrow - n_\downarrow}{n}\right)^{2/3} \right]. \tag{6.10}$$

Vydrov and van Voorhis explain the primary benefit of this new $S_{\mathbf{q},\mathbf{q}}$, that by focusing on the $q = q' = 0$ limit, they ensure that $\Phi(\mathbf{r}, \mathbf{r}')$ does not diverge in the limit of $|\mathbf{r} - \mathbf{r}'| \to 0$, as vdW-DF1 does. However, this form of $S_{\mathbf{q},\mathbf{q}}$ also came with a shortcoming: it violated one of the physical constraints of vdW-DF1, being non-charge conserving in the high-q limit. This can be seen in the fact that the auxiliary function of q and q' is non-frequency-dependent, such that it applies a spurious factor of $F_q = \exp\left(-Cq^2\right)$ to the number of electrons N, where instead there should be unity [154].

To amend this shortcoming of the VV09 functional, Vydrov and van Voorhis developed a successor, VV10, in the article "Nonlocal van der Waals density functional: The simpler the better". For this functional, they abandon the formalism of vdW-DF1—and the use of a plasmon propagator S—by instead proposing a simple ansatz for the interaction kernel:

$$\Phi(\mathbf{r}, \mathbf{r}')^{\mathrm{VV10}} = \frac{3e^4}{2m^2 g g'(g + g')}, \tag{6.11}$$

where g is defined as

$$g = \sqrt{\omega_g^2(\mathbf{r}) + \frac{\omega_p^2(\mathbf{r})}{3}} |\mathbf{r} - \mathbf{r}'|^2 + b \frac{3\pi\hbar^2}{2em^{3/2}} \left(\frac{n(\mathbf{r})}{9\pi} \right)^{1/6}. \tag{6.12}$$

and likewise for g'. In this equation, ω_p and ω_g retain the same definitions as in VV09, and b is an adjustable parameter that controls the short-range damping of the R^{-6} asymptote. The authors go on to state that this kernel has a long-range limit (i.e. $|\mathbf{r} - \mathbf{r}'| \to \infty$) of

$$\Phi \to \frac{3e^2}{2m^2 \omega_0(\mathbf{r}) \omega_0(\mathbf{r}') [\omega_0(\mathbf{r}) + \omega_0(\mathbf{r}')] |\mathbf{r} - \mathbf{r}'|^6},$$

which is identical to the long-range behavior of VV09. It is also constrained such that in the *short-range* limit, Φ is proportional to $-A + B|\mathbf{r} - \mathbf{r}'|^2$, in line with the theoretical findings of Ref. [155].

6.2 New Developments and a Path Forward

The innovations made by Vydrov and van Voorhis in the development of these three functionals is illustrative of the flexibility of the plasmon pole model and its applications towards the nonlocal correlation. While vdW-DF3 achieved significantly improved accuracy through an alternative form of the switching function, there remain many other avenues to explore. The functional vdW-DF09 demonstrates an ability to choose the form of ω_q, without any strict need to define an $h(y)$. It also, along with VV09, reveals a certain amount of freedom in the choice of $S_{\mathbf{q},\mathbf{q}'}$. And VV10 provides an example in which the homogeneous limits of the plasmon pole model can be used as a basis for a greatly simplified functional, yielding high accuracy at comparatively low computational cost.

For the development of a new nonlocal correlation functional, another property that is of interest is the contribution of S to the gradient correction. In the limit of slowly varying electron density, one can calculate the second order gradient coefficient of the nonlocal correlation as

$$\mu_{\mathrm{nl}} = -\frac{4}{27}\left(\frac{k_F}{\pi}\right)^4 \int_0^\infty du \int_0^\infty dq \left|\frac{\delta S_{\mathrm{uni}}}{\delta n}\right|^2, \tag{6.13}$$

where S_{uni} is the uniform density limit of $S_{\mathbf{q},\mathbf{q}}$. Conveniently, despite the different forms of $S_{\mathbf{q},\mathbf{q}}$ used by vdW-DF1 and vdW-DF09, both possess similar forms of $S_{\mathrm{uni}} = \omega_p^2/(\omega_q^2 + u^2)$, differing only in their definitions of ω_q. The chosen form of the plasmon dispersion law is thus the deciding factor in calculating μ_{nl}. And while not taken as an exact constraint in vdW-DF1, it is desireable that the gradient correction coefficient be constant in the high density limit, as the system becomes more similar to a homogeneous electron gas. This is, in fact, not the case for either vdW-DF1 *or* vdW-DF09. With their respective forms of ω_q,

it can be shown that Eq. 6.13 evaluates as

$$\mu_{\mathrm{nl}}^{\mathrm{DF1}} \approx -\frac{4}{27}\left(\frac{k_F}{\pi}\right)^4 \frac{14.9}{n^2} \approx -\frac{0.451}{n^{2/3}} \approx \frac{C_{\mathrm{DF1}}}{k_F^2}, \tag{6.14}$$

$$\mu_{\mathrm{nl}}^{\mathrm{DF09}} = -\frac{4}{27}\left(\frac{k_F}{\pi}\right)^4 \left[\sqrt{\frac{3}{2}}\left(\frac{31}{16}\right)\frac{\pi^4}{k_F^5}\right] = \frac{C_{\mathrm{DF09}}}{k_F}, \tag{6.15}$$

where C_{DF1} and C_{DF09} are constants, and k_F is the Fermi wavevector, which is proportional to $n(\mathbf{r})^{1/3}$. Importantly, this result shows that neither functional achieves the correct behavior in the slowly varying limit, although the coefficient of vdW-DF09 is less density-dependent. In developing vdW-DF09, Vydrov and van Voorhis also took additional steps to remove this spurious dependence, adding a fixed, artificial gradient correction to the energy:

$$E_{\mathrm{GC}} = \int d\mathbf{r} n(\mathbf{r}) \epsilon_{\mathrm{GC}} = \int d\mathbf{r} \frac{\kappa n(\mathbf{r})}{1 + \mu' s(\mathbf{r})^2/\kappa} - \kappa n(\mathbf{r}), \tag{6.16}$$

where the coefficient μ' is derived from μ_{nl} and κ is an empirical parameter which can be adjusted to make vdW-DF09 compatable with a particular semilocal exchange [144].

While the use of an E_{GC} term is a good workaround to the problem of a density-dependent μ_{nl}, it may also be instructive to calculate the gradient correction coefficient for different hypothetical forms of ω_q. The existing form proposed by vdW-DF09, for example, recaptures the exact q^2 and q^4 coefficients of Eq. 2.41. However, this comes at the cost of the q^0 term, which is left to carry an incorrect densitys dependence. This, in-turn, sacrifices accuracy in the uniform density limit, aka the long-range $q = 0$ case that later became the focal point of VV09 and VV10.

One could thus think of ω_q^{DF09} as being a *close-range* approximation to the analytical plasmon dispersion. By extension, one could then devise two alternatives: a *long-range* form which sacrifices the q^4 term for accurate q^2 and q^0, and an *outer* form which sacrifices the middle q^2 term for the sake of the q^0 and q^4 terms. Respectively, these can be written

as

$$\omega_q^{\text{long}} = \frac{\kappa}{4}\sqrt{\frac{k_F}{3\pi}}q^2 + 2\sqrt{\nu\pi n}, \tag{6.17}$$

$$\omega_q^{\text{outer}} = q^2/2 + 2\sqrt{\nu\pi n}, \tag{6.18}$$

where ν is a placeholder constant. In vdW-DF1, it is left equal to 1, but Vydrov and van Voorhis argue in favor of $\nu = 1/3$ in order to accurately reproduce the Clausius-Mossotti formula. In any case, if we take the same form of S_{uni} as either vdW-DF1 or vdW-DF09, then the gradient coefficient for both of these approximations may be calculated. They are

$$\mu_{\text{nl}}^{\text{long}} = -\frac{4}{27}\left(\frac{k_F}{\pi}\right)^4\left[\frac{49\pi^3(\nu n)^{4/3}}{256\cdot 3^{3/4}\sqrt{2}\nu^2 k_F^{1/4}n^2}\right] = C_{\text{far}}\frac{n^{7/12}}{\nu^{2/3}}, \tag{6.19}$$

$$\mu_{\text{nl}}^{\text{outer}} = -\frac{4}{27}\left(\frac{k_F}{\pi}\right)^4\left[\frac{79\pi^{11/4}(\nu n)^{3/4}}{2048\nu^2 n^2}\right] = C_{\text{outer}}\frac{n^{1/12}}{\nu^{5/4}}. \tag{6.20}$$

A few interesting results arise from this calculation. First is that both approximations yield coefficients that are directly proportional to the density, with the long-range approximation being particularly strongly dependent. This could serve as a reasonable indication that the purely long-range limit is not very suitable for use in a new functional. The outer-limit approximation, however, yields the smallest density dependence of all μ_{nl}'s yet found.

As final exercise, it is also useful to find out what possible form of ω_q could yield the correct slowly-varying density behavior of a completely constant μ_{nl}. That the close-range and outer-limit approximations yield an inverse and direct density dependence, respectively, implies the existence of a plasmon dispersion law in between that would yield no dependence. We now define a general form of the plasmon dispersion,

$$\omega_q^{\text{general}} = q^2/2 + \nu n^{\alpha}, \tag{6.21}$$

which in any case preserves the correct q^4 behavior when squared. One can then calculate μ_{nl} as a function of the density dependence α, which is

$$\mu_{\text{nl}}^{\text{general}} = -\frac{4}{27}\left(\frac{k_F}{\pi}\right)^4\left[\frac{(96+5\alpha(35\alpha-48))n^{-5\alpha/2}\pi^4}{64\sqrt{2}\nu^{5/2}}\right] = c_{\text{general}}\frac{n^{(4/3-5\alpha/2)}}{\nu^{5/2}}. \tag{6.22}$$

Thus it becomes clear that μ_{nl} becomes constant for $\alpha = 8/15$, quite close to the value of $1/2$ that is used in the outer-limit approximation.

The physical meaning behind this derived form ω_q remains unknown. It is, however, intriguing that it so closely captures the uniform density limit as VV09 and VV10 were intended to do. Further testing on a suitable benchmark system, such as a noble gas dimer, will provide valuable insight into the potential use of these approximations.

Chapter 7

Effect of Entropic Constraints on the Thermodynamics of Molecular Adsorption in Nano-Porous Materials

This chapter is a reprint of a published article with permission from Small, 2412312 (2025) [156]. Supporting Information for this chapter can be found at DOI: 10.1002/smll.202412312. I hold shared first-authorship on this paper, with contributions in the form of theory, calculations, writing, and editing.

7.1 Abstract

Gas separation is a critical industrial process that consumes a significant amount of energy due to the widely used techniques that are currently employed. Adsorptive materials—such as metal–organic frameworks—show promise as an energy-efficient alternative. Of particular current interest are novel, temperature-dependent separation processes in MOFs, such as the recently reported separation of ternary isomeric hydrocarbon mixtures within one-and-the-same material. However, the mechanisms of these highly desirable separations remain

poorly understood. Herein, through a combination of *ab initio* simulations and statistical mechanics, we show that the temperature dependence is the result of a constraint on the guest molecule's entropic degrees of freedom when loaded into the MOF, caused by the fortuitous tight fitting of the guest inside the pore. While our framework is applicable to all molecular adsorption in porous media, it is essential for the description of large molecules in small pores, which we demonstrate here using the separation of C6 isomers in CaMOF as a test case. Our developed framework and analysis not only reveal the reason why separation occurs, but it also predicts the temperatures at which it takes place, thus opening the door to newly designed MOFs with tailor-made precision.

7.2 Introduction

Gas separation within the context of fuel refinement is an immensely important industrial process, where branched alkanes are needed to increase the research octane number (RON) of a mixture [157]. Unfortunately, separating certain isomers is a challenging task due to their similar sizes and properties, and currently used methods such as distillation and cryogenics are very energy intensive [158, 159]. A promising alternative is to use porous materials such as metal–organic frameworks (MOFs), whose high volume-to-surface-area ratios yield extraordinary adsorption properties [160, 161]. Recently, MOFs for the specific application of separating mono- and di-branched isomers have also been reported [162–164]. Most interestingly, some of these studies involve the use of temperature to separate binary and even ternary mixtures, making such MOFs a highly desirable candidate for industrial use [141, 165–169]. Unfortunately, the underlying mechanism behind this temperature-dependent separation remains poorly understood, slowing progress toward the synthesis of new and im-proved MOF materials.

In most cases, studies of temperature-dependent sieving involve MOFs with pore size comparable to their respective guest molecules [141, 157, 162, 170, 171]. This detail is especially important for the separation of isomers and other molecules of similar size and weight. A well-researched example is the separation of C6 alkanes, where the larger, di-branched 2,2-dimethylbutane (22DMB) may be effectively excluded from loading at temperatures lower than either of the smaller mono-branched 3-methylpentane (3MP) or linear n-hexane (nHex) [167].

A vital aspect of such separations that is sometimes overlooked is the change in free energy for guest molecules upon adsorption. Such analyses may focus on enthalpic and entropic contributions to the free energy, providing important insights into adsorption dynamics [172–175]. The free energy difference, which depends on the partition function of the overall mixture, also includes contributions from the adsorbate and empty activated structure. The available energy states, and thus the partition function, change depending on whether a molecule is freely moving in the gas phase or confined within the MOF. In the gas phase all possible degrees of freedom are assumed to be allowed for the molecule.

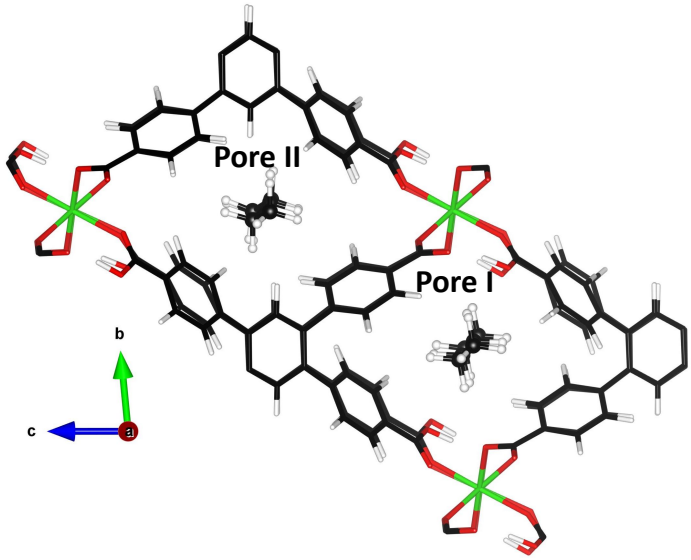

Figure 7.1: $2 \times 1 \times 1$ supercell of CaMOF with full loading shown here for the case of nHex, i.e. Pore I and Pore II are occupied. Note the orientation of the tcpb linker's central benzene ring, with terminal hydrogens pointing into Pore II, which makes the two pores chemically distinct.

Inside the MOF, however, space is limited, thereby reducing or outright eliminating contributions from certain degrees of freedom to the free energy. We refer to this phenomenon as "entropic constraint", because it manifests as a limitation on the number of microstates allowed to each guest molecule, and here we develop a complete theoretical framework for its description. This entropic constraint becomes most relevant in cases where a MOF's pores are comparable in size to a guest molecule's cross-section, as we show here using the case of C6 isomers (nHex, 3MP, 22DMB) in the microporous material Ca(H_2tcpb) (tcpb = 1,2,4,5- tetrakis(4-carboxyphenyl)-benzene), which we will refer to as "CaMOF" [167]. CaMOF, shown in Fig. 7.1, shows intriguing temperature-dependent separation of ternary mixtures of these C6 isomers. During this separation, 22DMB is effectively excluded from CaMOF at temperatures above 60 °C, 3MP is excluded at temperatures above 120 °C, and nHex remains loaded even up to 150 °C. Until now, the mechanism behind this complex adsorptive behavior of CaMOF was unknown. Here, we find that the entropic constraint precisely predicts the temperature dependent sieving of these isomers, and thus reveals the underlying mechanism for this tantalizing phenomenon. By understanding the mechanism

behind this temperature-dependent separation in MOFs, it becomes possible to accurately predict the favorability of loading for materials under given conditions and thus design new MOFs with precise temperature control of gas-mixture separation.

We note that (variable-cell) molecular dynamics simulations can also provide valuable insight into the temperature-dependent adsorption/desorption of guest molecules in MOFs [176]. However, such calculations are significantly more demanding—in particular for systems with a soft axis like CaMOF—compared to the entropic constraint principle we showcase here, which only requires ground-state calculations and the vibrational spectra.

7.3 Methods

All *ab initio* calculations were performed with VASP using plane waves and standard projected augmented wave (PAW) pseudopotentials [177]. The kinetic-energy cutoff was set to 600 eV, and its convergence was tested against higher values, which resulted in binding energy differences of less than 0.1%. The SCF convergence criterion was set to 10^{-6} eV. To capture long-range van der Waals forces, we employed the nonlocal vdW-DF3-opt1 functional [11]. A supercell of $2 \times 1 \times 1$ was constructed, containing 126 atoms, for which a $2 \times 2 \times 2$ k-point sampling was found to produce converged binding energies and vibrational contribution to the free energy to within 10 meV. The extended supercell was necessary to accommodate all guest molecules, which would not fit in the conventional unit cell. All supercell parameters and atomic positions were optimized until the forces on all atoms were smaller than 1 meV/Å. Note that the optimization of this system is challenging in that it has one axis (the b-axis) that is significantly softer than the other two [178]. Thus, a Pulay stress was calculated from differences in the stress between 600 eV and 1200 eV kinetic-energy cutoff calculations, and a correction value of -1.17 kBar was found. Despite its very small value, the Pulay stress has a noticeable effect on the soft b-axis. The configurational space is sampled with a thermal annealing method as discussed in Ref. [179]. The rotation of C6 alkanes within CaMOF was investigated with the help of a transition-state search algorithm, i.e. the climbing-image nudged elastic band (c-NEB) method [180, 181]. Moments of inertia for the guest molecules were calculated according to their standard tensor

definition with respect to the molecule's center of mass. The resulting tensor was then diagonalized to give the main axes momenta. Phonons were calculated using density functional perturbation theory, and Young's moduli were found through finite differences.

7.4 Review of Structure and Binding Energies

We begin with a review of the structural properties of the empty CaMOF. Our optimized lattice parameters of $a = 10.268$ Å, $b = 10.164$ Å, and $c = 15.011$ Å are compared to experimental values in Table S1 in the SI of Ref. [156]. This structure consists of two similar yet distinct pores (denoted as I and II, see Fig. 7.1), and we study adsorption in both. Binding energies for all combinations of guest and pore type are given in Table 7.1.

An important property of CaMOF is its flexibility, particularly the b-axis, which has been shown in prior investigation to extend up to 10% at a cost of 0.25 eV [178]. The relative flexibility is further assessed by calculating Young's moduli: Along the crystallographic a and c directions we find 23.2 and 77.8 GPa, respectively. In contrast, the Young's modulus along the b axis is as small as 9.0 GPa, revealing a high degree flexibility along this direction. For loaded CaMOF, various degrees of stretching of the b axis are also calculated. Small contractions of the a and c axes, which help facilitate the extension of the b axis, are also observed. All structural changes upon loading are gathered in Table S1 in the SI of Ref. [156].

Initially, it was postulated that these properties of CaMOF's structure might explain its temperature-dependent adsorption [167]. Its flexibility was thought to enable structural breathing (gate opening) at higher temperatures. While such gate opening phenomena are well-documented in other MOFs [179, 182–185], however, we did not observe any significant structural transformation and/or gate opening during the loading of any of the alkanes in CaMOF. Neither did the PXRD patterns show any appreciable change in structure as a function of temperature [167]. The intriguing temperature dependent uptake of CaMOF is thus not the result of any structural changes in the MOF itself and requires a different explanation.

Table 7.1: Binding energies (E_b) in units of eV for various C6 alkanes within Pore I and Pore II of CaMOF. Values are calculated for the loading of one guest molecule in one pore with the other pore left vacant.

	nHex	3MP	22DMB
Pore I E_b	−1.207	−0.951	−0.621
Pore II E_b	−1.023	−0.902	−0.638
average E_b	−1.115	−0.927	−0.629

7.5 Results and Discussion

7.5.1 Helmholtz Binding Free Energy

To uncover the cause of the temperature-dependent uptake in CaMOF, we examine the dynamics of the free energy in detail. At a given temperature, nHex, 3MP, and 22DMB all have different Helmholtz free energies depending on whether they are "free" in the gas phase or adsorbed and confined within the MOF. For adsorption to be favorable, the difference between these free energies must be overcome by the molecule's binding energy within the MOF. Below, we provide a framework to calculate the free energy difference, consisting mostly of text-book knowledge and equations [186–190], but to our knowledge it has not been assembled in this way and been applied to the loading of guest molecules in MOFs.

The Helmholtz free energy is defined as:

$$F \equiv U - TS \,, \tag{7.1}$$

where U, T, and S represent lattice internal energy, temperature, and entropy, respectively. This can also be rewritten as

$$F = -k_B T \ln(Z), \tag{7.2}$$

where Z is the partition function. The total partition function is the product of electronic, translational, rotational, and vibrational components, each of which vary based on whether the molecule is adsorbed or in the gas phase, leading to Z^{ads} and Z^{gas} and, in turn, to F^{ads} and F^{gas}.

The electronic partition function simply concerns the ground-state energies of the MOF

and molecule. We may write it as

$$Z_{elec} = \exp\left(-\frac{E_b}{k_B T}\right), \tag{7.3}$$

where E_b is the binding energy, taken from the average in Table 7.1. For a gas-phase molecule, E_b is assumed to be zero, indicating negligible intermolecular interaction, and Z_{elec}^{gas} thus equals 1. But for an adsorbed molecule, $E_b < 0$, indicating favorable binding to the MOF. When calculating F_{elec}^{ads}, the T-dependence of Eq. 7.3 is eliminated, and the total F is merely shifted by a constant E_b.

The translational partition function for the gas phase can be written as (approximating the sum as an integral):

$$Z_{trans}^{gas} = \left[\int_0^\infty \exp\left(-\frac{1}{k_B T}\ \frac{\pi^2 \hbar^2 n^2}{2ma^2}\right) dn\right]^3, \tag{7.4}$$

which sums over all possible states of the quantum mechanical "particle in a box". Here, m represents the mass of the alkane hydrocarbons (C_6H_14). The integral is evaluated as

$$Z_{trans}^{gas} = \ a^3\ \left(\frac{m\ k_B T}{2\pi\ \hbar^2}\right)^{3/2}, \tag{7.5}$$

where a^3 represents the volume of the fictitious "box" containing the molecule and can be approximated from the ideal gas law as

$$a^3 \equiv V/N = \frac{k_B T}{p}, \tag{7.6}$$

where p is the pressure of the gas. This gives us the gas-phase partition function Z_{trans}^{gas} as a function of T and p:

$$Z_{trans}^{gas} = \frac{(k_B T)^{5/2}}{p}\left(\frac{m}{2\pi\hbar^2}\right)^{3/2}. \tag{7.7}$$

Note that nHex, 3MP, and 22DMB all have the same mass, so this term does not contribute any differences between their free energies. It is however still necessary for determining accurate exclusion temperatures. For the partition function of the adsorbed molecule inside the MOF, the small translations allowed within CaMOF are captured through the partition

function of the phonon modes described below. To avoid double counting, we thus do not explicitly calculate a Z_{trans}^{ads} term for uninhibited translation of the adsorbed molecule.

For the rotational contributions to the free energy in the gas phase we treat each molecule classically as a rigid asymmetric top, taking the rotational partition function to be

$$Z_{rot}^{gas} = \frac{\sqrt{\pi}}{\sigma}\left(\frac{8\pi^2 k_B T}{h^2}\right)^{3/2}\sqrt{I_A I_B I_C}, \tag{7.8}$$

where I_A, I_B, and I_C are the molecule's principal moments of inertia and σ is the molecule's rotational symmetry number [190]. 3MP and 22DMB are both rotationally asymmetric, yielding a symmetry number of 1. In contrast, nHex has a twofold rotational symmetry along one axis, giving it a symmetry number equal to 2. For the adsorbed molecules, CaMOF confines the C6 isomers to an extent that only partial rotations, i.e. rocking motions, are allowed. These rocking motions are captured through the partition function of the vibrational modes described below. Again, to avoid double counting, we do not explicitly calculate a Z_{rot}^{ads} term for uninhibited rotation of the adsorbed molecule.

Lastly, the vibrational component of the partition function may be calculated using the normal mode frequencies with the equation

$$Z_{vib} = \prod_{i=1}^{3N}\sum_{n=0}^{\infty}\exp\left[-\frac{\hbar\omega_i}{k_B T}(n+1/2)\right]. \tag{7.9}$$

Here, i indexes the normal modes, N is the number of atoms, and n is the principal quantum number for each mode's vibrational energy. The geometric sum over n can be evaluated explicitly, yielding

$$Z_{vib} = \prod_{i=1}^{3N}\exp\left(-\frac{\hbar\omega_i}{2k_B T}\right)\left[1-\exp\left(-\frac{\hbar\omega_i}{k_B T}\right)\right]^{-1}. \tag{7.10}$$

For the gas-phase system, only intramolecular vibrations of the individual molecule and empty MOF contribute to the partition function. For the adsorbed molecule, small translations and librations of the molecule within the pore are included among the normal modes, with the latter accounting for each guest's ability to turn within the pore. Note that these rotational modes approximate partial rotations as a harmonic oscillator with an infinitely

large barrier. In cases with a finite rotation barrier, this approximation is only valid for states below the barrier height. Our c-NEB rotation-barrier calculations reveal barriers no less than 300 meV for the three adsorbed guest species. At 150 °C (i.e., the maximum relevant temperature for separation in experiment) 99.97% of rocking-type vibrational states are occupied below this barrier height, validating the use of Eq. 7.10.

When the guest molecule is inside the MOF, it is subject to several entropic constraints such that fewer states are available to it than in the gas phase, raising its Helmholtz Free Energy at higher temperatures. Overall, adsorption is favorable if

$$F^{ads} < F^{gas}, \tag{7.11}$$

where F^{ads} and F^{gas} are the Helmholtz free energies of the adsorbed and gas-phase molecule, respectively. In Fig. 7.2 we plot $F^{gas} - F^{ads}$ for nHex, 3MP, and 22DMB in CaMOF, showing this favorability as a function of temperature. Positive values indicate that adsorption is more favorable than the gas phase, while negative values indicate that the gas phase is more favorable.

By analyzing the Helmholtz free energies of each isomer, we are—for the first time—given a tool that can parse both qualitative and quantitative properties of temperature-dependent uptake in MOFs. The favorability curves in Fig. 7.2 for each of the three isomers studied show excellent agreement with reported experimental values [167]. In experiments with nHex, uptake is observed for the full range of temperatures up to 150 °C, which is exactly what our calculation of the free energy predicts. On the other hand, experimentally 3MP shows limited uptake up to 90 °C, but is effectively excluded at 120 °C. Again, this behavior is well-replicated by our calculations, with the relative free energy crossing below 0 at approximately 75 °C. Experimentally, 22DMB adsorbs at 30 °C and is excluded at 60 °C and above. Here, the free energies predict a slightly shifted behavior where exclusion begins already below 30 °C. We attribute this slight shift to the structure of CaMOF, which is highly flexible [178]. The relatively large cross-sectional area of 22DMB requires some stretching of CaMOF's *b*-axis in order to accommodate it. This allows 22DMB to continue adsorbing up to higher temperatures than those predicted by free energy calculations, which

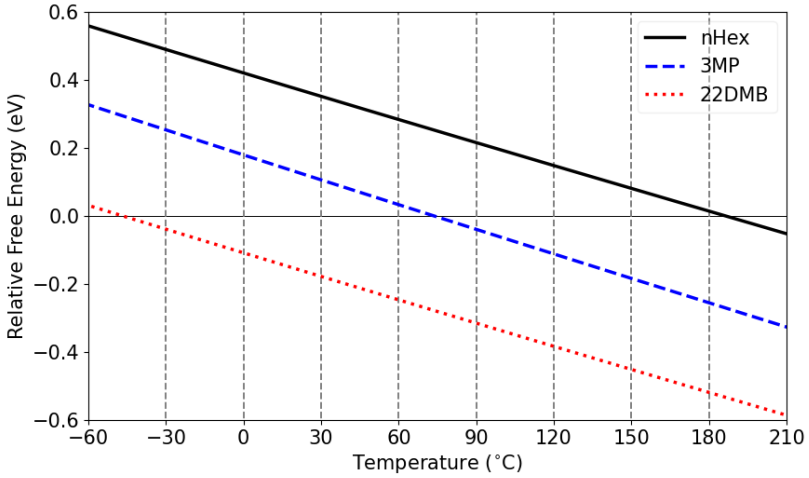

Figure 7.2: Relative free energies for nHex, 3MP, and 22DMB, defined as $F^{gas} - F^{ads}$. A positive free energy indicates that adsorption within the MOF is energetically favorable; negative, that adsorption is unfavorable.

do not fully account for the flexibility of the MOF. Over the temperature range of interest, the relative free energy curves in Fig. 7.2 can be well approximated as being linear in T, with some intercept and slope at 0 °C. All three molecules have different intercepts, resulting in a visible spacing of those three lines. These spacings are to a large extent determined by the binding energies of these molecules. The remainder is made up by the translational, rotational, and vibrational contributions. Considering that each component of the partition function makes up part of this spacing, their average contributions are 92% (binding energy), 0% (translational), 2% (rotational), and 6% (vibrational). Overall, the binding energies dominate the spacing; with rotational and vibrational contributions being approximately one order of magnitude smaller. For this reason, the binding energies in Fig. 7.2 are taken from the pore averages in Table 7.1, to remove as many cooperative effects in the binding as possible (in Fig. S1 in the SI of Ref. [156], we show an alternative plot of the relative free energy using binding energies of the fully loaded supercell). And as stated earlier, translational contributions make no difference in the spacing because our guest molecules are isomers with equal masses. Although the binding energies to a large extent determine the line spacings, they are temperature independent. Thus, the slopes in Fig. 7.2—and in turn each isomer's temperature of exclusion—are wholly due to the entropic constraint effects within the MOF. At 0 °C, this slope is −2.30 meV/K, −2.45 meV/K, and

−2.31 meV/K for nHex, 3MP, and 22DMB, respectively (approximately −2.35 meV/K on average). These can be calculated from the first derivatives of the three free energy components. For gas-phase translational contribution to the relative free energy in Fig. 7.2, this slope can be written as

$$\text{slope}_{trans} = -\frac{5}{2}k_B - k_B \ln\left[\frac{(k_B T_0)^{5/2}}{p}\left(\frac{m}{2\pi\hbar^2}\right)^{3/2}\right], \tag{7.12}$$

where $T_0 = 273.15$ K. With their equal masses and approximately equal saturation pressures, the translational component of the slope is approximately −1.84 meV/K for all three guest molecules.

Similarly, the rotational contribution to the relative free energy slope can be written as

$$\text{slope}_{rot} = -\frac{3}{2}k_B - \frac{1}{2}k_B \ln\left[\frac{\pi}{\sigma^2}\left(\frac{8\pi^2 k_B T_0}{h^2}\right)^3 I_A I_B I_C\right], \tag{7.13}$$

for which individual molecules will only differ due to their moments of inertia. For molecules of similar size, the resulting variation in slope is relatively small, e.g. the rotational component of the slope for nHex, 3MP, and 22DMB is −1.11 meV/K, −1.17 meV/K, and −1.16 meV/K, respectively.

The analytic expression for slope_{vib} is much more complex than Eqs. 7.12 and 7.13 due to each mode having an independent term, and thus we exclude it here for the sake of brevity. However, we can of course calculate the contributions to the relative free energy slope for nHex, 3MP, and 22DMB and find that they are 0.66 meV/K, 0.57 meV/K, and 0.69 meV/K, respectively. Not only is the variance in these values greater than that of the translational or rotational slopes, it is also important to note that the slope_{vib} is particularly sensitive to low frequency modes. For example, nHex's lowest mode inside the MOF has a frequency of around 21.1 cm^{-1}. By itself, this mode contributes 0.28 meV/K to the relative free energy slope at 0 °C. Small variations in these mode frequencies would therefore have a tangible impact on the molecule's temperature of exclusion.

All of our observations are in excellent agreement with the experimental isotherm measurements and explain the temperature-dependent separation performance of CaMOF. Our

analysis also shows that pore size and shape play a vital role in temperature-dependent adsorption, one that is at least equally as important as a guest molecule's binding energy. For this reason, CaMOF's unique ability to separate C6 isomers at low temperatures in a practical range is only made possible by the finely-tuned design of its pore size. If the pores were any larger, allowing for more free translations and librations of the adsorbed guest, the phonon modes of the loaded cell would be altered. If, in particular, the low frequency modes are impacted, it has a significant effect on the temperature dependence of the free energy, making tertiary separation of such a mixture more complicated. While the original creators of CaMOF tried to design its pores to be roughly comparable to the size of the guest molecule, we only now know that it was fortuitous that the pore size came out to allow for just the right amount of wiggle room and restricted molecular rotations such that the exclusion temperatures ended up in this favorable, industrially-relevant temperature range.

7.5.2 Simulated Loading Percentage

Calculating the partition functions involved in guest-MOF adsorption also allows us to directly simulate the temperature-dependent loading of the material. This may be done by calculating the total partition function of all guests within a closed system, and subsequently the average number of adsorbed guests per available MOF site. This calculation, which is carried out in detail in the SI of Ref. [156], yields an elegant description of CaMOF's loading percentage in terms of the adsorbed and gas-phase single-molecule partition functions (ζ^{ads} and ζ^{gas}):

$$P\,(\text{load}) = \frac{\zeta^{ads}}{\zeta^{ads} + \zeta^{gas}}. \tag{7.14}$$

Using the components of the partition functions as described in Eqs. 7.3–7.10, we plot loadings for each C6 guest molecule in CaMOF in Fig. 7.3. Our simulated loading curves are directly compared to experimental results from Ref. [167], where the authors report loading in mg/g. For nHex and 3MP, we consider the reported loadings at 30 °C to correspond to 100% loading in Fig. 7.3. Because 22DMB already shows limited uptake at 30 °C, we take its reported values relative to 3MP's maximum loading of 150 mg/g. At 30 °C, this

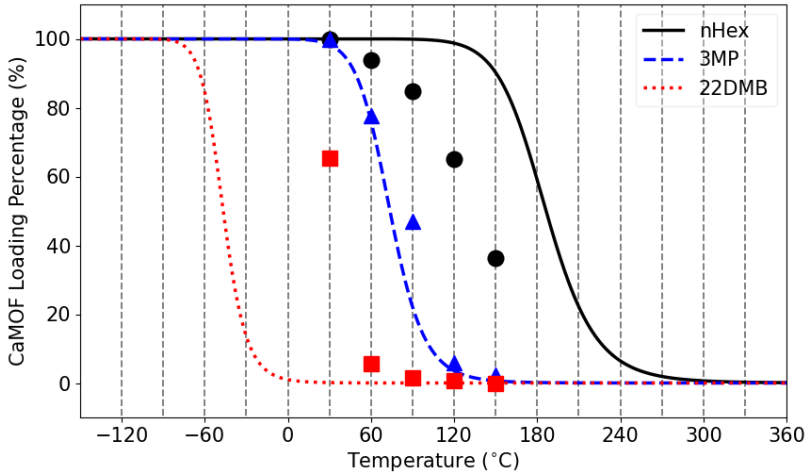

Figure 7.3: CaMOF loading percentage for nHex, 3MP, and 22DMB. Experimental isotherm measurements from Ref. [167]. are shown as points: nHex as black circles, 3MP as blue triangles, and 22DMB as red squares.

corresponds to approximately 65% loading within CaMOF. In Fig. 7.3, simulated loading correlates with the free energy curves shown in Fig. 7.2. When the relative free energy of a given guest molecule crosses 0 in Fig. 7.2, it indicates that the gas phase is just as favorable as adsorption, and thus corresponds to a loading of 50%. At this point, uptake decreases sharply as a function of temperature. In fact, this rate of decrease in loading is directly correlated to the relative free energy slope, which is discussed in the previous section. From Eq. S1 in the SI of Ref. [156], which rewrites Eq. 7.14 in terms of the molecule's relative free energy, we find that the temperature derivative of $P\,(load)$ near the equilibrium temperature is approximately

$$\frac{dP\,(\text{load})}{dT} \approx \frac{1}{4k_BT}\frac{d}{dT}(F^{gas} - F^{ads}). \tag{7.15}$$

Based on the average slope of the relative free energy, found to be around -2.35 meV/K, the decrease in loading near equilibrium can be approximated as $682/T_e$ percent per Kelvin—here, T_e is the equilibrium temperature for a given guest molecule in units of Kelvin, where $F^{gas}\,(T_e) = F^{ads}\,(T_e)$. In the case of C6 loading in CaMOF, this corresponds to a decrease of around $1009/T_e$ mg/g·K. Again, this behavior is in good agreement with experimental observations in Ref. [167]. For example, nHex loading in CaMOF was found to decrease by 44 mg/g between 120 and 150 °C, a rate of 1.47 mg/g·K. Assuming a T_e of around 135 °C, our

model would predict a decline of 2.5 mg/g·K. Our predicted T_e in Fig. 7.3 deviate somewhat from what is seen in experiment—although, overall, the trend and qualitative agreement is still excellent. As discussed in the previous section, this deviation is primarily due to differences in binding energy. In Fig. S2 in the SI of Ref. [156], we show loading percentage curves with binding energies fitted to experimental data, highlighting the accuracy of our predicted slopes. This analysis of the loading further shows that entropic constraints play a vital role in adsorptive separation. Without an adequate description of the temperature-dependence in the free energy, there is no practical way to predict when or how quickly a guest molecule is excluded from the MOF.

While the effect of entropic constraints is applicable to adsorption of all molecules in all MOFs, it plays a less important role when the molecules are not as tightly confined inside the pore. Looking at small molecule adsorption in large pores, such as H2, CO, CO2, NH3, H2O in e.g. MOF-74, MOF-5, or MIL-101, their pores put less constraint on the translational and rotational degrees of these small guest molecules [191–193]. Interesting design guidelines of novel MOFs follow and center around the capability to effectively limit (or eliminate) molecular translation, rotations, and/or vibrations. It also becomes conceivable to design pores that can separate molecules based on their differences in moment or inertia, as demonstrated by Eq. 7.13. Although not discussed in detail here, separation may also be possible through MOFs that effectively suppress vibrational motion upon molecular adsorption.

7.6 Conclusion

We have developed a theoretical framework to describe complex, temperature-dependent adsorption phenomena in porous systems. In particular, through *ab initio* modeling combined with statistical mechanics, we have identified the mechanism behind the temperature-dependent sieving of C6 isomers in CaMOF. We find that, although the MOF does not exhibit a significant structural change or gate-opening upon uptake, the tunable pore size and shape is vital in selectively separating nHex, 3MP, and 22DMB. By calculating the difference in free energies for the gas-phase and adsorbed molecules, we can accurately determine

the favorability of adsorption as a function of temperature, reproducing and explaining the experimentally observed adsorption behaviors of all three C6 isomers. We have found that the order in which nHex, 3MP, and 22DMB are excluded is largely due to their respective binding energies, but that the precise temperature ranges and rates of their exclusion are purely the result of their fortuitous tight-fitting within CaMOF. In this way, we show that the size and shape of the MOF's pore, by constraining a guest molecule's degrees of freedom, play a role that is equally important to the binding energy. Our findings provide an important tool for understanding and predicting temperature-dependent mechanism behind separations in MOFs, paving the way for more tunable frameworks to suit this purpose.

Chapter 8

THD-C Sheet: A Novel Nonbenzenoid Carbon Allotrope with Tetra-, Hexa-, and Dodeca-Membered Rings

This chapter is a reprint of a published article with permission from J. Phys. Chem. C 2024, 128, **26**, 10982 [194]. Supporting Information for this chapter can be found at DOI: 10.1021/acs.jpcc.4c01870. I am the first author on this paper, with contributions in the form of calculations, writing, and editing.

8.1 Abstract

We propose a novel two-dimensional carbon-based structure with tetra-, hexa-, and dodeca-membered rings, which we refer to by the abbreviated name, THD-C. The structure presents a mixture of sp–sp^2 hybridization and can potentially be synthesized by the topological assembly of 4-ethynyldiphenylacetylene molecules. By employing first-principles calculations, the stability and ease of synthesis of the sheet are investigated and compared with various C-allotropes. We predict its metallic behavior and excellent kinetic and dynamic stability.

Due to the crystal structure of the sheet, a strong mechanical anisotropy is observed. The effects of functionalization on the electronic properties of the material are also studied, and different semiconducting systems are obtained. The potential of THD-C for energy storage in metal-based batteries, hydrogen storage, and catalysis is also investigated, and we find a superior performance in comparison to graphite and other allotropes. The quantum confinement effect is investigated by constructing nanoribbons and nanotubes of various sizes. For ribbons, we find that tailor-made electronic and magnetic properties can be obtained and explored in potential spintronic devices. Additionally, we observe that nanotubes are conducting irrespective of their chirality and can potentially be used for capture, storage, and separation of industrially relevant small gas molecules.

8.2 Introduction

Carbon is the basic unit of life and one of the most abundant elements on earth. Due to the flexibility of the C–C bond, various C-allotropes are observed, ranging from $0D$ fullerene molecules, to $1D$ nanotubes, $3D$ graphite and diamond and, more recently, $2D$ graphene [195–198]. The so-called scotch tape exfoliation experiment for the isolation of graphene in 2004 was the first ever experimental realization of a $2D$ material [198]. Ever since, there has been rapid growth of the family of $2D$ materials, and the study of their properties and applications now represents a well-established field. Within the carbon family, numerous $2D$ allotropes were theoretically proposed and/or realized experimentally. These allotropes bear different electronic properties, ranging from semiconducting to semimetallic to metallic, and different crystal structures with various hybridizations.

Recently, C allotropes with mixed hybridization and/or non-benzenoid structures gained tremendous attention. A most prominent example is biphenylene, which has sp^2 hybridization and a non-benzenoid structure. This material was theoretically proposed more than a decade ago and has been successfully synthesized recently [199, 200]. The biphenylene sheet exhibits metallic behavior, anisotropic mechanical properties, and superior Li storage capacity [201]. Another sp^2 hybridized C allotrope is graphenylene, which has a small energy gap of 0.025 eV around the Fermi level and has the potential to be used as anode material for Li batteries [202, 203]. T-graphene, another allotrope, can adopt a planar or a buckled structure with high Fermi velocity and possesses Dirac-like character similar to graphene [204, 205]. Graphyne and graphdiyne present a mixed sp–sp^2 hybridization due to the presence of acetylenic bonds. They bear interesting electronic, catalytic, and sensing properties that were proposed and realized experimentally [206–208]. Additionally, mixed sp–sp^2 $3D$ networks of C allotropes with long acetylenic chains and/or phenyl rings were theoretically proposed [209] and have the potential to be used in energy storage and conversion applications [210]. More recently, another C allotrope—tolanene—with a mixed sp–sp^2 network with four, six, eight, and twelve-membered C rings has been theoretically proposed [211]. This material can potentially be synthesized from diphenylacetylene molecules. In such networks, the presence of acetylenic sites (sp bonds) usually result in

larger C rings that can successfully be utilized for the adsorption of alkali atoms in alkali-based batteries. Furthermore, these larger rings are suitable to accommodate bigger and heavier metal atoms (mostly transition atoms) to enhance the catalytic activity of such materials [206, 212, 213]. For the same reason, these materials hold promise to be investigated for the storage, capture, and separation of small gas molecules.

In that context, the separation of C_2 alkanes is critically important, as C_2H_4 is used as an important feedstock in the petrochemical industry [214–216]. The production of C_2H_4 is usually done by the decomposition of C_2H_6. Furthermore, trace amounts of C_2H_2 must be removed to get pure C_2H_4. Similarly, C_2H_2 has several industrially relevant applications, however, its production comes with the cost of CO_2 as a byproduct [217,218]. Unfortunately, the challenge in their separation lies in their similar sizes (C_2 alkanes and C_2H_2/CO_2). The commonly used distillation or cryogenic methods are energy-intensive and should be replaced with cost-efficient technologies. One potentially cost-effective method is adsorptive separation, in which gas capture/separation is driven by their thermodynamic or kinetic difference. Another valuable gas is CO, which is a reaction intermediate and used for the production of several important chemicals [219]. To address future energy demands without causing detrimental damage to the environment, the reduction of CO_2 to CO is a critical task, for which separative adsorption can also play a critical role. Finally, C capture is significantly important in the context of climate change, not only for capturing C from industry and air, but also for exploring alternatives to fossil fuels. Methane (CH_4), which is a major ingredient in natural gas, can be regarded as a cleaner and environmentally friendly gas with a significant promise for the replacement of fossil fuels [220–222]. However, CH_4 gas typically contains CO_2 as an impurity, which must be removed to get the desired benefits from CH_4. Therefore, the search for a potential material to realize the selective adsorption of these different gaseous molecules is of paramount interest.

In this work, we present a theoretical proposal for a novel $2D$ carbon allotrope, which we refer to by the abbreviation of its three ring types, THD-C. The structure can potentially be synthesized by the topological assembly of 4-ethynyldiphenylacetylene molecules, and consists of a mixed sp–sp^2 network with non-benzenoid carbon rings, similar to the recently proposed tolanene sheet (see Fig. 8.1) [211]. By employing first-principles calcula-

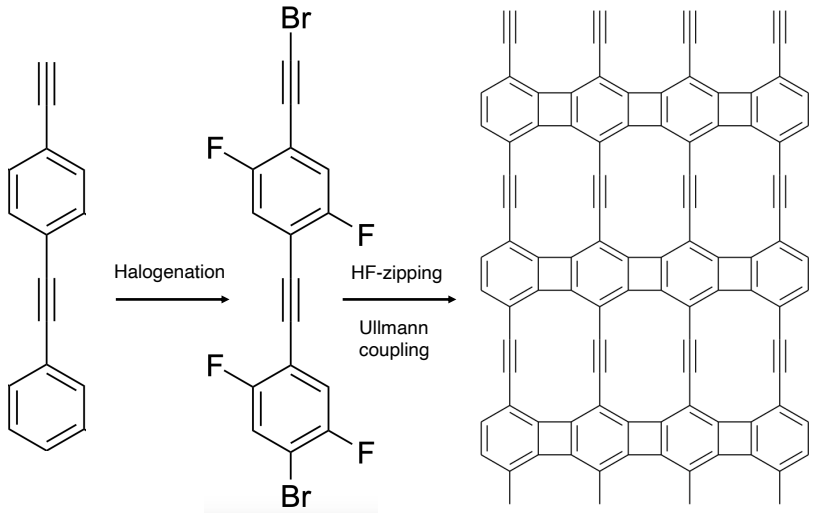

Figure 8.1: Proposed scheme for the synthesis of a THD-C sheet from 4-ethynyldiphenylacetylene molecules, following the scheme of Ref. [200]. The 4-ethynyldiphenylacetylene molecule (left) is halogenated (middle) and the THD-C sheet (right) may be produced through an on-surface interpolymer dehydrofluorination (HF-zipping) reaction.

tions, we investigate the structural, mechanical, electronic, and electrochemical properties of this material, as well as its stability and a possible synthesis route. The possibility of functionalization and its impact on the electronic properties is also discussed. We also study quasi-1D structures based on this sheet, such as nanoribbons and nanotubes, and discuss the effects of size and geometry on the electronic properties. Finally, we assess some potential applications, such as anode materials in metal-based batteries. We also examine the potential for gas storage, capture, and separation of industrially relevant small gas molecules. In doing so, we find great potential for the aforementioned C_2 separation, CO_2 capture, and H_2 storage within select sizes of THD-C nanotubes.

8.3 Methods

We use the Vienna Ab-initio Simulation Package (VASP) to carry out all *ab initio* calculations [4, 5, 177, 223]. The calculations were performed under the framework of a plane-wave (PW) basis sets with standard projected augmented wave (PAW) pseudopotentials (PP) [224,225]. A kinetic energy cutoff of 600 eV is found to be sufficient for well-converged

results. Van der Waals (vdW) interactions, which are relevant for multilayer geometries, were included using Grimme's DFT-D3 scheme [27]. The Brillouin Zone (BZ) was sampled with a $13 \times 9 \times 1$ Monkhorst-Pack k-point grid [226]. The ionic positions as well as the unit cell vectors were optimized until the forces on each atom were smaller than 0.001 eV/Å with an SCF accuracy of 10^{-8} eV. The effect of spurious interactions between periodic layers (along the non-periodic (z) direction) was mitigated by using a vacuum layer of 20 Å. We also employ Born-Oppenheimer (BO) *ab initio* molecular dynamic (AIMD) simulations to check the kinetic stability of the sheet. We use various temperatures, ranging from 300–3000 K with a time step of 1 fs—the total AIMD was 10 ps. The AIMD simulations were performed under a NVT ensemble, and the temperature was controlled by a Nose-Hoover thermostat. To confirm its dynamical stability, phonon dispersion calculations in a 4 × 2 × 1 supercell were carried out within a supercell approach with the help of the PHONOPY code [227]. A transition state search algorithm—the climbing image nudged elastic band (c-NEB) method—is used for studying the diffusion of guest-molecules [181]. Calculations for the hydrogen evolution reaction (HER) follow the procedure of Ref. [228].

8.4 Results

8.4.1 Structural Properties

Inspired by the recent synthesis of the biphenylene sheet [200], where DHTP molecules were used as building blocks through an on-surface interpolymer dehydrofluorination (HF-zipping) reaction, we propose that 4-ethynyldiphenylacetylene molecules can be assembled in a similar way, as shown in Fig. 8.1. The resulting structure forms a $2D$ periodic array of four-, six-, and twelve-membered C rings, hence we name it tetra-hexa-dodeca-carbon or, in short, THD-C. A similar strategy for the synthesis of tolanene, another nonbenzenoid carbon allotrope, was recently proposed by some of the authors of the present work [211]. The theoretical calculations revealed a formation energy quite close to that of biphenylene, thus indicating the feasibility of the synthesis. We discuss similar calculations below.

The unit cell of THD-C is shown in Fig. 8.2. The calculated lattice parameters are $a = 3.758(3)$ and $b = 7.115(8)$ Å and $\alpha = \beta = 90°$. We label the rings according to the

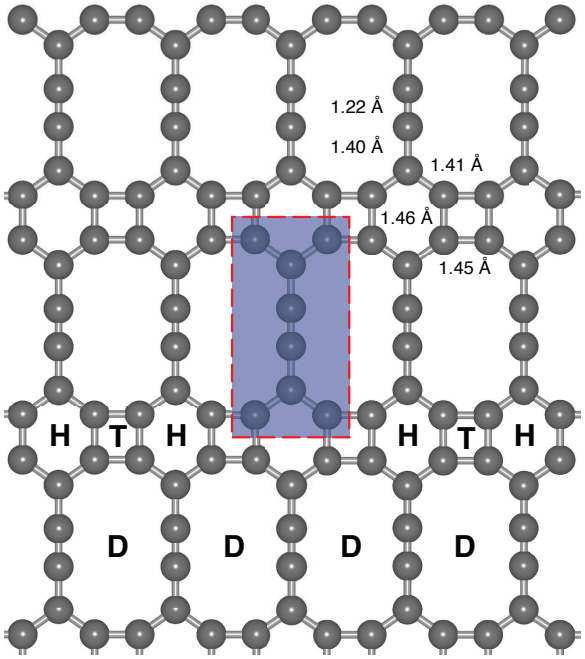

Figure 8.2: Single-layer structure of THD-C. The reduced cell is shown in gray. Lengths of each bond type are labeled in the top right. At the bottom, rings are labeled by their number of atoms (T = 4, H = 6, D = 12).

number of carbon atoms as tetra (T), hexa (H), and dodeca (D), as shown in the figure. The structure presents five non-equivalent C–C bonds and the corresponding lengths are shown in the figure. We can label them according to the neighboring rings as $d_{\mathrm{HT}} = 1.46$ Å, $d_{\mathrm{TD}} = 1.45$ Å and $d_{\mathrm{HD}} = 1.41$ Å. There are two bonds bridging adjacent D rings, which we label as $d_{\mathrm{sp^2}} = 1.40$ Åand $d_{\mathrm{sp}} = 1.22$ Å. The latter is much shorter than the other bonds and it can be regarded as a sp hybridized triple (acetylenic) bond, which is also characteristic of graphyne and its derivatives [140, 207, 208]. Therefore, the structure forms a mixed sp–$\mathrm{sp^2}$ hybridized lattice, in a similar fashion to tolanene [211].

The twelve-membered ring has a maximum diameter of 5.832 Å and can act as a potential site for the adsorption of alkali atoms and other small gases. The presence of this large ring makes THD-C quite suitable for applications as gas sensors and filters, giving it a competitive edge over other C-allotropes such as Me-graphene and biphenylene. We discuss these properties in more detail in Subsections 8.4.9 and 8.4.10.

8.4.2 Energetics and Stability

In order to estimate the strength of the structure, we calculate the cohesive energy as the difference between the energy of the sheet and the energy of isolated C atoms:

$$E_{\text{coh}} = (E_{\text{tot}} - nE_C)/n, \tag{8.1}$$

where E_{tot}, E_C, and n represents the total energy of a unit cell of the sheet, the energy of an isolated C atom, and the number of C atoms in the unit cell, respectively.

Using the above equation, the calculated cohesive energy of THD-C is -7.35 eV/atom, which is slightly higher than that of graphene (-8.00 eV/atom) and suggests an excellent stability of the sheet. In Fig. 8.3, we present a more complete comparison between the energetics of THD-C and various other C allotropes. All energies are calculated at the same level of theory. As we can see, THD-C presents a similar cohesive energy to that of graphyne and graphenylene, the latter of which is also composed of tetra-, hexa-, and dodeca-membered rings. The three structures also present comparable densities of carbon atoms, as shown in the top panel. However, unlike graphenylene, which possesses only sp^2 C atoms, THD-C and graphyne also contain acetylenic bonds. The degree of mixing between the two hybridizations can be estimated from the ratio between the number of sp hybridized atoms and the total number of atoms in the structure. A similar definition can be employed for mixed sp^2–sp^3 networks, as shown in the bottom panel of the figure. According to this estimate, the degree of mixing for THD-C is $2/8 = 25\%$, which is smaller than that of graphyne and graphdiyne.

Even though THD-C bears comparable stability with respect to other carbon allotropes, assessing the ease of experimental synthesis is a critical factor in checking whether the sheet can potentially be synthesized or not. To check the potential synthetic viability from the halogenated 4-ethynyldiphenylacetylene precursor, we use the following equation to evaluate its formation energy:

$$E_{\text{syn}} = (E_{\text{THD-C}} + E_{X_2} - E_{\text{precursor}})/n, \tag{8.2}$$

where $E_{\text{THD-C}}$, E_{X_2}, $E_{\text{precursor}}$, and n represent the total energy of a unit cell of the THD-C

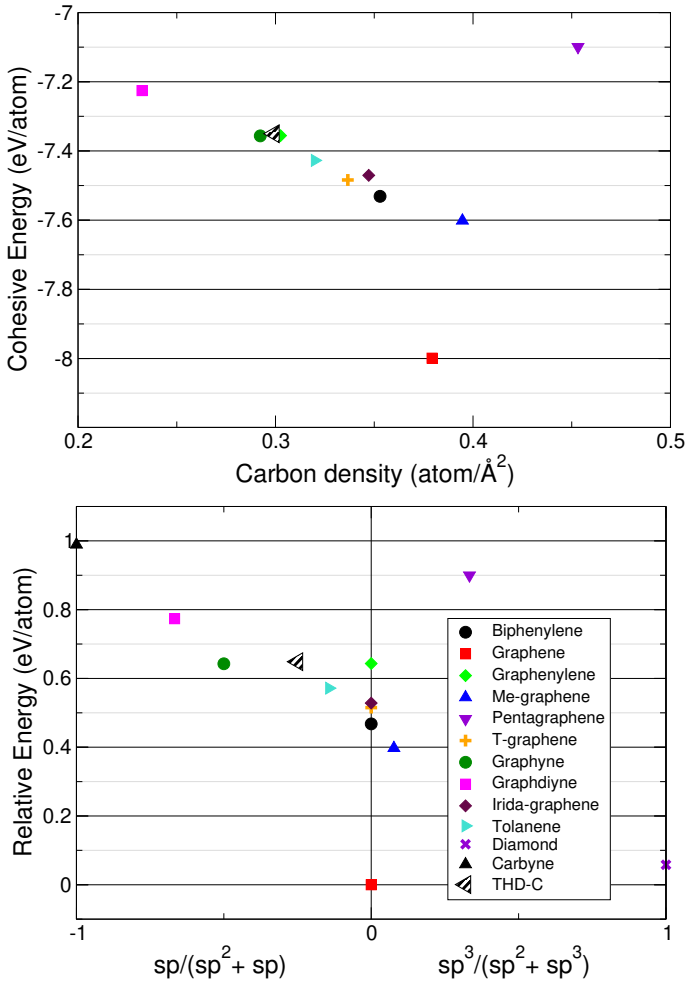

Figure 8.3: **Top**: Cohesive energy as a function of carbon atom density. **Bottom**: Relative cohesive energy (with respect to graphene) as a function of the fraction of sp hybridized (left) or sp^3 hybridized (right) carbon atoms in the structure of various C allotropes.

sheet, the total energy of isolated X_2 molecules (X = H, F, and Br), the total energy of the isolated halogenated 4-ethynyldiphenylacetylene molecule ($C_{16}H_4F_4Br_2$), and the number of C atoms in a unit cell of the THD-C sheet, respectively. Using the above equation, the synthetic formation energy of the THD-C sheet is calculated as 0.353 eV/atom. For comparison, we also calculate this energy for biphenylene and tolanene, at the same level of theory, and obtain 1.019 and 0.892 eV/atom, respectively. As such, the formation energy—i.e., the energy required to synthesize the structure—for THD-C is lower than both tolanene and biphenylene. Consequently, the synthetic procedure of THD-C sheet would have similar (or possibly fewer) challenges as those of biphenylene.

To further investigate the strength of this sheet, we calculate the electron localization function (ELF)—used to estimate the electron localization in a given system [229]. The points of interest are the three regions corresponding to a homogeneous electron gas (median or 0.5), a low electron density region (minimum or 0), and a high electron localization region (maximum or 1). From Fig. 8.4, it is clear that electrons are highly localized in between C atoms, indicating a strong covalent bond formation. Furthermore, sp–sp bonds (triple bonds) can clearly be distinguished from sp–sp^2 and sp^2–sp^2 bonds as there is a strong electronic localization between acetylenic sites, resulting in a π bond formation in the plane of the THD-C sheet. Additionally, simulated scanning tunneling microscopy (STM) images were obtained to assist future experiments on this material. Within the Tersoff-Hamann approximation [230], these images can be calculated by integrating the local density of states (LDOS) around the Fermi energy:

$$I(\mathbf{r}) \approx \int_{E_F}^{E_F+eV} \rho(\mathbf{r}, E)\, dE\ , \tag{8.3}$$

where E_F is the Fermi energy and $\rho(\mathbf{r}, E)$ is the LDOS, given by $\sum_i |\Psi_i(\mathbf{r})|^2 \delta(E - E_i)$ (the sum runs over all Kohn-Sham orbitals Ψ_i). The unoccupied or occupied electronic states around the Fermi level can be selected by employing negative or positive bias voltages V, respectively. The images shown in Fig. 8.4 were taken with bias voltages of ± 2.0 V and a constant height near the surface of the sheet. In particular, we see strong signatures near the acetylenic sites at negative bias voltages, which represent an out-of-plane π bond.

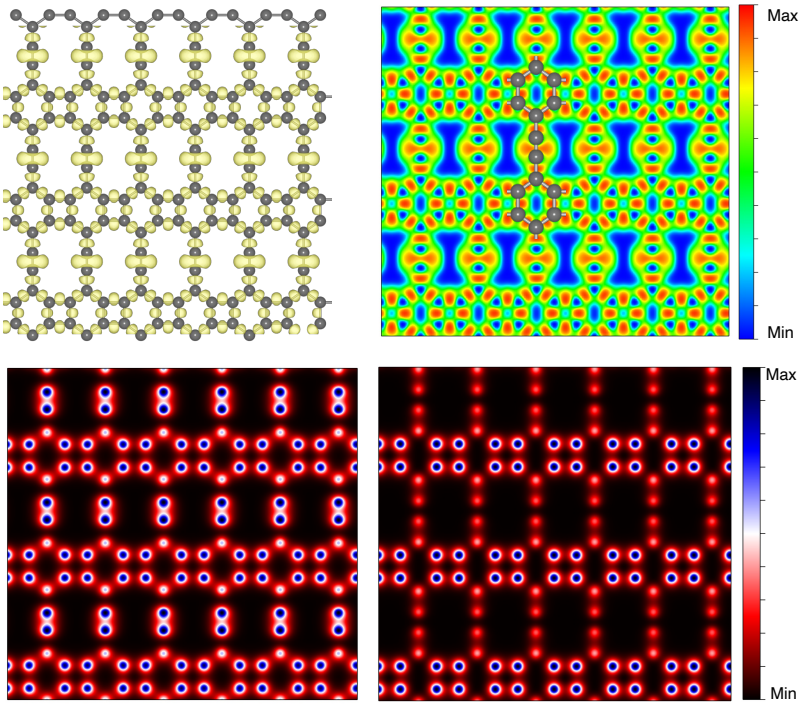

Figure 8.4: Electron localization function (top left) and its $2D$ cut in the plane of the sheet (top right). STM images with a bias voltage of -2.0 V (bottom left) and 2.0 V (bottom right).

8.4.3 Dynamic and Kinetic Stability

The strong nature of bonding in the THD-C sheet does not necessarily mean that the structure is a minimum over the potential energy surface. Hence, to find whether the structure can actually exist or not, we first calculate its phonon dispersion. As we can see in Fig. 8.5, this can be regarded as a stable structure due to the absence of imaginary modes, which would be related to structural instabilities. The phonon spectrum also shows a flat isolated mode around 66 THz (2222 cm^{-1}) which is coming from localized vibrations of the acetylenic bonds (see Fig. S23 in the SI of Ref. [194]). Such a mode is commonly found in other C allotropes that also contain triple bonds [211, 231]. Another low-dispersive mode appears around 48 THz (1636 cm^{-1}) which is the result of localized vibrations of all other C atoms in the sheet. This frequency is comparable to C structures without acetylenic sites, such as biphenylene and graphene [201].

Next, we study the kinetic stability of the structure by performing AIMD simulations under different temperatures. As we can see in Fig. 8.6, the calculations show that the

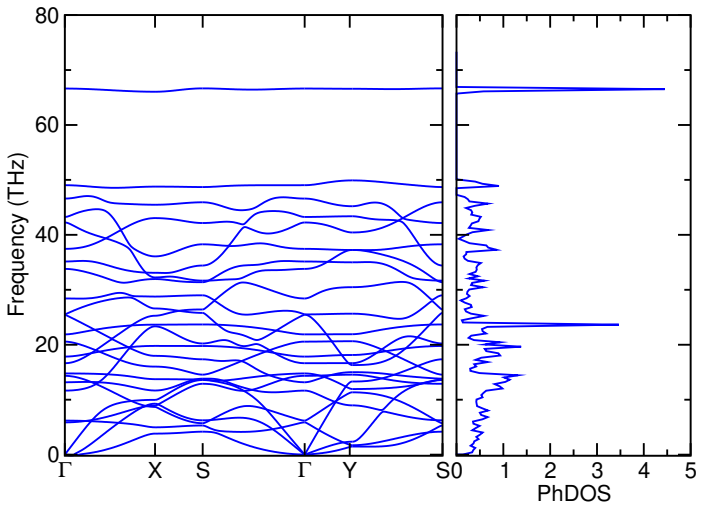

Figure 8.5: Phonon bandstructure (left) and the corresponding phonon density of states (right) of the THD-C sheet.

structure can be exposed to a temperature as high as 3273 K, which is in accordance with its excellent cohesive energy and strong covalent bonding. Such systems with a higher tolerance for temperature have many potential applications in high-temperature operating devices.

8.4.4 Mechanical Properties

The mechanical strength is another key aspect in assessing the performance of a material. To study the mechanical properties, we evaluate the energy-strain curves, extract the relevant elastic constants, and compare them with similar materials, such as biphenylene and tolanene. The data is gathered in Table S1 in the SI of Ref. [194]. For a $2D$ structure, the Young's modulus (E) and Poisson's ratio (ν) for deformations along an arbitrary axis in the ab plane can be calculated from the following expression:

$$E(\theta) = \frac{S_{12}}{C_{11}s^4 + [\frac{S_{12}}{C_{66}} - 2C_{12}]s^2c^2 + C_{12}c^4}, \tag{8.4}$$

$$\nu(\theta) = \frac{C_{12}s^4 + [C_{11} + C_{22} - \frac{S_{12}}{C_{66}}]s^2c^2 + C_{12}c^4}{C_{11}s^4 + [\frac{S_{12}}{C_{66}} - 2C_{12}]s^2c^2 + C_{12}c^4}, \tag{8.5}$$

where $S_{12} = C_{11}C_{22} - C_{12}^2$, $s = \sin\theta$, and $c = \cos\theta$. The polar angle θ is measured from the a (x) direction.

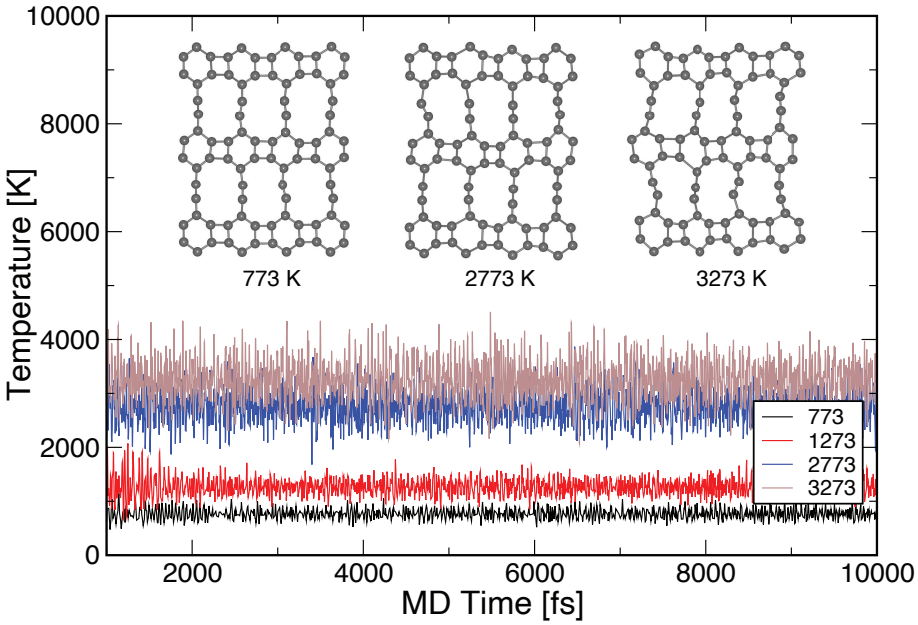

Figure 8.6: Kinetic stability of the THD-C sheet under various temperature ranges. The inset also shows the final geometry at the end of each AIMD simulation.

From our calculations, we have obtained $C_{11} = 170$, $C_{22} = 277$, $C_{12} = 76$ and $C_{66} = 13$ N/m. These values satisfy the criteria for mechanical stability—the Born–Huang stability criteria—of any $2D$ material, which are given by [232]:

$$C_{11} > 0, \quad C_{66} > 0, \quad C_{11}C_{22} > C_{12}^2 \, . \tag{8.6}$$

The corresponding polar maps for the Young's modulus and Poisson's ratio are shown in Fig. 8.7. Notice that a large anisotropy is observed in the mechanical properties, in a similar fashion to biphenylene and tolanene [200, 211]. This is a consequence of the crystal structure of the material. In particular, the presence of the acetylenic bonds results in a larger stiffness along the b (y) direction, while the Poisson ratio reaches its smallest values for uniaxial deformations along the a and b directions.

Our calculated values for E_x ($\theta = 0$) and E_y ($\theta = 90°$) are comparable to the reported values for biphenylene. The differences come from the introduction of the D sites and their acetylenic bonds in our structure, which result in a slightly larger value for E_y and a smaller value for E_x in the comparison. Our values are also quite comparable with tolanene, which

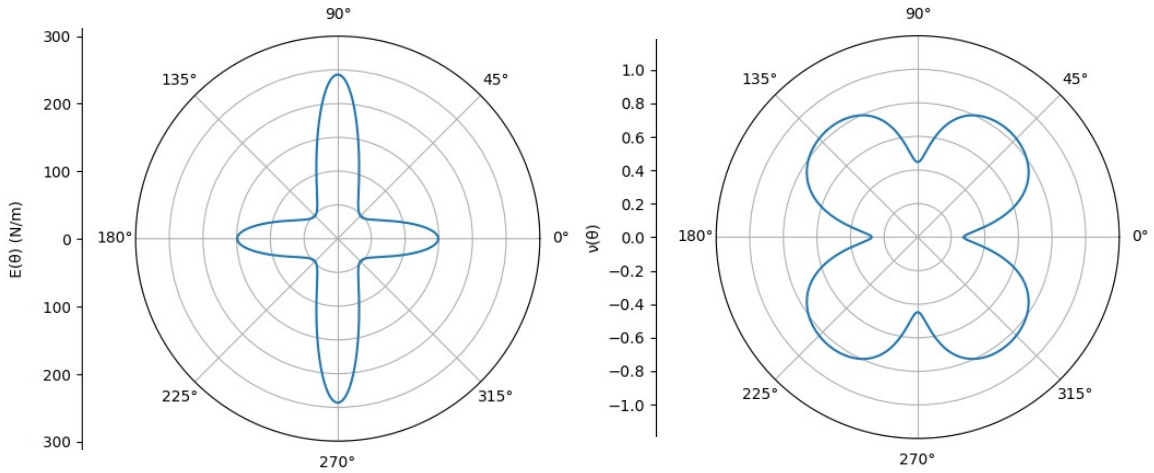

Figure 8.7: Polar angle dependence of the Young's Modulus (E) and Poisson's ratio (ν) for THD-C, showing strong anisotropy.

also contains the D sites. The small differences mainly result from the absence of the 8-membered rings in the present structure. Our calculated value for E_y is also comparable to hBN (275 N/m) and significantly larger than MoS_2 (123 N/m). It is also larger than that of graphenylene (216 N/m) [233] and graphyne (166 N/m) [234], thus showing the strength of this mixed sp–sp^2 network.

8.4.5 Graphite-Like Layered Structures

The possibility of forming a graphite-like layered structure by stacking THD-C layers is also considered. We consider several stacking configurations, including bilayers, trilayers, and their corresponding graphite-like bulk structures. The stability of these structures was assessed by evaluating their interlayer interaction energies (E_{II}), defined as

$$E_{II} = [-E_{\text{system}} + nE_{\text{sheet}}]/N, \tag{8.7}$$

where E_{system}, n and E_{sheet} represent, respectively, the total energy of a unit cell of the layered system, the number of layers in this cell, and the total energy of an isolated sheet. Finally, N is the number of atoms in the unit cell. Using this equation, we find that AA stacking is the most favorable configuration, as opposed to graphene in which AB stacking is preferred. Our results are consistent with a similar tolanene system, in which AA is

also energetically favored. Another close metastable configuration is the so-called AB3 configuration, for which the E_{II} is only 8.81 meV higher than the ground state (see Fig. S5 in the SI of Ref. [194]). The E_{II} of the most favorable bilayer (AA) and the graphite-like bulk THD-C are 18.9 and 19.8 meV/atom, respectively. At the same level of theory, the E_{II} of bilayer graphene and graphite are 21.7, and 25.5 meV/atom, respectively. In the most favorable configuration, the interlayer separation in the bilayer is 3.517 Å, which is slightly higher than the corresponding value in the graphite-like bulk form, which is 3.470 Å. For comparison, the interlayer distances in bilayer graphene and graphite are 3.455 Å, and 3.445 Å, respectively, at the same level of theory.

8.4.6 Electronic Properties

We have calculated the bandstructure and the **k**-resolved projected density of states for THD-C. The results are shown in Fig. 8.8. As we can see, the electronic behavior is metallic, as two bands cross the Fermi energy at several points in the first Brillouin zone. As expected, the low-energy bands around the Fermi energy are composed of p_z orbitals from the carbon atoms and, therefore, have a π character. The σ bands are seen at higher energies, which is consistent with the strength of the in-plane covalent bonds. A similar behavior is seen in graphene and other common $2D$ carbon allotropes. Interestingly, we see that one of the low energy bands is quite flat along the X-S high-symmetry line. By looking at the wavefunctions at these **k**-points (see Figs. S1–S3 in the SI of Ref. [194]). we see that this behavior results from an electronic localization around the b-axis, in which the electrons form $1D$ stripes along the chains defined by the T and H sites. A similar behavior is seen around 1.0 eV above the Fermi energy along the Y-Γ line and corresponds to a similar $1D$ localization pattern.

Another interesting feature of the bands is that a few Dirac-like tilted cones can be seen around the Fermi level, in a similar fashion to biphenylene and tolanene. Such Dirac-like cones may offer significantly fast transport for electrons. The corresponding Fermi velocities can be calculated from their slopes as

$$v_F = \frac{1}{\hbar}\frac{\partial E}{\partial k} \ , \tag{8.8}$$

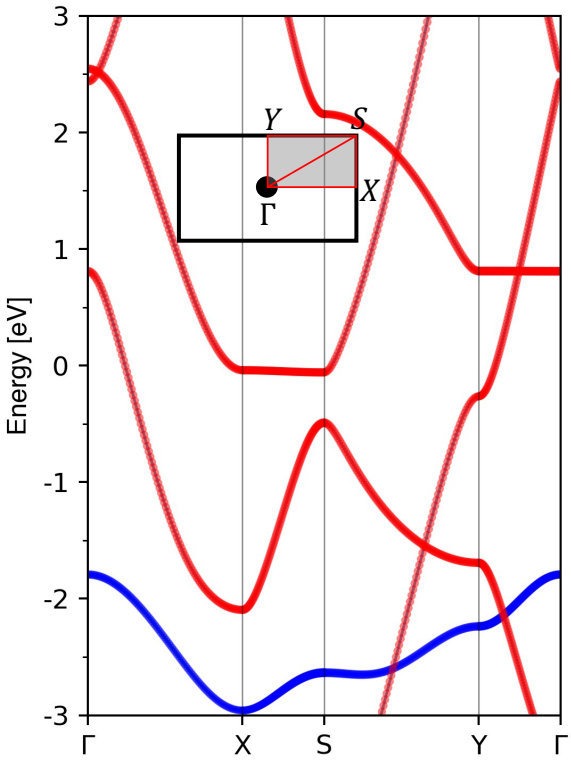

Figure 8.8: Electronic band structure of the THD-C sheet. The bands are colored according to contributions to the projected density of states (PDOS) coming from σ (blue) and π orbitals (red). The Fermi energy is set to zero.

where $\hbar$ is the reduced Planck's constant. For the non-flat portions of the bands, the calculated values for THD-C range from 0.842 to 0.875 $\times$ 10^6 m/s, which are quite comparable to graphene at the same level of theory [235, 236].

The lack of an energy gap around the Fermi level is a shortcoming for the THD-C sheet to be employed in nanoelectronic devices. However, it should be noted that this is the same limitation present in graphene, biphenylene, and other $2D$ metallic C allotropes. Therefore, the methods applied to all these $2D$ C allotropes to induce an energy gap could potentially be applied to THD-C. In particular, we discuss the possibility of functionalization below.

8.4.7 Functionalization

The possibility of functionalization of THD-C with H and F is also investigated in a similar fashion to hydrogenated graphene (graphane) and fluorinated graphene (fluorographene).

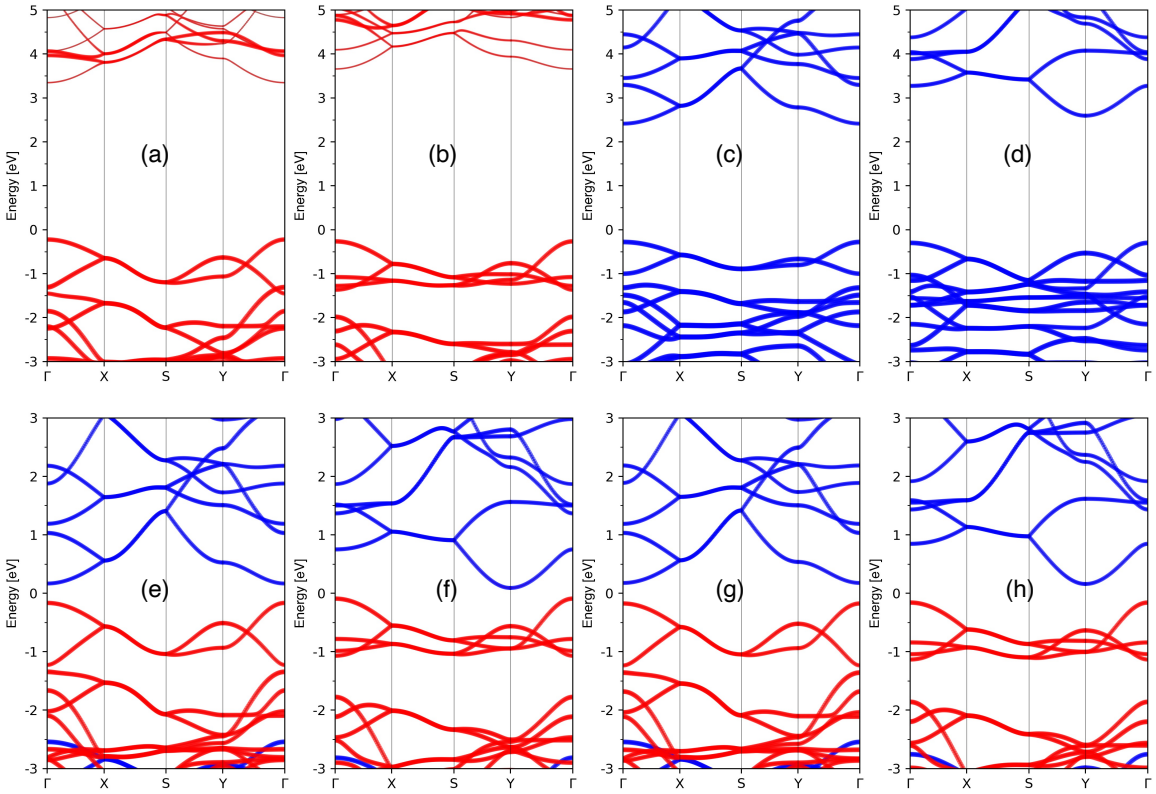

Figure 8.9: (a–d) Electronic band structure of different functionalized THD-C single layers: (a) Full hydrogenation, (b) hydrogenation without acetylenic sites, (c) full fluorination and (d) fluorination without acetylenic sites. (e–h) Electronic band structure of different functionalized Janus bilayers: (e) Full functionalization and AA stacking, (f) functionalization without acetylenic sites and AA stacking, (g) full functionalization and AB stacking, and (h) functionalization without acetylenic sites and AB stacking. The bands are colored according to contributions to the PDOS coming from orbitals in the hydrogenated (red) or fluorinated (blue) layer. The Fermi energy is set to zero in all cases.

We consider two possibilities for functionalization, one in which H or F atoms are added to all sites and another in which the acetylenic sites are not functionalized. The calculations were carried out in a $2 \times 1 \times 1$ supercell, which is the minimum required cell for these configurations. The adsorbed atoms induce out-of-plane structural distortions in the sheet, in a similar fashion to graphene. When all sites are functionalized, we observe buckling of 0.33 Å on each side of the sheet, for either H or F functionalization. When acetylenic sites are left non-functionalized, the buckling height increases to 0.41 Å. Both of these cases show significantly larger deformation than that of functionalized graphene, wherein the buckling heights of graphane and fluorographene are calculated to be 0.23 Å and 0.24 Å, respectively.

The band structures corresponding to the four studied functionalized configurations are

shown in Fig. 8.9 (top panels). We find that the hydrogenation and fluorination introduce an energy gap in THD-C, making it a semiconductor. The magnitude of the band gap depends on the conformation. In the case of hydrogenation, we see a direct gap at the Γ point of magnitude 3.57 eV with full functionalization and of 3.92 eV when the acetylenic sites are not functionalized. For the fully fluorinated case, a direct gap of 2.69 eV is also observed, but an indirect gap of 2.89 eV is observed when acetylenic sites are not functionalized. In the latter case, the valence band maximum (VBM) appears at the Γ point, while the conduction band minimum (CBM) appears at the Y point. Note that configurations with non-functionalized acetylenic sites have larger band gaps than their corresponding fully functionalized counterparts and that band gaps in hydrogenated configurations are larger than those found in the corresponding fluorinated ones. These trends agree with those found in the hydrogenation and fluorination of h-BP and h-BAs layers [237].

Furthermore, we have studied the electronic properties of functionalized Janus bilayers, in which one layer is composed of hydrogenated THD-C and the other of fluorinated THD-C, which has been shown to be an effective strategy to engineer band alignments and novel electronic properties [237]. Our results are shown in Fig. 8.9 (bottom panels), in which the bands are colored according to the projected density of states (PDOS) summed over atoms from each layer. We have considered two types of stacking between the sheets, AA and AB (see Fig. S6 in the SI of Ref. [194]), and the same functionalization configurations for both sheets. The AB configurations are the most favorable, but their total energies are only about 6–20 meV higher than the corresponding AA ones. In all cases, we see a type-II band alignment, in which the valence band comes from the hydrogenated layer and the conduction band from the fluorinated one. As a result, photoexcitation may produce interlayer excitons, in which electrons and holes are localized at different layers. Such excitons have larger recombination times in comparison with interlayer excitons and, therefore, may be potentially explored for applications in photovoltaic devices, similarly to heterobilayers of transition metal dichalcogenides (TMDs) [238, 239]. For fully functionalized systems, the gaps are direct and their magnitudes are 0.33 and 0.35 eV for AA and AB stacking, respectively. When the acetylenic sites are not functionalized, indirect gaps were obtained with magnitudes of 0.18 and 0.31 eV for AA and AB stacking, respectively.

8.4.8 Nanoribbons and Nanotubes

Another potential way to tune the electronic properties of $2D$ materials is by cutting them into nanoribbons or rolling them into nanotubes. By confining the electrons in these quasi-$1D$ structures, the resulting electronic structure may be qualitatively different from the bulk material and strongly depend on the geometry [136, 197, 240–244]. For that reason, first we consider nanoribbons with varying widths and two types of edge terminations. We name them "zigzag" and "armchair" following their resemblance to the corresponding terminations in graphene nanoribbons [136, 241, 242]. Their crystal structures are shown in Fig. 8.10. We consider ribbons with clear edges, in which dangling bonds are left unchanged, as well as ribbons with saturated edges, in which these bonds are completed with Hydrogen atoms. Five different widths for each edge morphology were calculated.

The calculated band structures are shown in the SI of Ref. [194] in Figs. S9 and S10 for saturated edges and Figs. S11–S13 for unsaturated edges. The effects of spin polarization are included in all cases. We find that all armchair configurations display a semiconducting behavior irrespective of the edge saturation. As shown in Fig. 8.11, the band gaps monotonically decrease as a function of the width of ribbons, as expected from the quantum confinement effect. The largest calculated gap is 1.11 eV. For the widest ribbons we have considered, we actually see an overlap between the valence and conduction bands, which is represented as a negative gap in the plot. On the other hand, all zigzag nanoribbons display a metallic character, irrespective of size and edge saturation. However, their band structures with edge saturation are very different from those without saturation. While the saturated ribbons are non-magnetic, unsaturated ribbons present magnetic ordering, with a ferromagnetic (FM) ground state. We also find an antiferromagnetic (AFM) state with a slightly higher energy (see Table S3 in the SI of Ref. [194]). Their possible occupation at 300 K is also given and estimated from the Boltzmann distribution. Additionally, the band structures of the unsaturated ribbons present weak-dispersive bands near the Fermi energy. These bands are responsible for the magnetization and correspond to electronic localization near the unpaired dangling bonds of these ribbons, as can be appreciated from the spin density plots in Fig. S15 in the SI of Ref. [194]. Therefore, the magnetic ordering

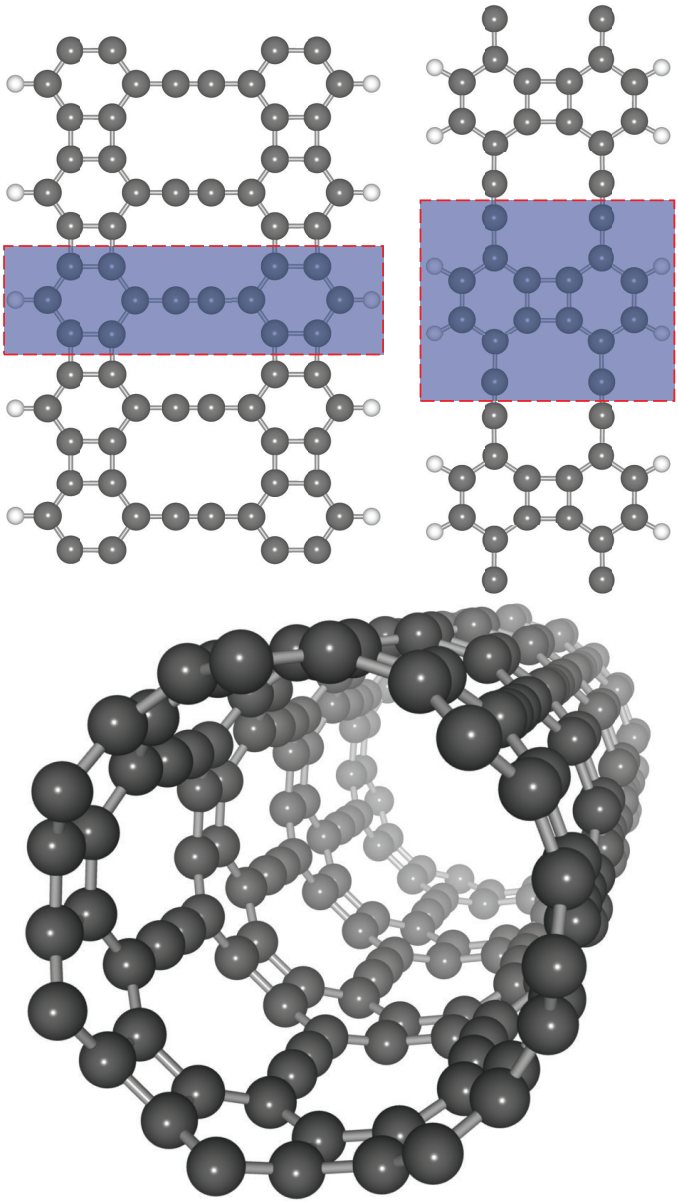

Figure 8.10: Nanoribbons with the zigzag (**top left**) and armchair (**top right**) morphologies, and a nanotube with the zigzag morphology (**bottom**). For the nanoribbons, the unit cell is shown as the shaded area. Grey and white spheres represent carbon and hydrogen atoms, respectively.

at the edges and the potential switching between FM and AFM configurations in these ribbons may be explored for future applications in spintronic devices. Notice that these weak-dispersive bands are absent in unsaturated armchair ribbons, in which the dangling bonds appear in neighboring pairs and compensate one another (see Fig. 8.10). As a result, these ribbons are non-magnetic in all cases.

We also studied the electronic properties of zigzag and armchair nanotubes of various diameters. We considered zigzag tubes with diameters between 3.58 and 10.7 Å and armchair tubes with diameters between 4.53 and 13.6 Å. These tubes can be parameterized by an integer N which corresponds to the number of primitive lattice vectors from the pristine THD-C sheet that make up the circumference of the tube, such that $3 \leq N \leq 9$ and $2 \leq N \leq 6$ make up each morphology. The corresponding band structures are shown in Figs. S16 and S19 in the SI of Ref. [194]. We find that all configurations display a metallic character, irrespective of edge morphology and diameter. Additionally, the zigzag morphologies present an unique feature. They show weak-dispersive bands near the Fermi energy. For even values of the integer N, flat bands lie precisely at the Fermi energy, while they appear at higher energies for odd values of N. By inspecting the wavefunctions of these bands at the Γ point (see Fig. S18 in the SI of Ref. [194]), we see that they present an electronic localization along the tube axis, as expected. In fact, the electronic density forms stripes along the H and T rings in the circumferential direction, reminiscent of the same pattern discussed in the electronic structure of the bulk THD-C sheet (see Fig. 8.8 and the related discussion). Such patterns are absent in the armchair morphology, where the stripes formed by the H and T rings lie along the tube axis and correspond to extended states.

8.4.9 Interaction with Alkali Atoms

Next, we investigate the potential of THD-C as an anode material for metal-ion batteries. To that end, we study the adsorption of alkali atoms at the T, H, and D sites (see Fig. 8.2) in a $3 \times 2 \times 1$ supercell of a AA-stacked THD-C bilayer with 96 C atoms to mimic a bulk,

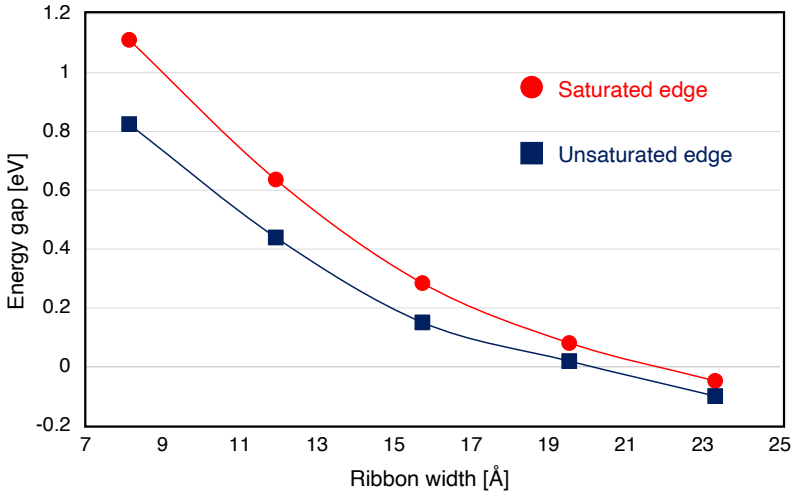

Figure 8.11: Band gap evolution of armchair THD-C nanoribbons as a function of width. The negative gap represents an overlap between the conduction and valence bands.

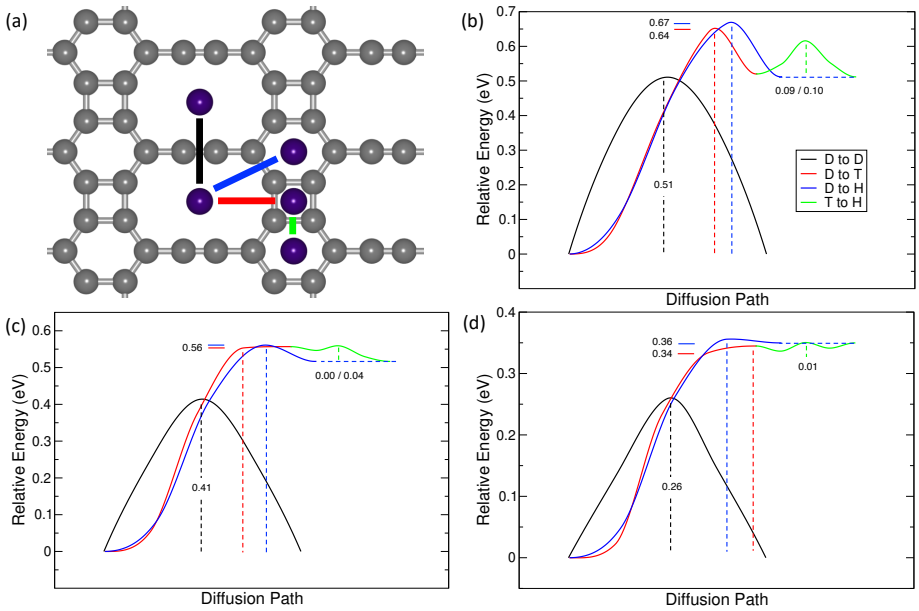

Figure 8.12: Diffusion paths (a) and energy barriers (in eV) for the diffusion of the alkali metal ions Li (b), Na (c), and K (d) over THD-C. Four different diffusion paths are considered: D to D (black), D to H (blue), D to T (red), and T to H (green), and all relative energies are color coded accordingly. All barriers are taken relative to the respective ion's binding energy at the D site.

multilayered structure. The adsorption energy is defined as

$$E_{\text{ads}} = -E_{\text{tot}} + E_{\text{anode}} + E_X, \tag{8.9}$$

where E_{tot}, E_{slab}, and E_X represent the total energy of the alkali adsorbed system (THD-C + adsorbent), the total energy of the anode material (pristine THD-C), and the total energy of a single alkali atom, respectively. The adsorbing atom is placed above the top layer and the whole supercell is allowed to relax.

The results are summarized in Table S2 in the SI of Ref. [194], where we also compare them with adsorption energies calculated for biphenylene and graphene at the same level of theory. According to our calculations, we see quite strong interactions between THD-C and alkali atoms. All three high symmetry positions (D, H, and T) result in favorable binding for Li, Na, and K, with the D site being the most favorable. This is expected, given the larger size of this pore. The energies at the H and T sites are comparable to the values found at the same sites in biphenylene and larger than the values found in graphene at the H site. The relative strengths of the adsorption energies among the studied alkali atoms follow the general trend Li > K > Na at each site, which is consistent with previous studies in graphene and other substrates [245–247]. We also observe slight local distortions in the layer during adsorption. At all three symmetry sites, this average distortion is strongest with Li, which pulls nearby C atoms out-of-plane by 0.16 Å. In contrast, Na and K create average distortions of only around 0.126 and 0.13 Å, respectively. The order of the distortion size, which follows Li > K > Na, is consistent with each alkali's respective binding energy. The charge transfer between the adsorbed atom and the THD-C bilayer is calculated with the help of Bader analysis [248]. We find that charges of 0.999, 0.992, and 0.897 e^- are transferred to the sheet from Li, Na, and K, respectively, which are consistent with a strong ionic binding.

To study the ionic diffusivity of alkali atoms on the surface of THD-C, we make use of the c-NEB method to calculate the diffusion barriers across different paths, as shown in Fig. 8.12. Starting from the D site, the path with the smallest barrier for all alkali atoms we have considered is the D–D path, with barriers of 0.51, 0.41, and 0.26 eV for

Li, Na, and K, respectively. For comparison, the minimum energy barrier for Li diffusion in a similar graphydiyene sheet—consisting of acetylenic sites—is 0.52 eV, which matches excellently with the 0.51 eV value for Li diffusion in THD-C sheet [249]. For a similar tolanene and biphenylene sheet, the minimum energy barrier for the diffusion of Li is 0.61, and 0.43 eV [211, 250]. For the D–H–D path, the energy barriers are 0.64, 0.56, and 0.34 eV for Li, Na, and K, respectively. We also calculate the barriers for D–T–D, D–T–H–D, and D–H–T–D paths, and the corresponding values are shown in Fig. 8.12. Note that the barrier for going from T to H is particularly small, which is related to the similar adsorption energies found at these sites. Additionally, note that the diffusion barriers tend to decrease as the size of the alkali atom increases. Li shows pronounced barriers in every diffusion path, including H–D, while smaller barriers are found for Na and K.

Another key requirement for evaluating the efficiency of an anode material is its storage capacity. It can be calculated as

$$C = n\frac{F}{M} \times \frac{1000}{3600}, \tag{8.10}$$

where F is the Faraday constant, M is the molar mass of the THD-C sheet, and n is the number of adsorbed alkali atoms. The numerical factor $\frac{1000}{3600}$ is used to convert the results to units of mAh. According to this equation, the theoretical storage capacity of THD-C for all three alkali atoms (Li, Na, and K)—with full occupation at D, H, and T sites (C_8Y_6, Y = Li, Na, K)—can potentially be as high as 1674 mAhg^{-1}. For comparison, the Li storage capacity of graphite—a commercial anode material—is limited to 372 mAhg^{-1} only. Furthermore, the Li storage capacities of Ψ-graphene (372 mAhg^{-1}) [251], M-graphene (279 mAhg^{-1}) [252], phagraphene (487 mAhg^{-1}), biphenylene (632 mAhg^{-1}) [250], tolanene (638 mAhg^{-1}) [211], and graphdiyne (744 mAhg^{-1}) [249] are all significantly lower than THD-C. For larger alkali atoms such as Na, the storage capacity is as low as 35 mAhg^{-1} in graphite. Consequently, THD-C offers more than 4 times the capacity for Li storage and an impressive 47 times the capacity for Na in comparison with graphite. And while the performance of C materials with hexagonal rings can be enhanced by introducing defects [253, 254], THD-C's larger D site matches this with strong interaction, and the potential to accommodate

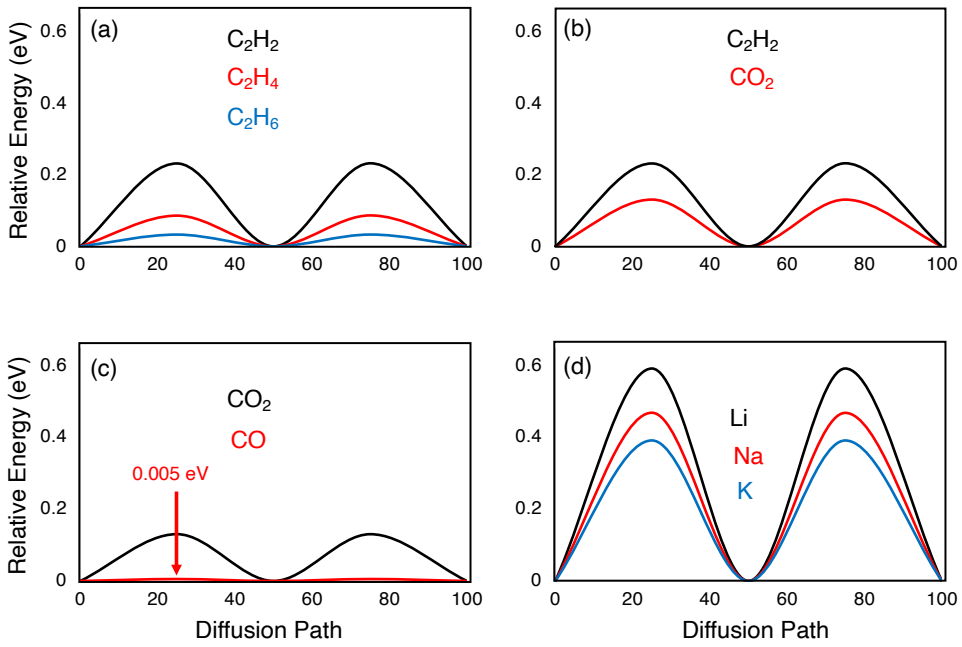

Figure 8.13: Energy barriers for diffusion of (a) C_2 alkanes, (b) C_2H_2/CO_2, (c) CO_2/CO, and (d) alkali atoms within a zigzag THD-C nanotube of size $N = 7$.

more than a single alkali. For this reason, we also check the possibility of C_8Li_8. The geometry of such a configuration can be appreciated in Fig. S21 in the SI of Ref. [194]. This configuration corresponds to a huge capacity of 2231 $mAhg^{-1}$. We stress, however, that further calculations should be performed in order to fully elucidate the storage capacity of this material, such as a study of the adsorption energies when the number of alkali atoms and the number of THD-C layers are systematically increased. These studies are beyond the scope of the present work.

Finally, we have also investigated the adsorption and diffusion of alkali atoms in THD-C nanotubes. To that end, we focused on a zigzag nanotube with a circumference defined by $N = 7$, as shown in Fig. S22 in the SI of Ref. [194]. The same morphology is used in our study on the adsorption of gaseous molecules, discussed in the next section. As in the sheet, the D site is the most favorable for adsorption and the corresponding energies are reported in Table S2. The values are comparable to those found in the sheet, with Li being slightly less bound, while Na and K become more strongly bound. The energy barriers for diffusion along the same paths considered for the THD-C sheet are shown in Fig. 8.13 (d). We find

that the ionic mobilities are comparable to those of the sheet, as expected.

8.4.10 Adsorption/Separation of Small Gaseous Molecules

The adsorption of industrially relevant small gas molecules is also considered both on a THD-C bilayer and within a THD-C nanotube. For that purpose, we select several important molecules such as C_2H_2, C_2H_4, C_2H_6, CO_2, CO, H_2O, CH_4 and NH_3. As mentioned above, we use a zigzag nanotube with a circumference defined by $N = 7$. We choose this configuration because it exhibits the greatest adsorption energy for the largest molecule in our study, C_2H_6. In doing so, we prevent the exclusion of C_2H_6 due to its size, while also ensuring that the smaller molecules can interact with the nanotube.

The adsorption energies of these gas molecules on the tube and the sheet, as defined in Eq. 8.9, are reported in Table 8.1. Our calculations suggest that the THD-C tube can outperform the THD-C sheet in this context, as the binding energies are significantly stronger for every molecule we considered. If we consider the THD-C tube for C_2 separation, we see similar binding strengths for C_2H_4 and C_2H_6 molecules, while a relatively weaker binding energy is calculated for C_2H_2. To study the kinetics, c-NEB calculations were performed. Figure 8.13 (top left) shows the diffusion energy barriers for C_2 alkanes in the tube. It can be seen that the tube offers the highest energy barrier for C_2H_2, while the lowest barrier is observed for C_2H_6. Therefore, we conclude that C_2H_4 can be separated from C_2H_2 and C_2H_6 or a ternary mixture by using THD-C tubes. The C_2H_4/C_2H_2 separation is both thermodynamic and kinetic driven, whereas the separation between C_2H_4 and C_2H_6 is kinetic driven.

For CO_2, we calculate a notably lower barrier in comparison with C_2H_2. Furthermore, the binding affinities of the tube towards CO_2 and C_2H_2 are 0.420 and 0.487 eV, respectively. As such, there is a significant preference for C_2H_2 to bind compared to CO_2. Consequently, CO_2 can effectively be separated from a CO_2/C_2H_2 mixture to get a pure C_2H_2 gas. Furthermore, as mentioned earlier, CO_2 reduction into CO is another critical application of separative adsorption. In fact, it is on NASA's MARS agenda to utilize CO_2 resources [245,255–258], but extremely pure CO is required and even a trace amount of CO_2 should be removed. To this purpose, THD-C shows great potential, as the binding energy

Table 8.1: Adsorption energy (eV) of several small gas molecules within three different THD-C nanotubes of size N, as well as the THD-C bilayer and MOF-74 [260].

	THD-C $N = 6$	**THD-C** $N = 7$	**THD-C** $N = 8$	**THD-C bilayer**	**MOF-74**
H_2O	0.460	0.347	0.300	0.243	0.642
CO_2	0.344	0.420	0.215	0.218	0.424
CO	0.547	0.268	0.331	0.149	0.362
CH_4	0.358	0.342	0.233	0.126	0.196
NH_3	0.470	0.393	0.300	0.191	0.766
H_2	0.200	0.111	0.066	0.075	0.103
C_2H_2	0.587	0.487	0.372	0.165	0.393
C_2H_4	0.500	0.526	0.354	0.144	0.414
C_2H_6	0.365	0.529	0.379	0.161	0.456

of CO at the most favorable site in the tube is notably smaller than the binding energy of CO_2, just 0.268 eV to CO_2's 0.420 eV. Moreover, the tube offers a negligible barrier for CO diffusion in comparison with CO_2. Thus, the retention time for CO_2 will be substantial due to its stronger binding energy and higher diffusion energy barrier in comparison with CO.

The interaction of methane (CH_4) is also studied since, as mentioned above, it is considered a cleaner fuel. The binding energy of CH_4 in the tube is 0.342 eV, which is significantly lower than the binding energy of CO_2. Consequently, there is a preference for trapping of CO_2 over CH_4 in the tube and a CH_4/CO_2 mixture may have a higher purity of CH_4, resulting in a higher quality of the natural gas. Similarly, ammonia (NH_3) can also be captured using the tube even in the presence of water due to the preferential binding for NH_3 over H_2O.

To further test the size effect of the tube on the interaction with the guest molecules/atoms, we also consider zigzag nanotubes of size $N = 6$ and $N = 8$. We find that the binding energy is heavily dependent on the tube size (see Table 8.1). For all the guests considered except the C_2 alkanes, the binding energy roughly follows $(N = 6) > (N = 7) > (N = 8)$. Binding strength is also size-dependent for the C_2 alkanes. Due to the smaller size of C_2H_2, the strongest binding is calculated within the $N = 6$ tube, whereas the larger C_2H_4 and C_2H_6 prefer $N = 7$. Most importantly, we see a substantial increase in the binding energy of H_2 when narrowing the tube circumference, optimizing at $N = 6$ for ambient temperature hydrogen storage [259]. This can be attributed to the small size of H_2.

All of these results were compared with the prototypical metal-organic framework (MOF-74)—which is specifically tailored for gas storage and separation applications (see Table 8.1 and Ref. [260]). We find that the tube we have studied actually outperforms MOF-74 in several ways. For example, the presence of water is detrimental to coadsorbed species in MOF-74, as it preferentially adsorbs water molecules [142]. In fact, water has the second strongest binding energy in MOF-74, the strongest being NH_3 [140]. On the other hand, the tube offers a weaker interaction with water in comparison with CO_2 and the C_2 alkanes, depending on tube diameter. We also see a larger difference between the binding energies of CO_2 and CO. Furthermore, the binding energy and diffusion barrier of C_2H_4 and C_2H_6 are similar in MOF-74, resulting in a poor C_2H_4/C_2H_6 separation performance [261]. On the other hand, the tube displays similar binding energies for C_2H_4 and C_2H_6 but substantially different diffusion barriers, thus making it an eligible candidate for the desirable purification of C_2H_4 from the C_2H_4/C_2H_6 mixture. And in contrast with MOF-74, THD-C tubes can be tailored for adsorption of certain molecules by their size, and can be used for optimal H_2 storage at ambient temperature.

8.4.11 Catalysis of Hydrogen Evolution Reaction (HER)

Due to the metallic nature of the THD-C sheet, we assess its potential as a catalyst in HER with the following two reactions

$$\mathrm{H^+ + e^- + ^* \rightarrow H^*}, \tag{8.11}$$

$$\mathrm{H^+ + e^- + H^* \rightarrow H_2}, \tag{8.12}$$

where * and H^* represent the activation site and adsorbed hydrogen atom on that site, respectively. We consider the change in the Gibbs free energy of the intermediate (H^*) as

$$\Delta G_{\mathrm{H^*}} = \Delta E_{\mathrm{H}} + \Delta E_{\mathrm{ZPE}} - T\Delta S\ , \tag{8.13}$$

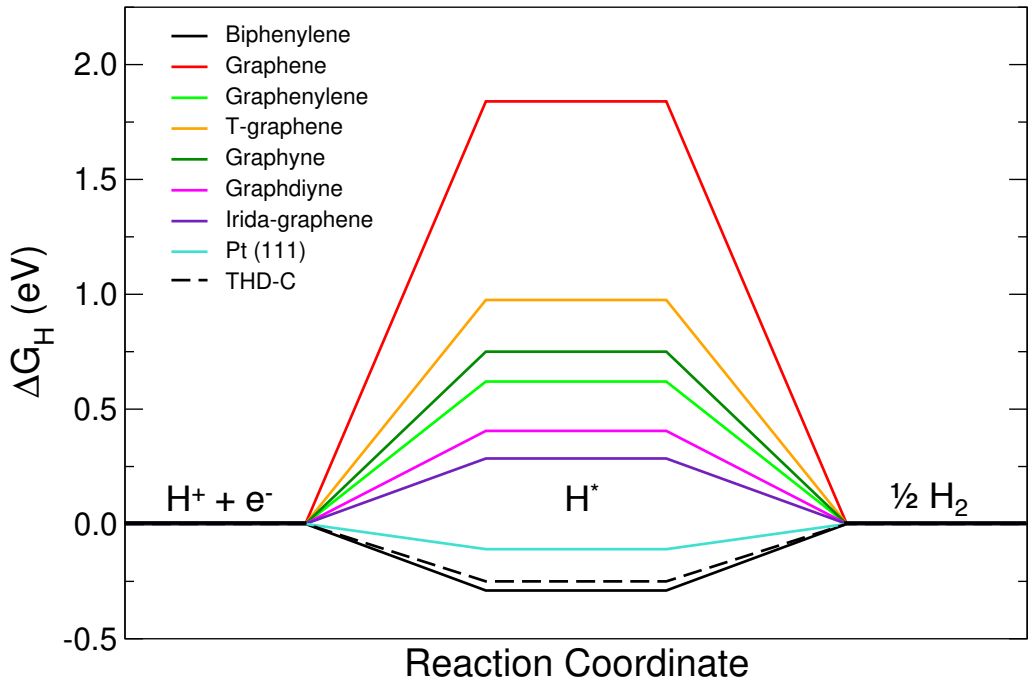

Figure 8.14: Gibbs free energy barrier of the hydrogen evolution reaction for THD-C and several other C allotropes, as well as a Pt(111) slab.

where ΔE_{H} is the hydrogen binding energy and ΔE_{ZPE} is the zero-point energy difference between the gas phase H_2 and H adsorbed system. ΔE_{H} can be calculated as

$$\Delta E_{\mathrm{H}} = E_{\mathrm{slab+H}} - E_{\mathrm{slab}} - \frac{1}{2}E_{\mathrm{H_2}} \ , \tag{8.14}$$

where $\frac{1}{2}E_{\mathrm{H_2}}$ is the energy of a single H atom taken from an H_2 molecule. According to this equation, a negative binding energy refers to the favorable adsorption of H.

Following the recipe in Ref. [228], ΔE_{ZPE} of H adsorption on a metallic surface is 0.04 eV. Consequently, at room temperature (298.15 K) Eq. 8.13 simplifies into $\Delta G_{\mathrm{H^*}} = \Delta E_{\mathrm{H}} + 0.24$ eV. This is a reasonable method when we compare the performance of various catalysts. For the adsorption of the H atom on the THD-C sheet, we construct a 3×2×1 supercell consisting of 48 C atoms. The most favorable binding site is any of the atoms on the T ring. The binding energy corresponding to the aforementioned site is −0.49 eV, which yields a Gibbs free energy barrier of −0.25 eV for HER. In Fig. 8.14 we compare the catalytic performance of THD-C with several other metallic or semi-metallic C allotropes at the same level of theory (see Table S4 in the SI of Ref. [194] for more detailed results). We

also do the same calculation for HER on a Pt(111) slab, finding excellent agreement with a previous study in both binding energy and Pt-H bond length [228, 262]. We find that THD-C's ΔG_{H} is comparable in magnitude to that of biphenylene (-0.29 eV) and iridagraphene (0.29 eV), and is considerably improved over other C allotropes. It should also be noted that the presence of a twelve-membered ring can easily accommodate metal atoms, thus providing the possibility for THD-C to be explored as a single-atom catalyst similar to graphdiyne [212].

8.5 Conclusions

In summary, we propose a novel two-dimensional carbon allotrope that can be potentially synthesized from the topological assembly of 4-ethynyldiphenylacetylene molecules. It forms a rectangular lattice consisting of tetra, hexa, and do-deca membered rings. The sheet possesses excellent kinetic and dynamical stability with strong anisotropic mechanical properties and interesting electronic properties with the presence of tilted Dirac cones. Although the structure shows a metallic character, a tunable band gap can be introduced through functionalization and/or the formation of quasi-1D structures. The band alignment and the optical properties of the system can also be tuned by the stacking of different functionalized layers. Moreover, the pure sheet displays magnetic ordering when zigzag edges are exposed, which can potentially be explored in spintronic devices. The THD-C sheet and tube also display very competitive electrochemical properties, surpassing rival 2D C allotropes and graphite when it comes to the storage capacity of alkali atoms. The sheet also outperforms several other C allotropes in HER performance, displaying a potential for catalysis that is close to platinum. Most interestingly, the tube can be used for the storage, capture, and separation of industrially important small gas molecules, and can potentially outperform the prototypical MOF-74. We believe that the work is of significant interest to spark future investigations on many potential applications of this material.

Chapter 9

Important Co-Authored Projects

In previous chapters, I have provided a few examples of how DFT can be used as a predictive tool for the properties of functional materials. I have also detailed some of the inner workings of van der Waals density functionals, and highlighted possible avenues to increase the predictive power of vdW-DFT. However, as discussed in the beginning of Chapter 2, intersectionality between experiment and computation is an important part of modern materials physics, particularly when trying to solve problems in industry. In such cases, collaborative efforts between different disciplines is often the most effective way to drive technological and industrial advancement. My own research is no exception to this, and I have taken part in several collaborative projects with research groups at other universities which use experimental techniques to synthesize and characterize novel functional materials. In these projects, the material would often be designed with a specific use-case in mind, i.e., the separation of two or more isomers. But as we see with the case of the MOF Ca(H_2tcpb) in Chapter 7, the mechanisms that give these materials their functionality is not always clear from *in situ* measurements. DFT thus becomes an invaluable tool for verifying and decoding their properties. The following sections of this chapter outline my work in characterizing several functional materials—primarily MOFs tailor-made for gas storage and/or separation.

9.1 Decoding the Gate Opening Mechanism of the Flexible Framework RPM3–Zn upon Hydrocarbon Inclusion

Chapter 7 provides an in-depth study of the thermodynamics of molecular adsorption in porous materials, which was motivated by the curious temperature-dependent sieving of C6 isomers by Ca(H_2tcpb). In Section 7.2, we also briefly discuss the possibility that this behavior arises from "gate-opening", a phenomenon observed in flexible MOFs whereby a reversible structural change leads to sharp increases in gas uptake. Although gate opening was ultimately not determined to occur for Ca(H_2tcpb), this project examined the uptake mechanism for a material with known gate-opening behavior: the MOF RPM3–Zn.

Originally designed for the detection of high explosives, RPM3–Zn was later found to exhibit gate-opening for several alkane species [183, 263]. Experimental loading isotherms were found for CH_4, C_2H_6, C_3H_8, and C_4H_{10}, with each exhibiting a unique adsorption profile as a function of pressure. Each guest showed little to no uptake up to some critical pressure—on the order of 3 torr for C_4H_{10}, 50 torr for C_3H_8, 200 torr for C_2H_6, and more than 800 torr for CH_4. At these pressures, the respective guest molecules show a sudden and sharp increase in uptake, indicative of gate opening in the MOF. This behavior is highly desireable, as it could be used to effectively separate mixtures of the C1–C4 alkanes via pressure-tuning. The ability to tailor-design MOFs with similar gate-opening characteristics for different guest species would also represent a significant advancement. However, the mechanism that underlies gate opening in RPM3–Zn and other MOFs has remained a mystery, slowing progress in the synthesis of new materials. The aim of this project was thus to gain clarity on how and why gate-opening takes place within RPM3–Zn.

To uncover this mechanism, we calculated several properties of the loaded and empty MOF which might impact gate opening. Five guest species—C_2H_2, C_2H_4, C_2H_6, C_3H_8, and C_4H_{10}—were placed within the MOF at loadings of 1–4 guest molecules per pore. By doing so, we found that two traits contribute to the gate opening. The first is the stretching of a bond in the carbon linker near one of the zinc sites, weakening the support of the linker on the overall structure. RPM3-Zn has a triclinic unit cell with a shallow c-axis length, Zn sites at each corner in the a–b plane, and organic linkers connecting each Zn site. When viewed

from a cross-section of the pore, it appears as a parallelogram bordered by carbon linkers. The aforementioned bond breaking allows the angle of the linkers, and by extension the cell axis angles, to change significantly. This changes the overall shape of the pore from a highly oblique parallelogram into something closer to a rectangle, which increases the cell volume by a significant amount to accommodate additional guest molecules as shown in Fig. 9.1. This mechanism is supported by our elasticity calculations, which showed that inclusion of more guest molecules generally lowered the bulk and shear moduli, demonstrating that the linker supports had weakened in the process of changing its shape and that the MOF had become more flexible. By gaining these insights into the mechanism of gate-opening in MOFs, we provide a means of fine-tuning molecular uptake for loading and storage. These findings could also potentially be used for the design of new materials with similar behaviors. This work has been published in Ref. [179].

9.2 Metal–Organic Frameworks with Optimal Pore Structure for Complete Discrimination of C6 Hydrocarbons

While the pressure-tuned separation of chemically distinct hydrocarbons is an enticing prospect in the petrochemical industry, a significantly more challenging problem is the separation of isomers—compounds that are chemically identical but geometrically distinct. An example of this is the hexane isomers, which are examined in detail in Chapter 7. The chemical formula C_6H_{14} can manifest as one of several isomeric configurations, including linear nHex, mono-branched 3MP, and di-branched 2,3-dimethylbutane (23DMB). Despite their similar structures, each of these three isomers possesses different thermodynamic properties, which give them different applications as fuel components. Raising the research octane number of a C6 alkane mixture requires the discrimination of branched isomers, which is very costly using temperature-based methods like distillation and cryogenics. The use of separative adsorption in porous materials is thus a desireable alternative, and we have already seen how tailor-made MOFs such as Ca(H_2tcpb) can be used to significantly reduce these energy costs.

This project concerns another material produced by our collaborators, a nickel-based

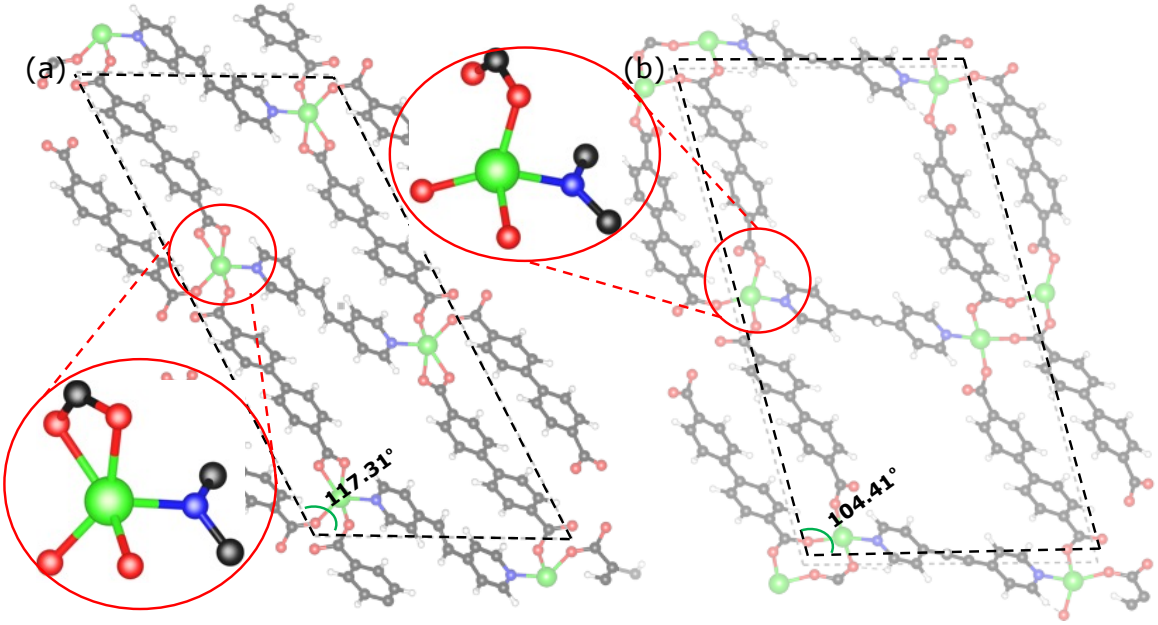

Figure 9.1: As-synthesized (left) and butane-loaded (right, one guest molecule of butane per pore) RPM3–Zn. To emphasize the structural change, the guest molecules are not shown here. The corresponding insets show an intact COO–Zn bonding stabilizer (left) and a damaged/stretched bonding (right). As soon as the COO–Zn bond stretches, the structure becomes less resistant to external agents and turns into a flexible material. A change in the unit cell (black dotted lines) shape/volume is evident. The unit cell of empty MOF is more oblique with $\alpha = 117.31°$ and the unit cell of loaded MOF is more of a rectangular shape with reduced α of 104.41°. Reprinted with permission from Chem. Mater. **34**, 3246 (2022) [179]. Copyright © 2022 American Chemical Society.

MOF with the chemical formula Ni-(4-PyC)$_2$ (4-PyC = 4-pyridinecarboxylate). With approximately square pores that are 5.5 Å across, this MOF was carefully-designed to preferentially adsorb nHex, which is smaller in cross-section than its branched counterparts, 3MP and 23DMB. This behavior was confirmed through experimental adsorption isotherms, which at 30 °C showed maximum loadings of approximately 130 mg/g for nHex, 70 mg/g for 3MP, and less than 20 mg/g for 22DMB. But, while the adsorption behavior of Ni-(4-PyC)$_2$ represented a positive outcome, further study through methods like IR spectroscopy and our own *ab initio* calculations were crucial to provide insight into adsorption dynamics. To examine this in detail, we began with structural optimizations of nHex, 3MP, and 23DMB within the MOF, which were used to obtain interaction energies and binding configurations for each guest. We found binding strengths in the order of nHex > 3MP > 23DMB, with each guest forming hydrogen bonds with carboxylates near the metal site of the MOF, supporting the experimental findings of our collaborators. Though nHex's greater uptake was initially assumed to be the result of its smaller cross section, our calculations revealed another, equally-important mechanism: the greater length of nHex, which allowed it to bind simultaneously with two adjacent metal sites.

Another important detail that impacts loading in MOFs is the ability of guest molecules to diffuse through the material. If binding sites in each unit cell of the MOF represent an energetic optimum for the guest molecule, then they must overcome some diffusion barrier in order to move from one site to the next. In this project, we also examined diffusivity of guest molecules through the MOF by performing "nudged elastic band" (NEB) optimizations, which calculate the energy of a guest molecule as it transitions between binding sites. The diffusion barriers were found to correlate Ni-(4-PyC)$_2$ with the guest molecules' cross section, resulting in heights in the order of 23DMB > 3MP > nHex. Though in all cases, diffusion barriers were smaller in magnitude than the respective binding energies, this trend demonstrates an ease of diffusion in nHex which is not present for 3MP and, to a greater extent, 23DMB. This work is published in Ref. [264].

In addition to Ni-(4-PyC), we have carried out similar studies of C6 adsorption in other MOFs, such as the aluminum-based MIL-120 [265]. Due to the tight confinement of MIL-120's pore, we find stronger binding for nHex and 3MP than for 22DMB. Diffusion barrier

calculations also show a large stratification in barrier height: 0.05 eV for nHex, 0.26 eV for 3MP, and 0.77 eV for 22DMB. Both of these results contribute to a body of evidence that MIL-120 shows good potential as a filter for C6 alkanes. The manuscript for this project is currently under preparation.

The separation of C6 molecules is not just limited to the alkanes either. The cyclic hydrocarbons benzene (C_6H_6), cyclohexene (C_6H_{10}), and cyclohexane (C_6H_{12}) are also important in the petrochemical industry, with specific applications in nylon manufacturing. In a recent multi-disciplinary study with our colleagues at Rutgers and the University of North Texas, we showed that the MOF Zn-BDC [266] is an ideal candidate for the discrimination of these cyclic C6 molecules. Similar to CaMOF, this separation can be temperature-tuned, with benzene readily adsorbing at higher temperatures in experiment than cyclohexene and particularly cyclohexane. By performing *ab initio* calculations on the system, we see that this is due to subtle differences in the binding energy and diffusion barrier. Cyclohexane, for example, binds 24 meV less strongly than benzene and cyclohexene, which demonstrate similar binding to one another. Cyclohexene, however, shows a diffusion barrier that is nearly 30 meV higher than that of benzene, introducing a kinetic effect to the rate of adsorption that would assist in the separation. This work is published in Ref. [267].

9.3 Selective Adsorption and Diffusion in MOF NU2100: A Computational Study

The previous two sections showcase the benefits of using computation and experiment in tandem to provide a full picture of relevant physical mechanisms in functional materials. This project concerns another use of computational methods, which is to quickly and effectively explore many possible applications for existing materials, similar to our characterization of THD-C in Chapter 8. Recently, researchers at Northwestern University synthesized a MOF called NU2100, whose structure possesses several intriguing characteristics: it is air-stable, flexible, lacks oxygen in its chemical formula, and perhaps most importantly, possesses open Cu(I) sites for ease-of-access by adsorbed gas molecules [268]. NU-2100's flexibility and large pore size of up to 50 $Å^2$ makes it an enticing candidate for gas separation. For this

reason, our group has designed a systematic framework to study adsorption and potential gas separation in NU2100. We have identified several candidate guest molecules for adsorption: C_2H_2, C_2H_4, C_2H_6, CO_2, and H_2O. The latter two are of particular interest, as CO_2 is an unwanted byproduct in many industrial processes and can cause significant damage to the environment. Porous materials that can effectively remove CO_2 from gaseous mixtures are thus in high demand. However, the search for such materials is further complicated by the possible presence of water, which is also a common byproduct. Many metal–organic frameworks are chemically unstable under humid conditions, requiring careful environmental control. Those that *are* water-stable often encounter another problem: the preferential adsorption of water over more desired adsorbates like CO_2 and hydrocarbons. This is in part due to water's tendency to form dense, hydrogen-bonded clusters, which add cooperative effects to their binding in porous materials.

For each guest molecule, we perform *ab initio* calculations of the binding energy and diffusion barrier to assess NU2100's possible suitability for petrochemical applications. Unlike some of the other MOF studies mentioned in this thesis, NU2100's pore is significantly larger than our guest molecules of interest, allowing for more in-depth study of the effects of increased loading per pore. Curiously, despite NU2100's large pore size, experimental isotherm measurements found little to no uptake of C_2H_4 and C_2H_6, which the authors of Ref. [269] attribute to a size-exclusion effect of the guest molecules. While pursuing this hypothesis, our calculations of the unloaded and loaded MOF revealed a remarkable flexibility of NU2100 that leads to unit-cell collapse during structural optimizations. This flexibility presents an added challenge to DFT calculations, especially in combination with the presence of copper atoms. Traditional DFT methods, such as the LDA and GGA, have frequently struggled in the description of transition metal compounds. This error can be eliminated through the use of a Hubbard U correction, which adds an on-site coulomb interaction term to better describe strongly correlated electronic environments. Using this "DFT+U" approach in our study, we find that, remarkably, the Hubbard correction has a noticeable effect on the MOF's cell structure. We hypothesize that the resulting contraction of the framework does result in size-exclusion for the hydrocarbons, but still allows CO_2 uptake due to its small cross-sectional area. Isotherm data also shows some uptake of water,

which could be the result of a structural gate-opening once clusters begin to form with the material.

From our guest-loaded calculations we find that the adsorption behavior of the studied guests within NU2100 is governed primarily by kinetics rather than thermodynamics. Binding strengths were found in the order of $CO_2 > C_2H_6 \approx C_2H_4 > C_2H_2 > H_2O$. The strong binding of CO_2 relative to water is especially promising for the reasons discussed earlier. At the same time, the C2 alkanes were discovered to have noticeably higher barriers of diffusion, between 0.12 eV and 0.23 eV. CO_2 and H_2O, in contrast, demonstrate a much greater ease of movement through the framework, with barriers on the order of 30 meV. These findings support the possibility for NU2100's general use of extracting CO_2 from industrial byproducts. In the process, we also gain a comprehensive picture of the mechanisms that enable this preferential adsorption, while also excluding the C2 alkanes. This manuscript is under preparation, with plans to publish in 2025.

9.4 A Coordinated Framework for Water Harvesting and Storage

The previous section highlights the usefulness of a framework that exhibits high CO_2 uptake, particularly if it is preferred over water. However, water is also a common byproduct in petrochemical processes, and a greenhouse gas like CO_2. If properly recycled, waste water also has a variety of potential uses in other processes. It could thus be desireable to have frameworks which exhibit exceptional uptake of water, so that it can later be extracted and re-processed. Toward this end, our experimental collaborators at Rutgers University have developed and synthesized a novel framework for use in water harvesting and storage, called M-PyC. Unlike other MOFs presented in this chapter, which mostly utilize physisorption to bind guest molecules, M-PyC undergoes a structural phase transition under moisture exposure. Several water molecules chemisorb to the framework's metal sites, in a reversible process which allows individual M-PyC molecules, denoted as a-M$(PyC)_2$, to link together and form a hydrogen-bonded organic framework (HOF).

In order to characterize the adsorbtion of water within M-PyC, we performed several

DFT calculations with varying metallic species as the "M" in M-PyC. Cohesive energies were calculated for the $3D$ coordinated structure, using the formula

$$E_{coh} = \frac{1}{N}\left(E_{\mathrm{M-PyC}} - N\,E_{amorph}\right)\,, \tag{9.1}$$

where $E_{\mathrm{M-PyC}}$ is the total energy of the coordinated M-PyC structure, E_{amorph} is the energy of the amorphous fragment with four terminal waters added, a-$\mathrm{M(PyC)_2} + 4\mathrm{H_2O}$, and N is the number of amorphous fragments per unit cell of the crystal structure. We find that two separate interactions contribute to the overall cohesion of the coordinated framework: hydrogen bonds between terminal waters and carboxylate groups, and weak π bonds between adjacent pyradine rings. The strength of these π bonds was calculated separately as 0.58 eV per a-$\mathrm{M(PyC)_2}$ fragment. Subtracting it from the cohesive energy shows the strength of each hydrogen bond to be around 0.85 eV, with variations of up to 20 meV, depending on the metal species used.

Another indicator of the stability of the hydrated M-PyC phase is the binding energy of water to the metal site. We probe this via calculations of the dehydrated and hydrated forms of a single a-$\mathrm{M(PyC)_2}$ fragment, calculating the binding energy per water molecule,

$$E_b = \frac{1}{4}(E_{amorph+4\mathrm{H_2O}} - E_{amorph} - 4E_{\mathrm{H_2O}})\,. \tag{9.2}$$

In the hydrated phase, each metal site can accomodate up to four water adsorbates, each with a binding energy of 0.6 eV or higher, depending on the metal species. The strength of these bonds, along with the strong cohesion due to hydrogen-bonding and π–π stacking, supports the exceptional water uptake found for this framework, and opens the way to other materials that utilize structural transformations to maximize loading. The manuscript for this project is currently under preparation.

Chapter 10

Conclusions and Future Outlook

The research outlined in this dissertation provides several examples of how materials physics can inform new advances in industry and technology. From an experimental approach, the synthesis of novel functional materials presents an exciting paradigm for the solution of pressing industrial problems. The synthesis of metal–organic frameworks and other porous materials, which can suit a variety of purposes ranging from catalysis to fuel refinement, is a recent and well-researched subfield of these functional materials. However, further progress in this area would be hindered without a comprehensive understanding of the mechanisms that give these materials their functionality. To this end, density functional theory presents an invaluable tool due to its accuracy and efficiency relative to some other modes of computation. The ability of vdW-DFT to describe dispersion interactions, such as those seen in MOF-based adsorption, has also been paramount to this field.

That being said, the vdW-DF model still contains ample room for improvement. This is true of not only the nonlocal correlation, which is vital for fully capturing dispersion effects, but for the GGA exchange as well. As our analysis of the reduced-gradient in Chapters 3 and 4 has shown, the so-called "semilocal" effects of the GGA show significant overlap with the nonlocal correlation, and are quite impactful to the structures of van der Waals complexes. This fact has a profound effect where van der Waals functional development is concerned, necessitating a good balance between semilocal and nonlocal terms, which generally yield repulsive and attractive contributions to interactions at equilibrium, respectively. This can be seen in the performance of vdW-DF3's optimizations on graphene-adsorbed systems.

The GGA exchange term, which was carefully chosen and matched with vdW-DF3's novel form of the nonlocal correlation, presented a smaller overall contribution to the interaction energy. As a direct result, vdW-DF3 avoids the underestimation of binding energies that is seen in variants of vdW-DF2.

In addition to its use as a diagnostic tool, we also show how reduced-gradient analysis can inform the development of new and more accurate functionals. In Chapter 5, this is demonstrated in the development of vdW-DF3-mc, an optimization of vdW-DF3 that is tailored to the broad and widely-studied group of molecular crystals. Through a carefully curated set of reference materials, and a new, flexible form the GGA exchange, we have developed a functional with exceptional accuracy for these materials—in many cases even surpassing the popular force-field corrected DFT-D3 method. This accuracy is only made possible by our chosen exchange form, which possesses the degrees of freedom necessary to take advantage of the molecular crystals' reduced-gradient signature.

With further improvements to the DFT and vdW-DFT methods, computational materials physics advances further in not only the accurate *description* of materials; it can become *prescriptive* as well. Several examples of the former can be found throughout my research, particularly in my collaborative projects outlined in Chapter 9. In these cases, *ab initio* DFT can provide additional context to existing experimental observations, such as verifying binding sites or the order of binding for different molecules. Alternatively, DFT may be used to reveal information that proves elusive in experiment, like the gate-opening mechanism of RPM3–Zn. However, even compared with these useful applications, the potential of DFT to prescribe materials properties is significantly more enticing. The mystery of temperature-dependent uptake in CaMOF of Chapter 7, for example, led us to develop an entirely new model by which *ab initio* techniques and "textbook" thermodynamics could combine to inform the development of precise, tailor-made materials for gas separation applications. Through prescriptive DFT, we also show in Chapter 8 predicted synthesis paths and a wide array of possible technological uses for a novel $2D$ carbon allotrope, THD-C. And with increasingly more accurate functionals, such as vdW-DF3-mc, the list of potential applications only grows.

Altogether, my research shows that DFT has made great strides in its 60 year history,

and that further development will only continue to shrink the historic gap between computation and experiment. The field of vdW-DFT in particular has seen great improvement since its advent in 2004. Yet even now, there exists the prospect of increasing vdW-DFT's accuracy through a refined balance between nonlocal correlation and semilocal exchange terms, or even improvements to the plasmon-pole model from which the nonlocal correlation is derived. By making good use of this improved description, we open up a path to many more novel functional materials with much broader applications, paving the way to a bright future for materials physics and human industry as a whole.

Bibliography

[1] B. Kesanli, Y. Cui, M. R. Smith, E. W. Bittner, B. C. Bockrath, and W. Lin, *Highly interpenetrated metal–organic frameworks for hydrogen storage*, Angew. Chem. Int. Ed. **44**, 72 (2005), DOI: 10.1002/anie.200461214.

[2] N. L. Rosi, J. Kim, M. Eddaoudi, B. Chen, M. O'Keeffe, and O. M. Yaghi, *Rod packings and metal–organic frameworks constructed from rod-shaped secondary building units*, J. Am. Chem. Soc. **127**, 1504 (2005), DOI: 10.1021/ja045123o.

[3] M. Dion, H. Rydberg, E. Schröder, D. C. Langreth, and B. I. Lundqvist, *Van der Waals density functional for general geometries*, Phys. Rev. Lett. **92**, 246401 (2004), DOI: 10.1103/PhysRevLett.92.246401.

[4] P. Hohenberg and W. Kohn, *Inhomogeneous electron gas*, Phys. Rev. **136**, B864 (1964), DOI: 10.1103/PhysRev.136.B864.

[5] W. Kohn and L. J. Sham, *Self-consistent equations including exchange and correlation effects*, Phys. Rev. **140**, A1133 (1965), DOI: 10.1103/PhysRev.140.A1133.

[6] J. P. Perdew, K. Burke, and M. Ernzerhof, *Generalized gradient approximation made simple*, Phys. Rev. Lett. **77**, 3865 (1996), DOI: 10.1103/PhysRevLett.77.3865.

[7] J. Tao, J. P. Perdew, V. N. Staroverov, and G. E. Scuseria, *Climbing the density functional ladder: Nonempirical meta-generalized gradient approximation designed for molecules and solids*, Phys. Rev. Lett. **91**, 146401 (2003), DOI: 10.1103/PhysRevLett.91.146401.

[8] J. Sun, A. Ruzsinszky, and J. P. Perdew, *Strongly constrained and appropriately normed semilocal density functional*, Phys. Rev. Lett. **115**, 036402 (2015), DOI: 10.1103/PhysRevLett.115.036402.

[9] O. A. Vydrov and T. Van Voorhis, *Nonlocal van der Waals density functional: The simpler the better*, J. Chem. Phys. **133**, 244103 (2010), DOI: 10.1063/1.3521275.

[10] K. Lee, É. D. Murray, L. Kong, B. I. Lundqvist, and D. C. Langreth, *Higher-accuracy van der Waals density functional*, Phys. Rev. B **82**, 81101 (2010), DOI: 10.1103/PhysRevB.82.081101.

[11] D. Chakraborty, K. Berland, and T. Thonhauser, *Next-generation nonlocal van der Waals density functional*, J. Chem. Theory Comput. **16**, 5893 (2020), DOI: 10.1021/acs.jctc.0c00471.

[12] T. Jenkins, K. Berland, and T. Thonhauser, *Reduced-gradient analysis of van der Waals complexes*, Electron. Struct. **3**, 034009 (2021), DOI: 10.1088/2516-1075/ac25d7.

[13] L. Kronik and A. Tkatchenko, *Understanding molecular crystals with dispersion-inclusive density functional theory: Pairwise corrections and beyond*, Acc. Chem. Res. **47**, 3208 (2014), DOI: 10.1021/ar500144s.

[14] T. Rangel, K. Berland, S. Sharifzadeh, F. Brown-Altvater, K. Lee, P. Hyldgaard, L. Kronik, and J. B. Neaton, *Structural and excited-state properties of oligoacene crystals from first principles*, Phys. Rev. B **93**, 115206 (2016), DOI: 10.1103/PhysRevB.93.115206.

[15] P. J. Diemer, J. Hayes, E. Welchman, R. Hallani, S. J. Pookpanratana, C. A. Hacker, C. A. Richter, J. E. Anthony, T. Thonhauser, and O. D. Jurchescu, *The influence of isomer purity on trap states and performance of organic thin-film transistors*, Adv. Electron. Mater. **3**, 1600294 (2017), DOI: 10.1002/aelm.201600294.

[16] R. Gomez-Bombarelli, J. Aguilera-Iparraguirre, T. D. Hirzel, D. Duvenaud, D. Maclaurin, M. A. Blood-Forsythe, H. S. Chae, M. Einzinger, D.-G. Ha, T. Wu,

G. Markopoulos, S. Jeon, H. Kang, H. Miyazaki, M. Numata, S. Kim, W. Huang, S. I. Hong, M. Baldo, R. P. Adams, and A. Aspuru-Guzik, *Design of efficient molecular organic light-emitting diodes by a high-throughput virtual screening and experimental approach*, Nat. Mater. **15**, 1120 (2016), DOI: 10.1038/nmat4717.

[17] K. Lee, B. Kolb, T. Thonhauser, D. Vanderbilt, and D. C. Langreth, *Structure and energetics of a ferroelectric organic crystal of phenazine and chloranilic acid*, Phys. Rev. B **86**, 104102 (2012), DOI: 10.1103/PhysRevB.86.104102.

[18] S. Ishibashi, S. Horiuchi, and R. Kumai, *Computational findings of metastable ferroelectric phases of squaric acid*, Phys. Rev. B **97**, 184102 (2018), DOI: 10.1103/PhysRevB.97.184102.

[19] A. M. Reilly and A. Tkatchenko, *Role of dispersion interactions in the polymorphism and entropic stabilization of the aspirin crystal*, Phys. Rev. Lett. **113**, 055701 (2014), DOI: 10.1103/PhysRevLett.113.055701.

[20] K. Tan, S. Zuluaga, E. Fuentes, E. C. Mattson, J.-F. Veyan, H. Wang, J. Li, T. Thonhauser, and Y. J. Chabal, *Trapping gases in metal-organic frameworks with a selective surface molecular barrier layer*, Nat. Commun. **7**, 13871 (2016), DOI: 10.1038/ncomms13871.

[21] H. Wang, X. Dong, J. Lin, S. J. Teat, S. Jensen, J. Cure, E. V. Alexandrov, Q. Xia, K. Tan, Q. Wang, D. H. Olson, D. M. Proserpio, Y. J. Chabal, T. Thonhauser, J. Sun, Y. Han, and J. Li, *Topologically guided tuning of Zr-MOF pore structures for highly selective separation of C_6 alkane isomers*, Nat. Commun. **9**, 1745 (2018), DOI: 10.1038/s41467-018-04152-5.

[22] B. Li, X. Dong, H. Wang, D. Ma, K. Tan, S. Jensen, B. J. Deibert, J. Butler, J. Cure, Z. Shi, T. Thonhauser, Y. J. Chabal, Y. Han, and J. Li, *Capture of organic iodides from nuclear waste by metal-organic framework-based molecular traps*, Nat. Commun. **8**, 485 (2017), DOI: 10.1038/s41467-017-00526-3.

[23] S. Jensen, K. Tan, W. P. Lustig, D. S. Kilin, J. Li, Y. J. Chabal, and T. Thonhauser, *Structure-driven photoluminescence enhancement in a Zn-based metal-organic framework*, Chem. Mater. **31**, 7933 (2019), DOI: 10.1021/acs.chemmater.9b02056.

[24] J. Cure, E. Mattson, K. Cocq, H. Assi, S. Jensen, K. Tan, M. Catalano, S. Yuan, H. Wang, L. Feng, P. Zhang, S. Kwon, J.-F. Veyan, Y. Cabrera, G. Zhang, J. Li, M. Kim, H.-C. Zhou, Y. J. Chabal, and T. Thonhauser, *High stability of ultra-small and isolated gold nanoparticles in metal-organic framework materials*, J. Mater. Chem. A **7**, 17536 (2019), DOI: 10.1039/C8TA12334A.

[25] S. Grimme, *Accurate description of van der Waals complexes by density functional theory including empirical corrections*, J. Comput. Chem. **25**, 1463 (2004), DOI: 10.1002/jcc.20078.

[26] S. Grimme, J. Antony, T. Schwabe, and C. Mück-Lichtenfeld, *Density functional theory with dispersion corrections for supramolecular structures, aggregates, and complexes of (bio)organic molecules*, Org. Biomol. Chem. **5**, 741 (2007), DOI: 10.1039/b615319b.

[27] S. Grimme, *Density functional theory with London dispersion corrections*, WIREs Computational Molecular Science **1**, 211 (2011), DOI: 10.1002/wcms.30.

[28] A. Tkatchenko and M. Scheffler, *Accurate molecular van der Waals interactions from ground-state electron density and free-atom reference data*, Phys. Rev. Lett. **102**, 073005 (2009), DOI: 10.1103/PhysRevLett.102.073005.

[29] A. Tkatchenko, R. A. DiStasio, R. Car, and M. Scheffler, *Accurate and efficient method for many-body van der Waals interactions*, Phys. Rev. Lett. **108**, 236402 (2012), DOI: 10.1103/PhysRevLett.108.236402.

[30] A. Ambrosetti, A. M. Reilly, R. A. DiStasio, and A. Tkatchenko, *Long-range correlation energy calculated from coupled atomic response functions*, J. Chem. Phys. **140**, 18A508 (2014), DOI: 10.1063/1.4865104.

[31] A. Ambrosetti, N. Ferri, R. A. DiStasio, and A. Tkatchenko, *Wavelike charge density fluctuations and van der Waals interactions at the nanoscale*, Science **351**, 1171 (2016), DOI: 10.1126/science.aae0509.

[32] O. A. Vydrov and T. Van Voorhis, *Nonlocal van der Waals density functional made simple*, Phys. Rev. Lett. **103**, 063004 (2009), DOI: 10.1103/PhysRevLett.103.063004.

[33] O. A. Vydrov and T. Van Voorhis, *Dispersion interactions from a local polarizability model*, Phys. Rev. A **81**, 062708 (2010), DOI: 10.1103/PhysRevA.81.062708.

[34] S. Grimme, A. Hansen, J. G. Brandenburg, and C. Bannwarth, *Dispersion-corrected mean-field electronic structure methods*, Chem. Rev. **116**, 5105 (2016), DOI: 10.1021/acs.chemrev.5b00533.

[35] K. Szalewicz, *Symmetry-adapted perturbation theory of intermolecular forces*, WIREs Comput. Mol. Sci. **2**, 254 (2012), DOI: 10.1002/wcms.86.

[36] L. A. Burns, A. Vazquez-Mayagoitia, B. G. Sumpter, and C. D. Sherrill, *Density-functional approaches to noncovalent interactions: A comparison of dispersion corrections (DFT-D), exchange-hole dipole moment (XDM) theory, and specialized functionals*, J. Chem. Phys. **134**, 084107 (2011), DOI: 10.1063/1.3545971.

[37] J. Klimeš and A. Michaelides, *Perspective: Advances and challenges in treating van der Waals dispersion forces in density functional theory*, J. Chem. Phys. **137**, 120901 (2012), DOI: 10.1063/1.4754130.

[38] T. Thonhauser, S. Zuluaga, C. A. Arter, K. Berland, E. Schröder, and P. Hyldgaard, *Spin signature of nonlocal correlation binding in metal-organic frameworks*, Phys. Rev. Lett. **115**, 136402 (2015), DOI: 10.1103/PhysRevLett.115.136402.

[39] D. C. Langreth, B. I. Lundqvist, S. D. Chakarova-Käck, V. R. Cooper, M. Dion, P. Hyldgaard, A. K. Kelkkanen, J. Kleis, L. Kong, S. Li, P. G. Moses, E. D. Murray, A. Puzder, H. Rydberg, E. Schröder, and T. Thonhauser, *A density functional for sparse matter*, J. Condens. Matter Phys. **21**, 084203 (2009), DOI: 10.1088/0953-8984/21/8/084203.

[40] K. Berland, V. R. Cooper, K. Lee, E. Schröder, T. Thonhauser, P. Hyldgaard, and B. I. Lundqvist, *van der Waals forces in density functional theory: a review of the vdW-DF method*, Rep. Prog. Phys. **78**, 066501 (2015), DOI: 10.1088/0034-4885/78/6/066501.

[41] P. Hyldgaard, Y. Jiao, and V. Shukla, *Screening nature of the van der Waals density functional method: A review and analysis of the many-body physics foundation*, J. Condens. Matter Phys. **32**, 393001 (2020), DOI: 10.1088/1361-648X/ab8250.

[42] D. J. Lacks and R. G. Gordon, *Pair interactions of rare-gas atoms as a test of exchange-energy-density functionals in regions of large density gradients*, Phys. Rev. A **47**, 4681 (1993), DOI: 10.1103/PhysRevA.47.4681.

[43] Y. Zhang, W. Pan, and W. Yang, *Describing van der Waals interaction in diatomic molecules with generalized gradient approximations: The role of the exchange functional*, J. Chem. Phys. **107**, 7921 (1997), DOI: 10.1063/1.475105.

[44] F. O. Kannemann and A. D. Becke, *van der Waals interactions in density-functional theory: Rare-gas diatomics*, J. Chem. Theory Comput. **5**, 719 (2009), DOI: 10.1021/ct800522r.

[45] É. D. Murray, K. Lee, and D. C. Langreth, *Investigation of exchange energy density functional accuracy for interacting molecules*, J. Chem. Theory Comput. **5**, 2754 (2009), DOI: 10.1021/ct900365q.

[46] R. Laplaza, F. Peccati, R. A. Boto, C. Quan, A. Carbone, J.-P. Piquemal, Y. Maday, and J. Contreras-García, *NCIPLOT and the analysis of noncovalent interactions using the reduced density gradient*, WIREs Comput. Mol. Sci. **11**, e1497 (2021), DOI: 10.1002/wcms.1497.

[47] E. R. Johnson, S. Keinan, P. Mori-Sánchez, J. Contreras-García, A. J. Cohen, and W. Yang, *Revealing noncovalent interactions*, J. Am. Chem. Soc. **132**, 6498 (2010), DOI: 10.1021/ja100936w.

[48] H. Rydberg, *Nonlocal Correlations in Density Functional Theory*, Ph.D. thesis, Chalmers University of Technology and Göteborg University (2001).

[49] K. Berland, *Connected by Voids: Interactions and Screening in Sparse Matter*, Ph.D. thesis, Chalmers University of Technology (2012).

[50] P. Hyldgaard, K. Berland, and E. Schröder, *Interpretation of van der Waals density functionals*, Phys. Rev. B **90**, 075148 (2014), DOI: 10.1103/PhysRevB.90.075148.

[51] E. Schröder, V. R. Cooper, K. Berland, B. I. Lundqvist, P. Hyldgaard, and T. Thonhauser, *The vdW-DF family of nonlocal exchange-correlation functionals*, in A. O. de la Roza and G. A. DiLabio, eds., *Non-Covalent Interactions in Quantum Chemistry and Physics, Theory Applications*, chapter 8, pp. 241–274, (Elsevier, Amsterdam2017), DOI: 10.1016/B978-0-12-809835-6.00009-8.

[52] J. P. Perdew, M. Ernzerhof, and K. Burke, *Rationale for mixing exact exchange with density functional approximations*, J. Chem. Phys. **105**, 9982 (1996), DOI: 10.1063/1.472933.

[53] P. J. Stephens, F. J. Devlin, C. F. Chabalowski, and M. J. Frisch, *Ab initio calculation of vibrational absorption and circular dichroism spectra using density functional force fields*, J. Phys. Chem. **98**, 11623 (1994), DOI: 10.1021/j100096a001.

[54] S. Grimme, J. Antony, S. Ehrlich, and H. Krieg, *A consistent and accurate ab initio parametrization of density functional dispersion correction (DFT-D) for the 94 elements H-Pu*, J. Chem. Phys. **132**, 154104 (2010), DOI: 10.1063/1.3382344.

[55] J. P. Perdew, K. Burke, and Y. Wang, *Generalized gradient approximation for the exchange-correlation hole of a many-electron system*, Phys. Rev. B **54**, 16533 (1996), DOI: 10.1103/PhysRevB.54.16533.

[56] Y. Zhang and W. Yang, *Comment on "Generalized gradient approximation made simple"*, Phys. Rev. Lett. **80**, 890 (1998), DOI: 10.1103/PhysRevLett.80.890.

[57] I. Hamada and M. Otani, *Comparative van der Waals density-functional study of graphene on metal surfaces*, Phys. Rev. B **82**, 153412 (2010), DOI: 10.1103/PhysRevB.82.153412.

[58] H. Yildirim, T. Greber, and A. Kara, *Trends in adsorption characteristics of benzene on transition metal surfaces: Role of surface chemistry and van der Waals interactions*, J. Phys. Chem. C **117**, 20572 (2013), DOI: 10.1021/jp404487z.

[59] W. Liu, J. Carrasco, B. Santra, A. Michaelides, M. Scheffler, and A. Tkatchenko, *Benzene adsorbed on metals: Concerted effect of covalency and van der Waals bonding*, Phys. Rev. B **86**, 245405 (2012), DOI: 10.1103/PhysRevB.86.245405.

[60] K. Berland, C. A. Arter, V. R. Cooper, K. Lee, B. I. Lundqvist, E. Schröder, T. Thonhauser, and P. Hyldgaard, *van der Waals density functionals built upon the electron-gas tradition: Facing the challenge of competing interactions*, J. Chem. Phys. **140**, 18A539 (2014), DOI: 10.1063/1.4871731.

[61] V. R. Cooper, *Van der Waals density functional: An appropriate exchange functional*, Phys. Rev. B **81**, 161104 (2010), DOI: 10.1103/PhysRevB.81.161104.

[62] R. M. Martin, *Electronic Structure: Basic Theory and Practical Methods*, (Cambridge University Press 2004), DOI: 10.1017/CBO9780511805769.

[63] L. C. Balbás, J. L. Martins, and J. M. Soler, *Evaluation of exchange-correlation energy, potential, and stress*, Phys. Rev. B **64**, 165110 (2001), DOI: 10.1103/PhysRevB.64.165110.

[64] P. Giannozzi, O. Andreussi, T. Brumme, O. Bunau, M. Buongiorno Nardelli, M. Calandra, R. Car, C. Cavazzoni, D. Ceresoli, M. Cococcioni, N. Colonna, I. Carnimeo, A. Dal Corso, S. de Gironcoli, P. Delugas, R. A. DiStasio Jr, A. Ferretti, A. Floris, G. Fratesi, G. Fugallo, R. Gebauer, U. Gerstmann, F. Giustino, T. Gorni, J. Jia, M. Kawamura, H.-Y. Ko, A. Kokalj, E. Küçükbenli, M. Lazzeri, M. Marsili, N. Marzari, F. Mauri, N. L. Nguyen, H.-V. Nguyen, A. Otero-de-la Roza, L. Paulatto, S. Poncé, D. Rocca, R. Sabatini, B. Santra, M. Schlipf, A. P. Seitsonen, A. Smogunov, I. Timrov, T. Thonhauser, P. Umari, N. Vast, X. Wu, and S. Baroni, *Advanced capabilities for materials modelling with Quantum ESPRESSO*, J. Condens. Matter Phys. **29**, 465901 (2017), DOI: 10.1088/1361-648X/aa8f79.

[65] K. F. Garrity, J. W. Bennett, K. M. Rabe, and D. Vanderbilt, *Pseudopotentials for high-throughput DFT calculations*, Comput. Mater. Sci. **81**, 446 (2014), DOI: 10.1016/j.commatsci.2013.08.053.

[66] H. Peng, Z.-H. Yang, J. P. Perdew, and J. Sun, *Versatile van der Waals density functional based on a meta-generalized gradient approximation*, Phys. Rev. X **6**, 041005 (2016), DOI: 10.1103/PhysRevX.6.041005.

[67] T. Björkman, A. Gulans, A. V. Krasheninnikov, and R. M. Nieminen, *van der Waals bonding in layered compounds from advanced density-functional first-principles calculations*, Phys. Rev. Lett. **108**, 235502 (2012), DOI: 10.1103/PhysRevLett.108.235502.

[68] T. Björkman, *Testing several recent van der Waals density functionals for layered structures*, J. Chem. Phys. **141**, 074708 (2014), DOI: 10.1063/1.4893329.

[69] A. M. Reilly and A. Tkatchenko, *Understanding the role of vibrations, exact exchange, and many-body van der Waals interactions in the cohesive properties of molecular crystals*, J. Chem. Phys. **139**, 024705 (2013), DOI: 10.1063/1.4812819.

[70] K. Berland, T. L. Einstein, and P. Hyldgaard, *Rings sliding on a honeycomb network: Adsorption contours, interactions, and assembly of benzene on Cu(111)*, Phys. Rev. B **80**, 155431 (2009), DOI: 10.1103/PhysRevB.80.155431.

[71] L. Gráfová, M. Pitoňák, J. Řezáč, and P. Hobza, *Comparative study of selected wave function and density functional methods for noncovalent interaction energy calculations using the extended S22 data set*, J. Chem. Theory Comput. **6**, 2365 (2010), DOI: 10.1021/ct1002253.

[72] J. Klimeš, D. R. Bowler, and A. Michaelides, *Chemical accuracy for the van der Waals density functional*, J. Condens. Matter Phys. **22**, 022201 (2010), DOI: 10.1088/0953-8984/22/2/022201.

[73] K. Berland and P. Hyldgaard, *Exchange functional that tests the robustness of the plasmon description of the van der Waals density functional*, Phys. Rev. B **89**, 035412 (2014), DOI: 10.1103/PhysRevB.89.035412.

[74] I. Hamada, *van der Waals density functional made accurate*, Phys. Rev. B **89**, 121103 (2014), DOI: 10.1103/PhysRevB.89.121103.

[75] J. P. Perdew and Y. Wang, *Accurate and simple density functional for the electronic exchange energy: Generalized gradient approximation*, Phys. Rev. B **33**, 8800 (1986), DOI: 10.1103/PhysRevB.33.8800.

[76] P. Jurecka, J. Sponer, J. Cerny, and P. Hobza, *Benchmark database of accurate (MP2 and CCSD(T) complete basis set limit) interaction energies of small model complexes, DNA base pairs, and amino acid pairs*, Phys. Chem. Chem. Phys. **8**, 1985 (2006), DOI: 10.1039/B600027D.

[77] K. Berland and P. Hyldgaard, *Analysis of van der Waals density functional components: Binding and corrugation of benzene and C_{60} on boron nitride and graphene*, Phys. Rev. B **87**, 205421 (2013), DOI: 10.1103/PhysRevB.87.205421.

[78] F. Tran, L. Kalantari, B. Traoré, X. Rocquefelte, and P. Blaha, *Nonlocal van der Waals functionals for solids: Choosing an appropriate one*, Phys. Rev. B **3**, 063602 (2019), DOI: 10.1103/PhysRevMaterials.3.063602.

[79] T. Bjorkman, A. Gulans, A. V. Krasheninnikov, and R. M. Nieminen, *Are we van der Waals ready?*, J. Condens. Matter Phys. **24**, 424218 (2012), DOI: 10.1088/0953-8984/24/42/424218.

[80] J. Moellmann and S. Grimme, *DFT-D3 study of some molecular crystals*, J. Phys. Chem. C **118**, 7615 (2014), DOI: 10.1021/jp501237c.

[81] T. Jenkins, D. Chakraborty, K. Berland, and T. Thonhauser, *Reduced-gradient analysis of molecular adsorption on graphene with nonlocal density functionals*, Phys. Rev. B **109**, 035427 (2024), DOI: 10.1103/PhysRevB.109.035427.

[82] Y. Tang, Z. Yang, and X. Dai, *A theoretical simulation on the catalytic oxidation of CO on Pt/graphene*, Phys. Chem. Chem. Phys. **14**, 16566 (2012), DOI: 10.1039/c2cp41441d.

[83] M. Groves, A. Chan, C. Malardier-Jugroot, and M. Jugroot, *Improving platinum catalyst binding energy to graphene through nitrogen doping*, Chem. Phys. Lett. **481**, 214 (2009), DOI: 10.1016/j.cplett.2009.09.074.

[84] K. Takeuchi, S. Yamamoto, Y. Hamamoto, Y. Shiozawa, K. Tashima, H. Fukidome, T. Koitaya, K. Mukai, S. Yoshimoto, M. Suemitsu, Y. Morikawa, J. Yoshinobu, and I. Matsuda, *Adsorption of CO_2 on graphene: A combined TPD, XPS, and vdW-DF study*, J. Phys. Chem. C **121**, 2807 (2017), DOI: 10.1021/acs.jpcc.6b11373.

[85] J. Ma, A. Michaelides, D. Alfè, L. Schimka, G. Kresse, and E. Wang, *Adsorption and diffusion of water on graphene from first principles*, Phys. Rev. B **84**, 033402 (2011), DOI: 10.1103/PhysRevB.84.033402.

[86] I. Hamada, *Adsorption of water on graphene: A van der Waals density functional study*, Phys. Rev. B **86**, 195436 (2012), DOI: 10.1103/PhysRevB.86.195436.

[87] K. R. Paserba and A. J. Gellman, *Effects of conformational isomerism on the desorption kinetics of n-alkanes from graphite*, J. Chem. Phys. **115**, 6737 (2001), DOI: 10.1063/1.1398574.

[88] R. Zhang, X. Yu, Q. Yang, G. Cui, and Z. Li, *The role of graphene in anti-corrosion coatings: A review*, Construction and Building Materials **294**, 123613 (2021), DOI: 10.1016/j.conbuildmat.2021.123613.

[89] D. J. Burke and W. A. Brown, *Ice in space: surface science investigations of the thermal desorption of model interstellar ices on dust grain analogue surfaces*, Phys. Chem. Chem. Phys. **12**, 5947 (2010), DOI: 10.1039/b917005g.

[90] F. Schedin, A. K. Geim, S. V. Morozov, E. W. Hill, P. Blake, M. I. Katsnelson, and K. S. Novoselov, *Detection of individual gas molecules adsorbed on graphene*, Nat. Mater. **6**, 652 (2007), DOI: 10.1038/nmat1967.

[91] Y. Dan, Y. Lu, N. J. Kybert, Z. Luo, and A. T. C. Johnson, *Intrinsic response of graphene vapor sensors*, Nano Lett. **9**, 1472 (2009), DOI: 10.1021/nl8033637.

[92] A. Paton-Carrero, P. Sanchez, L. Sánchez-Silva, and A. Romero, *Graphene-based materials behaviour for dyes adsorption*, Mater. Today Commun. **30**, 103033 (2022), DOI: 10.1016/j.mtcomm.2021.103033.

[93] M. Sweetman, S. May, N. Mebberson, P. Pendleton, K. Vasilev, S. Plush, and J. Hayball, *Activated carbon, carbon nanotubes and graphene: Materials and composites for advanced water purification*, C-J. Carbon Res. **3**, 18 (2017), DOI: 10.3390/c3020018.

[94] Y. Xu, H. Bai, G. Lu, C. Li, and G. Shi, *Flexible graphene films via the filtration of water-soluble noncovalent functionalized graphene sheets*, J. Am. Chem. Soc. **130**, 5856 (2008), DOI: 10.1021/ja800745y.

[95] Y. Han, Z. Xu, and C. Gao, *Ultrathin graphene nanofiltration membrane for water purification*, Adv. Funct. Mater. **23**, 3693 (2013), DOI: 10.1002/adfm.201202601.

[96] A. Aghigh, V. Alizadeh, H. Wong, M. S. Islam, N. Amin, and M. Zaman, *Recent advances in utilization of graphene for filtration and desalination of water: A review*, Desalination **365**, 389 (2015), DOI: 10.1016/j.desal.2015.03.024.

[97] D. B. Wells, M. Belkin, J. Comer, and A. Aksimentiev, *Assessing graphene nanopores for sequencing DNA*, Nano Lett. **12**, 4117 (2012), DOI: 10.1021/nl301655d.

[98] S. J. Heerema and C. Dekker, *Graphene nanodevices for DNA sequencing*, Nat. Nanotechnol. **11**, 127 (2016), DOI: 10.1038/nnano.2015.307.

[99] H. W. C. Postma, *Rapid sequencing of individual DNA molecules in graphene nanogaps*, Nano Lett. **10**, 420 (2010), DOI: 10.1021/nl9029237.

[100] Z. Wang, S. Wu, L. Colombi Ciacchi, and G. Wei, *Graphene-based nanoplatforms for surface-enhanced raman scattering sensing*, The Analyst **143**, 5074 (2018), DOI: 10.1039/C8AN01266K.

[101] K. Burke, *Perspective on density functional theory*, J. Chem. Phys. **136**, 150901 (2012), DOI: 10.1063/1.4704546.

[102] S. F. Sousa, P. A. Fernandes, and M. J. Ramos, *General performance of density functionals*, J. Phys. Chem. A **111**, 10439 (2007), DOI: 10.1021/jp0734474.

[103] A. Pribram-Jones, D. A. Gross, and K. Burke, *DFT: A theory full of holes?*, Annual Rev. Phys. Chem. **66**, 283 (2015), DOI: 10.1146/annurev-physchem-040214-121420.

[104] S. Tsuzuki, H. Houjou, Y. Nagawa, M. Goto, and K. Hiratani, *Cooperative enhancement of water binding to crownophane by multiple hydrogen bonds: Analysis by high level ab initio calculations*, J. Am. Chem. Soc. **123**, 4255 (2001), DOI: 10.1021/ja0037264.

[105] U. Zimmerli, M. Parrinello, and P. Koumoutsakos, *Dispersion corrections to density functionals for water aromatic interactions*, J. Chem. Phys. **120**, 2693 (2004), DOI: 10.1063/1.1637034.

[106] M. J. Allen and D. J. Tozer, *Helium dimer dispersion forces and correlation potentials in density functional theory*, J. Chem. Phys. **117**, 11113 (2002), DOI: 10.1063/1.1522715.

[107] A. Tkatchenko and O. A. von Lilienfeld, *Adsorption of Ar on graphite using London dispersion forces corrected Kohn-Sham density functional theory*, Phys. Rev. B **73**, 153406 (2006), DOI: 10.1103/PhysRevB.73.153406.

[108] S. Grimme, *Semiempirical GGA-type density functional constructed with a long-range dispersion correction*, J. Comput. Chem. **27**, 1787 (2006), DOI: 10.1002/jcc.20495.

[109] E. Caldeweyher, S. Ehlert, A. Hansen, H. Neugebauer, S. Spicher, C. Bannwarth, and S. Grimme, *A generally applicable atomic-charge dependent London dispersion correction*, J. Chem. Phys. **150**, 154122 (2019), DOI: 10.1063/1.5090222.

[110] Y. Zhao and D. G. Truhlar, *A new local density functional for main-group thermochemistry, transition metal bonding, thermochemical kinetics, and noncovalent interactions*, J. Chem. Phys. **125**, 194101 (2006), DOI: 10.1063/1.2370993.

[111] J. W. Furness, A. D. Kaplan, J. Ning, J. P. Perdew, and J. Sun, *Accurate and numerically efficient r^2SCAN meta-generalized gradient approximation*, J. Phys. Chem. Lett. **11**, 8208 (2020), DOI: 10.1021/acs.jpclett.0c02405.

[112] K. Berland, D. Chakraborty, and T. Thonhauser, *van der Waals density functional with corrected C_6 coefficients*, Phys. Rev. B **99**, 195418 (2019), DOI: 10.1103/PhysRevB.99.195418.

[113] K. Berland, Y. Jiao, J.-H. Lee, T. Rangel, J. B. Neaton, and P. Hyldgaard, *Assessment of two hybrid van der Waals density functionals for covalent and non-covalent binding of molecules*, J. Chem. Phys. **146**, 234106 (2017), DOI: 10.1063/1.4986522.

[114] V. Shukla, Y. Jiao, J.-h. Lee, E. Schröder, J. B. Neaton, and P. Hyldgaard, *Accurate nonempirical range-separated hybrid van der Waals density functional for complex molecular problems, solids, and surfaces*, Phys. Rev. X **12**, 041003 (2022), DOI: 10.1103/PhysRevX.12.041003.

[115] R. Sabatini, T. Gorni, and S. de Gironcoli, *Nonlocal van der Waals density functional made simple and efficient*, Phys. Rev. B **87**, 041108 (2013), DOI: 10.1103/PhysRevB.87.041108.

[116] S. D. Chakarova-Käck, E. Schröder, B. I. Lundqvist, and D. C. Langreth, *Application of van der Waals density functional to an extended system: Adsorption of benzene and naphthalene on graphite*, Phys. Rev. Lett. **96**, 146107 (2006), DOI: 10.1103/PhysRevLett.96.146107.

[117] Ø. Borck and E. Schröder, *Methylbenzenes on graphene*, Surf. Sci. **664**, 162 (2017), DOI: 10.1016/j.susc.2017.06.012.

[118] E. Schröder, *Methanol adsorption on graphene*, J. Nanomater. **2013**, 1 (2013), DOI: 10.1155/2013/871706.

[119] E. Londero, E. K. Karlson, M. Landahl, D. Ostrovskii, J. D. Rydberg, and E. Schröder, *Desorption of n-alkanes from graphene: a van der Waals density functional study*, J. Condens. Matter Phys. **24**, 424212 (2012), DOI: 10.1088/0953-8984/24/42/424212.

[120] D. Le, A. Kara, E. Schröder, P. Hyldgaard, and T. S. Rahman, *Physisorption of nucleobases on graphene: a comparative van der Waals study*, J. Condens. Matter Phys. **24**, 424210 (2012), DOI: 10.1088/0953-8984/24/42/424210.

[121] J. Åkesson, O. Sundborg, O. Wahlström, and E. Schröder, *A van der Waals density functional study of chloroform and other trihalomethanes on graphene*, J. Chem. Phys. **137**, 174702 (2012), DOI: 10.1063/1.4764356.

[122] K. Berland, S. D. Chakarova-Käck, V. R. Cooper, D. C. Langreth, and E. Schröder, *A van der Waals density functional study of adenine on graphene: single-molecular adsorption and overlayer binding*, J. Condens. Matter Phys. **23**, 135001 (2011), DOI: 10.1088/0953-8984/23/13/135001.

[123] S. D. Chakarova-Käck, Ø. Borck, E. Schröder, and B. I. Lundqvist, *Adsorption of phenol on graphite(0001) and α-Al_2O_3(0001): Nature of van der Waals bonds from first-principles calculations*, Phys. Rev. B **74**, 155402 (2006), DOI: 10.1103/PhysRevB.74.155402.

[124] R. S. Smith, R. A. May, and B. D. Kay, *Desorption kinetics of Ar, Kr, Xe, N_2, O_2, CO, methane, ethane, and propane from graphene and amorphous solid water surfaces*, J. Phys. Chem. B **120**, 1979 (2016), DOI: 10.1021/acs.jpcb.5b10033.

[125] T. R. Rybolt, D. L. Logan, M. W. Millburn, H. E. Thomas, and A. B. Waters, *Correlations of Henry's law gas-solid virial coefficients and chromatographic retention times for hydrocarbons and halocarbons adsorbed on carbopack C carbon*, J. Colloid Interface Sci. **220**, 148 (1999), DOI: 10.1006/jcis.1999.6522.

[126] S. L. Tait, Z. Dohnálek, C. T. Campbell, and B. D. Kay, *n-alkanes on Pt(111) and on C(0001)/Pt(111): Chain length dependence of kinetic desorption parameters*, J. Chem. Phys. **125**, 234308 (2006), DOI: 10.1063/1.2400235.

[127] R. Zacharia, H. Ulbricht, and T. Hertel, *Interlayer cohesive energy of graphite from thermal desorption of polyaromatic hydrocarbons*, Phys. Rev. B **69**, 155406 (2004), DOI: 10.1103/PhysRevB.69.155406.

[128] N. Varghese, U. Mogera, A. Govindaraj, A. Das, P. K. Maiti, A. K. Sood, and C. N. R. Rao, *Binding of DNA nucleobases and nucleosides with graphene*, ChemPhysChem **10**, 206 (2009), DOI: 10.1002/cphc.200800459.

[129] P. A. Redhead, *Thermal desorption of gases*, Vacuum **12**, 274 (1962), DOI: 10.1016/0042-207X(62)90978-8.

[130] E. Freire, O. L. Mayorga, and M. Straume, *Isothermal titration calorimetry*, Anal. Chem. **62**, 950 (1990), DOI: 10.1016/B978-0-12-816548-5.00009-5.

[131] S. Greene and H. Past, *The determination of heats of adsorption by gas-solid chromatography*, J. Phys. Chem. **62**, 55 (1958), DOI: 10.1021/j150559a015.

[132] A. Zupan, J. P. Perdew, K. Burke, and M. Causa, *Density-gradient analysis for density functional theory: Application to atoms*, Int. J. Quantum Chem. **61**, 835 (1997), DOI: 10.1002/(SICI)1097-461X(1997)61:5⟨835::AID-QUA9⟩3.0.CO;2-X.

[133] Cortés-Arriagada, *Intermolecular driving forces on the adsorption of DNA/RNA nucleobases to graphene and phosphorene: An atomistic perspective from DFT calculations*, J. Mol. Liq. **325**, 115229 (2021), DOI: 10.1016/j.molliq.2020.115229.

[134] D. Cortés-Arriagada and D. E. Ortega, *Effects on the aromatic character of DNA/RNA nucleobases due to its adsorption onto graphene*, Int. J. Quantum Chem. **118**, e25699 (2018), DOI: 10.1002/qua.25699.

[135] J.-H. Lee, Y.-K. Choi, H.-J. Kim, R. H. Scheicher, and J.-H. Cho, *Physisorption of DNA nucleobases on h-BN and graphene: vdW-corrected DFT calculations*, J. Phys. Chem. C **117**, 13435 (2013), DOI: 10.1021/jp402403f.

[136] A. H. Castro Neto, F. Guinea, N. M. R. Peres, K. S. Novoselov, and A. K. Geim, *The electronic properties of graphene*, Rev. Mod. Phys. **81**, 109 (2009), DOI: 10.1103/RevModPhys.81.109.

[137] S. Tsuzuki, T. Kaneko, and K. Sodeyama, *Accuracy of intermolecular interaction energies, particularly those of hetero atom containing molecules obtained by van der*

Waals DFT calculations, ChemistrySelect **8**, e202203754 (2023), DOI: 10.1002/slct.202203754.

[138] J. Klimeš, D. R. Bowler, and A. Michaelides, *Van der Waals density functionals applied to solids*, Phys. Rev. B **83**, 195131 (2011), DOI: 10.1103/PhysRevB.83.195131.

[139] H.-Q. Yin, K. Tan, S. Jensen, S. J. Teat, S. Ullah, X. Hei, E. Velasco, K. Oyekan, N. Meyer, X.-Y. Wang, T. Thonhauser, X.-B. Yin, and J. Li, *A switchable sensor and scavenger: detection and removal of fluorinated chemical species by a luminescent metal–organic framework*, Chem. Sci. **12**, 14189 (2021), DOI: 10.1039/D1SC04070G.

[140] K. Tan, S. Ullah, H. Pandey, E. M. Cedeño-Morales, H. Wang, K. Wang, H.-C. Zhou, J. Li, and T. Thonhauser, *Competitive adsorption of NH_3 and H_2O in metal-organic framework materials: MOF-74*, Chem. Mater. **34**, 7906 (2022), DOI: 10.1021/acs.chemmater.2c01637.

[141] Y. Lin, L. Yu, S. Ullah, X. Li, H. Wang, Q. Xia, T. Thonhauser, and J. Li, *Temperature-programmed separation of hexane isomers by a porous calcium chloranilate metal–organic framework*, Angew. Chem. Int. Ed. **61**, e202214060 (2022), DOI: 10.1002/anie.202214060.

[142] S. Ullah, K. Tan, D. Sensharma, N. Kumar, S. Mukherjee, A. A. Bezrukov, J. Li, M. J. Zaworotko, and T. Thonhauser, *CO_2 capture by hybrid ultramicroporous TIFSIX-3-Ni under humid conditions using non-equilibrium cycling*, Angew. Chem. Int. Ed. **61**, e202206613 (2022), DOI: 10.1002/anie.202206613.

[143] E. Velasco, G. Zhang, S. J. Teat, K. Tan, S. Ullah, T. Thonhauser, and J. Li, *Luminescent metal–organic framework for the selective detection of aldehydes*, Inorg. Chem. **62**, 16435 (2023), DOI: 10.1021/acs.inorgchem.3c02115.

[144] O. A. Vydrov and T. Van Voorhis, *Improving the accuracy of the nonlocal van der Waals density functional with minimal empiricism*, J. Chem. Phys. **130**, 104105 (2009), DOI: 10.1063/1.3079684.

[145] D. R. Hamann, *Optimized norm-conserving Vanderbilt pseudopotentials*, Phys. Rev. B **88**, 085117 (2013), DOI: 10.1103/PhysRevB.88.085117.

[146] J. Řezáč, K. E. Riley, and P. Hobza, *S66: A well-balanced database of benchmark interaction energies relevant to biomolecular structures*, J. Chem. Theory Comput. **7**, 2427 (2011), DOI: 10.1021/ct2002946.

[147] L. Maschio, B. Civalleri, P. Ugliengo, and A. Gavezzotti, *Intermolecular interaction energies in molecular crystals: Comparison and agreement of localized Møller–Plesset 2, dispersion-corrected density functional, and classical empirical two-body calculations*, J. Phys. Chem. A **115**, 11179 (2011), DOI: 10.1021/jp203132k.

[148] M. Cutini, B. Civalleri, M. Corno, R. Orlando, J. G. Brandenburg, L. Maschio, and P. Ugliengo, *Assessment of different quantum mechanical methods for the prediction of structure and cohesive energy of molecular crystals*, J. Chem. Theory Comput. **12**, 3340 (2016), DOI: 10.1021/acs.jctc.6b00304.

[149] J. G. Brandenburg, T. Maas, and S. Grimme, *Benchmarking DFT and semiempirical methods on structures and lattice energies for ten ice polymorphs*, J. Chem. Phys. **142**, 124104 (2015), DOI: 10.1063/1.4916070.

[150] F. Della Pia, A. Zen, D. Alfè, and A. Michaelides, *DMC-ICE13: Ambient and high pressure polymorphs of ice from diffusion Monte Carlo and density functional theory*, J. Chem. Phys. **157**, 134701 (2022), DOI: 10.1063/5.0102645.

[151] J. G. Brandenburg and S. Grimme, *Organic crystal polymorphism: a benchmark for dispersion-corrected mean-field electronic structure methods*, Acta Cryst. **72**, 502 (2016), DOI: 10.1107/S2052520616007885.

[152] Z. H. Levine and S. G. Louie, *New model dielectric function and exchange-correlation potential for semiconductors and insulators*, Phys. Rev. B **25**, 6310 (1982).

[153] C. Gutle, A. Savin, J. B. Krieger, and J. Chen, *Correlation energy contributions from low-lying states to density functionals based on an electron gas with a gap*, Int. J.

Quantum Chem. **75**, 885 (1999), DOI: 10.1002/(SICI)1097-461X(1999)75:4/5⟨885::AID-QUA53⟩3.0.CO;2-F.

[154] D. C. Langreth and B. I. Lundqvist, *Comment on "nonlocal van der Waals density functional made simple"*, Phys. Rev. Lett. **104**, 099303 (2010), DOI: 10.1103/PhysRevLett.104.099303.

[155] A. Koide, *A new expansion for dispersion forces and its application*, J. Phys. B **9**, 3173 (1976), DOI: 10.1088/0022-3700/9/18/009.

[156] S. Ullah, T. Jenkins, K. Tan, J. Li, S. M. Winter, and T. Thonhauser, *Effect of entropic constraints on the thermodynamics of molecular adsorption in nano-porous materials*, Small p. 2412312 (2025), DOI: 10.1002/smll.202412312.

[157] L. Yu, S. Ullah, H. Wang, Q. Xia, T. Thonhauser, and J. Li, *High-capacity splitting of mono- and dibranched hexane isomers by a robust zinc-based metal–organic framework*, Angew. Chem. Int. Ed. **61**, e202211359 (2022), DOI: 10.1002/anie.202211359.

[158] D. S. Sholl and R. P. Lively, *Seven chemical separations to change the world*, Nature **532**, 435 (2016), DOI: 10.1038/532435a.

[159] R. A. Myers, *Handbook of Petroleum Refining Processes*, (McGraw-Hill, New York 2004).

[160] J.-R. Li, R. J. Kuppler, and H.-C. Zhou, *Selective gas adsorption and separation in metal–organic frameworks*, Chem. Soc. Rev. **38**, 1477 (2009), DOI: 10.1039/b802426j.

[161] F. Xie, L. Yu, H. Wang, and J. Li, *Metal–organic frameworks for C6 alkane separation*, Angew. Chem. Int. Ed. **62**, e202300722 (2023), DOI: 10.1002/anie.202300722.

[162] L. Yu, S. Ullah, K. Zhou, Q. Xia, H. Wang, S. Tu, J. Huang, H.-L. Xia, X.-Y. Liu, T. Thonhauser, and J. Li, *A microporous metal–organic framework incorporating both primary and secondary building units for splitting alkane isomers*, J. Am. Chem. Soc. **144**, 3766 (2022), DOI: 10.1021/jacs.1c12068.

[163] Z. R. Herm, B. M. Wiers, J. A. Mason, J. M. van Baten, M. R. Hudson, P. Zajdel, C. M. Brown, N. Masciocchi, R. Krishna, and J. R. Long, *Separation of hexane isomers in a metal-organic framework with triangular channels*, Science **340**, 960 (2013), DOI: 10.1126/science.1229369.

[164] L. Yu, X. Dong, Q. Gong, S. R. Acharya, Y. Lin, H. Wang, Y. Han, T. Thonhauser, and J. Li, *Splitting mono- and dibranched alkane isomers by a robust aluminum-based metal–organic framework material with optimal pore dimensions*, J. Am. Chem. Soc. **142**, 6925 (2020), DOI: 10.1021/jacs.0c01769.

[165] Z. Zhang, S. B. Peh, C. Kang, K. Chai, and D. Zhao, *Metal-organic frameworks for C6–C8 hydrocarbon separations*, EnergyChem **3**, 100057 (2021), DOI: 10.1016/j.enchem.2021.100057.

[166] W.-G. Cui, T.-L. Hu, and X.-H. Bu, *Metal–organic framework materials for the separation and purification of light hydrocarbons*, Adv. Mater. **32** (2020), DOI: 10.1002/adma.201806445.

[167] H. Wang, X. Dong, E. Velasco, D. H. Olson, Y. Han, and J. Li, *One-of-a-kind: A microporous metal–organic framework capable of adsorptive separation of linear, mono- and di-branched alkane isomers via temperature- and adsorbate-dependent molecular sieving*, Energy Environ. Sci. **11**, 1226 (2018), DOI: 10.1039/C8EE00459E.

[168] H. Wang and J. Li, *Microporous metal–organic frameworks for adsorptive separation of C5–C6 alkane isomers*, Acc. Chem. Res. **52**, 1968 (2019), DOI: 10.1021/acs.accounts.8b00658.

[169] F. Xie, L. Chen, E. M. Cedeño Morales, S. Ullah, Y. Fu, T. Thonhauser, K. Tan, Z. Bao, and J. Li, *Complete separation of benzene-cyclohexene-cyclohexane mixtures via temperature-dependent molecular sieving by a flexible chain-like coordination polymer*, Nat. Commun. **15**, 2240 (2024), DOI: 10.1038/s41467-024-46556-6.

[170] L. Yu, X. Han, H. Wang, S. Ullah, Q. Xia, W. Li, J. Li, I. da Silva, P. Manuel, S. Rudić, Y. Cheng, S. Yang, T. Thonhauser, and J. Li, *Pore distortion in a metal–*

organic framework for regulated separation of propane and propylene, J. Am. Chem. Soc. **143**, 19300 (2021), DOI: 10.1021/jacs.1c10423.

[171] L. Yu, J. Zhang, S. Ullah, J. Yao, H. Luo, J. Huang, Q. Xia, T. Thonhauser, J. Li, and H. Wang, *Separating xylene isomers with a calcium metal–organic framework*, Angew. Chem. Int. Ed. **62** (2023), DOI: 10.1002/anie.202310672.

[172] S. Ullah, S. Jensen, Y. Liu, K. Tan, H. Drake, G. Zhang, J. Huang, J. Klimeš, D. M. Driscoll, R. P. Hermann, H.-C. Zhou, J. Li, and T. Thonhauser, *Magnetically induced binary ferrocene with oxidized iron*, J. Am. Chem. Soc. **145**, 18029 (2023), DOI: 10.1021/jacs.3c05754.

[173] L. Kollias, D. C. Cantu, V.-A. Glezakou, R. Rousseau, and M. Salvalaglio, *On the role of enthalpic and entropic contributions to the conformational free energy landscape of MIL–101(Cr) secondary building units*, Adv. Theory Simul. **3**, 2000092 (2020), DOI: 10.1002/adts.202000092.

[174] F. Saiz and L. Bernasconi, *Entropic influence on the generation of Fe(IV)O species at mononuclear Fe(II) sites in metal–organic frameworks*, Catal. Sci. Technol. **13**, 5689 (2023), DOI: 10.1039/D3CY00392B.

[175] C. O. Arean, B. Bonelli, M. R. Delgado, and E. Garrone, *Hydrogen storage via physisorption: the combined role of adsorption enthalpy and entropy*, Turk. J. Chem. **33**, 599 (2009), DOI: 10.3906/kim-0812-22.

[176] L. Chen, J. P. Mowat, D. Fairen-Jimenez, C. A. Morrison, S. P. Thompson, P. A. Wright, and T. Düren, *Elucidating the breathing of the metal-organic framework mil-53(sc) with ab initio molecular dynamics simulations and in situ x-ray powder diffraction experiments*, J. Am. Chem. Soc. **135**, 15763 (2013), DOI: 10.1021/ja403453g.

[177] G. Kresse and J. Furthmüller, *Efficiency of ab-initio total energy calculations for metals and semiconductors using a plane-wave basis set*, Comput. Mater. Sci. **6**, 15 (1996), DOI: 10.1016/0927-0256(96)00008-0.

[178] S. Ullah and T. Thonhauser, *Flexible mofs as pressure-tunable filters for hydrocarbon separation*, J. Phys. Chem. C (2024), DOI: 10.1021/acs.jpcc.4c02559.

[179] S. Ullah, S. Jensen, K. Tan, G. Zhang, T. Jenkins, A. Elias, M. D. Gross, J. Li, and T. Thonhauser, *Decoding the gate opening mechanism of the flexible framework RPM3–Zn upon hydrocarbon inclusion*, Chem. Mater. **34**, 3246 (2022), DOI: 10.1021/acs.chemmater.2c00037.

[180] G. Mills, H. Jónsson, and G. K. Schenter, *Reversible work transition state theory: Application to dissociative adsorption of hydrogen*, Surf. Sci. **324**, 305 (1995), DOI: 10.1016/0039-6028(94)00731-4.

[181] G. Henkelman, B. P. Uberuaga, and H. Jonsson, *A climbing image nudged elastic band method for finding saddle points and minimum energy paths*, J. Chem. Phys. **113**, 9901 (2000).

[182] H. Wu, C. G. Thibault, H. Wang, K. A. Cychosz, M. Thommes, and J. Li, *Effect of temperature on hydrogen and carbon dioxide adsorption hysteresis in an ultramicroporous mof*, Micro. Meso. Mater. **219**, 186 (2016), DOI: 10.1016/j.micromeso.2015.08.005.

[183] N. Nijem, H. Wu, P. Canepa, A. Marti, K. J. Balkus, T. Thonhauser, J. Li, and Y. J. Chabal, *Tuning the gate opening pressure of metal–organic frameworks (MOFs) for the selective separation of hydrocarbons*, J. Am. Chem. Soc. **134**, 15201 (2012), DOI: 10.1021/ja305754f.

[184] J. A. Mason, J. Oktawiec, M. K. Taylor, M. R. Hudson, J. Rodriguez, J. E. Bachman, M. I. Gonzalez, A. Cervellino, A. Guagliardi, C. M. Brown, P. L. Llewellyn, N. Masciocchi, and J. R. Long, *Methane storage in flexible metal–organic frameworks with intrinsic thermal management*, Nature **527**, 357 (2015), DOI: 10.1038/nature15732.

[185] A. Schneemann, V. Bon, I. Schwedler, I. Senkovska, S. Kaskel, and R. A. Fischer, *Flexible metal–organic frameworks*, Chem. Soc. Rev. **43**, 6062 (2014), DOI: 10.1039/C4CS00101J.

[186] D. J. Griffiths and D. F. Schroeter, *Introduction to Quantum Mechanics*, (Cambridge University Press 2018), 3rd edition.

[187] J. P. Sethna, *Statistical Mechanics: Entropy, Order Parameters and Complexity*, (Oxford University Press 2006).

[188] L. E. Reichl, *A Modern Course in Statistical Physics*, (Wiley-VCH Verlag 1998), 2nd edition.

[189] M. Baus and C. F. Tejero, *Equilibrium Statistical Physics: Phases, Phase Transitions, and Topological Phases*, (Springer Nature Switzerland AG 2021).

[190] H. L. Friedman, *A Course in Statistical Mechanics*, (Pearson College Div 1985).

[191] S. R. Caskey, A. G. Wong-Foy, and A. J. Matzger, *Dramatic tuning of carbon dioxide uptake via metal substitution in a coordination polymer with cylindrical pores*, J. Am. Chem. Soc. **130**, 10870 (2008), DOI: 10.1021/ja8036096.

[192] N. L. Rosi, J. Eckert, M. Eddaoudi, D. T. Vodak, J. Kim, M. O'Keeffe, and O. M. Yaghi, *Hydrogen storage in microporous metal-organic frameworks*, Science **300**, 1127 (2003), DOI: 10.1126/science.1083440.

[193] G. Ferey, C. Mellot-Draznieks, C. Serre, F. Millange, J. Dutour, S. Surblé, and I. Margiolaki, *A chromium terephthalate-based solid with unusually large pore volumes and surface area*, Science **309**, 2040 (2005), DOI: 10.1126/science.1116275.

[194] T. Jenkins, A. M. Silva, M. G. Menezes, T. Thonhauser, and S. Ullah, *Thd-c sheet: A novel nonbenzenoid carbon allotrope with tetra-, hexa-, and dodeca-membered rings*, J. Phys. Chem. C **128**, 10982 (2024), DOI: 10.1021/acs.jpcc.4c01870.

[195] H. W. Kroto, J. R. Heath, S. C. O'Brien, R. F. Curl, and R. E. Smalley, *C_{60}: Buckminsterfullerene*, Letters to Nature **318**, 162 (1985).

[196] S. Iijima, *Helical microtubules of graphitic carbon*, Letters to Nature **354**, 56 (1991).

[197] G. Dresselhaus, M. S. Dresselhaus, and R. Saito, *Physical properties of carbon nanotubes*, (World scientific 1998).

[198] K. S. Novoselov, A. K. Geim, S. V. Morozov, D. Jiang, Y. Zhang, S. V. Dubonos, I. V. Grigorieva, and A. A. Firsov, *Electric field effect in atomically thin carbon films*, Science **306**, 666 (2004).

[199] M. A. Hudspeth, B. W. Whitman, V. Barone, and J. E. Peralta, *Electronic properties of the biphenylene sheet and its one-dimensional derivatives*, ACS Nano **4**, 4565 (2010), DOI: 10.1021/nn100758h.

[200] Q. Fan, L. Yan, M. W. Tripp, O. Krejčí, S. Dimosthenous, S. R. Kachel, M. Chen, A. S. Foster, U. Koert, P. Liljeroth, and J. M. Gottfried, *Biphenylene network: A nonbenzenoid carbon allotrope*, Science **372**, 852 (2021), DOI: 10.1126/science.abg4509.

[201] Y. Luo, C. Ren, Y. Xu, J. Yu, S. Wang, and M. Sun, *A first principles investigation on the structural, mechanical, electronic, and catalytic properties of biphenylene*, Sci. Rep. **11**, 19008 (2021), DOI: 10.1038/s41598-021-98261-9.

[202] Q. Song, B. Wang, K. Deng, X. Feng, M. Wagner, J. D. Gale, K. Müllen, and L. Zhi, *Graphenylene, a unique two-dimensional carbon network with nondelocalized cyclohexatriene units*, J. Mater. Chem. C **1**, 38 (2013), DOI: 10.1039/C2TC00006G.

[203] Y.-X. Yu, *Graphenylene: a promising anode material for lithium-ion batteries with high mobility and storage*, J. Mater. Chem. A **1**, 13559 (2013), DOI: 10.1039/c3ta12639k.

[204] Y. Liu, G. Wang, Q. Huang, L. Guo, and X. Chen, *Structural and electronic properties of T graphene: A two-dimensional carbon allotrope with tetrarings*, Phys. Rev. Lett. **108**, 225505 (2012), DOI: 10.1103/PhysRevLett.108.225505.

[205] Z. Tong, A. Pecchia, C. Yam, T. Dumitrică, and T. Frauenheim, *Ultrahigh electron thermal conductivity in T-graphene, biphenylene, and net-graphene*, Adv. Energy Mater. **12**, 2200657 (2022), DOI: 10.1002/aenm.202200657.

[206] Y. Fang, Y. Liu, L. Qi, Y. Xue, and Y. Li, *2D graphdiyne: an emerging carbon material*, Chem. Soc. Rev. **51**, 2681 (2022), DOI: 10.1039/D1CS00592H.

[207] X. Gao, H. Liu, D. Wang, and J. Zhang, *Graphdiyne: Synthesis, properties, and applications*, Chem. Soc. Rev. **48**, 908 (2019), DOI: 10.1039/C8CS00773J.

[208] H. Li, J. H. Lim, Y. Lv, N. Li, B. Kang, and J. Y. Lee, *Graphynes and graphdiynes for energy storage and catalytic utilization: Theoretical insights into recent advances*, Chem. Rev. **123**, 4795 (2023), DOI: 10.1021/acs.chemrev.2c00729.

[209] J.-T. Wang, C. Chen, H.-D. Li, H. Mizuseki, and Y. Kawazoe, *Three-dimensional carbon allotropes comprising phenyl rings and acetylenic chains in $sp + sp^2$ hybrid networks*, Sci. Rep. **6**, 24665 (2016), DOI: 10.1038/srep24665.

[210] Y. Wang, P. Yang, L. Zheng, X. Shi, and H. Zheng, *Carbon nanomaterials with sp^2 or/and sp hybridization in energy conversion and storage applications: A review*, Energy Storage Mater. **26**, 349 (2020), DOI: 10.1016/j.ensm.2019.11.006.

[211] S. Ullah, M. G. Menezes, and A. M. Silva, *Theoretical characterization of tolanene: A new 2D sp-sp^2 hybridized carbon allotrope*, Carbon **217**, 118618 (2024), DOI: 10.1016/j.carbon.2023.118618.

[212] Y. Xue, B. Huang, Y. Yi, Y. Guo, Z. Zuo, Y. Li, Z. Jia, H. Liu, and Y. Li, *Anchoring zero valence single atoms of nickel and iron on graphdiyne for hydrogen evolution*, Nat. Commun. **9**, 1460 (2018), DOI: 10.1038/s41467-018-03896-4.

[213] M. Zhao, L. Jiang, and Q. Yu, *Environmental applications of single-atom catalysts based on graphdiyne*, Catal. Sci. Technol. **13**, 5154 (2023), DOI: 10.1039/D3CY00240C.

[214] L. Li, R.-B. Lin, R. Krishna, H. Li, S. Xiang, H. Wu, J. Li, W. Zhou, and B. Chen, *Ethane/ethylene separation in a metal-organic framework with iron-peroxo sites*, Science **362**, 443 (2018), DOI: 10.1126/science.aat0586.

[215] I. Amghizar, L. A. Vandewalle, K. M. Van Geem, and G. B. Marin, *New trends in olefin production*, Engineering **3**, 171 (2017), DOI: 10.1016/J.ENG.2017.02.006.

[216] S. Chu, Y. Cui, and N. Liu, *The path towards sustainable energy*, Nat. Mater. **16**, 16 (2017), DOI: 10.1038/nmat4834.

[217] H. Schobert, *Production of acetylene and acetylene-based chemicals from coal*, Chem. Rev. **114**, 1743 (2014), DOI: 10.1021/cr400276u.

[218] P. J. Stang and F. Diederich, *Modern acetylene chemistry*, (John Wiley & Sons 2008).

[219] B. Singh, A. Saxena, A. K. Srivastava, and R. Vijayaraghavan, *Impregnated carbon based catalyst for protection against carbon monoxide gas*, Appl. Catal. B **88**, 257 (2009), DOI: 10.1016/j.apcatb.2008.11.016.

[220] Y. He, W. Zhou, G. Qian, and B. Chen, *Methane storage in metal-organic frameworks*, Chem. Soc. Rev. **43**, 5657 (2014), DOI: 10.1039/C4CS00032C.

[221] S. Chaemchuen, N. A. Kabir, K. Zhou, and F. Verpoort, *Metal-organic frameworks for upgrading biogas via CO_2 adsorption to biogas green energy*, Chem. Soc. Rev. **42**, 9304 (2013), DOI: 10.1039/c3cs60244c.

[222] H.-M. Wen, B. Li, L. Li, R.-B. Lin, W. Zhou, G. Qian, and B. Chen, *A metal-organic framework with optimized porosity and functional sites for high gravimetric and volumetric methane storage working capacities*, Adv. Mater. **30**, 1 (2018), DOI: 10.1002/adma.201704792.

[223] G. Kresse and D. Joubert, *From ultrasoft pseudopotentials to the projector augmented-wave method*, Phys. Rev. B **59**, 1758 (1999), DOI: 10.1103/PhysRevB.59.1758.

[224] P. E. Blöchl, *Projector augmented-wave method*, Phys. Rev. B **50**, 17953 (1994).

[225] G. Kresse and J. Furthmüller, *Efficiency of ab-initio total energy calculations for metals and semiconductors using a plane-wave basis set*, Comput. Mater. Sci. **6**, 15 (1996).

[226] H. J. Monkhorst and J. D. Pack, *Special points for brillouin-zone integrations*, Phys. Rev. B **13**, 5188 (1976).

[227] A. Togo, F. Oba, and I. Tanaka, *First-principles calculations of the ferroelastic transition between rutile-type and $CaCl_2$-type SiO_2 at high pressures*, Phys. Rev. B **78**, 134106 (2008), DOI: 10.1103/PhysRevB.78.134106.

[228] J. K. Nørskov, T. Bligaard, A. Logadottir, J. Kitchin, J. G. Chen, S. Pandelov, and U. Stimming, *Trends in the exchange current for hydrogen evolution*, J. Electrochem. Soc. **152**, J23 (2005).

[229] A. Savin, R. Nesper, S. Wengert, and T. F. Fässler, *ELF: The electron localization function*, Angew. Chem. Int. Ed. **36**, 1808 (1997), DOI: 10.1002/anie.199718081.

[230] J. Tersoff and D. R. Hamann, *Theory of the scanning tunneling microscope*, Phys. Rev. B **31**, 805 (1985), DOI: 10.1103/PhysRevB.31.805.

[231] J. Y. Jo and B. G. Kim, *Carbon allotropes with triple bond predicted by first-principle calculation: Triple bond modified diamond and T-carbon*, Phys. Rev. B **86**, 075151 (2012), DOI: 10.1103/PhysRevB.86.075151.

[232] F. Mouhat and F.-X. Coudert, *Necessary and sufficient elastic stability conditions in various crystal systems*, Phys. Rev. B **90**, 224104 (2014), DOI: 10.1103/PhysRevB.90.224104.

[233] X. Xu, B. Jiang, Y. Guo, and Y. Cai, *THD-graphene used for a selective gas detector*, Mater. Chem. and Phys. **200**, 50 (2017), DOI: 10.1016/j.matchemphys.2017.07.076.

[234] J. Kang, J. Li, F. Wu, S.-S. Li, and J.-B. Xia, *Elastic, electronic, and optical properties of two-dimensional graphyne sheet*, J. Phys. Chem. C **115**, 20466 (2011), DOI: 10.1021/jp206751m.

[235] L. Boeri, O. Dolgov, and A. A. Golubov, *Is $LaFeAsO_{1-x}F_x$ an electron-phonon superconductor?*, Phys. Rev. Lett. **101**, 026403 (2008).

[236] C.-H. Park, F. Giustino, C. D. Spataru, M. L. Cohen, and S. G. Louie, *Angle-resolved photoemission spectra of graphene from first-principles calculations*, Nano Lett. **9**, 4234 (2009).

[237] S. Ullah, P. A. Denis, and F. Sato, *Hydrogenation and fluorination of 2D boron phosphide and boron arsenide: A density functional theory investigation*, ACS Omega **3**, 16416 (2018), DOI: 10.1021/acsomega.8b02605.

[238] P. Rivera, J. R. Schaibley, A. M. Jones, J. S. Ross, S. Wu, G. Aivazian, P. Klement, K. Seyler, G. Clark, N. J. Ghimire, J. Yan, D. G. Mandrus, W. Yao, and X. Xu, *Observation of long-lived interlayer excitons in monolayer $MoSe_2$-WSe_2 heterostructures*, Nat. Commun. **6**, 6242 (2015), DOI: 10.1038/ncomms7242.

[239] Y. Jiang, S. Chen, W. Zheng, B. Zheng, and A. Pan, *Interlayer exciton formation, relaxation, and transport in TMD van der Waals heterostructures*, Light Sci. Appl. **10**, 72 (2021), DOI: 10.1038/s41377-021-00500-1.

[240] L. Jiao, L. Zhang, X. Wang, G. Diankov, and H. Dai, *Narrow graphene nanoribbons from carbon nanotubes*, Nature **458**, 877 (2009).

[241] X. Li, X. Wang, L. Zhang, S. Lee, and H. Dai, *Chemically derived, ultrasmooth graphene nanoribbon semiconductors*, Science **319**, 1229 (2008), DOI: 10.1126/science.1150878.

[242] Y.-W. Son, M. L. Cohen, and S. G. Louie, *Energy gaps in graphene nanoribbons*, Phys. Rev. Lett. **97**, 216803 (2006), DOI: 10.1103/PhysRevLett.97.216803.

[243] H. Dai, *Carbon nanotubes: opportunities and challenges*, Surf. Sci. **500**, 218 (2002), DOI: 10.1016/S0039-6028(01)01558-8.

[244] M. F. L. De Volder, S. H. Tawfick, R. H. Baughman, and A. J. Hart, *Carbon nanotubes: Present and future commercial applications*, Science **339**, 535 (2013), DOI: 10.1126/science.1222453.

[245] Y. Liu, B. V. Merinov, and W. A. Goddard III, *Origin of low sodium capacity in graphite and generally weak substrate binding of na and mg among alkali and alkaline earth metals*, PNAS **113**, 3735 (2016).

[246] S. Ullah, P. A. Denis, and F. Sato, *First-principles study of dual-doped graphene: Towards promising anode materials for Li/Na-ion batteries*, New J. Chem. **42**, 10842 (2018), DOI: 10.1039/C8NJ01098F.

[247] S. Ullah, P. A. Denis, and F. Sato, *Hexagonal boron phosphide as a potential anode nominee for alkali-based batteries: A multi-flavor DFT study*, Appl. Surf. Sci. **471**, 134 (2019), DOI: 10.1016/j.apsusc.2018.12.020.

[248] G. Henkelman, A. Arnaldsson, and H. Jónsson, *A fast and robust algorithm for Bader decomposition of charge density*, Comput. Mater. Sci. **36**, 354 (2006), DOI: 10.1016/j.commatsci.2005.04.010.

[249] H. Zhang, Y. Xia, H. Bu, X. Wang, M. Zhang, Y. Luo, and M. Zhao, *Graphdiyne: A promising anode material for lithium ion batteries with high capacity and rate capability*, J. Appl. Phys. **113**, 044309 (2013), DOI: 10.1063/1.4789635.

[250] D. Ferguson, D. J. Searles, and M. Hankel, *Biphenylene and phagraphene as lithium ion battery anode materials*, ACS Appl. Mater. Interfaces **9**, 20577 (2017), DOI: 10.1021/acsami.7b04170.

[251] X. Li, Q. Wang, and P. Jena, *ψ-graphene: a new metallic allotrope of planar carbon with potential applications as anode materials for lithium-ion batteries*, J. Phys. Chem. Lett. **8**, 3234 (2017).

[252] C. Kou, Y. Tian, M. Zhang, E. Zurek, X. Qu, X. Wang, K. Yin, Y. Yan, L. Gao, M. Lu, and W. Yang, *M-graphene: a metastable two-dimensional carbon allotrope*, 2D Mater. **7**, 025047 (2020), DOI: 10.1088/2053-1583/ab7977.

[253] R. Guo, C. Lv, W. Xu, J. Sun, Y. Zhu, X. Yang, J. Li, J. Sun, L. Zhang, and D. Yang, *Effect of intrinsic defects of carbon materials on the sodium storage performance*, Adv. Energy Mater. **10**, 1903652 (2020).

[254] S. Ullah, P. A. Denis, and F. Sato, *Unusual enhancement of the adsorption energies of sodium and potassium in sulfur-nitrogen and silicon-boron codoped graphene*, ACS omega **3**, 15821 (2018).

[255] H. B. Gray, *Powering the planet with solar fuel*, Nat. Chem. **1**, 7 (2009), DOI: 10.1038/nchem.141.

[256] J.-M. Savéant, *Molecular catalysis of electrochemical reactions. mechanistic aspects*, Chem. Rev. **108**, 2348 (2008).

[257] Y. Oh and X. Hu, *Organic molecules as mediators and catalysts for photocatalytic and electrocatalytic CO_2 reduction*, Chem. Soc. Rev. **42**, 2253 (2013), DOI: 10.1039/C2CS35276A.

[258] K. S. Walton and M. D. LeVan, *A novel adsorption cycle for co2 recovery: Experimental and theoretical investigations of a temperature swing compression process*, Separation science and technology **41**, 485 (2006).

[259] D. E. Jaramillo, H. Z. Jiang, H. A. Evans, R. Chakraborty, H. Furukawa, C. M. Brown, M. Head-Gordon, and J. R. Long, *Ambient-temperature hydrogen storage via vanadium (ii)-dihydrogen complexation in a metal–organic framework*, J. Am. Chem. Soc. **143**, 6248 (2021).

[260] K. Lee, J. D. Howe, L.-C. Lin, B. Smit, and J. B. Neaton, *Small-molecule adsorption in open-site metal–organic frameworks: A systematic density functional theory study for rational design*, Chem. Mater. **27**, 668 (2015), DOI: 10.1021/cm502760q.

[261] E. Chapman, S. Ullah, H. Wang, L. Feng, K. Wang, H.-C. Zhou, J. Li, T. Thonhauser, and K. Tan, *Tuning the adsorption properties of metal-organic frameworks through coadsorbed ammonia*, ACS Appl. Mater. Interfaces **13**, 43661 (2021), DOI: 10.1021/acsami.1c11876.

[262] I. Hamada and Y. Morikawa, *Density-functional analysis of hydrogen on Pt(111): Electric field, solvent, and coverage effects*, J. Phys. Chem. C **112**, 10889 (2008).

[263] A. Lan, K. Li, H. Wu, D. H. Olson, T. J. Emge, W. Ki, M. Hong, and J. Li, *A luminescent microporous metal–organic framework for the fast and reversible detection of high explosives*, Angew. Chem. Int. Ed. **48**, 2334 (2009), DOI: 10.1002/anie.200804853.

[264] F. Xie, L. Yu, T. Jenkins, J. Shutak, K. Tan, T. Thonhauser, H. Wang, and J. Li, *Nickel isonicotinate framework with optimal pore structure for complete discrimina-*

tion of hexane isomers, ACS Mater. Lett. **6**, 43 (2024), DOI: 10.1021/acsmaterialslett.3c01278.

[265] C. Volkringer, T. Loiseau, M. Haouas, F. Taulelle, D. Popov, M. Burghammer, C. Riekel, C. Zlotea, F. Cuevas, M. Latroche, D. Phanon, C. Knöfelv, P. L. Llewellyn, and G. Férey, *Occurrence of uncommon infinite chains consisting of edge-sharing octahedra in a porous metal organic framework-type aluminum pyromellitate $Al_4(OH)_8[C_{10}O_8H_2]$ (MIL-120): Synthesis, structure, and gas sorption properties*, Chem. Mater. **21**, 5783 (2009), DOI: 10.1021/cm9023106.

[266] H. Li, M. Eddaoudi, T. L. Groy, and O. M. Yaghi, *Establishing microporosity in open metal–organic frameworks: Gas sorption isotherms for Zn(BDC) (BDC = 1,4-benzenedicarboxylate)*, J. Am. Chem. Soc. **120**, 8571 (1998), DOI: 10.1021/ja981669x.

[267] F. Xie, L. Yu, T. Jenkins, T. Thonhauser, H. Wang, and J. Li, *Flexible layered metal–organic framework for temperature-dependent discrimination of cyclic hydrocarbons*, ACS Mater. Lett. **7**, 780 (2025), DOI: 10.1021/acsmaterialslett.4c02402.

[268] D. Sengupta, P. Melix, S. Bose, J. Duncan, X. Wang, M. R. Mian, K. O. Kirlikovali, F. Joodaki, T. Islamoglu, T. Yildirim, R. Q. Snurr, and O. K. Farha, *Air-stable Cu(I) metal–organic framework for hydrogen storage*, J. Am. Chem. Soc. **145**, 20492 (2023), DOI: 10.1021/jacs.3c06393.

[269] D. Sengupta, S. Bose, X. Wang, N. M. Schweitzer, C. D. Malliakas, H. Xie, J. Duncan, K. O. Kirlikovali, T. Yildirim, and O. K. Farha, *Integrated CO_2 capture and conversion by a robust Cu(I)-based metal–organic framework*, J. Am. Chem. Soc. **146**, 27006 (2024), DOI: 10.1021/jacs.4c08757.

Curriculum Vitae

Trevor Jenkins

Winston Salem, NC, USA jenktc19@wfu.edu +1 (919) 605-9953

ABOUT ME

I am a materials physicist with a focus on computational materials modeling using density functional theory. In my journey towards obtaining my physics Ph.D, I have used computational methods to characterize and predict functional materials—novel solids that are tailor-made to solve real-world problems. My work has required a keen understanding of computational physics and the strengths and weaknesses of its various applications. In particular, my research has emphasized the importance of the subtle dipole interactions within materials, which form the basis of hydrogen bonds and the London dispersion force. My goal as a researcher is to improve the descriptive power of currently-used computational methods, so that they can be used to address pressing needs in modern industries.

EDUCATION

Ph.D in Physics 2025
Wake Forest University, North Carolina, USA
- **Advisor**: Prof. Thonhauser
- **Field of Study**: Computational & Theoretical Solid State Physics
- **Thesis:** Modeling van der Waals Interactions with Density Functional Theory

B.Sc. in Physics 2019
University of North Carolina Asheville, North Carolina, USA
- **Advisor**: Prof. Lundgren
- **Field of Study**: Major in Physics with minor courses in Mathematics and Astronomy
- **Research**: Quantifying Star Formation in the Early Universe by Analyzing Adsorption Spectra of Quasar Light

CERTIFICATIONS & AWARDS

- Received Department of Physics Outstanding Peer-Mentor Award (2024)
- Received Award for Distinguished Service as a Teaching Assistant (2021)
- Received Physics B.Sc. Magna Cum Laude (2019)
- Inducted into the Physics Honors Society, $\Sigma\Pi\Sigma$ (2018)

PUBLICATIONS

*Indicates co-first authorship

1. **T. Jenkins**, K. Berland, & T. Thonhauser, Reduced-Gradient Analysis of van der Waals Complexes. *Electronic Structure, 3*(3), 034009 (2021). doi: 10.1088/2516-1075/ac25d7

2. S. Ullah, S. Jensen, K. Tan, G. Zhang, **T. Jenkins**, A. Elias, M.D. Gross, J. Li, & T. Thonhauser, Decoding the Gate Opening Mechanism of the Flexible Framework RPM3–Zn upon Hydrocarbon Inclusion. *Chem. Mater., 34*(7), 3246–3252 (2022). doi: 10.1021/acs.chemmater.2c00037

3. **T. Jenkins**, D. Chakraborty, K. Berland, & T. Thonhauser, Reduced-Gradient Analysis of Molecular Adsorption on Graphene with Nonlocal Density Functionals. *Phys. Rev. B, 109*(3), 035427 (2024). doi: 10.1103/PhysRevB.109.035427

4. F. Xie, L. Yu, **T. Jenkins**, J. Shutak, K. Tan, T. Thonhauser, H. Wang, & J. Li, Nickel Isonicotinate Framework with Optimal Pore Structure for Complete Discrimination of Hexane Isomers. *ACS Mater. Lett., 6*, 43–48 (2024). doi: 10.1021/acsmaterialslett.3c01278

5. **T. Jenkins**, A.M. Silva, M.G. Menezes, T. Thonhauser, & S. Ullah, THD-C Sheet: A Novel Nonbenzenoid Carbon Allotrope with Tetra-, Hexa-, and Dodeca-Membered Rings. *J. Phys. Chem. C, 128*(26), 10982–10996 (2024).
doi: 10.1021/acs.jpcc.4c01870

6. F. Xie, L. Yu, **T. Jenkins**, T. Thonhauser, H. Wang, & J. Li. Flexible Layered Metal-Organic Framework for Temperature-Dependent Discrimination of Cyclic Hydrocarbons. *ACS Mater. Lett., 7*, 780-786 (2025).
doi: 10.1021/acsmaterialslett.4c02402

7. S. Ullah*, **T. Jenkins***, K. Tan, J. Li, S.M. Winter, & T. Thonhauser, Effect of Entropic Constraints on the Thermodynamics of Molecular Adsorption in Nano-porous Materials. *Small*, pre-print (2025). doi: 10.1002/smll.202412312

8. **T. Jenkins**, S. Seyedroufi, K. Berland, & T. Thonhauser, van der Waals Density Functional Optimized for Molecular Solids. *Manuscript in preparation, to be submitted in May 2025 to Phys. Rev. B.*

9. **T. Jenkins**, S. Ullah, S.M. Winter, & T. Thonhauser, Effect of Conformational Isomerism on the Kinetics of Molecular Adsorption in Nano-porous Materials. *Manuscript in preparation, to be submitted in May 2025 to Chem. Mater.*

10. W. Graham, **T. Jenkins**, Y. Zeng, E. Hill, J.H. West, C. Fivecoat, S. Ullah, & T. Thonhauser, Selective Adsorption and Diffusion in MOF NU2100: A Computational Study. *Manuscript in preparation, to be submitted in June 2025 to ACS Mater. Lett.*

PRESENTATIONS

- **Oral Presentation at the 2025 APS Global Physics Summit** - Effect of Entropic Constraints and Conformational Isomerism on the Thermodynamics and Kinetics of Molecular Adsorption in Nano-porous Materials.
- **Poster at the Center for Functional Materials 2024 Research Day** - Effect of Entropic Constraints on the Thermodynamics and Kinetics of Molecular Adsorption in Nano-porous materials
- **Poster at the Center for Functional Materials 2023 Research Day** - The Diverse Applications of Metal–Organic Frameworks
- **Virtual Invited Talk at the Norwegian University of Life Sciences (2023)** - van der Waals Density Functional Optimized for Molecular Crystals.
- **Oral Presentation at the 2023 APS March Meeting** - van der Waals Density Functional Optimized for Molecular Crystals.
- **Oral Presentation at the 2022 APS March Meeting** - Reduced-Gradient Analysis of van der Waals Complexes.
- **Poster at UNC Asheville's Spring 2019 Research Symposium** - The Effectiveness of Peer Facilitated Study Groups in Encouraging Physics Student Learning and Attitudes

SKILLS

- **Languages**: English
- **Coding Languages**: Python, Mathematica, Bash, MATLAB, R
- **Electronic Structure Software**: VASP, Quantum ESPRESSO, VESTA, Avogadro, Jmol
- **Other**: LaTeX, Microsoft Office, Linux OS, Vim editor, Wordpress

RESEARCH EXPERIENCE

- Leading research into the properties of coordinated materials, working closely with experimentalists and theorists from other institutions.

- Modeling and characterizing materials such as metal–organic frameworks (MOFs) and $2D$ carbon allotropes. Extensive experience using the Vienna Ab-initio Simulation Package (VASP) and Quantum ESPRESSO, and visualization software such as Avogadro and the "Visualization for Electronic and STructural Analysis" software (VESTA).

- Developing new methods in density functional theory (DFT), particularly in the generalized gradient approximation (GGA) and with van der Waals density functionals (vdW-DF). Led projects that developed new functionals, improving upon the accuracy of currently-used techniques.

OTHER EXPERIENCE

Physics Teaching Assistant August 2019 – May 2025
Wake Forest University, North Carolina, USA

- Six years of experience independently teaching labs (in-person and remote), conducting tutorial sessions, and grading assignments for undergraduate physics courses. Subjects covered include Introductory Physics and Quantum Mechanics.
- Assisted in updating and revising Introductory Physics curricula, which included transferring Lab Manuals from Microsoft Word to LaTeX formatting and assisting in the creation of new lab exercises for undergraduate students.
- Multiple years of experience managing and updating the websites of the Wake Forest University's Physics Department and the Center for Functional Materials. Work was done in Word Press, and included adding publication information, updating departmental directories, and making announcements.

Honor Council Representative August 2020 – May 2025
Wake Forest University, North Carolina, USA

- Five years of experience serving on the Honor Council for the Graduate School of Wake Forest University. Duties included reviewing evidence for pre-honor hearing procedures and attending hearings for academic misconduct.

Physics Tutor August 2018 - May 2019
UNC Asheville, North Carolina, USA

- One year of experience as a tutor for the UNC Asheville Physics Department, independently conducting group study sessions for students of introductory physics courses.
- Conducted a study on Physics pedagogy, analyzing the effectiveness of peer facilitated study groups in encouraging student learning.

REFERENCES

Timo Thonhauser
(*Ph.D. supervisor*)
Professor
Dept. of Physics,
Wake Forest Univ.
thonhauser@wfu.edu

Stephen Winter
Professor
Dept. of Physics,
Wake Forest Univ.
winters@wfu.edu

Oana Jurchescu
Professor
Dept. of Physics,
Wake Forest Univ.
jurchescu@wfu.edu

Jing Li
(*Collaborator*)
Professor
Dept. of Chemistry,
Rutgers Univ.
jingli@rutgers.edu